Characterization of Ozone and the Oxidizing Capacity of the Tropical West Pacific Troposphere

Dissertation

Zur Erlangung des akademischen Grades
Doktor der Naturwissenschaften (Dr. rer. nat.)
im
Fachbereich Physik und Elektrotechnik
der
Universität Bremen

vorgelegt von

Katrin Müller

am 29.05.2020

1. Gutachter: Prof. Dr. Justus Notholt
2. Gutachter: Prof. Dr. Markus Rex

Kolloquium: Bremen, den 12.11.2020

Abstract

Motivated by previous measurements of very low tropospheric O_3 concentrations in the Tropical West Pacific (TWP) and the implied low oxidizing capacity of this key region for transport into the stratosphere, we set up an atmospheric research station in the center of the warm pool in Palau (7°N 134°E) and established a continuous balloon-borne O_3 measurement program with Electrochemical Concentration Cell (ECC) ozonesondes. Preparation, execution and quality management of the bi-weekly soundings and intensive measurement campaigns have been an integral part of this doctoral project, with this final thesis as the first presentation of the unprecedented 4-year time series. Furthermore, we show the development and first measurements of an instrumental device for in-flight monitoring of the so-called background current in ECC sondes.

Our analysis of the tropospheric O_3 observations at Palau from 01/2016-10/2019 confirms the year-round dominance of a low O_3 background in the mid-troposphere and a previously found strong annual O_3 cycle in the Tropical Tropopause Layer (TTL) in this part of the TWP. Layers of enhanced O_3 in the free troposphere (3-14 km) are often anti-correlated with water vapor (H_2O) and occur frequently (referred to as "O_3+RH-"). A previously proposed universal bimodal structure of free tropospheric O_3 in the TWP in this context could not be verified. Moreover, the occurrence of respective layers shows a strong seasonality. The seasons FMA (February-March-April) and ASO (August-September-October), shifted by one month compared to the mid-latitude seasons, are identified as most disparate, both regarding the frequency of O_3+RH- air intrusions and their background O_3 values. We quantified the seasonal differences by defining a monthly atmospheric background profile for O_3 and relative humidity (RH) based on observed statistics. Deviations from this background reveal a bimodal distribution of RH anomalies for all seasons except the MJJ (May-June-July) season. Observations of O_3+RH- air in the 5-10 km altitude range were made in 71 % of profiles in FMA compared to 25 % in ASO.

Back trajectory calculations confirm that throughout the year the mid-tropospheric background is controlled by local convective processes and the origin of air masses is the Pacific Ocean, mainly East of Palau. Dry and ozone-rich air (O_3+RH-) originates in tropical Asia and reaches Palau in anticyclonic conditions over an area stretching from India to the Philippines. This supports the hypothesis of several studies which attribute O_3 enhancement against the low O_3 background to pollution events on the ground such as biomass burning. A potential vorticity (PV) analysis revealed no stratospheric influence, and we thus propose large-scale descent within the tropical troposphere as responsible for dehydration of air masses on their way to Palau.

The relevance of distinct layers deviating from the background led us to investigate their influence on the otherwise low oxidizing capacity of the TWP. Chemical box model calculations constrained by our O_3 and H_2O measurements for clear sky conditions at 400 hPa in Palau in ASO revealed that the predominant anti-correlation of O_3 with H_2O buffers the effect of both constituents on daily mean OH concentrations.

Table of contents

Titlepage . . . i
Table of Contents . . . v
List of Figures . . . vii
List of Tables . . . xi

1. Introduction 1

2. Atmospheric Dynamics and Chemistry in the Tropical West Pacific 5
- 2.1. Tropospheric Dynamics and Transport . . . 5
  - 2.1.1. General Circulation . . . 5
  - 2.1.2. Fluctuations of the General Circulation . . . 8
  - 2.1.3. Convective Activity . . . 10
  - 2.1.4. Stratosphere-Troposphere Exchange . . . 14
- 2.2. Tropospheric O_3 Chemistry and Oxidizing Capacity . . . 17
  - 2.2.1. O_3 Production and Loss . . . 18
  - 2.2.2. OH Production and Loss . . . 21
  - 2.2.3. Impact on Chemical Lifetimes and STE . . . 22

3. Observations and Modelling 23
- 3.1. ECC Ozonesonde Observations . . . 23
  - 3.1.1. Measurement Principle . . . 24
  - 3.1.2. Measurement Uncertainties . . . 25
  - 3.1.3. Operating Procedures and Post-processing . . . 28
  - 3.1.4. Instrumental Development . . . 30
- 3.2. Overview of the Palau Time Series . . . 36
  - 3.2.1. Data Description/Time frame . . . 36
  - 3.2.2. Technical Details/Issues . . . 36
  - 3.2.3. Statistical Assessment . . . 39
- 3.3. Auxiliary Observational Data . . . 41
  - 3.3.1. SHADOZ Stations . . . 42
  - 3.3.2. Palau Weather Station (NOAA) . . . 44
- 3.4. Modelling and Methods . . . 45
  - 3.4.1. Trajectory Analysis . . . 45
  - 3.4.2. Chemical Box Model . . . 46

4. Results and Discussion 49
- 4.1. Tropospheric O_3 Variability . . . 49
  - 4.1.1. Overview . . . 49

4.1.2. Mid-tropospheric Cycle . . . 57
4.1.3. TTL Cycle . . . 59
4.2. Background Atmosphere and Deviating Layers . . . 61
4.2.1. General Definition . . . 61
4.2.2. Relation between O_3 and Relative Humidity . . . 63
4.2.3. Identification of the Background Atmosphere . . . 74
4.2.4. Relevance of O_3+RH- Layers . . . 80
4.2.5. Discussion . . . 82
4.3. Transport and Origin . . . 84
4.3.1. Transport Pathways . . . 84
4.3.2. Trajectory Analysis Results . . . 86
4.3.3. Discussion . . . 94
4.4. Oxidizing Capacity . . . 97
4.4.1. Chemical Box Model Constraints . . . 97
4.4.2. Chemical Box Model Results . . . 98
4.4.3. Discussion . . . 104

5. Summary and Outlook 106

Acknowledgements 109

Acronyms 113

Bibliography 117

A. Appendix 139
A.1. Stratosphere-Troposphere Exchange (Sect.2.1.4) . . . 139
A.2. Instrumental Development (Sect.3.1.4) . . . 140
A.3. Tropospheric O_3 Variability (Sect.4.1) . . . 142
A.4. Relation between O_3 and Relative Humidity (Sect.4.2.2) . . . 144
A.5. Trajectory Analysis Results (Sect.4.3.2) . . . 146

List of Figures

1.1. Overview of the instrumentation at the Palau Atmospheric Observatory . . 4

2.1. Schematic of the ITCZ movement across Palau 7
2.2. North-South march of the ITCZ averaged from TRMM (1998-2009) 8
2.3. Anomalies in OLR above the TWP from the climatological mean (1981-2010) 9
2.4. Climatology of the Cold Point Tropopause, Lapse Rate Minimum and average Outgoing Longwave Radiation for Koror, Palau, and Darwin, Australia 11
2.5. Different atmospheric layers related to convective activity in the TWP and annual mean profiles of static stability 13
2.6. Schematics of the TTL in a latitude-height cross-section showing major dynamical influences and as defined by profiles of temperature, potential temperature gradient, O_3 and water vapor 17

3.1. Uncertainties of individual parameters relative to O_3 partial pressure with altitude 25
3.2. Tropospheric O_3 VMR profile examples and the effect of different background current corrections 27
3.3. Background current I_{b2} for all Palau soundings 28
3.4. Images of the technical setup of ozonesonde and device 31
3.5. Sensor current measurements for two dual launches 33
3.6. O_3 VMR profiles for a dual launch with a modified and unmodified ECC sonde 34
3.7. Sensor current and differences between sondes for a trio launch in Ny Ålesund 34
3.8. Tropospheric (0-20 km) time-height cross-sections of the Palau sounding data for O_3 VMR and RH 37
3.9. Tropospheric O_3 VMR profiles from intensive sounding campaigns 2016 until 2018 38
3.10. Time series (2006-2009) of tropospheric column O_3 at Palau derived from TES 38
3.11. Illustration of four different averaging approaches to arrive at a seasonal mean 41
3.12. Comparison between seasonal mean and median, illustrated as absolute difference and by unbiased sample skewness 42
3.13. Map of SHADOZ site locations 43
3.14. Tropospheric time-height cross-section for zonal and meridional wind at the Palau weather station 44

4.1. TTL (14-20 km) time-height cross-section of the Palau sounding data for O_3 VMR and temperature 51

4.2. Monthly arithmetic means, anomalies from the annual mean and the annual mean profiles . . . 52
4.3. Zonal and meridional wind monthly means derived from daily radio soundings at the Palau weather station . . . 53
4.4. Seasonal mean O_3 VMR profiles for Palau . . . 54
4.5. Variability of seasonal mean O_3 VMR profiles for Palau against the long-term annual mean . . . 55
4.6. Mean O_3 VMR of individual soundings of all years in 300 m layers . . . 58
4.7. Statistical measures for the 5-10 km altitude range . . . 59
4.8. Tropospheric (0-20 km) time-height cross-section of the Palau sounding data for O_3 VMR with coinciding RH observations below 30 % . . . 59
4.9. Example tropospheric O_3 and RH profiles for the background atmosphere and deviating layers . . . 62
4.10. Free-tropospheric (3-14 km) relation between O_3 and RH . . . 65
4.11. Boxplots for free-tropospheric (3-14 km) O_3 VMR $\leq$ 100 ppb, colored by the group categories derived from O_3/RH distributions . . . 66
4.12. Seasonal free-tropospheric (3-14 km) relation between O_3 and RH for group 3 stations, including Palau . . . 68
4.13. Seasonal free-tropospheric (3-14 km) relation between O_3 and RH for group 1 and group 2 stations . . . 69
4.14. Fraction of occurrences of O_3 VMR below 20 ppb at different altitude levels 72
4.15. Relative frequency distribution (normalized to the layer maximum) of tropospheric (0-15 km) O_3 VMR with altitude . . . 73
4.16. Monthly O_3 VMR statistics for Palau tropospheric profiles per km . . . 76
4.17. Monthly RH statistics for Palau tropospheric profiles per km . . . 77
4.18. Free-tropospheric (3-14 km) relation between O_3 and RH for Palau in absolute values and as an anomaly from the monthly background profiles . . . 78
4.19. Seasonal free-tropospheric (3-14 km) relation between O_3 and RH for Palau 79
4.20. Occurrence of air masses classified in nine O_3RH groups within each season for Palau observations in the 5-10 km altitude range . . . 81
4.21. Schematic for transport pathways to Palau . . . 85
4.22. 10-days backward trajectories by season and altitude level . . . 88
4.23. Backward trajectory ending points at 5-10 km by season and 3, 5 or 10 days backwards . . . 89
4.24. 5-days backward trajectory ending points at 5-10 km by season, color-coded either by difference in pressure altitude or RH . . . 93
4.25. 5-days backward trajectory ending points at 5-10 km, color-coded by season and difference in pressure altitude for air masses of different O_3RH groups . 95
4.26. Box modeled daily mean OH VMR in relation to daily mean O_3 VMR for varying NO_x and CO VMR . . . 98
4.27. Box modeled daily mean OH VMR at 400 hPa for varying O_3 and H_2O VMR, with fixed NO_x and CO VMR in clear-sky conditions . . . 100
4.28. Box modeled daily mean OH VMR in relation to O_3 VMR input for varying H_2O and NO_x, with fixed CO at 400 hPa in clear-sky conditions in ASO . 103

A.1. Meridional cross-section illustrating Stratosphere-Troposphere Exchange . 139
A.2. Sensor current measurements for a twin launch . . . 140

A.3. Modified ECC sonde launched in Palau, 02.02.2016 141
A.4. Comparison of all averaging versions for the seasonal mean 142
A.5. Comparison between mean and median for seasonal averages 143
A.6. All measured individual O_3 VMR profiles sorted by month and year 144
A.7. Seasonal relative frequency distribution of tropospheric O_3 VMR with altitude for selected cases 145
A.8. 5-days backward trajectory ending points arriving at 2-5 km per season, color-coded by difference in pressure altitudes 146
A.9. 5-days backward trajectory ending points arriving at 10-14 km per season, color-coded by difference in pressure altitudes 147
A.10. 10-days backward trajectories arriving at 2-5 km, 5-10 km and 10-14 km by season, color-coded by O_3 VMR 148
A.11. 5-days backward trajectory ending points arriving at 5-10 km color-coded by season and difference in pressure altitude for air masses of different O_3RH groups 149
A.12. Seasonal KDE distributions of O_3RH groups from 5-days backward trajectories within 5-10 km 150

List of Tables

1.1. Overview of important tropospheric O_3 research activities in the TWP . . 3

3.1. Major specifications and SOP of O_3 soundings at the PAO 29
3.2. SHADOZ sites and respective time record used in this thesis 43

4.1. Overview of the number of profiles and data points per season and altitude range used in the trajectory analysis 86
4.2. Box modeled daily mean OH VMR cases at 400 hPa 101

1. Introduction

> Ungil a eanged.
> The heavens are good.
>
> *(Palauan saying)*

Ozone (O_3) is an important component of the troposphere. As a chemically active species with a wide range of lifetimes, it has a great temporal and spatial variability (Hartmann et al., 2013). Although 90 % of atmospheric O_3 resides in the stratosphere, comprising the important ozone layer, the tropospheric fraction has great influence on the Earth's climate and life. As a toxic substance, it is harmful for humans and plants on the ground, where it is produced in situ by photo-chemical reactions of precursor gases, for example combustion products which lead to development of photo-chemical smog. Free tropospheric O_3 is a powerful greenhouse gas with a substantial contribution to global radiative forcing (RF). The present-day RF due to changes in tropospheric O_3 based on changes in anthropogenic emissions is estimated as 0.40 $W\ m^{-2}$, i.e. comparable to the RF of methane (Myhre et al., 2013). O_3 plays a crucial role for atmospheric composition as it controls oxidation processes in the troposphere via its photo-chemical derivative, the hydroxyl (OH) radical. The short-lived OH defines the lifetime of hundreds of chemical species and thus the oxidizing capacity of the troposphere (see Sect.2.2.3). As it is difficult to measure in situ, the variability of tropospheric OH in space and time continues to be an active field of research (e.g. Montzka et al., 2011).

In the Tropical West Pacific (TWP), an area extending from the Maritime Continent to the International Date Line, the oxidizing capacity is of great relevance. The region is considered the major transport pathway from the troposphere to the stratosphere during Northern Hemispheric (NH) winter (Fueglistaler et al., 2004; Krüger et al., 2008; Newell and Gould-Stewart, 1981). Air masses entering the stratosphere here also originate in the TWP boundary layer (Rex et al., 2014). Palau (7.34° N 134.47° E), a small island nation in Micronesia, is located right in the center of the TWP warm pool area, with the highest global sea surface temperatures (SST) (see map in Fig.2.3). The resulting high energy convection comprises the upwelling branches of global atmospheric circulation patterns, which are following the seasonal movement of the Intertropical Convergence Zone (ITCZ). Driven mainly by the tropical Hadley circulation, surface winds are predominantly transporting clean, Pacific air to the TWP and Palau from the East which has not undergone much anthropogenic influence. This dynamically interesting setup is complemented by the unique chemistry of the clean, marine air. O_3 destruction in the local boundary layer and vertical mixing by convection leads to a zonal wave-one pattern in column O_3 with a persistent tropospheric O_3 minimum in the TWP (see e.g. Rex et al., 2014; Thompson et al., 2003a). The close coupling of O_3 and OH in this environment (Levy, 1971) fosters a corresponding OH minimum in the TWP, which can be estimated from O_3 and water vapor (H_2O) measurements (Kley et al., 1996; Rex et al., 2014). The resulting increased lifetimes of chemical species can lead to enhanced entry into the global stratosphere, which is not captured well in atmospheric models (Rex et al., 2014). The Tropical Tropopause Layer (TTL), with its globally lowest temperatures, controls final dehydration of air masses and thus stratospheric H_2O, a driver of important O_3 loss cycles in the stratosphere (Randel and Jensen, 2013). A dynamically driven seasonal cycle of O_3 in the TTL, in turn, influences TTL temperatures (Randel et al., 2007).

The monitoring and seasonal characterization of O_3 in the TWP is therefore of great relevance to improve our understanding of this hot spot for stratosphere-troposphere exchange (STE). Balloon-borne measurements with Electrochemical Concentration Cell (ECC) ozonesondes are the most practical way to observe O_3 in situ, especially at more remote sites (see e.g. Thompson et al., 2019). The high vertical resolution of O_3 profiles obtained with ECC sondes and long-term time series are essential for satellite data retrieval algorithm development and later validation (e.g. Hubert et al., 2016). Ground-based instrumentation observing column O_3, e.g. FTIR and microwave sounders, are validated by O_3 soundings as well (e.g. Vigouroux et al., 2008). The ECC sonde measurement technique itself is being continuously validated to yield a current overall accuracy of 5 %-15 % in the troposphere, if standard operating procedures are followed (see Smit et al., 2007; Thompson et al., 2019). Careful procedural techniques are of paramount importance especially in the Tropics, as the instrumental uncertainty is highest in the TTL and critically dependent on the so-called background current. Reports of near-zero O_3 concentrations in the upper troposphere (UT) of the TWP (Kley et al., 1996; Rex et al., 2014) have been accused of a lack of quality in sonde operation by other studies (Newton et al., 2016; Voemel and Diaz, 2010).

The TWP constitutes a gap in the international O_3 sounding network (see `https://woudc.org/data/stations/`). However, temporally limited research activities focusing on tropospheric air chemistry have been conducted in the wider region since the late 1980s (see Tab.1.1 for an overview of important studies). They highlight the importance of O_3 as a tracer for both convective processes and long-range transport to the region (e.g. Pan et al., 2015). Dry intrusions of enhanced O_3 volume mixing ratios (VMR) have been reported as a characteristic feature of the mid-troposphere for the wider tropical Pacific by many studies (see Anderson et al., 2016). The origin and impact of these distinct layers on the local radiative budget and oxidizing capacity are the subject of an ongoing debate (Anderson et al., 2016; Randel et al., 2016, see Sect.4.2.4). Backward trajectories based on meteorological reanalysis data are a common tool to assess air mass origin and transport pathways in this context.

Within the EU-project StratoClim (`www.stratoclim.org`), which focused on dynamics and chemistry of pathways to the stratosphere mainly in the Asian Monsoon region, the Palau Atmospheric Observatory (PAO) was established to fill the observational gap in this key region of stratospheric entry. Figure 1.1 gives an overview of the comprehensive setup of the station, which includes the balloon program with ECC, water vapor (CFH) and aerosol (COBALD) sondes, a Fourier transform infrared (FTIR) instrument, measuring

Acronym	Title	Timeframe	(Lead) Publications
TOGA-COARE	Tropical Ocean and Global Atmosphere Response Experiment	1988	Kley et al., 1997
PEM Tropics/West	Pacific Exploratory Missions	09/10 1991, 02/03 1994	Hoell et al., 1999; Newell et al., 1996
CEPEX	Central Equatorial Pacific Experiment	1993	Kley et al., 1996
MOZAIC	Measurement of Ozone and Water Vapor by Airbus In-Service Aircraft	1994-2004	Newell et al., 1999; Thouret et al., 2000
STRAT	Stratospheric Tracers for Atmospheric Transport	1995-6	Jaeglé et al., 1997; Wennberg et al., 1998
BIBLE	Biomass Burning and Lightning Experiment	09/10 1998, 08/09 1999	Kita et al., 2002; Kondo et al., 2002
SHADOZ	Southern Hemispheric ADditional Ozonesondes	1998-present	see Sect.3.3.1
TransBrom	Short lived bromine compounds in the ocean and their transport pathways into the stratosphere	10/2009	Krüger and Quack, 2013; Rex et al., 2014; Ridder et al., 2012
CONTRAST, CAST, ATTREX	Convective Transport of Active Species in the Tropics, Coordinated Airborne Studies in the Tropics, Airborne Tropical Tropopause Experiment	01/02 2014	Jensen et al., 2017a; Pan et al., 2017
StratoClim – PAO	Stratospheric and upper tropospheric processes for better Climate predictions – Palau Atmospheric Observatory	2016-present	this thesis
POSIDON	Pacific Oxidants, Sulfur, Ice, Dehydration, and cONvection	10/2016	Jensen et al., 2017b, measurements at PAO
ACCLIP	Asian Summer Monsoon Chemical Impact Project	planned for 07/2021	measurements planned at PAO
TroStra	Transport of tracegases via the tropopause region in the WP observed by FTIR spectrometry	2020-2023	measurements at PAO

Table 1.1.: Overview of important tropospheric O_3 research activities in the Tropical West Pacific (as referenced in this study); most relevant activities for this study are highlighted in bold letters.

total and partial columns of a variety of chemical species (incl. O_3 and COS), a Multi Axis Differential Optical Absorption Spectroscopy (MaxDOAS) instrument (Pandora-2S, `www.pandonia-global-network.org`) for total column O_3, NO_2 and aerosols and a lidar system (MuLid in 2016, ComCAL since 2018), measuring cloud and aerosols. The specific focus of this doctoral project was to establish the first multi-year time series of tropospheric O_3 above Palau to capture seasonal and to a certain extent inter-annual variations of this important trace gas. After an introduction to dynamical and chemical processes relevant for the tropospheric O_3 and OH distribution in the TWP (Chapt.2), Chapter 3 describes the methods behind our observational and modelling approaches. We carried out careful execution of recommended operating routines (Smit, 2014, Sect.3.1.3) in order to address the controversy of near-zero O_3 measurements in the TWP. In an experimental assessment of the critical background current parameter (Voemel and Diaz, 2010), we developed an instrumental device to measure it in-flight, which was extensively

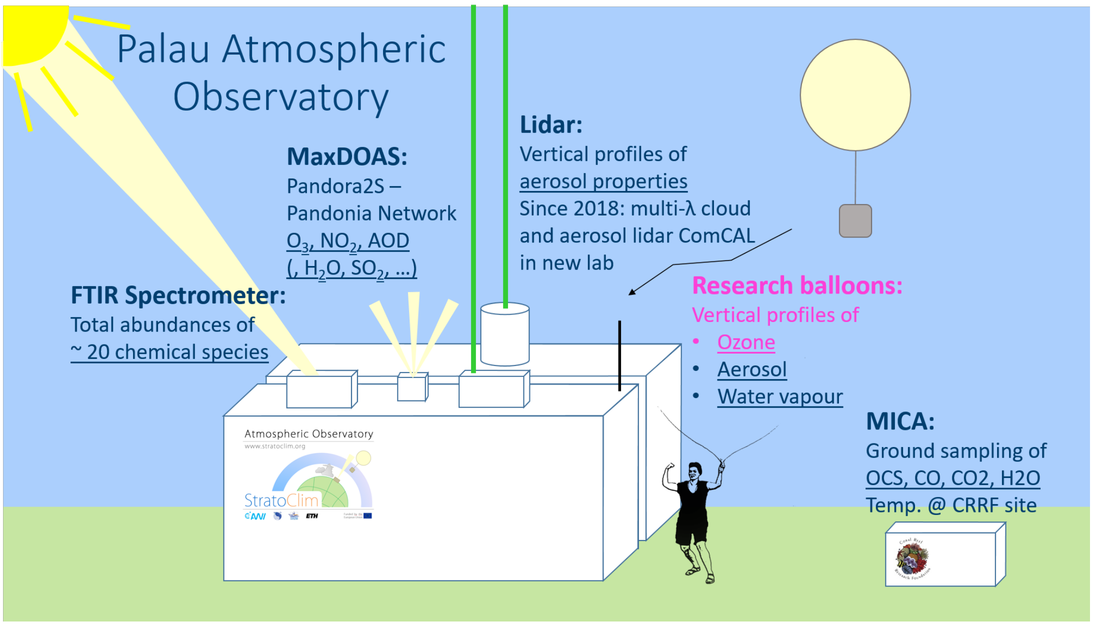

Figure 1.1.: Overview of the instrumentation at the Palau Atmospheric Observatory (PAO), original image design by Markus Rex, original photo by J.Graeser.

tested in the laboratory and field (Arctic and tropical conditions, see Sect.3.1.4). A first descriptive overview of the Palau time series is given in Sect.3.2, followed by the introduction to other observational data used in this study (Sect.3.3). Chapter 4, the presentation and discussion of our results, begins with an extensive statistical assessment of the data set to establish seasonal characteristics (Sect.4.1). We then put the Palau measurements into context in the TWP and greater Tropics in a comparison with data from selected SHADOZ stations and the CONTRAST campaign (see Tab.1.1, Sect.4.2). Section 4.2.3 presents the identification of a local background atmosphere and deviating layers from this background, enabled by the unique nature of the free-tropospheric O_3/RH distribution in Palau. We use the resulting classification of air masses with respect to their O_3/RH content in a back trajectory analysis for the full climatology of soundings to examine transport pathways, their seasonality and underlying processes, presented in Section 4.3.2. Finally, we simulate the oxidizing capacity of the clean background atmosphere with a chemical box model and study the effects of layers deviating from this background (Sect.4.4). This thesis closes with a summary of the main results and an outlook for how the expanding Palau time series will shed more light on remaining research questions in this unique region (Chapt.5).

This doctoral project has resulted in nearly 4 years of data including 145 ECC ozone soundings, giving insight into the seasonality of tropospheric O_3 above Palau. A characteristic zonal annual cycle in the TTL was observed, with a low O_3 background dominating from July until October and layers of enhanced O_3 most frequently occurring from February until April. The maximum of the mid-tropospheric cycle can be associated with long-range transport mainly from potentially polluted areas West of Palau by back trajectory analysis. There was no evidence of transport from the extra-tropical stratosphere. The anti-correlation of O_3 and RH in dry, ozone-rich layers which interrupt a low O_3 and high RH background atmosphere buffers their effect on the oxidizing capacity.

2. Atmospheric Dynamics and Chemistry in the Tropical West Pacific

Ozone is a chemically active compound of the atmosphere. A wide range of lifetimes in the troposphere, between days and several months, leads to different, also nonlinear interactions and patterns of temporal and spatial variability (e.g. Hartmann et al., 2013). The tropospheric O_3 abundance above the Tropical West Pacific (TWP) is affected by long-range transport and local photo-chemistry alike. In the following, most important dynamical and chemical processes relevant to this study are introduced.

2.1. Tropospheric Dynamics and Transport

On a global scale and averaged over a climate-relevant period the tropospheric flow is characterized by the general circulation, maintaining local thermal equilibrium by horizontal heat transfer (Sect.2.1.1). Palau's climate is specifically affected by the position of the Innertropical convergence zone (ITCZ), the Western Pacific Monsoon (WPM) and the trade winds. In this context subseasonal and interannual variations are considered as low-frequency fluctuations (Sect.2.1.2). Dealing with observational in situ profiles, we often consider the motion of a single air parcel or well-defined local air mass. Thus, weather-related phenomena add to the complexity and variability of air transport and composition. The TWP warm pool area in particular is a global center of (deep) convective activity inducing large-scale mixing (Sect.2.1.3). High-energy uplift of tropospheric air is complemented by tropical upwelling in the Tropical Tropopause Layer (TTL), making this a globally unique region of Stratosphere-Troposphere-Exchange (STE) (Sect.2.1.4).

2.1.1. General Circulation

The Palau Atmospheric Observatory's (PAO) location at 7.3° N and 134.5° E in the TWP warm pool is a hotspot for the complex interplay of general circulation patterns, such as the Hadley, Walker and Monsoon Circulations. The year-around high sea surface temperatures (SST) and moist marine environment guarantee high upward fluxes of latent and sensible heat (e.g. Salby and Salby, 2012). Thus convective processes are closely tied to the large scale atmospheric motion.

Hadley

The thermally direct meridional Hadley circulation is a closed-cell overturning circulation between 35° N and 30° S. The uprising branch lies within the Intertropical Convergence Zone (ITCZ, see below) and is associated with condensation and cloud formation (see Sect.2.1.3). Diverging air in the upper troposphere detrains from clouds and flows pole-wards. During descent at the tropics of Cancer/Capricorn, collocated with the subtropical high pressure systems, air masses are warmed and convective activity is suppressed. On the ground, the easterly trade winds close the Hadley circulation. Under the influence of the Coriolis force, they are inclined from the ideal pole-wards flow. Over the Pacific and in the mean, trade winds prevail even in higher tropospheric altitudes and anti-trades are missing (e.g. Riehl, 1954). These deep trades or equatorial easterlies are restricted to a zonal band, narrow in winter and broadest in summer. In the special case of Palau, the strong southern easterlies reach the islands as westerlies (after crossing the equator) during the monsoon season from July until October. In general, the Hadley circulation and thus the trade winds are strongest in the winter time of the respective hemisphere (e.g. Holton, 2004). It then controls the occurrence and position of subtropical highs. In summer, the subtropical ridge is tied to planetary waves.

Walker

In the vicinity of the equator with a lack of Coriolis force a major thermodynamic circulation also forms on the zonal-height plane, driven by surface temperature differences and the resulting pressure gradients. The so-called Walker circulation has its strongest rising branch over the Maritime Continent, where SST are globally highest and surface roughness is low. For this dominant Pacific cell, air masses are sinking again in the equatorial Eastern Pacific. The trade winds transport air across the Pacific from east to west on the surface, while upper-level west winds connect ascending and descending branches. During extreme El Niño conditions this circulation can be completely reversed (see Sect.2.1.2, Bjerknes, 1969). For Palau, the combined effect of Walker and Hadley circulation manifests itself in the dominance of North Easterly (NE) winds and high convective activity.

Intertropical Convergence Zone

The dynamical situation in Palau is closely linked to the migration of the Intertropical Convergence Zone (ITCZ). It is defined as a near-equatorial band, where moist and warm trade winds converge, forming the ascending branches of the Hadley and Walker circulation. Usually, it is determined as a belt of deep convective clouds (Waliser and Gautier, 1993) or a maximum in mean precipitation (Philander et al., 1996, see Fig.2.1). On average, the ITCZ is located 6° North of the equator, but it moves towards the warming hemisphere throughout the year with interannual variations e.g. caused by the ENSO (see Sect.2.1.2, see Fig.2.2). The mechanisms controlling its position and rainfall intensity are not fully understood (Schneider et al., 2014). Near the maritime continent, a band of convergence splits from the ITCZ and the TWP warm pool and stretches southwards, forming the so-called South Pacific Convergence Zone (SPCZ). Palau's location is close to the ITCZ throughout the year, but closest during its northern most position, from July until October (see Fig.2.2, Shonk et al., 2018; Smith et al., 2012). The dominant influence of the Northern Hadley cell and transport of air masses to Palau with the NE trade winds is only interrupted during these few months. Figure 2.1 displays the importance of the position for Palau's surface wind regime and rainfall. In summer, the West Pacific Monsoon (WPM, see below) brings heavier rainfall to Palau with SE trade winds deflected west after crossing the equator (compare maximum in OLR in Fig.2.4, Sect.2.1.3). In the wedge between ITCZ and SPCZ in late summer/fall, the high convective energy shields Palau from continental outflow and transport of polluted air to the region (Browell et al., 2001).

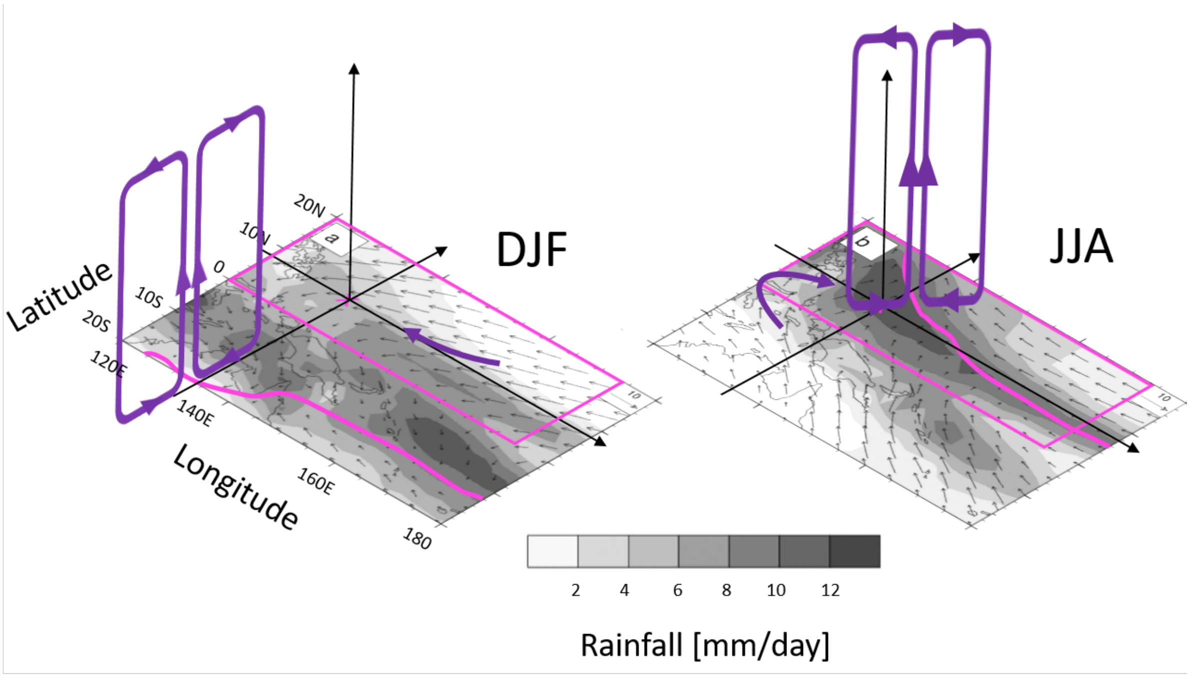

Figure 2.1.: Schematic of the ITCZ movement across Palau (pink cross and centre of coordinate plane); on the horizontal plane, maps show climatological (1971-2000) seasonal rainfall (shaded gray contours, in mm/day) and near-surface winds (arrows) for winter (left panel, December, January, February: DJF) and summer (right panel, June, July, August: JJA), the pink line highlights the approximate position of the ITCZ, the pink box indicates the region used for averaging in Fig.2.2, the purple line highlights the trade winds approaching Palau; on the vertical plane, the two schematic Hadley cells, following the location of the ITCZ, are indicated in purple (adapted from Smith et al., 2012, see original source for details on the data).

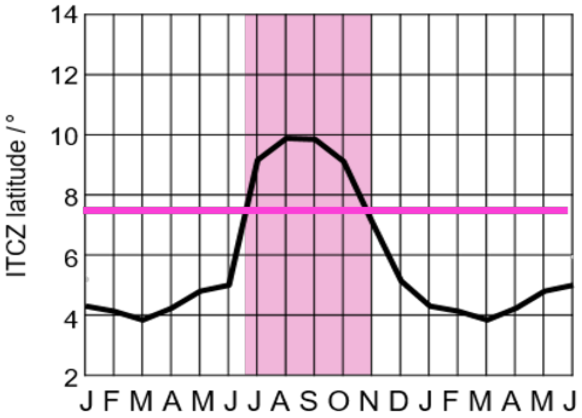

Figure 2.2.: North-South march of the ITCZ averaged from TRMM (1998-2009) for 125-175° E, 0-20° N (see pink box in Fig. 2.1), pink line indicates Palau's latitude, pink shading the months with the ITCZ located north of Palau (adapted from Shonk et al., 2018).

Western Pacific Monsoon

The Western Pacific Monsoon (WPM) is considered as the eastern edge of the Australian/Asian Monsoon system. It affects a broad region in the West Pacific on both hemispheres, which experiences low-level westerly winds and increased rainfall during the wet season. As a seasonal climate phenomenon, it is affected by both natural climate variability and climate change (e.g. Brown et al., 2013; Smith et al., 2012). In Palau, the heavy rainfall during the WPM (> 400 mm/month, PCCSR, 2011; 9-12 mm/day, Brown et al., 2013) exerts a strong seasonal influence on the atmospheric moisture profile despite high average rainfall throughout the year (see Sect.2.1.3). The high moisture favors O_3 destruction and convective uplift redistributes low O_3 in the entire tropospheric column (see Sect.2.2.1 and 4.2.1). Low-level equatorial westerlies and rainfall are positively correlated in the Palau region (Smith et al., 2012) and model projections suggest increasing strength in both (Brown et al., 2013), which presumably strengthens the minimum O_3 season in Palau.

2.1.2. Fluctuations of the General Circulation

The general circulation is affected by large temporal fluctuations, also called low frequency variations. In the TWP, the most relevant phenomena are the El Niño Southern Oscillation (ENSO) and the Madden-Julian Oscillation (MJO).

El Niño Southern Oscillation

Interannual variations of tropospheric O_3 in the TWP are dominated by the El Niño Southern Oscillation (ENSO) (e.g. Gettelman and Forster, 2002; Shiotani, 1992; Smith et al., 2012). This coupled ocean-atmosphere phenomenon first described by Bjerknes (1969) is characterized by low frequency variations in SST, sea-level pressure, surface winds and outgoing longwave radiation (OLR) over the equatorial Pacific. Via teleconnections it most prominently affects remote regions in the extra-tropics. The predictability of the ENSO cycle is still a field of active research (e.g. Hartmann et al., 2013). In the TTL, the coupling between ENSO and the Quasi-Biennial Oscillation (QBO) is a main driver of interannual variability of O_3 and H_2O (e.g. Diallo et al., 2018; Garfinkel and Hartmann, 2007; Taguchi, 2010).

There are various indicators tracking the progress of the oscillation by using observations from different key parameters. The most prominent indices are the Southern Oscillation Index (SOI) and Equatorial SOI, the Oceanic Nino Index (ONI) and the Multivariate ENSO Index (MEI). The SOI compares the sea-level air pressure between the western and eastern tropical Pacific, Tahiti and Darwin, Australia (Allan et al., 1991; Troup, 1965). The equatorial SOI uses average sea-level pressures over larger equatorial regions centered over Indonesia and the eastern central Pacific (Bell and Halpert, 1998). These two indices correlate well with changes in ocean temperatures, which are in turn focus of the ONI, a 3-month running mean of SST anomalies in a certain equatorial region (Nino 3.4, used by NOAA, see e.g. Bamston et al., 1997). The bi-monthly MEI combines oceanic and atmospheric variables in an Empirical Orthogonal Function (EOF) based analysis (Wolter and Timlin, 2011). For each index, threshold criteria are used to mark a strong enough departure from neutral conditions to call out an extreme ENSO event.

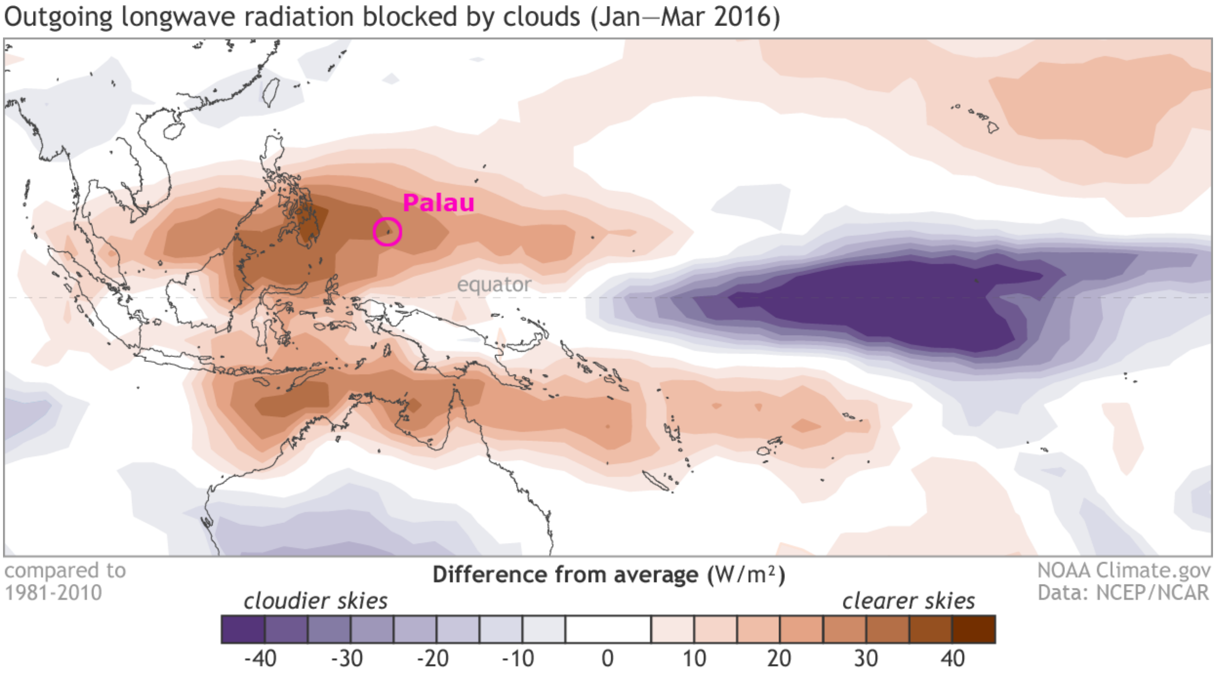

Figure 2.3.: Anomalies in outgoing longwave radiation (OLR) above the TWP from the climatological mean (1981-2010) based on NCEP/NCAR reanalysis for January until March 2016, positive anomalies (brown colors) indicate clearer skies, negative anomalies (purple colors) cloudier skies, location of Palau marked with a pink circle; adapted from Di Liberto, 2016.

During El Niño, the so-called warm phase, the warm pool shifts towards the central Pacific. The TWP in turn experiences negative SST and positive OLR anomalies and weakening of the trade winds, i.e. suppressed convection and less cloud coverage and precipitation (compare Fig.2.3). For La Niña episodes (the cold phase), the opposite conditions dominate.

The beginning of the Palau time series in January 2016 coincides with a very strong record El Niño event (according to ONI). The two indices SOI and MEI show a return to neutral conditions in this context in May and May/June 2016 respectively. Compared to earlier El Niño events this change occurs early in the year. The following years 2017 and 2018 show departures from normal conditions towards La Niña (so-called "double dip La Niña"). Since September 2018 a subtle El Nino pattern was present but only in February 2019 the index threshold was crossed. This weak El Nino event lasted until August 2019.

Madden-Julian Oscillation

Intraseasonal variations in equatorial convection and thus the atmospheric composition of the TWP are mainly caused by the Madden-Julian Oscillation (MJO). This half-understood tropical phenomenon is characterized by anomalous patterns of cloud and rainfall propagating eastward with time periods of 30 to 90 days (Madden and Julian, 1971, 1994; Yoo and Son, 2016). An assessment of this variability goes beyond the scope of the first analysis of the Palau time series, but will be interesting in the future. The MJO impacts many aspects of the tropical weather and climate system and modulates tropospheric moisture and O_3 variability over the TWP (e.g. Yoneyama, 2003; Ziemke et al., 2007). Its complex interplay with other atmospheric fluctuations like ENSO and the QBO (see Sect.2.1.4) is under ongoing investigation (e.g. Hendon and Abhik, 2018; Yoo and Son, 2016; Zhang and Zhang, 2018)

2.1.3. Convective Activity

Convection plays a fundamental role in maintaining various tropospheric circulation patterns occurring in the tropics. In terms of atmospheric chemistry, it promotes both the formation or destruction of O_3 and thus complicates realistic simulations (e.g. Thompson et al., 1997, see Sect.4.4). Whether transport or local convective processes and thus vertical mixing determine TWP air composition, depends on the strength of convective activity. During transport, the vertical displacement of air parcels is also affected by large scale convection resulting in uplift. In clear-sky conditions radiative cooling by water vapor and subsidence of air masses dominate (e.g. Folkins and Martin, 2005; Gettelman and Forster, 2002).

Climatological Overview

The tropics in general show little fluctuation in the amount of sunlight, resulting in a uniform tropospheric temperature distribution throughout the year. Seasonal variations in weather or air composition in the TWP are therefore mostly attributed to changes in precipitation and related to the shifting of the ITCZ and SPCZ. According to the Köppen classification, Palau has a tropical rainforest or equatorial climate: hot, humid and wet conditions all year, with no distinct dry season (precipitation always above 200 mm/month, see PCCSR, 2011). The year-round deep convective activity for Palau can be explained by the continuous vicinity of the ITCZ. Months drier than others coincide with the most southern position of the ITCZ (see Fig.2.2). Highest convective activity occurs from June until October, lowest in March/April according to a long-term OLR climatology derived from satellite observations (see Fig.2.4).

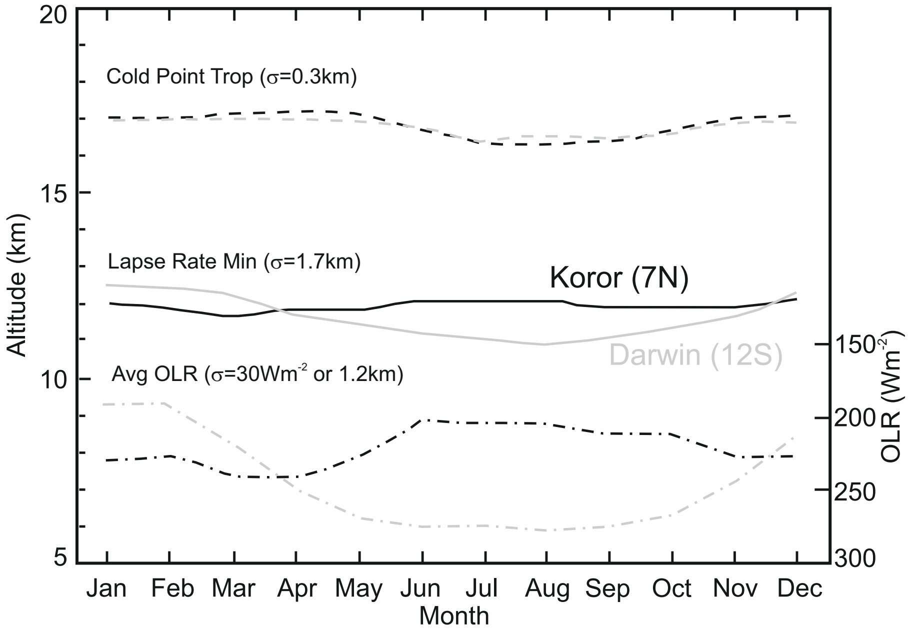

Figure 2.4.: Climatology of the altitude of the Cold Point Tropopause (CPT, dashed line) and Lapse Rate Minimum (LRM, solid line) and average Outgoing Long-wave Radiation (OLR, dashed-dotted line, right hand axis) for Koror, Palau (black), and Darwin, Australia (gray), based on data from 1979-1997 (radiosoundings from the Palau weather station and averages from multiple satellite observations provided by NOAA) (adapted from Gettelman and Forster, 2002, see orginal source for more details on the data).

Vertical Extent

The process of mixing e.g. pollutants from the boundary layer into higher levels of the troposphere involving clouds is called "venting". Whether precipitating or not, clouds influence chemical reaction and photolysis rates (NRC, 1991; Thompson et al., 1997). Depending on their size and type, clouds have a different effect on vertical transport of chemical species. Typical forms of tropical convective clouds are shallow cumuli, cumulus congestus and deep cumulonimbus clouds. They, respectively, detrain mostly at the trade wind related boundary layer inversion (ca. 2 km), into a shallow (2-5 km, i.e. up to the melting point) or a deep (10-17 km, up to the cold point) outflow layer (e.g. Folkins and Martin, 2005; Johnson et al., 1999). While the trade wind inversion is mostly absent close to the ITCZ, shallow and deep convection, both tied to the Hadley circulation (see Dessler and Minschwaner, 2007), are closely coupled. While downdrafts arising from deep convective precipitation initiate shallow convection, the latter sets the thermodynamic stage for the development of deep convective clouds in the first place (Folkins and Martin, 2005).

Between 5 and 10 km, Figure 2.5 shows how the static stability profile for Palau and other close-by locations follows a theoretical moist pseudoadiabat (condensing to water) with a surface pseudoequivalent temperature of 350 K (Folkins and Martin, 2005, compare Mapes, 2001). This stable stratification of the pseudoadiabatic temperature indicates a weak cloud-mass divergence, i.e. cloud outflow is suppressed in this altitude range. The dominating source of water vapor here is precipitation-induced evaporate moistening (Folkins and Martin, 2005). In a convective atmosphere, entrainment and mixing are dominant processes in this altitude range producing a well-mixed O_3 profile (Pan et al., 2015; Paulik and Birner, 2012, see Sect.4.2.1).

Between 10 and 14 km, in the deep outflow layer, we enter the transition zone between troposphere and stratosphere, the TTL, where the final dehydration of air masses occurs (see Sect.2.1.4). The level of minimum stability (LMS) is located here, defined as the minimum in static stability as shown in Fig.2.5 or by the minimum of the potential temperature gradient $d\theta/dz$ (compare Fig.2.6 in Sect.2.1.4). It corresponds to the level of (potential temperature) lapse rate minimum (LRM) which indicates a change in stability from convective equilibrium below (i.e. constant saturated equivalent potential temperature) to radiative equilibrium above (see Gettelman and Forster, 2002 for more details, Paulik and Birner, 2012). It is therefore used as a lower boundary of the TTL by some studies, marks the level of maximum convective impact on temperatures and is often coincidental with a minimum in O_3 VMR, also called chemopause (e.g. Folkins, 2002; Gettelman and Forster, 2002; Pan et al., 2014). Hence, O_3 is an ideal tracer for deep convection with a chemical lifetime similar to the timescale of the overturning Hadley circulation ($\approx$ 1 month, Folkins, 2002; Gettelman et al., 2009; Paulik and Birner, 2012; Solomon et al., 2005). Convective transport therefore essentially controls the distribution of O_3 in the TTL (Pan et al., 2015). The level of neutral buoyancy (LNB), located above the LMS/LRM, is associated with the level of maximum detrainment and main poleward flow in the Hadley circulation (Dessler and Minschwaner, 2007; Pan et al., 2014). Once an air parcel crosses its level of free convection, it is lifted until reaching its LNB. When moist air parcels rise above the LNB, we speak of convective overshooting. This is an important process in the TTL, which contributes to the stratospheric water vapor budget, but remains not well represented in model studies (e.g. Schoeberl et al., 2015; Sherwood and Dessler, 2003).

For Palau, the LRM/LMS is on average located around 12 km (see Fig.2.4). In areas of non-active (deep) convection the LMS/LRM is lower (see climatology for Darwin in

SH winter in Fig.2.4) and the chemopause diverts from the LRM (Folkins et al., 1999). Figure 2.4 also shows that deep convective outflow (and in consequence the chemopause) is not correlated with the cold point tropopause (CPT) and occurs well below this level.

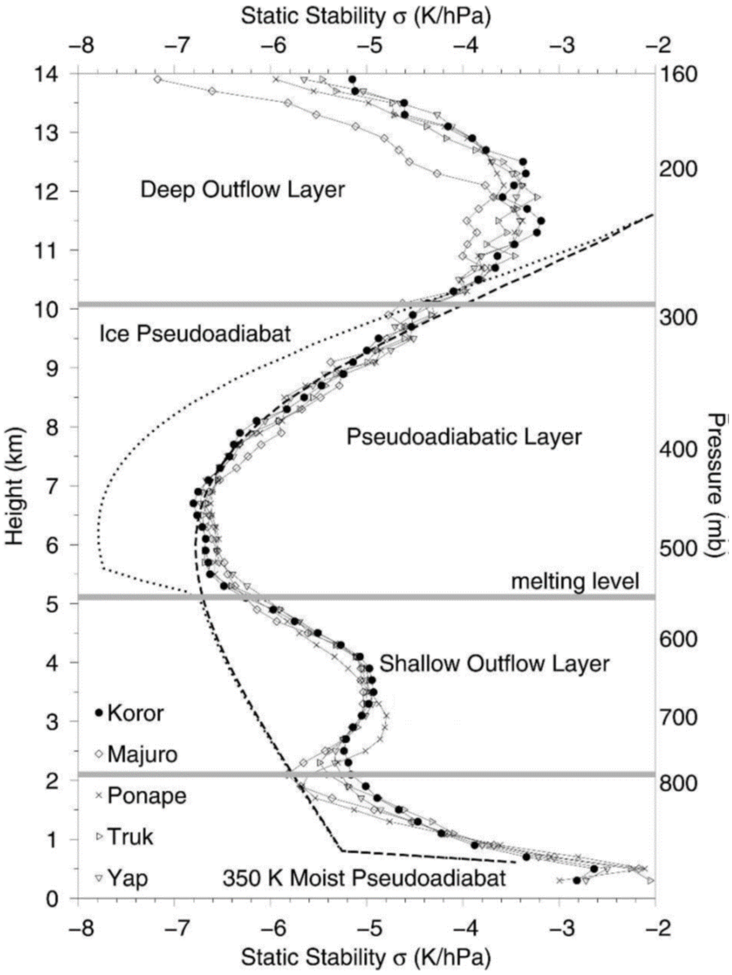

Figure 2.5.: Different atmospheric layers related to convective activity in the TWP and annual mean profiles of static stability [K/hPa] from average radiosounding data (1999-2001) at Palau (Koror, filled circle) and close by stations in the Federate States of Micronesia (other markers), see original source for more details on data and measures; thick lines indicate static stability for a moist pseudoadiabat, with water vapor either condensing to water (dashed) or ice (dotted) (adapted from Folkins and Martin, 2005).

At 14-15 km, the level of zero (clear-sky) radiative heating (LZH) constitutes a vertical mixing barrier, i.e. vertical mixing is inhibited above (Folkins and Martin, 2005; Folkins et al., 1999). It marks the upper limit of the Hadley circulation and the beginning of thermal stratification and large-scale radiative heating. Air parcels detraining above this level are more probable to ascend further into the stratosphere (Folkins and Martin, 2005; Gettelman and Forster, 2002).

2.1.4. Stratosphere-Troposphere Exchange

The tropical Upper Troposphere, Lower Stratosphere (UTLS) is a globally relevant region for stratosphere-troposphere exchange (STE) (e.g. Fueglistaler et al., 2009; Randel and Jensen, 2013). The TWP warm pool is in fact considered to be the major source region for stratospheric air in boreal winter (e.g. Fueglistaler et al., 2004; Krüger et al., 2008; Newell and Gould-Stewart, 1981; Rex et al., 2014). Here, air rising from the troposphere towards the stratosphere also passes its Lagrangian Cold Point (LCP), i.e. a minimum temperature "cold trap", where it loses its water vapor content via condensation (Pan et al., 2019). It is the last time when soluble substances are removed from the air before entering the stratosphere. The conditions at this LCP define the chemical composition of stratospheric air, its "chemical imprint". Rex et al. (2014) showed, that the source and transit region of air masses reaching their LCP lies within the TWP as well.

Two-way exchange across the tropopause occurs via cut-off lows, tropopause folds or blocking anticyclones mostly in mid-latitudes or along the subtropical jet (e.g. Holton et al., 1995, see Fig.A.1). Despite numerous studies in the past decade, there is still need to improve our understanding of STE processes in the tropics to improve their representation in general circulation models and thus climate models (see e.g. Schoeberl et al., 2015). The analyses of this thesis do not focus on the complex phenomena of this altitude range, but a few relevant concepts and definitions are introduced in the following.

Brewer-Dobson Circulation

The Brewer-Dobson (BD) circulation (e.g. Brewer, 1949; Butchart, 2014) is the slow, mean meridional circulation in the stratosphere, driven by atmospheric wave breaking (Holton, 1990; Rosenlof and Holton, 1993). It redistributes air risen in the tropics polewards in the winter hemisphere and thus creates a direct pathway from the TWP to the poles, where air masses subside again. The tropical stratospheric diabatic upwelling should not be confused with the uprising branches of tropospheric circulation patterns. While the Hadley circulation "pushes" from below, the BD circulation functions as a suction pump from above (Holton, 1990; Holton et al., 1995, see Fig.A.1). It thus lifts and cools the tropopause when it is strongest in boreal winter (compare Fueglistaler et al., 2009). In a region around 16 km mass fluxes in the BD circulation are comparable to those in the Hadley circulation (Folkins, 2002; Pan et al., 2014). Its seasonality modulates STE and affects the chemical composition of the TTL, e.g. the annual cycles of H_2O and O_3 (e.g. Fueglistaler et al., 2009, see Sect.4.1.3). Variations of the BD circulation occur from subseasonal to decadal timescales, also in connection with ENSO (e.g. Diallo et al., 2018; Konopka et al., 2016).

Quasi-Biennial Oscillation

The Quasi-Biennial Oscillation (QBO) is a quasi-periodic (mean period close to two years) oscillation between easterly and westerly zonal winds in the tropical stratosphere. It is responsible for most of the interannual O_3 variability above 20 km near the equator and thus relevant for the tropical total O_3 column (Logan et al., 2003; Shiotani, 1992; Thompson et al., 2003b). The influence of the QBO on the tropospheric O_3 distribution in Palau could not be analyzed within the scope of this thesis and the short Palau time series, but should be taken into account in future studies.

The easterly phase is associated with a strengthening of the BD circulation: enhanced upwelling transports low tropospheric O_3 to the lower stratosphere, while the anomalously cold tropopause causes low water vapor levels in the UTLS (see Diallo et al., 2018). The westerly phase of the QBO reduces the upwelling, thus enhancing horizontal transport and mixing in the stratosphere polewards, and increasing UTLS O_3 (compare Ploeger et al., 2011). In 2016 an anomalous disruption of the QBO tape recorder signal occurred, possibly caused by a combination of extra-tropical wave breaking and coincidence with the strong El Niño event (Barton and McCormack, 2017; Diallo et al., 2018). The complex interplay of QBO, ENSO and MJO has a significant impact on O_3 and water vapor distributions in the UTLS (e.g. Diallo et al., 2018; Yoo and Son, 2016).

Tropical Tropopause Layer

The tropopause can be defined in several ways: the temperature minimum (CPT), the thermal lapse rate minimum (WMO definition, see e.g. Pan et al., 2018) or changes in chemical tracer concentrations or vertical gradients, such as O_3 or water vapor (Prather et al., 2011; Sivakumar et al., 2011). Looking at the atmospheric processes happening in the vicinity of the tropopause, a clear distinction between troposphere and stratosphere is however not always adequate. In the tropics, in particular, the thermodynamic transition takes places over a range of several kilometers (Atticks and Robinson, 1983; Fueglistaler et al., 2009; Highwood and Hoskins, 1998), which for example is reflected by the height discrepancy between the O_3 chemopause, i.e. the UT minimum in O_3, and the CPT (Pan et al., 2014).

As a transition zone, the so-called Tropical Tropopause or Transition Layer (TTL) shares dynamical and chemical qualities of both realms: the stable-layered, radiatively-controlled stratosphere hosting the O_3 layer and the vertically well mixed, convectively-driven troposphere. Thus, the TTL encompasses the levels of main convective outflow and zero net radiative heating (compare Sect.2.1.3). It is laterally confined by the subtropical jets (Fueglistaler et al., 2009). Overlapping processes are the dominating, slow radiatively driven ascent, the beginning of in situ photo-chemical O_3 production (as seen in the strong vertical gradient) and the meridional mixing of air from the extra-tropical lower stratosphere. For the O_3 profile in the TTL this results in a chemopause well below the tropopause (Folkins et al., 1999). In contrast, the so-called ozonopause, which we define as the level of 90 ppb O_3 VMR in the TTL on the basis of the artifical tracer concept by Prather et al. (2011), relates to the seasonality of photo-chemical processes and follows the temperature cycle.

The final dehydration of air masses takes place in the TTL, controlling global lower stratospheric moisture (e.g. Fueglistaler, 2012; Gettelman and Forster, 2002; Randel and Jensen, 2013; Schoeberl and Dessler, 2011). In the stratosphere water vapor drives important gas-phase O_3 loss cycles as the primary source of HO_x and is involved in the heterogeneous chemical processes leading to the formation of polar stratospheric clouds, thus eventually promoting chlorine activation and resulting in polar ozone loss (e.g. Crutzen et al., 1995; Manney et al., 1994; Solomon et al., 1986, see Diallo et al., 2018 and references therein).

The actual definition of the TTL, including a vertical range, varies for different studies (compare e.g. Thompson et al., 2012). Essentially, there are two conceptually different, yet coexisting models: a "tropical tropopause layer" defined from mass-fluxes (Folkins, 2002; Fu et al., 2007; Fueglistaler et al., 2009) and a "tropical transition layer" built on a thermal definition (Gettelman and Forster, 2002, see Pan et al., 2014 for discussion). The mass-flux definition recognizes the TTL as a "gateway" for air masses into the stratosphere and a boundary layer, where the magnitude of mass fluxes for the tropospheric Hadley and the stratospheric BD circulation are comparable (Folkins, 2002). Using averaged tropical radiative heating rates and LS temperature and wind information, Fueglistaler et al. (2009) proposed a commonly acknowledged average vertical range of 14 km (150 hPa, 355 K) to 18.5 km (70 hPa, 425 K) with a latitudinal confinement by the position of the subtropical jets. The lower boundary corresponds to the level of zero net radiative heating (see Sect.2.1.3), while the upper boundary denotes the level with mass fluxes comparable to the BD circulation.

The thermal definition relies solely on local instantaneous measurements of the thermodynamic structure of the atmosphere, acknowledging the TTL as a transition zone from a dominance of tropospheric convection to stratospheric radiative stability. Thus, the boundaries are defined as the LMS, i.e. the level of maximum convective impact, and the CPT (Gettelman and Forster, 2002, see Sect.2.1.3). In good agreement with the thermal definition, Pan et al. (2014) propose a TTL definition based on a chemical tracer-tracer relationship, they coined "chemically measurable" via usage of balloon-borne measurements of O_3 and water vapor (see Fig.2.6b). They point out the benefits of their method over deriving a difference in mass-fluxes from available direct measurements.

Wave Activity

Atmospheric waves influence the chemical composition throughout the whole troposphere and lower stratosphere. In turn, their impact can be inferred from O_3 variability (e.g. Fujiwara et al., 1998; Paulik and Birner, 2012; Schoeberl et al., 2015; Thompson et al., 2011). While the appearance of Rossby waves is observed infrequently in tropical soundings, equatorial gravity or Kelvin waves are detected more often (Thompson et al., 2011). Stratospheric Kelvin waves are convectively coupled equatorial waves, excited by fluctuations in large-scale convection, which can cause significant temperature perturbations (e.g. Kiladis et al., 2009; Wang, 2002). Alongside the MJO, Kelvin waves are proposed as the main cause of intraseasonal variability of the tropical CPT temperature (Kim and Son, 2012). Breaking of equatorial Kelvin waves can lead to downward transport of stratospheric air into the UT (e.g. Fujiwara et al., 1998). Dehydration of the TTL is determined by horizontal transport above the top of convection and thus also influenced on a subseasonal scale by tropical waves (Pan et al., 2019).

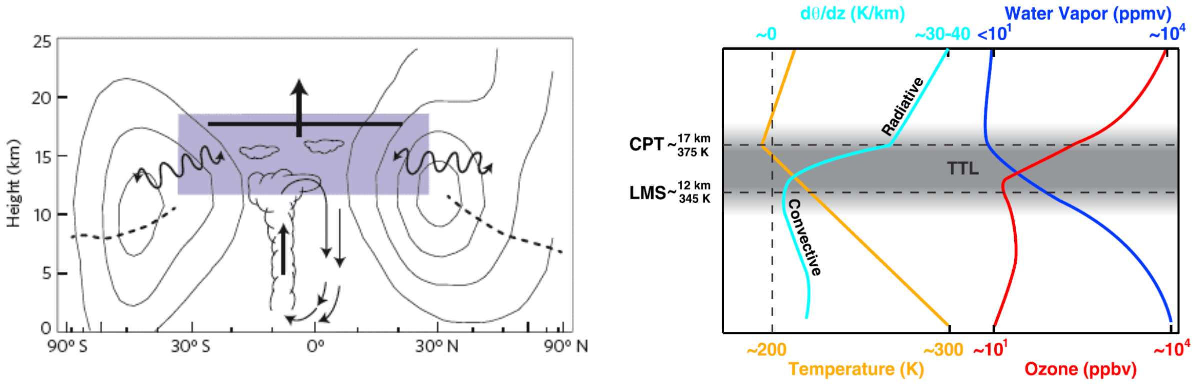

(a)

(b)

Figure 2.6.: Schematics of the TTL (shaded regions) in a latitude-height cross-section showing major dynamical influences (a) and as defined by profiles of temperature, potential temperature gradient ($d\theta/dz$), O_3 and water vapor (b); (a): contours indicate zonal average winds, dashed line represents the extra-tropical cold point tropopause (CPT), solid thick line the tropical CPT, wriggled lines indicate two-way exchange between extra-tropics and TTL, thick arrow highlights tropical upwelling while the smaller arrows and the cloud tower represent deep convective circulation, cited from Randel and Jensen (2013); (b): the lower boundary (dashed lines) of the TTL is marked by the level of minimum stability (LMS) as the minimum in the potential temperature gradient (in cyan) and the UT minimum in O_3 (in red), the upper boundary is defined by the CPT, i.e. the temperature minimum (in yellow) and a water vapor threshold < 10 ppm (in blue), cited from Pan et al. (2014).

2.2. Tropospheric O_3 Chemistry and Oxidizing Capacity

The special environmental conditions in Palau play an important role for tropospheric O_3 chemistry. Far from industrial human activities in the remote TWP, it might be the place of the cleanest air worldwide - for sure, the lowest tropospheric O_3 columns are found here year-round (e.g. Rex et al., 2014). Although O_3 is a powerful oxidant itself, the oxidizing capacity of the troposphere is mainly determined by its photo-chemical derivative, the fast-reacting hydroxyl radical OH (e.g. Levy, 1971; Montzka et al., 2011), also called the “detergent” of the atmosphere. OH is the dominant sink for various chemical substances and thus defines their lifetimes. Tropospheric O_3 is a principal precursor of OH and their coupling is of specific relevance in the clean marine atmosphere of the tropical Pacific (Kley et al., 1996; Rex et al., 2014; Tan et al., 2001). This section describes the important mechanisms for net O_3 and OH production and briefly introduces the consequences of variations in chemical lifetimes for STE.

2.2.1. O_3 Production and Loss

Photo-dissociation of molecular oxygen is responsible for the great abundance of O_3 in the stratosphere (Chapman, 1930). High energy UV radiation in the tropics make this the main source region for stratospheric O_3 globally. Until the 1970s the control of tropospheric O_3 was attributed to downward transport from the stratosphere (Junge, 1962, compare e.g. Lelieveld and Dentener, 2000 and references therein). In situ photo-chemical formation in the troposphere was first only associated with pollution (photo-chemical smog, Haagen-Smit, 1952) before the relevant interactions with long-lived tropospheric trace gases were discovered (Chameides and Walker, 1973; Crutzen, 1973).

In the free troposphere the chemical production of O_3 is governed by the OH-initiated oxidation of CO, CH_4 and non-methane hydrocarbons (NMHC), also referred to as volatile organic compounds (VOC). These processes require the presence of odd nitrogen NO_x, i.e. NO + NO_2. For the remote marine location of Palau the influence of NMHC is small and can be neglected, leaving the following dominating reaction chains for CO and CH_4, first yielding HO_2:

$$\mathrm{CO + OH \longrightarrow CO_2 + H} \tag{2.1}$$

$$\mathrm{H + O_2 + M \longrightarrow HO_2 + M} \tag{2.2}$$

and

$$\mathrm{CH_4 + OH \longrightarrow CH_3 + H_2O} \tag{2.3}$$

$$\mathrm{CH_3 + O_2 + M \longrightarrow CH_3O_2 + M} \tag{2.4}$$

$$\mathrm{CH_3O_2 + NO(\,+ O_2) \longrightarrow NO_2 + HO_2 + CH_2O}, \tag{2.5}$$

followed by the NO_x-mediated formation of O_3:

$$\mathrm{HO_2 + NO \longrightarrow OH + NO_2} \tag{2.6}$$

$$n(\mathrm{NO_2} + h\nu\,(\nu < 400\,\mathrm{nm}) \longrightarrow \mathrm{NO + O(^3P)}) \tag{2.7}$$

$$n(\mathrm{O(^3P) + O_2 + M \longrightarrow O_3 + M}) \tag{2.8}$$

with $n = 1$ for the CO reaction chains and $n = 2$ for the CH_4 chains. The net reactions of O_3 formation are thus:

$$\mathrm{CO + 2\,O_2} + h\nu \longrightarrow \mathrm{CO_2 + O_3} \tag{2.9}$$

and

$$\mathrm{CH_4 + 4\,O_2} + h\nu \longrightarrow \mathrm{CH_2O + H_2O + 2\,O_3}. \tag{2.10}$$

Due to the great abundance of long-lived CH_4 even in areas remote from pollution, the production of O_3 can be estimated as

$$P(\mathrm{O_3}) = k_{2.6}[\mathrm{HO_2}][\mathrm{NO}] + k_{2.5}[\mathrm{CH_3O_2}][\mathrm{NO}] \tag{2.11}$$

with k_i as the temperature-dependent reaction rate constants for the respective reactions i. The contribution of organic peroxy radicals, i.e. the second term of $P(O_3)$, is small enough to be neglected in the free and upper troposphere (e.g. Jaegle et al., 2001).

While CH_4 and CO are consumed during the above reactions, the cycling of NO_x as a catalyst plays the critical role. For low NO_x levels, the oxidation of CO, for example, takes a different turn in reaction 2.6 resulting in the termination of HO_x (i.e. OH + HO_2) cycling and net O_3 destruction instead:

$$\mathrm{HO_2} + \mathrm{O_3} \longrightarrow \mathrm{H_2O} + 2\,\mathrm{O_2} \tag{2.12}$$

$$net : \mathrm{CO} + \mathrm{O_3} \longrightarrow \mathrm{CO_2} + \mathrm{O_2}. \tag{2.13}$$

The rate constant of reaction 2.6 is larger than the one of reaction 2.12 with O_3 production dominating for a NO to O_3 ratio greater than 1:4000. For example, for a tropospheric O_3 VMR of 50 ppb the critical NO VMR level would be 10 ppt (e.g. Bozem et al., 2017; Graedel et al., 1994), i.e. higher NO_x levels lead to net O_3 production, while lower concentrations destroy O_3. Observations in the TWP found low NO_x concentrations resulting in an O_3 loss rate of 3.4 % per day (Crawford et al., 1997).

There are several reasons for low tropospheric NO_x concentrations in the TWP. NO_x itself is typically converted within a few days to highly soluble gaseous acid (HNO_3) and particulate nitrates and subsequently removed from the troposphere via wet and dry deposition. The resulting short lifetime of NO_x causes a rapid decrease in concentrations with distance from the source (factor 10 for 1000 km) (Graedel et al., 1994). Besides anthropogenic or biogenic air pollution, lightning is a relevant source of NO_x in the free troposphere. While the TWP region is far from pollution sources, deep convection as a premise for lightning is a common phenomenon. However, satellite observations revealed a lack of lightning activity in this region with a negligible annual flashrate below 1 flash $km^{-2}yr^{-1}$ (Cecil et al., 2014). On average the occurrence of lightning in deep convection is 10 times higher over land compared to ocean, with little seasonal variations (Christian, 2003). Crawford et al. (1997) proposed a dominant influence of marine, thus lightning-free convection favoring wash-out of NO_x derivatives as the cause of low NO_x levels in the TWP (compare Gao et al., 2014; Kley et al., 1996).

Photo-chemically, NO, NO_2 and O_3 are in a state of equilibrium during daylight on a timescale of approx. 100 s (Brasseur et al., 2003) via reactions 2.7, 2.8 and:

$$\mathrm{NO} + \mathrm{O_3} \longrightarrow \mathrm{NO_2} + \mathrm{O_2}. \tag{2.14}$$

For a low O_3 environment, this recycling of NO to NO_2 is suppressed, while the efficiency of the photolysis of NO_2 (reaction 2.7) remains constant (compare Gao et al., 2014). Thus,

NO_x essentially equals NO. Oxidation of NO_2 to HNO_3 (reaction 2.21) is also a possible loss mechanism for O_3. For the low to modest NO_2 levels, however, O_3 destruction via this reaction chain is insignificant (e.g. Crawford et al., 1997).

The main mechanisms for chemical O_3 destruction are either photolysis yielding $O(^1D)$ or reaction with OH, HO_2 or certain VOC:

$$O_3 + h\nu\,(\nu < 310\,\text{nm}) \longrightarrow O_2 + O(^1D) \tag{2.15}$$

$$O_3 + OH \longrightarrow HO_2 + O_2 \tag{2.16}$$

$$O_3 + HO_2 \longrightarrow OH + 2\,O_2. \tag{2.17}$$

A permanent loss of O_3 initiated by reaction 2.15 is dependent on the subsequent fate of the electronically excited $O(^1D)$ radical. It can either be deactivated by quenching upon collision with N_2 or O_2 and recycled to O_3, or facilitate the formation of OH radicals in the presence of water (Levy, 1971):

$$O(^1D) + H_2O \longrightarrow OH + OH. \tag{2.18}$$

In the warm and humid tropical marine boundary layer this particular loss mechanism is very efficient, leading to a lifetime of around five days for boundary layer O_3 over the equatorial Pacific (see e.g. Kley et al., 1997; Liu et al., 1983). Tropospheric O_3 loss is hence given by

$$L(O_3){=}\alpha J(O(^1D))[O_3] + k_{2.16}\,[OH][O_3] + k_{2.17}\,[HO_2][O_3], \tag{2.19}$$

where $J(O(^1D))$ is the respective O_3 photolysis rate constant (reaction 2.15) and α is the branching ratio for the reactions of $O(^1D)$ with H_2O.

Net O_3 production, $P(O_3)$ - $L(O_3)$, is dependent on NO_x and HO_x in a non-linear way, since NO_x is the driver of O_3 production, but also the cause of termination within the partitioning of odd hydrogen HO_x, i.e. OH + HO_2 (e.g. Bozem et al., 2017, see also next subsection 2.2.2, reactions 2.22 and 2.23).

The conditions in the TWP for O_3 production and loss outlined above have several implications for O_3 life times in the free troposphere: Low NO_x concentrations in a pollution-free troposphere favor O_3 loss over in situ photo-chemical production. Especially in the marine boundary layer, net O_3 production, or in this case loss, can be solely described by equation 2.19, resulting in the life time of around 5 days. The absolute H_2O concentrations and corresponding rates of O_3 destruction decrease with altitude, which results in increasing O_3 life times from the ground to the tropopause. A forced convective ascent of an O_3 molecule from the boundary layer to altitudes above 9 km increases its life time to 40 days. Further up in the tropopause region it can live for several months (Thompson et al., 1997).

2.2.2. OH Production and Loss

Primary formation of OH occurs via photolysis of O_3 in the presence of H_2O, especially in low altitudes. This coupling has already been introduced in the previous section (reaction 2.15 and 2.18). Within seconds, the fast-reacting OH is converted to HO_2, in the unpolluted troposphere mostly by reaction with CO (70 %) and CH_4 (30 %) (Brasseur et al., 2003) (reactions 2.1-2.5). In sunlight, a steady state between OH and HO_2 is established with a typical HO_2:OH ratio of 100:1. Daily mean OH VMR is the relevant quantity for most tropospheric degradation processes. We will therefore often speak of OH and the tropospheric "oxidizing capacity" synonymously.

Formation of HO_x also occurs via photolysis of carbonyl compounds, mainly formaldehyde (CH_2O), which itself is a product of methane oxidation (reaction 2.5). The latter process only becomes relevant at levels of the TTL and above (see e.g. Hanisco et al., 2001), and shall therefore not be described any further here. In dry conditions (H_2O VMR < 100 ppm), as encountered in the TTL, the photolysis of acetone also becomes a major source of HO_x (Jaegle et al., 2001). The lifetime of HO_x in the upper troposphere is around 30 min (e.g. Jaegle et al., 2001).

The rate of production for free-tropospheric OH can thus be estimated as:

$$\frac{d[\mathrm{OH}]}{dt} = \frac{2k_{2.18}[\mathrm{H_2O}]J(\mathrm{O}(^1\mathrm{D}))}{k_{O_2}[\mathrm{O_2}] + k_{N_2}[\mathrm{N_2}]} \tag{2.20}$$

with k_{O_2} and k_{N_2} as the reaction rate constants for the quenching of $O(^1D)$ with either O_2 or N_2 (see also reaction 2.11).

A major net loss mechanism for HO_x in the free troposphere is the reaction with NO_2:

$$\mathrm{OH} + \mathrm{NO_2} + \mathrm{M} \longrightarrow \mathrm{HNO_3} + \mathrm{M}. \tag{2.21}$$

This reaction, however, is not very efficient in low to medium NO_x regimes (e.g. Crawford 1997). The termination of NO_x chemistry and the usual fate of HNO_3 was already discussed in Section 2.2.1. In addition, heterogeneous chemistry involving HNO_3 during the night can either produce or further destroy HO_x (Hanisco et al., 2001).

With low NO_x concentrations, a more significant sink of HO_x lies within its self-reactions:

$$\mathrm{OH} + \mathrm{HO_2} \longrightarrow \mathrm{H_2O} + \mathrm{O_2} \tag{2.22}$$

$$\mathrm{HO_2} + \mathrm{HO_2} \longrightarrow \mathrm{H_2O_2} + \mathrm{O_2}. \tag{2.23}$$

Here, H_2O_2 acts as a reservoir gas and can regenerate HO_x via photolysis, which becomes more relevant in the upper troposphere (e.g. Tan et al., 2001). As a product of HO_x recombinations, H_2O_2 is an indicator for the efficiency of free radical chemistry in the troposphere (Brasseur et al., 2003).

The critical role of NO_x as a terminator for radical chemistry (reaction 2.6 and 2.12) was pointed out already in our description of the formation of O_3. Indeed, a consequence of low NO_x is the loss of OH during the oxidation of CO in reaction 2.1, followed by reaction 2.12.

By analyzing aircraft observations, Jaegle et al. (2001) found that daily mean tropospheric HO_x concentrations are determined by their primary production rate from the $O(^1D)$-H_2O reaction (reaction 2.18) and NO_x concentrations. Rohrer and Berresheim (2006) determined the proportionality of free tropospheric OH concentrations to the photolysis rate $J(O(^1D))[O_3]$ from a long time series of in situ measurements (compare also Gao et al., 2014). Moreover, they discovered that variations in OH can statistically be explained by the intensity of ultraviolet sunlight alone. In the face of the complex interplay of O_3, H_2O and NO_x with HO_x in tropospheric oxidation chemistry, this is a surprising result and possibly a consequence of the correlations between involved chemical drivers which cloud the individual impact of single chemical species (Wennberg, 2006).

In summary, a solid estimation of OH requires information about other radicals (HO_2,RO_2), NO_x and photolysis rates ($J(O^1D)$) in addition to the measurements of O_3 and H_2O (Bozem et al., 2017).

2.2.3. Impact on Chemical Lifetimes and STE

As described in Section 2.1.4, the TWP is a key source region of the stratosphere. In this context, the coincidence of a tropospheric O_3 minimum and a correlated OH minimum, as found by several studies, is of great relevance (Gao et al., 2012; Kley et al., 1996; Rex et al., 2014; Tan et al., 2001). A reduced oxidizing capacity diminishes soluble decomposition and subsequent wash-out of various chemical species, such as SO_2, very short-lived halogenated carbons and VOCs. With the resulting increased chemical lifetimes, transport processes become more relevant and may dominate over chemical reactions for species' concentrations at a given location. The dynamical conditions in the TWP, as the source and transit region of air masses entering the stratosphere, and increased lifetimes enable enhanced entry of chemical species from the local boundary layer into the global stratosphere.

For dibromomethane (CH_2Br_2), a short-lived bromine species which is involved in heterogeneous polar O_3 destruction, Rex et al. (2014) estimate a lifetime of 188 days in the OH minimum of the TWP at 500 hPa compared to 55 days in the tropical Atlantic (OH maximum). Their study shows that the fraction of air masses with CH_2Br_2 from the boundary layer reaching the stratosphere doubles in very low OH conditions compared to regular Pacific conditions. This addition to the global stratospheric halogen budget in the TWP and the redistribution within the stratosphere by the BD circulation fosters O_3 depletion in the polar stratosphere (Rex et al., 2014) and connects these two remote regions. This emphasizes the importance of monitoring of air composition in the TWP for our understanding of globally relevant atmospheric processes. The exact OH abundance in the TWP and the extent of the OH minimum is part of ongoing research (see Nicely et al., 2016).

3. Observations and Modelling

The tropospheric O_3 content of the TWP is characterized in a predominantly observational approach in this thesis. The basis of all analyses are ozonesonde measurements at the new Palau Atmospheric Observatory (PAO), its setup being part of this doctoral work project within the EU project StratoClim. The large spatial and temporal variability of tropospheric O_3 as well as the limited prospects of remote retrieval methods still make in situ balloon-borne profile measurements with Electrochemical Concentration Cell (ECC) ozonesondes the best method to assess this trace gas. Closing an observational gap in the global O_3 sounding network is of great relevance, since ozonesonde measurements provide a-priori profiles for many remote sensing techniques including satellites and microwave or FTIR instruments. The sounding data set is complemented by measurements from other sounding stations and reanalysis data products. Analysis of the data includes the usage of the trajectory scheme of the Langrangian transport model ATLAS and the chemical box model AWIP, in order to assess the origin of air masses and the oxidizing capacity.

This chapter first describes the measurement technique of ECC ozonesondes and their data processing in detail (Sect.3.1). An overview of the Palau data set follows in Section 3.2, also addressing the statistical handling of the short time series. All auxiliary observational data are introduced next in Section 3.3 before methods of the model approaches are discussed (Sect.3.4).

3.1. ECC Ozonesonde Observations

Developed in the 1960s by Walter Komhyr (Komhyr, 1969), the basic electrochemical measurement principle of ECC ozonesondes and the related equations are still valid. Improvements in manufacturing and numerous laboratory and field evaluations led to refinements of operating procedures and post-processing of the raw signal (e.g. Smit, 2014). This section describes the measurement principle, relevant equations and the state-of-the-art raw data processing applied in this thesis. Data quality and uncertainties are described with a special focus on the controversial parameter of the background current (e.g. Newton et al., 2016; Voemel and Diaz, 2010), which is most relevant in the tropical UT (e.g. Rex et al., 2014; Smit, 2014). The resulting imperative of robust UT O_3 measurements from Palau, motivated an instrumental development to lower the detection limit of ECC ozonesondes as part of this thesis, which is summarized in Section 3.1.4.

3.1.1. Measurement Principle

The measurement principle of Electrochemical Concentration Cells (ECC) is based on the conversion of O_3 into an electrical current (Komhyr, 1969). In an ECC ozonesonde ambient air is forced through an aqueous potassium iodide (KI) sensing solution in the cathode cell by a small gas sampling pump. All components of the sonde in contact with the sampled air are made of Teflon, which is inert to O_3. Thus, via the redox reaction

$$2\,\mathrm{KI} + \mathrm{O_3} + \mathrm{H_2O} \longrightarrow 2\,\mathrm{KOH} + \mathrm{I_2} + \mathrm{O_2}, \tag{3.1}$$

in the solution, all sampled O_3 is converted to iodine (I_2). In contact with the platinum electrode of the cathode cell, I_2 is reduced back to iodide (I^-) by an uptake of two electrons e^- per I_2 and, hence, O_3 molecule:

$$\mathrm{I_2} + 2\,e^- \longrightarrow 2\,\mathrm{I}^-. \tag{3.2}$$

The anode cell is filled with a saturated KI solution and attached to the cathode cell by an ion bridge. Here, the oxidation of I^- takes place under loss of 2 electrons:

$${}_3\mathrm{I}^- \longrightarrow \mathrm{I}_3^- + 2\,e^-\,. \tag{3.3}$$

The generated electrical current I_m $[\mu A]$ in the external circuit connecting the cells, corrected for a residual background current I_b (see Sect.3.1.2), is directly proportional to the partial pressure of O_3 ($P_{\mathrm{O_3}}$), calculated by

$$P_{\mathrm{O_3}} = \frac{R}{2F\eta_C} \cdot (I_m - I_b) \cdot T_{box} \cdot \frac{c_{pumpcorr}}{f_{pump}}, \tag{3.4}$$

with R as the universal gas constant, F as the Faraday constant (factor 2 accounts for the stoichiometry, i.e. 2 e^- per O_3 molecule), $\eta_C \approx 1$ as a factor for the conversion efficiency, T_{box} $[K]$ as the so-called "box" or pump temperature, f_{pump} $[cm^3 s^{-1}]$ as the gas volume flow rate and finally, $c_{pumpcorr}$ as an empirical correction factor for the pump efficiency depending on pressure (see Tab.3.1 for details on corrections).

The sensor response time τ attributed to reaction 3.1 is 20-30 s. ECC sondes are built for atmospheric profiling using balloons, which can reach altitudes up to 35 km. With a typical ascent rate of 5 m/s, the vertical resolution of ECC sonde measurements is between 100-150 m (e.g. Smit et al., 2007). Radiosondes are flown in one payload with ozonesondes and transmit their data, the GPS-based location as well as pressure, temperature and humidity. Secondary processes, possibly involving buffer substances added to the KI solution, introduce a second, longer time reaction constant τ' of 20-30 minutes (Davies et al., 2000; Johnson, 2002; Voemel and Diaz, 2010). The resulting hysteresis effect is observed in the decay rate of the sensor current $I_m(t)$ during a controlled response test with a step change from high to no O_3 (at t_0) and is dependent on the particular recipe of the sensing solution (KI concentration, buffered or not). The ECC response function can be described as (see Voemel and Diaz, 2010 for details):

$$I_m(t) = I_0 e^{-\frac{t-t_0}{\tau}} + I_0' e^{-\frac{t-t_0}{\tau'}}\,. \tag{3.5}$$

3.1.2. Measurement Uncertainties

Overview

The uncertainty of O_3 measurements obtained with ECC sondes is a combination of uncertainties in the individual parameters in equation 3.4 (see Fig.3.1a). Since the 1990s, quality assessments and inter-comparisons of ozonesondes are regularly conducted in field campaigns (e.g. Deshler et al., 2008; Komhyr et al., 1995) and extensive laboratory studies at the World Calibration Center for Ozone Sondes (WCCOS) at Forschungszentrum Jülich (FZJ) (Smit et al., 2000). The so-called JOSIE-campaigns at the WCCOS aim to improve the instrumental accuracy by tracking instrumental changes and investigating all aspects affecting the O_3 observations under realistic atmospheric conditions in a controlled laboratory environment, such as various parameters of Eq.3.4, differences between manufacturers and operating procedures (Smit, 2014; Smit et al., 2007; Smit and Kley, 1998; Thompson et al., 2019). Resulting from these enormous community efforts, the overall precision of ECC sondes when handled according to standard operating procedures (SOP) is estimated to be 3-5 % with absolute accuracies between 5 and 15 % in the tropical troposphere (see e.g. Smit et al., 2007; Thompson et al., 2019).

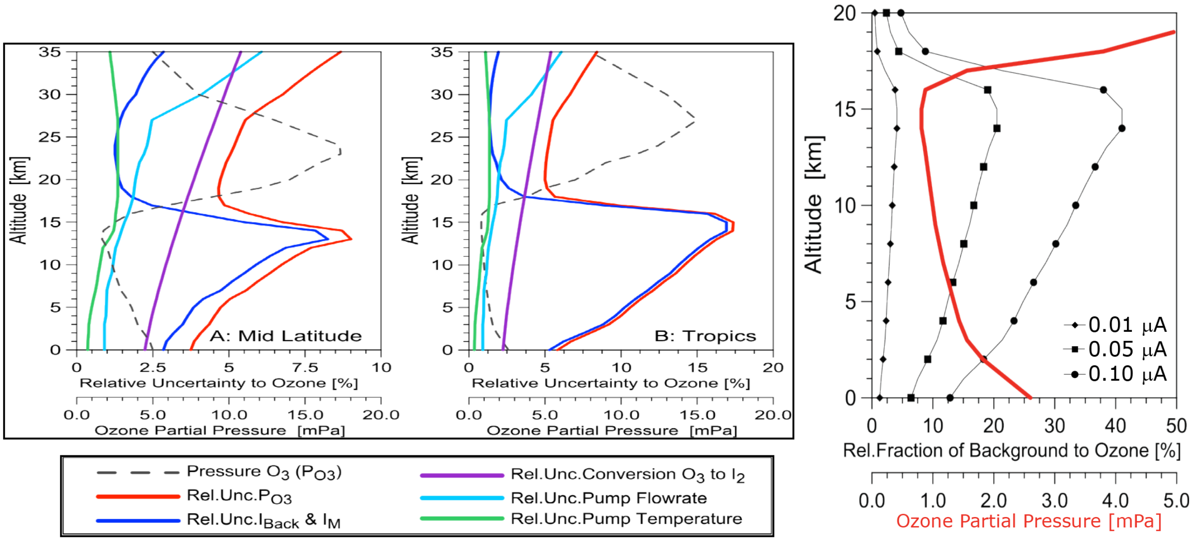

(a) (b)

Figure 3.1.: Uncertainties of individual parameters (colored lines) relative to O_3 partial pressure with altitude (a) for a mid-latitude profile (dashed line, left panel) and a tropical profile (right panel), (b) shows the background current I_b as a relative fraction of tropospheric O_3 partial pressure (black lines) with altitude for different I_b (different markers) and the tropical standard O_3 partial pressure profile (red line, same as dashed line in right panel of (a)); both based on JOSIE results and adapted from Smit (2014).

The right panel in Figure 3.1a shows profiles of the uncertainties of individual parameters (colored solid lines). The overall uncertainty within the TTL reaches 18 % (red solid line) (based on JOSIE results, Smit, 2014). Thompson et al. (2019) found an underestimation of TTL O_3 reaching up to more than 30 % during the most recent JOSIE-SHADOZ inter-comparison study. The greatest contribution to the overall uncertainty comes from uncertainties in the measured cell current I_m, mostly attributed to the so-called background current I_b. In the TWP, very low O_3 concentrations are observed at this altitude region, close to the detection limit of ECC sondes tied to I_b (see dashed line in Fig.3.1a and e.g. Kley et al., 1996; Rex et al., 2014). Despite the long history of the measurement technique and diversity of related studies, origin and time evolution of I_b during flight remain poorly understood (e.g. Smit, 2014). Its exact value is therefore unknown and highly sensitive to the quality of the operating procedures, which spurred doubt in past observations of near-zero O_3 measurements by ECC sondes in the TWP tropopause region (e.g. Newton et al., 2016; Voemel and Diaz, 2010).

Background Current

The background current I_b is a “residual” response of the ECC sonde during exposure to purified air, i.e. despite zero O_3 concentration, the sonde detects a sensor current. During pre-flight preparations, the sonde response is tested several times: at the end of the first preparation and three times during the second preparation (see Sect.3.1.3), i.e. before exposing the sensing solutions to high O_3 concentrations (equivalent to $I_m = 5\mu A$) in the laboratory (I_{b0}), 10 minutes after the high O_3 exposure (step change to ozone-filtered air)(I_{b1}) and after 10 minutes of exposure to ozone-filtered air just prior to launch (I_{b2}). All I_b tend to be different, with usually $I_{b0} < I_{b2} < I_{b1}$. It is recommended to use I_{b2} measured right before launch for calculation (Smit, 2014).

Figure 3.1b shows profiles of relative fraction of I_b at different magnitudes (black lines) to O_3 partial pressure (tropical standard profile as red line) based on JOSIE studies (Smit, 2014). Increasing the background current by a factor 10 (0.01 to 0.1 μA) leads to more than a factor 10 in the fraction of the I_b error to the measured O_3 in the TTL (3 % compared to 40 %). The importance of accurate measurements of I_b in this region motivated our experimental efforts to lower the detection limit, see Section 3.1.4.

The origin of I_b is probably multi-causal. Separating its effect on the O_3 signal from other known sources of uncertainties remains a challenge. For example, artifacts caused by a conversion efficiency differing from the ideal (2 e^- per O_3) could be submerged in I_b. These result from evaporation of the sensing solution during ascent and are difficult to quantify (e.g. Smit et al., 2012). It is further believed, that a residual current I_b is a consequence of the second, slow part of the response function (Eq.3.5, see Sect.3.1.1) and could thus be isolated by data convolution methods (De Muer and Malcorps, 1984). These methods are however mathematically complex and would require prior smoothing of the profile. Therefore, even if this proves to be the physical explanation, practical correction methods for I_b might remain empirical.

As a possible alternative cause of I_b, we postulate an unknown contamination of the solution from residue which remains in small micro-cavities of the cell walls or tubing, not purged by pre-launch procedures. During flight, this residue diffuses into the solution at an unknown rate. The resulting dependency on the individual sonde means that for each trajectory of a specific sonde in the 5-dimensional parameter space of time, temperature, pressure, O_3 concentration and "shaking" of the sonde, the background current will develop in a distinct way. Hence, a universal correction formula would be impossible.

Due to lack on consensus, different correction methods are applied within the international ozonesounding network, most prominently: no correction, a subtraction of the constant I_b or a pressure-dependent correction. A dependence on oxygen could not be confirmed by several laboratory studies (Thornton and Niazy, 1982, 1983). Smit (2014) therefore suggest application of a constant correction using "I_{b2}". This, however, may significantly underestimate low O_3 concentrations, as observed in the TTL (Rex et al., 2014; Voemel and Diaz, 2010). Figure 3.2 shows three example tropospheric profiles from the Palau record and the range of different corrections. According to a constant correction, we observed several near-zero O_3 events in the TTL above Palau during the study period, but no physically unrealistic negative O_3 concentrations, due to the generally low I_b (compare Rex et al., 2014). However, based on experimental results with our custom-made ozonesonde attachment (Sect.3.1.4) and against current SOP recommendations, the pressure-dependent background current correction and "I_{b2}" are used throughout this thesis. This is usually indicated by the phrase "Ib press.dep." in figure labels.

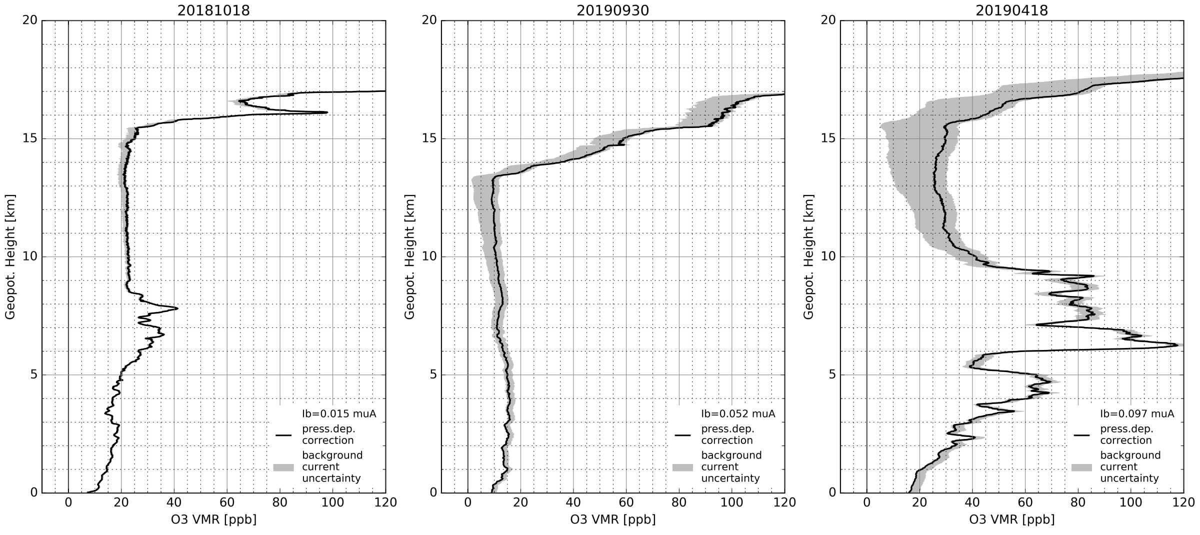

(a) (b) (c)

Figure 3.2.: Tropospheric O_3 VMR profile examples and the effect of different background current (I_b) corrections with particular low (0.015 μA in (a)) or high I_b (0.052 μA in (b), 0.097 μA in (c)), left edge of gray shading results from a constant correction, right edge from no correction, thick line from pressure-dependent correction.

The manufacturing process for O_3 sondes has been improved over the years with notable positive implications for I_b-related uncertainties. One remaining major problem are inaccurate measurements of I_b during preparation due to inappropriate O_3 destruction filters. Especially humidity, which is difficult to avoid at tropical sites, diminishes the efficiency of certain commonly used filters (e.g. Smit et al., 2012, personal communication with Herman Smit). In Palau, we observed a median background current before flight (I_{b2}) of 0.024 μA for older batches of ECC sondes (ECC Serial Number < 30000) and 0.03 μA for newer batches (see Figure 3.3). Occasional values above 0.05 or even 0.1 μA were common several years ago (e.g. Smit et al., 2012; Witte et al., 2018) and are still declared as tolerable by the manufacturer. Witte et al. (2017) recommend setting I_b to 0.05 μA if it exceeds this threshold. We did not follow this recommendation. The jump in serial numbers (SN) (see red and blue circles in Fig.3.3b) is accompanied by a jump in the background current readings. This is especially evident in the first day preparation, when the median values are double for the new batch (0.06 compared to 0.03 μA, not shown here). Several sondes did not pass the initial response test, some were sorted out due to I_{b2} exceeding 0.1 μA. Changes in the laboratory setup or solutions could be ruled out as possible causes for this discrepancy, no changes of the production process are known. We assume impurities from manufacturing for the specific batch and will closely monitor this development in the future.

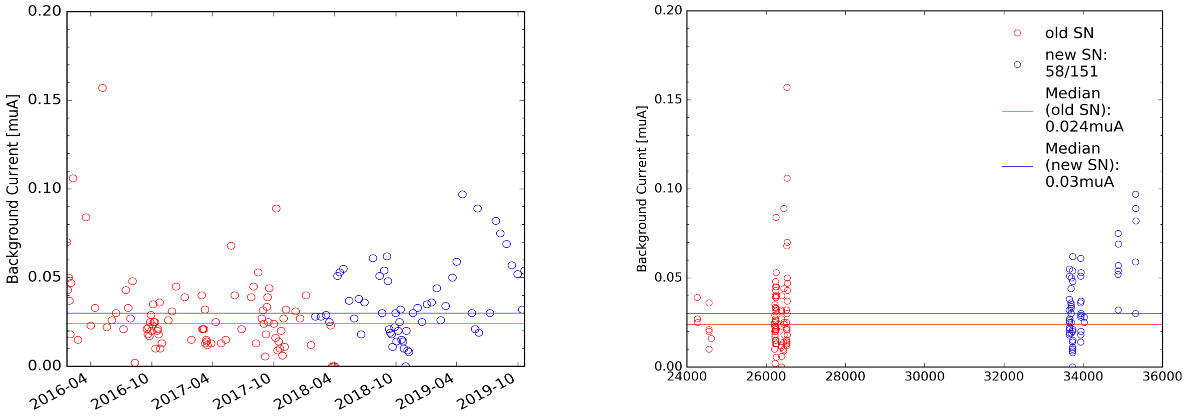

(a) Date

(b) Serial Number (SN)

Figure 3.3.: Background current I_{b2}, measured right before launch, for all Palau soundings, sorted by date (a) and ECC sonde Serial Number (SN)(b); older SN (<30000) are in red, newer SN (58 of 151 in total) in blue, median marked by a horizontal line in the respective color; 6 of the 151 soundings included here were discarded in the analysis e.g. due to early balloon burst.

3.1.3. Operating Procedures and Post-processing

The controversial debate about near-zero O_3 measurements in the TWP demanded a particular focus on quality of all used equipments and during all steps required in generating Palau's data record, which include the pre-flight preparations of the sonde and the post-processing of the raw signal, to ensure comparability with other observations. An international consortium of ozonesonde experts under the umbrella of the WMO's Global

Atmosphere Watch (GAW) program has put together a reference for standard operating procedures (SOP) based on extensive assessments (GAW Report 201, current version: Smit, 2014). A follow-up initiative coordinates efforts to homogenize present and historic ozonesonde data to improve the quality of the global long-term record (Smit et al., 2012). These recommendations for our sonde model, type 6A manufactured by Science Pump Corporation (SPC), have been carefully followed for the Palau measurements from the beginning and are summarized in Table 3.1.

Specification	PAO	Comments
Ozonsonde Type	SPC, model 6A	
Radiosonde Type	Vaisala RS92-SGP and RS41-SGP	change in October 2017
Sensing Solution Type	1.0 % KI, full buffer	
Cathode Solution Volume	3ml	
Background Current	all recorded	I_{b2} used for correction
Temperature Pump Location	internal	in Teflon block of pump
Pumpflow Measurement	bubble flow meter	
Source of Zero Ozone	Vaisala chemical destruction filter or self-built charcoal/desiccant filter	dry storage ensured
Laboratory Conditions	pressure, temperature and relative humidity recorded	air-conditioned and de-humidified laboratory space
Software Data Reduction	retrieval with commercial Vaisala software package	own calculations from raw cell current used in post-processing and data analysis
	Corrections applied for	
Background Current	yes	pressure-dependent, see Sect.3.1.2 and 3.2.2
Pump Efficiency	yes	according to Komhyr (1986)
Humidity Effect in Flow Rate	no	contribution was found to be -1 to -2 % or -1 ppb in the free troposphere
Total Column Ozone	no	

Table 3.1.: Major specifications of O_3 soundings at the Palau Atmospheric Observatory (PAO), in accordance with recommendations from Smit et al. (2012) and Smit (2014), except for the applied pressure-dependent background current correction.

Preparation of the ECC sondes according to SOP is done in two steps, one three to seven days before launch, and a second preparation up to 24 hours before launch, usually on the launch day. In Palau, all preparatory steps and storage in between take place inside an air-conditioned and de-humidified lab container, providing a stable environment with temperatures around 25 °C and RH around 40 %. All parameters measured during preparations are documented and available as meta data. Raw pump current measurements during flight are available upon request in addition to the Vaisala software output files and sounding data in NASA Ames format. Data presented in this thesis have been calculated from raw data with specifically developed software (using Eq.3.4 and corrections summarized in Tab.3.1) and are also available upon request.

3.1.4. Instrumental Development

Motivated by controversies about near-zero O_3 measurements in the TWP, we developed an instrumental device attachable to an ECC sonde to monitor how the background current develops during flight. Ozonesondes modified in this way are not meant for operational usage in O_3 profiling, but will improve our understanding of the background current and contribute to the ongoing debate about corrections (see Sect.3.1.2). This thesis presents the current status quo of the on-going development of the device.

Technical Design and Operation

The technical design and pictures of the instrumental setup, ozonesonde and attached device, are shown in Figure 3.4. The main components of the device are a magnetic latching valve, a micro-controller and corresponding logic mounted on a circuit board, an ozone destruction filter and tubing for connections. The engineering was done in cooperation with impres GmbH.

In programmable time intervals, the modified ECC sonde "sees" either ambient air or ozone-free air, i.e. ambient air that passed through the ozone destruction filter first. This is realized by two separate inlets (marked by dark gray and white arrows in Fig.3.4b) connected to a three-port magnetic latching valve (LHLA0531111H solenoid valve, used in UV photometer presented in Kalnajs and Avallone, 2010). A common outlet port (light gray circle in Fig.3.4b) is attached to the ozonesonde. Switching of the latching valve between the ambient air port (dark gray circle) and the so-called "no-ozone" air port (white circle), is triggered by an interval timer via a micro-controller (ATtiny45, circuit diagram and code available upon request). Timing is accurate within approximately 30 seconds. Valve and micro-controller are powered by the ozonesonde battery. Energy consumption is sufficiently low to not interfere with the sonde's own power demand. Peak voltage during switching is 5 V, but only for a few seconds. Each switch triggers a signal transmission to the auxilliary port of the radiosonde (channel 3 of model RS92, see Sect.3.2.2) in order to track exact switching times. The filter is a simple PE container filled half with charcoal, half with desiccant (see Fig.3.4b). Incoming air is thus first dried and filtered of macroscopic particles, before O_3 is filtered out by the charcoal. Teflon is used as tubing material as it is inert to O_3. Pictures in Figure 3.4 still show bent connectors made of flexible silicone, but these could be avoided in the final setup.

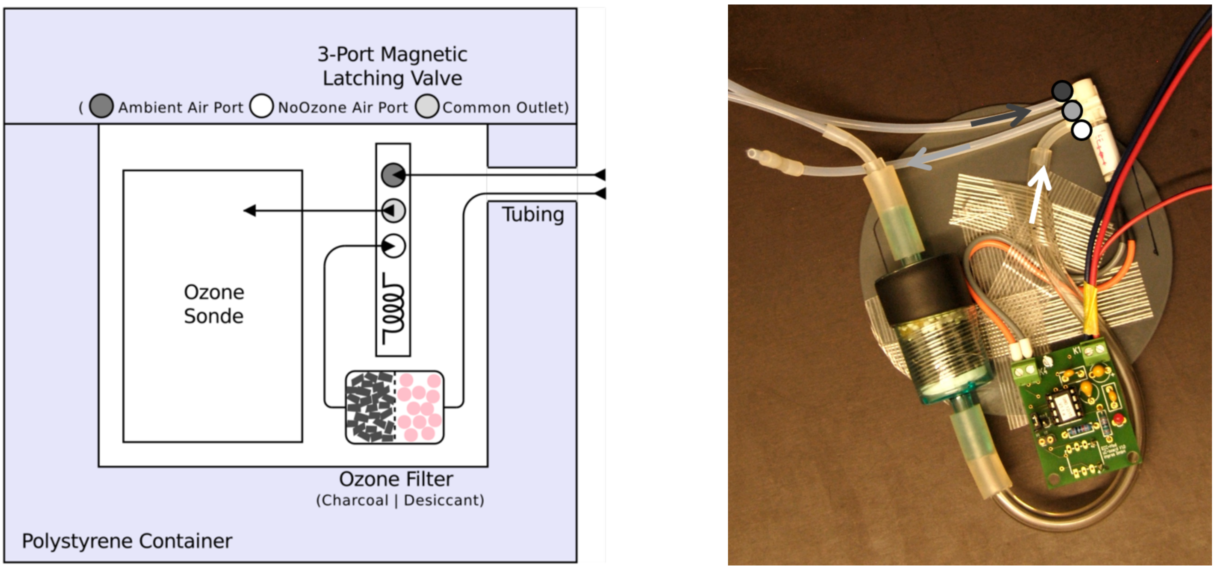

(a) Schematic of the technical setup of the modified ozonesonde in the polystyrene container

(b) Photo of the technical setup of the device

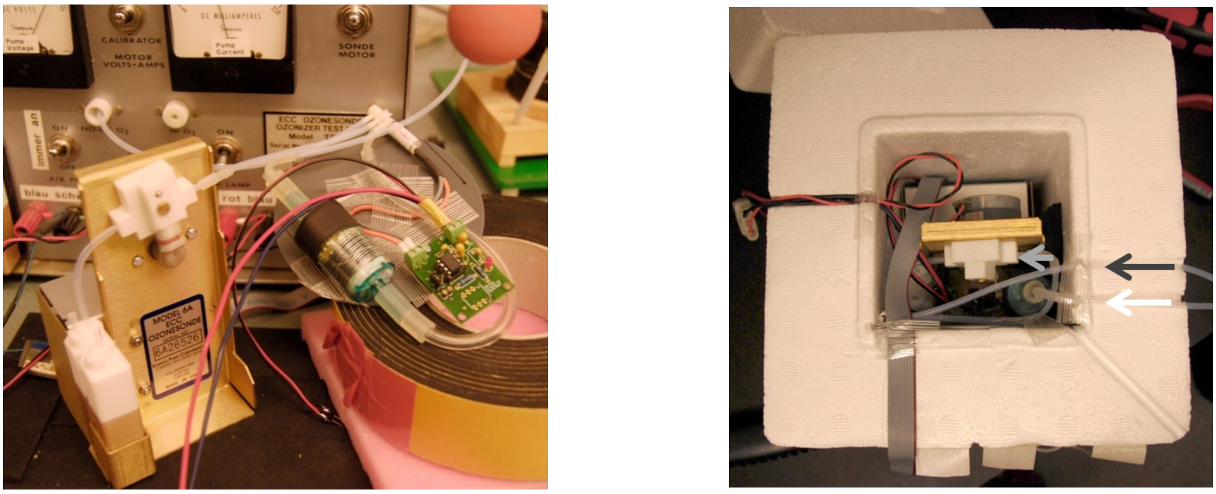

(c) Full setup during preparation

(d) Packed for launch

Figure 3.4.: Images of the technical setup of ozonesonde and device, see subcaptions for details, the different ports of the magnetic latching valve (marked with a spring in (a)) are shown as circles: dark gray for ambient air, light gray for common and white for the no-ozone air port ((a) and (b)), arrows indicate direction of flow ((a), (b) and (d)).

During preparation, all regular SOP tests (Smit, 2014) are conducted with the device attached and the latching valve set to the ambient air port. An additional testing routine is added at the end of the second preparation to check pump pressure, pump current and flow rate for the no-ozone port. Differences between the flow rates for ambient and no-ozone air occur, but stay below 1 %. The fully assembled modified ozonesonde fits into its original polystyrene container by adding an extra slot for a second inlet (see Fig.3.4d).

Laboratory and Field Test Results

Latching valve, micro-controller and timer-software pass general function tests on the ground. During flight, the sensor response to switching of channels is comparable to laboratory tests. The measured ECC sensor current drops quickly to very low values during no-ozone periods and rises again quickly after switching to the ambient air channel (see Fig. 3.5). The capability of the filter to destruct O_3 was successfully tested in the laboratory by exposure to high O_3 VMR (approximately 200 ppb).

To analyze the capabilities of the device in flight, dual launches with one modified and one standard ECC sonde ascending in one payload have been performed. The relaxation of the current during no-ozone periods with time is known and has been extensively studied in the laboratory (Voemel and Diaz, 2010, e.g. Smit and Sträter, 2004a,b). For an assessment in-flight within two dual launches in Palau, the modified ECC sondes were programmed for 60 minute long no-ozone periods after a first sampling of ambient air for 10 minutes (see Fig.3.5). Both profiles show negative sensor currents after long exposure to no-ozone air, i.e. after 30 and 50 minutes respectively (see Fig.3.5a, 3.5b). Figure 3.6 shows O_3 VMR calculated for the dual sounding in Fig.3.5b with the measurements from the modified sonde (in blue) and measurements from the unmodified ozonesonde (in pink). This modified sounding and a similar earlier single modified ECC launch (see Fig.A.3) support the usage of the pressure-dependent background current correction (thick blue line in Fig.3.6). The constant correction (lower edge of the blue shading) yields physically unrealistic results (compare Rex et al., 2014), which is also tied to the fairly high background current of 0.13 μA. The modified sounding with a very low background current of 0.011 μA (Fig.3.5a) does not allow any conclusions for correction methods.

A more striking observation of the dual launches and other measurements was the difference between the modified and unmodified sonde observations during the ambient air measurement period. After switching back from no-ozone air to ambient air after 60 minutes, the sensor current initially rises within seconds to about 50 % (Fig.3.5a) to 75 % (Fig.3.5b) of the unmodified sonde signal. The general trend of the unmodified signal is followed by the modified sonde thereafter, but the bias remains. Shorter exposure to no-ozone air, as programmed for the dual launch presented in Fig.A.2, corresponds to a smaller bias in the subsequent measurement of ambient air.

Figure 3.7 shows results from a trio sounding with one unmodified (E1) and two modified (K1, K2) ECC sondes on the same balloon, launched in Ny Ålesund, Spitsbergen. Both modified sondes have identical channel switching routines in short intervals (10 minutes of no-ozone followed by six minutes of ambient air), though slightly time-delayed (K1, in pink, switches earlier than K2, in green). With focus on the ambient air periods, both modified sondes follow the signal of the accompanying unmodified sonde, including characteristic peaks (see Fig.3.7a), but with a bias, differing in height and/or time (Fig.3.7b). Despite a difference in background currents of 0.05 μA, the two modified sondes agree well with each other. The errors in sensor current relative to the unmodified sonde are around 10 to 15 % (Fig.3.7b).

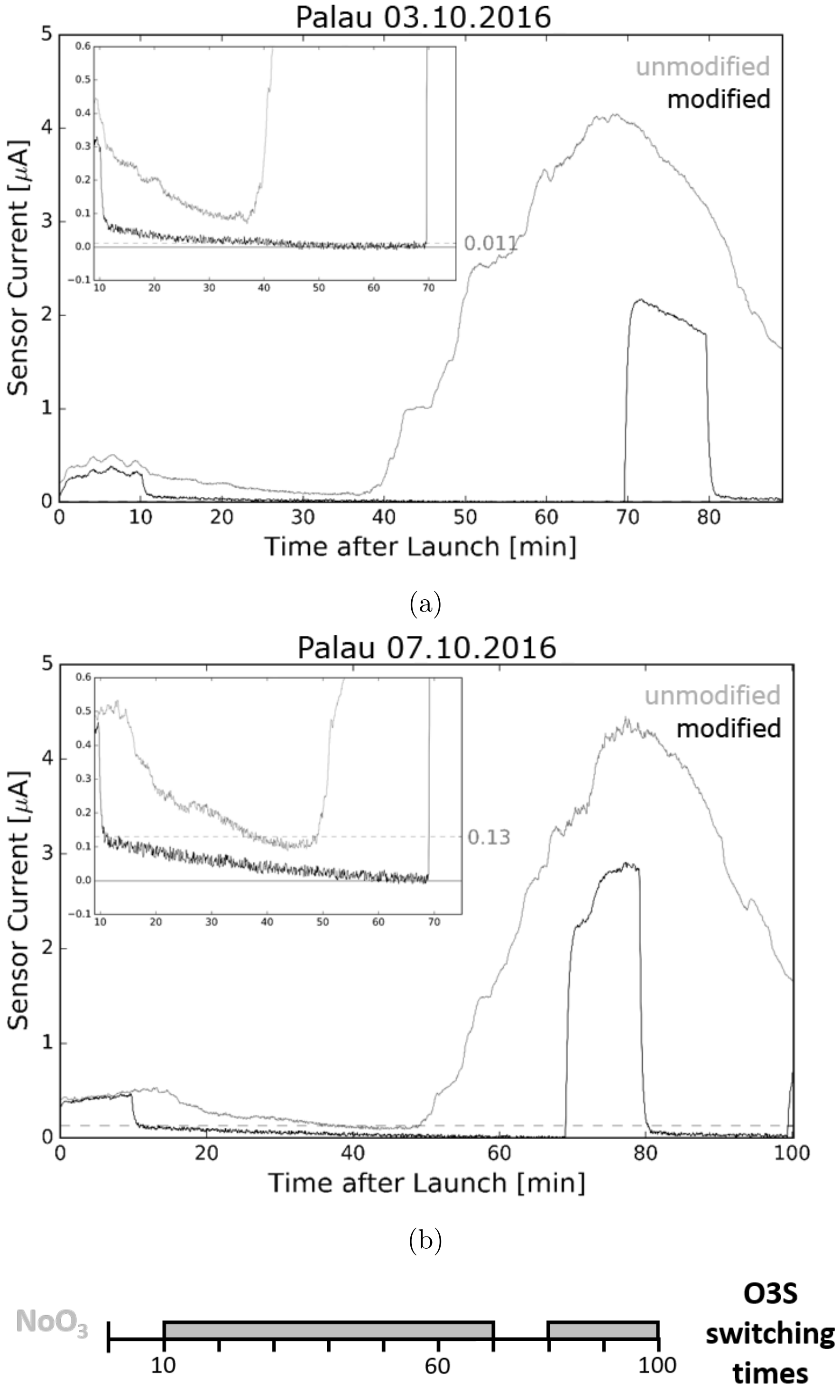

(a)

(b)

(c)

Figure 3.5.: Sensor current measurements for two dual launches with one modified (black line) and one unmodified (gray line) ECC sonde on the same balloon, conducted in Palau in 2016, the no-ozone periods for (a) and (b) were from 10 to 70 minutes (see detail inlet plot) and 80 minutes after launch until burst (timeline shown in (c)), background current of the modified sonde indicated by a gray dashed line and noted in gray on the right of each inlet plot; see Fig.A.2 for another example.

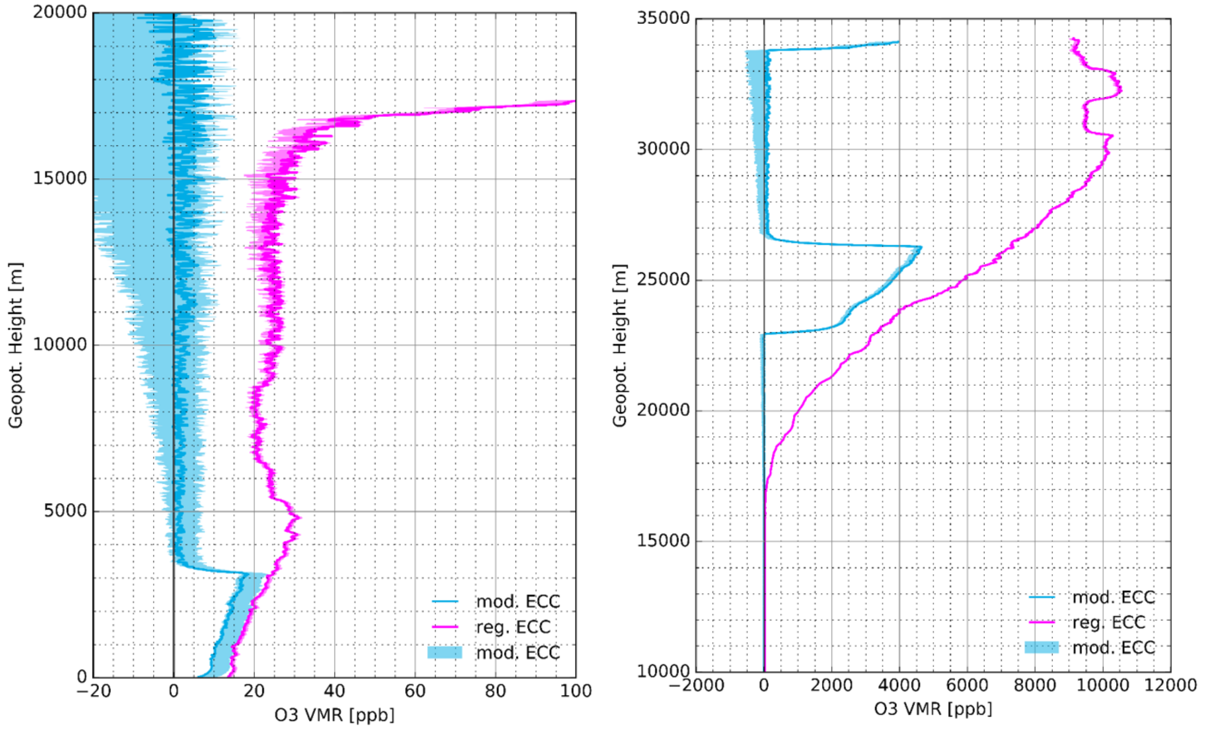

(a) (b)

Figure 3.6.: O_3 VMR profiles for a dual launch (7.10.2016) in Palau with a modified (in blue) and unmodified (in pink) ECC sonde, see Fig.3.5b for sensor current profiles, troposphere in (a), upper troposphere and stratosphere in (b).

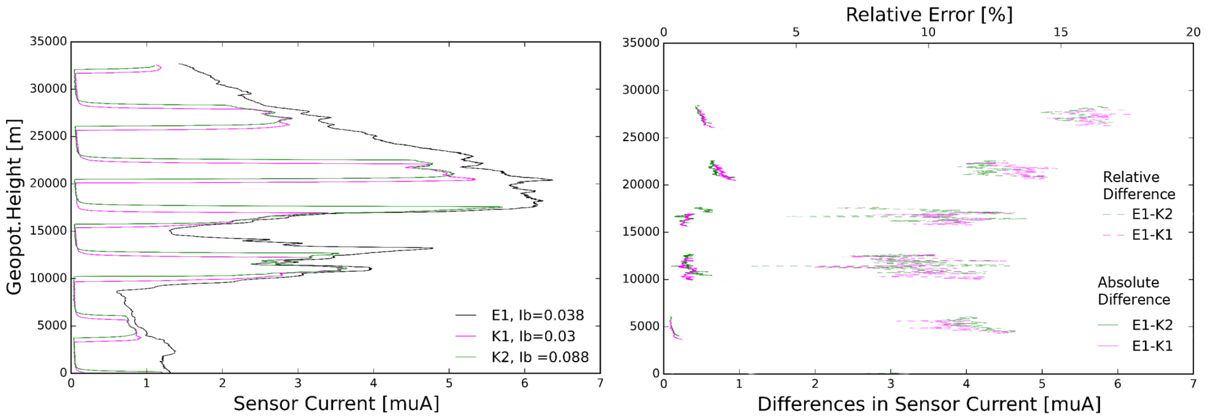

(a) (b)

Figure 3.7.: Sensor current (a) for a trio launch in Ny Ålesund, Spitsbergen (04.05.2016), with two modified (K1, K2, in green and pink) and one unmodified (E1, in black) ECC sonde attached to the same balloon, (b) shows the absolute (solid lines) and relative (dashed lines) differences between E1 and K1 (in pink) as well as E1 and K2 (in green), background currents (Ib) are given in (a).

It is not surprising that the sensor needs a certain time span to detect very high (stratospheric) O_3 concentrations after a no-ozone period. Exposure to a known, constant O_3 concentration in controlled laboratory studies showed an according relaxation behavior during the ambient air periods. A standard UV-photometer run on bottled, purified air, was provided by FZJ (courtesy of Herman Smit) as an O_3 source to validate the modified ECC sonde measurements. Upon switch from no-ozone to ambient air, the current rises to an O_3 level close to, but below the actual O_3 signal within seconds and then continually increases towards or even up to 5 % above the given O_3 level over time. In reality, this behavior is never observed, because there is no constant signal. The relaxation of the current can probably be explained by a mixture of several causes, immanent to the ECC measurement technique, i.e. previous no-ozone exposure leading to extreme contrast to ambient O_3 (depending on length of exposure and O_3 level afterwards), the second time constant and conversion efficiency (see Sect.3.1.1). However, a large error of up to 50 %, as seen during field tests, must be related to an instrumental fault of the device or full modified setup during flight. Thus, unfortunately, the laboratory tests could not explain the decreased O_3 concentrations in the ambient air channel during a modified sounding.

Conclusion and Outlook

An attachable device for ozonesondes to provide an in-flight measurement of the background current has been developed in this thesis. Basic functionality of all individual components of the setup on the ground is given. The device enables time-controlled intermissions of no-ozone measurements during flight and, apart from the delicate assembly, does not complicate preparatory processes. The no-ozone measurement periods in modified ECC sondes launches in Palau and Ny Ålesund support the application of a pressure-dependent background current correction to the raw tropospheric signal, which has therefore been adopted in this thesis. All results have to be treated with caution though, because too low O_3 concentrations were measured by the modified sondes during the ambient air measurement periods in comparison with simultaneous unmodified ECC sondes. The error of up to 50 % cannot be explained by known measurement uncertainties or the measurement principle of ECC sondes. Extensive laboratory tests could not yet reveal the cause of this bias. Possible technical problems of the setup could be a leakage of the no-ozone channel into the ambient channel inside the latching valve, i.e. the valve does not fully separate the channels. Whether the no-ozone filter builds up pressure affecting the pump performance, which could provoke issues, can now be assessed with the new RS41 radiosonde that can monitor the ozonesonde pump current in flight. Further studies in a pressurized chamber e.g. available at WCCOS could help to clarify the issue and validate the no-ozone measurements.

However, improvements in manufacturing (e.g. for the ion bridge and electrodes) have significantly decreased the background current and thus diminished the relevance of additional corrections within the O_3 calculations (see Sect.3.1.2). The purity of no-ozone air during preparation remains the major contributor to the background current. Development of the instrumental device was therefore paused in this doctoral project in favor of scientific analysis of the Palau data set.

3.2. Overview of the Palau Time Series

3.2.1. Data Description/Time frame

The main data set used in this thesis is comprised of ECC ozonesonde measurements conducted at the Palau Atmospheric Observatory (PAO), located in downtown Koror, 7.34° N 134.47° E. Processing of the raw data is described in the previous section (see also Tab.3.1). Altogether 145 launches were successfully performed from 21.01.2016 until 31.10.2019. In addition to bi-weekly ozonesonde launches performed since 2016, at least one intensive campaign with several launches a week, including night-time launches, took place every year. Unfortunately, logistical issues caused some gaps in the time series. Most soundings were conducted during the day (no fixed hour, usually mid-day). There are 17 night-time launches with additional load of Cryogen Frostpoint Hygrometer (CFH) and Compact Optical Backscatter and Aerosol Lidar Detector (COBALD) sondes and/or coinciding measurements with the Compact Cloud and Aerosol Lidar (ComCAL) (see Fig.1.1). In this thesis, no differentiation between day- or night-time launches was made, i.e. we assume no significant diurnal cycle for O_3 and RH within the tropospheric column (compare Sect.4.1.1). Figure 3.8 introduces the data set in a time-height cross-section for O_3 VMR (a) and RH (b) up to 19 km, including marks (arrows) for the individual soundings and significant measurement gaps (white space).

The quality of observations has been monitored closely throughout the full measurement period. Personnel from our local partner CRRF (Coral Reef Research Foundation) has been trained to perform the soundings in our absence, guaranteeing a high standard. In anticipation of the seasonality of the tropospheric O_3 minimum, the intensive campaigns were planned and conducted in fall and spring. The interannual persistence and year-round existence of the tropospheric O_3 minimum in the TWP was already evident from satellite observations (see Rex et al., 2014 and Fig.3.10) and was confirmed using the in situ measurements collected at the PAO. Geo-spatially, the minimum follows the warm pool and is thus affected by ENSO. For the study period, ENSO activity is summarized in Section 4.1.1. Figure 3.9 shows individual soundings during these campaigns from 2016 to 2018.

3.2.2. Technical Details/Issues

Vaisala radiosondes were used for data transmission as well as to measure pressure, temperature and humidity. The RS92-SGP model and its interface to the ECC sonde was used until October 2017 (see Dirksen et al., 2014 for technical details and quality assessment). Thereafter, the ground receiving unit and software were switched to facilitate use of Vaisala's new standard radiosonde RS41-SGP (Sun et al., 2019; Vaisala, 2017). In support of international efforts to assess differences between the old and new radiosonde (for example by the Global Climate Observing System Reference Upper-Air Network, GRUAN) four dual soundings with both radiosonde types, RS92 and RS41, were conducted in spring 2018 (Dirksen et al., 2019). We expect no major impact due to this

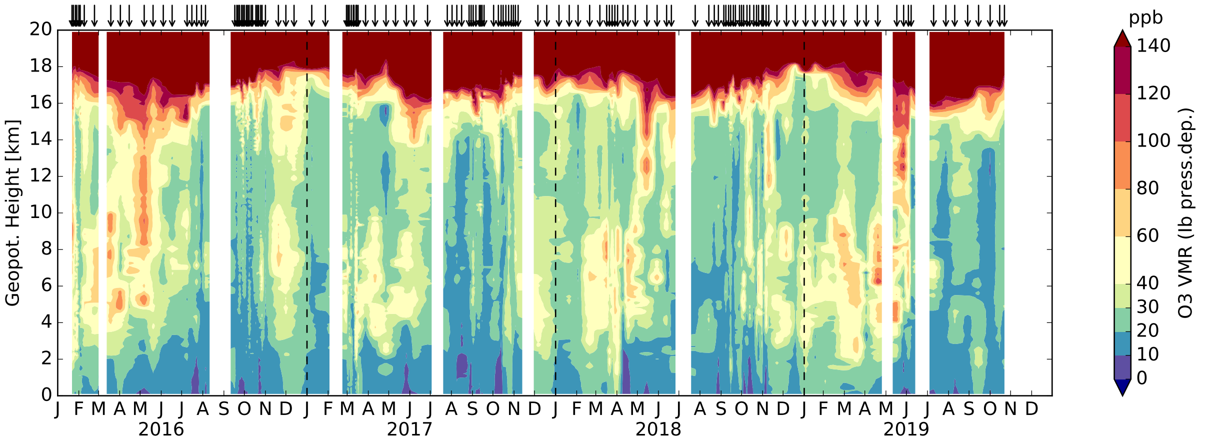

(a) O_3 volume mixing ratios (VMR)

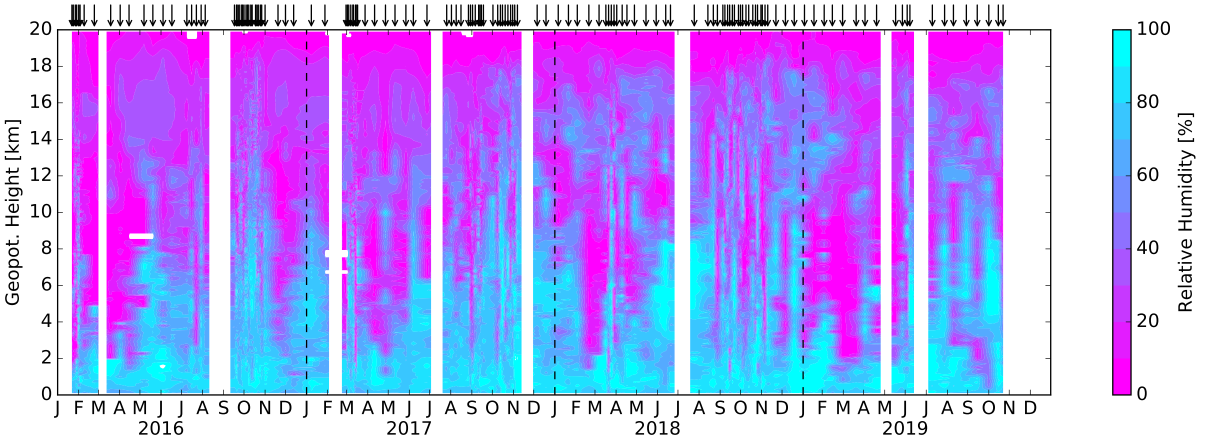

(b) Relative Humidity (RH)

Figure 3.8.: Tropospheric (0-20 km) time-height cross-sections of the Palau sounding data for O_3 VMR (a) and RH (b), arrows on top indicate individual soundings, data is linearly interpolated in between, measurement gaps longer than 20 days are superimposed on the interpolated data as white space, beginning 7 days after/before the last/next sounding, note the non-linear scaling for O_3, O_3 VMR are calculated using a pressure dependent background current correction ("Ib press.dep.", see Sect.3.1.2); see Fig.4.1 for close-up on the tropopause region.

change regarding the tropospheric O_3 monitoring and neglect possible biases in meteorological readings of the radiosondes.

The new RS41 radiosondes facilitate monitoring of the ECC sonde voltage and motor current. First measurements with the new RS41 revealed suspected performance issues of ECC sonde wet cell batteries, which were then discarded. Comparison with satellite observations from Aura MLS (Microwave Limb Sounder, Froidevaux et al., 2008, not shown here) reveal discrepancies in stratospheric O_3 observations for around 20 % of soundings in the data set. At pressure levels below 20 hPa, the affected ozonesondes measured 1-2 ppm less O_3 (10-20 %) than the average of 5 satellite measurements of

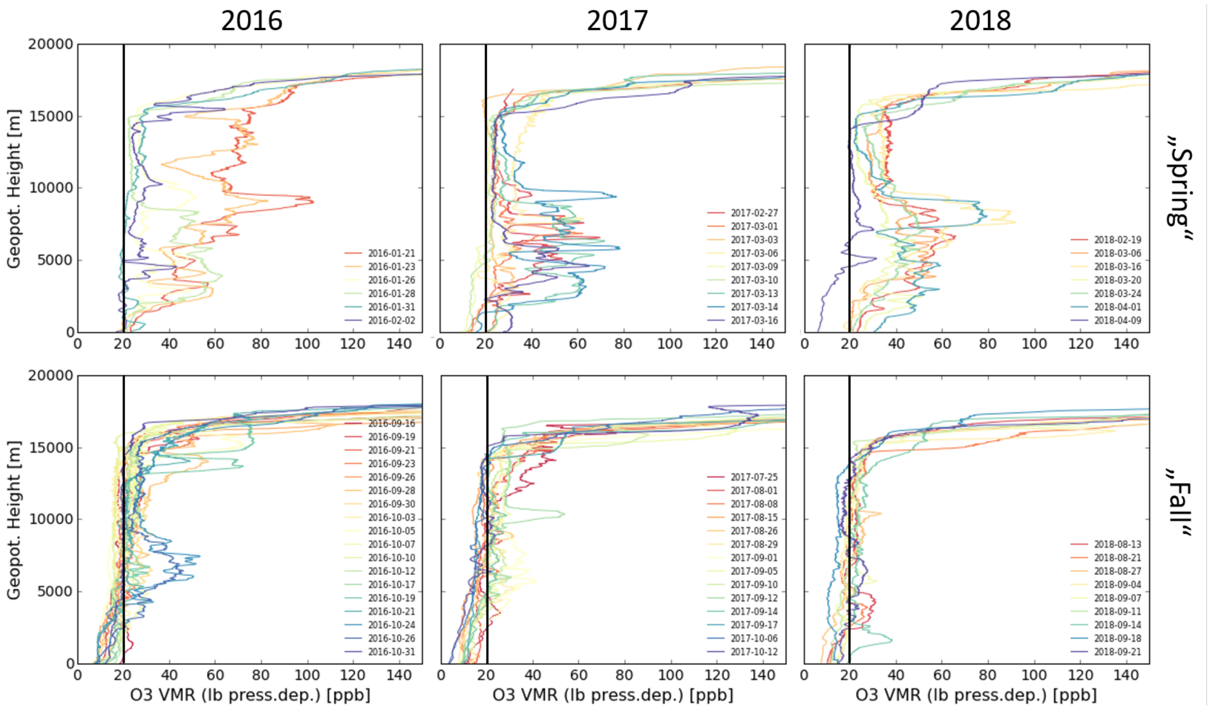

Figure 3.9.: Tropospheric O_3 VMR profiles from intensive sounding campaigns 2016 until 2018 around spring (upper row) and fall time (lower row), individual soundings in different colors, black vertical line indicates a VMR of 20 ppb.

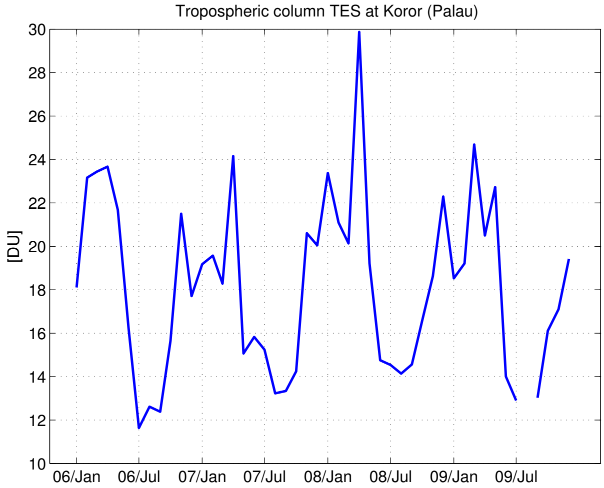

Figure 3.10.: Time series (2006-2009) of tropospheric column O_3 derived from the Tropospheric Emissions Spectrometer (TES) aboard NASA's Aura satellite (see e.g. Worden et al., 2007) and interpolated to Palau's location, courtesy of Ingo Wohltmann, compare Fig.5 in Rex et al., 2014.

the nearest overpass. An early drop of the battery voltage due to the defect wet cell batteries would be a possible cause, but as the battery voltage was not monitored with RS92 radiosondes, clarification of this effect is not possible. We assume no impact on the tropospheric profiles below 20 km and advise to be cautious of this effect when using the time series of either total column or stratospheric O_3.

3.2.3. Statistical Assessment

The sparsity of the O_3 data with a sounding frequency of zero to eleven launches per month and the resulting non-Gaussian distribution of the data complicates the assessment of the temporal variability in our climatologically speaking short 4-year time series. We use monthly, seasonal and annual statistics to assess our data and to compare with other data sets, but have to keep in mind, that these statistical measures are not very robust quantities (compare e.g. Thompson et al., 2003b).

Day-to-day variations are a relevant source of uncertainty for tropical O_3 soundings (e.g. Oltmans et al., 2001). Furthermore, irregular sampling frequencies in an area of high convective activity bear the risk of a clear-sky bias on the one hand (i.e. due to technical/logistical limitations no balloon launches during heavy rain/gusty conditions, even though these might occur regularly) and an observation of rather isolated air masses within an convective updraft (i.e. the sonde is lifted inside the convective cell instead of profiling the surrounding atmospheric conditions) on the other hand. These possible biases should be analyzed for a longer time series, but were neglected in this first assessment of seasonal characteristics of the Palau ozonesonde record.

There are different ways to derive a climatological season average and choosing the best-suited definition is not trivial with our given data set. Data from an individual sounding are first averaged within 300 m height bins using an arithmetic mean (hereafter referred to as “mean”), which essentially complies with the vertical measurement resolution, introducing only a slightly further smoothing (compare Sect.3.1). In the following temporal binning, the order of required steps must be considered as they lead to different values in our time series. There are four different possible sequences for (i) monthly, (ii) seasonal and (iii) annual averaging (compare also Fig.3.11):

1. Individual profiles $x_i(m, y)$ of a month m of year y are first averaged to a monthly mean of the year, monmean(m, y), and then to a seasonal mean, seasmean(s, y), of season s and year y, which is summed up finally over all years and divided by the number of years to yield a climatological season mean, climseasmean$_1(s)$:

$$\text{monmean}(m, y) = \frac{1}{N(m, y)} * \sum_{i=1}^{N(m,y)} x_i(m, y) \tag{3.6}$$

$$\text{seasmean}(s, y) = \frac{1}{M(s)} * \sum_{i=1}^{M(s)} \text{monmean}(i, y) \tag{3.7}$$

$$\text{climseasmean}_1(s) = \frac{1}{Y} * \sum_{i=1}^{Y} \text{seasmean}(s, i), \tag{3.8}$$

with $M(s)$ as the months in season s, $N(m, y)$ as the number of profiles in month m of year y and Y as the number of years.

2. Individual profiles of a month $x_i(m, y)$ of year y are first averaged to a monthly mean of the year, monmean(m, y) (see Eq.3.6), then averaged to a monthly mean of all years, climmonmean$_2(m)$, and finally make up a climatological season mean of all years, climseasmean$_2(s)$:

$$\text{climmonmean}_2(m) = \frac{1}{Y} * \sum_{i=1}^{Y} \text{monmean}(m, i) \tag{3.9}$$

$$\text{climseasmean}_2(s) = \frac{1}{M(s)} * \sum_{i=1}^{M(s)} \text{climmonmean}_2(i). \tag{3.10}$$

3. Individual profiles of month m of all years are directly averaged to a climatological month mean, climmonmean$_3(m)$, then to a climatological season mean over all years, climseasmean$_3(s)$:

$$\text{climmonmean}_3(m) = \frac{1}{\sum_{j=1}^{Y} N(m, j)} * \sum_{j=1}^{Y} \sum_{i=1}^{N(m,j)} x_i(m, j) \tag{3.11}$$

$$\text{climseasmean}_3(s) = \frac{1}{M(s)} * \sum_{i=1}^{M(s)} \text{climmonmean}_3(i). \tag{3.12}$$

4. Individual profiles of season s of all years are directly averaged to a climatological season mean, climseasmean$_4(s)$:

$$\text{climseasmean}_4(s) = \frac{1}{\sum_{l=1}^{Y} \sum_{j=1}^{M(s)} N(j, l)} * \sum_{l=1}^{Y} \sum_{j=1}^{M(s)} \sum_{i=1}^{N(j,l)} x_i(j, l). \tag{3.13}$$

The same possibilities to order the individual steps can be considered for the calculation of an annual average. Figure A.4 in the Appendix shows a comparison of the different methods used to calculate shifted seasonal mean tropospheric O_3 profiles from Palau soundings (compare Sect.4.1.1). For the description of the dataset as a whole, and if not mentioned explicitly otherwise, we will use the third averaging procedure described above. climseasmean$_3(s)$ will not overestimate single months with very few and/or outlying profiles, assuming the interannual variability of the months is small compared to variations between different months.

Median values can be derived in a similar manner and can arguably be a better choice for the non-Gaussian data distribution. The mostly negative difference between the seasonal median and mean over the whole tropospheric column and the right (unbiased) skew of the sample (see Fig.3.12) show the tendency of the arithmetic mean to overestimate. Thus, depending on the research question to be answered, different quantiles, median or mean values are discussed in this thesis. Since the differences of mean and median within a season are small (compare also Fig.A.5), we present the mean and respective standard deviations in the general description of the O_3 variability in Sect.4.1 for convenience.

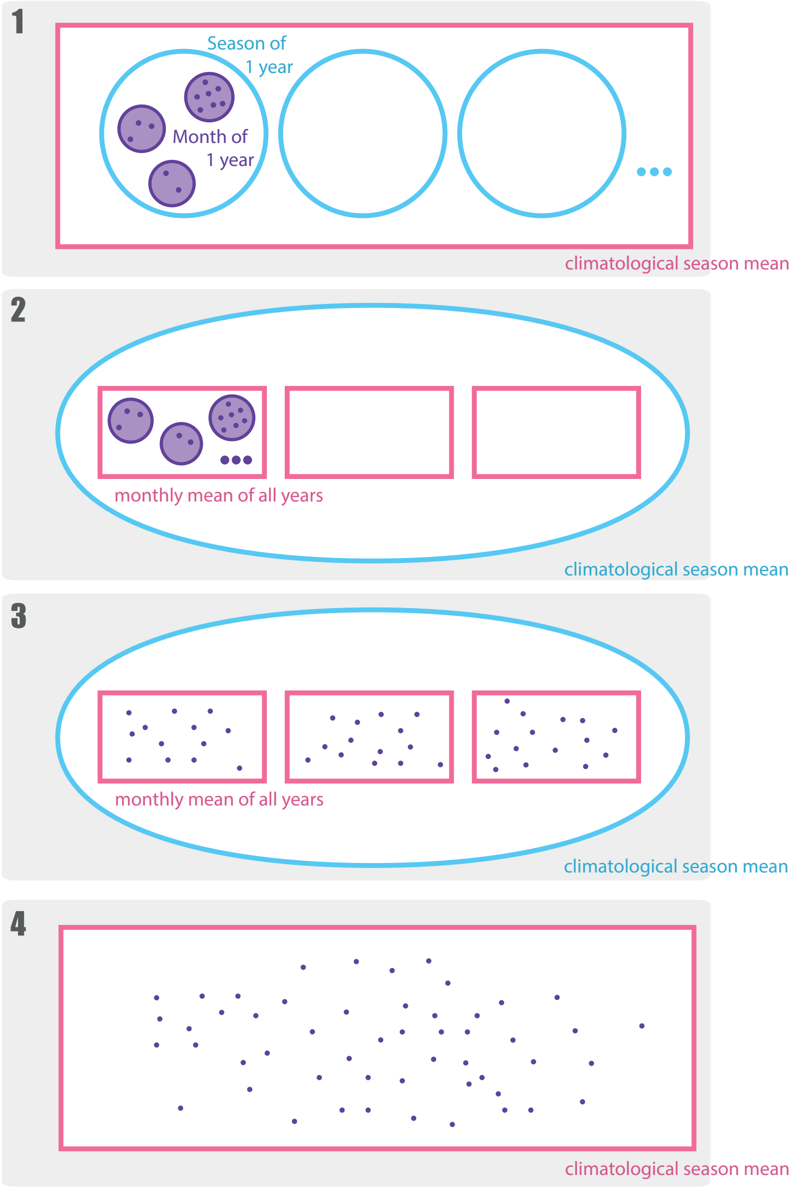

Figure 3.11.: Illustration of four different averaging approaches to arrive at a seasonal mean, purple dots represent individual soundings, pink squares indicate climatological averages over several years, circles all other means (blue for season, purple for month) see text for mathematical formulations.

3.3. Auxiliary Observational Data

The in situ profile measurements conducted at the PAO characterize the atmospheric column above the station well in the given time frame. To embed the Palau observations in a larger spatial and temporal context, we use measurements from other sounding stations. Comparison with satellite data has not been a focus of this thesis, but data products from the Microwave Limb Sounder (MLS) and Tropospheric Emissions Spectrometer (TES) aboard NASA's Aura satellite were used in pre-studies and are described briefly when mentioned in the respective sections. Data retrieved at the Palau weather

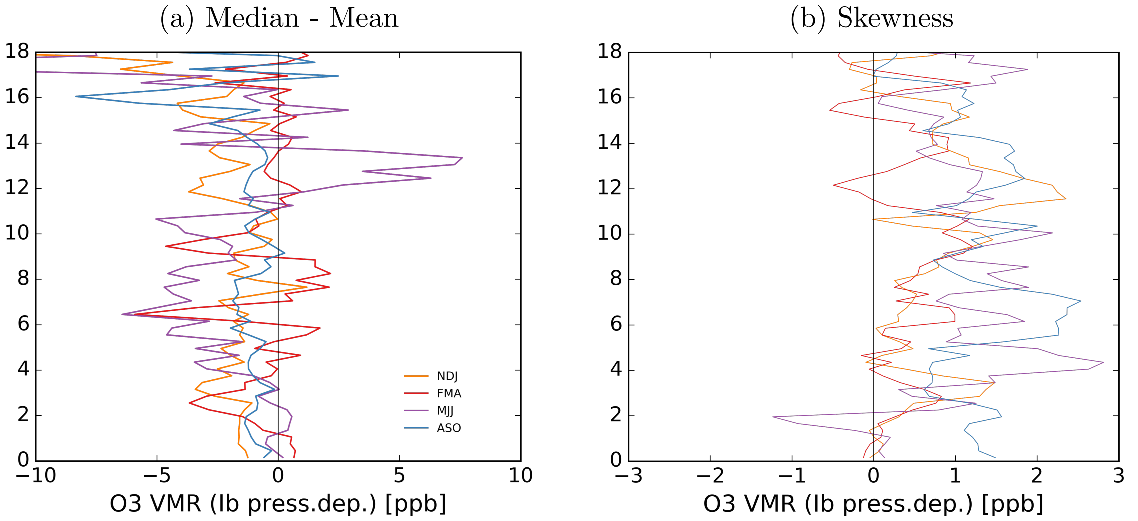
(a) Median - Mean

(b) Skewness

Figure 3.12.: Comparison between seasonal mean (climseasmean$_3$, Eq.3.12) and median, illustrated as absolute difference (a) and by unbiased sample skewness (adjusted Fisher-Pearson standardized moment coefficient G_1, applied to climseasmean$_4(s)$, see Joanes and Gill, 1998)(b); median value derived in resemblance to climseasmean$_3$, first creating a median monthly profile from all individual profiles of a month of all years and then averaging towards a seasonal mean in the arithmetic sense again (compare Fig.A.5).

station (Sect.3.3.2) and data provided by the Pacific Climate Change Science Program (PCCSR, 2011, see `www.pacificclimatechangescience.org`) have been reviewed for the climatological scope of the key parameters temperature, wind and rainfall.

3.3.1. SHADOZ Stations

As a tropical station Palau shares technical challenges as well as certain atmospheric characteristics with O_3 measurement stations assembled in the SHADOZ network (Southern Hemispheric ADditional OZonesondes, Thompson et al., 2003a,b, 2007, 2011). Since 1998, SHADOZ fills observational gaps in the ozonesonde record of the Southern Hemisphere and the tropics by providing consistent data from remote tropical and subtropical sites. Palau, as a highly suitable candidate for SHADOZ, is envisioned to be included in the network (private conversation with SHADOZ's principal investigator Anne Thompson). To embed our O_3 profile observations in a regional context, we compare our data with the results of previous studies which use SHADOZ soundings (e.g. Folkins, 2002; Hayashi et al., 2008; Oltmans et al., 2001; Randel et al., 2007; Solomon et al., 2005; Thompson et al., 2012) and include data from a selected number of stations in our own analysis (see Sect.4.2.2).

Data from the SHADOZ network has been used in many studies (see e.g. overviews in Thompson et al., 2012). Initially, the validation of satellite instruments was the main motivation behind SHADOZ (Thompson et al., 2012), however, also chemical-transport

Figure 3.13.: Map of SHADOZ site locations (from e.g. Thompson et al., 2012).

or coupled chemistry-climate models are validated using the database. To provide the best possible data set to users, the SHADOZ data are constantly re-assessed in a community-wide effort (e.g. Smit, 2014; Smit et al., 2007; Thompson et al., 2019). The current data version No.6 is used in this study and incorporates a reprocessing of all data according to state-of-the-art procedures (see Deshler et al., 2017; Smit et al., 2012; Thompson et al., 2017; Witte et al., 2017, 2018). The latest JOSIE campaign (see Sect.3.1.3) was dedicated to tropical stations and their particular challenges and confirmed the high quality of the methods and operating procedures used within SHADOZ (Thompson et al., 2019).

Site	Location [°lat, lon]	Time Record mm/yyyy	Distance to Palau [km]
Java	7.5S, 112.6E	01/1998-10/2013	3100
Hanoi	21N, 106E	09/2004-06/2018	3400
Kuala Lumpur	2.7N, 102E	01/1998-10/2018	3700
Fiji	18S, 178 E	01/1998-01/2019	5600
American Samoa	14S, 171W	01/1998-02/2019	6500
Hilo	19N, 157 W	01/1998-02/2019	7400
Costa Rica	10N, 84W	07/2005-10/2018	15400

Table 3.2.: SHADOZ stations and respective time record used in this thesis, with distance as the crow flies to Palau; compare e.g. Thompson et al., 2012.

In terms of common characteristics in free-tropospheric and TTL ozone, the SHADOZ stations can be divided into several groups: the Western Pacific and eastern Indian Ocean (Kuala Lumpur, Java, Fiji, American Samoa) the equatorial Americas (San Cristobal, Costa Rica, Paramaribo), the Subtropics (Hanoi, Hilo, Irene, Réunion) and the Atlantic and Africa (Natal, Ascension, Cotonou, Nairobi) (Thompson et al., 2012). As Palau would be associated with the Western Pacific stations, we focus our comparison on these four stations. In addition, Hanoi, being the second closest SHADOZ station, Costa Rica, located at a similar latitude, and Hilo, as another Pacific station North of the equator, are considered (compare Table 3.2, see Section 4.2.2).

3.3.2. Palau Weather Station (NOAA)

Located 800 m South-West of the PAO on a slope on the same island, the US National weather service and NOAA operate a general weather station (PTRO 91408) with radio soundings twice a day. The data is openly available (e.g. via the upper-air sounding database provided by the University of Wyoming: `weather.uwyo.edu/upperair/sounding.html`). The high temporal resolution of these observations is exploited to characterize wind seasonality. Figures 3.14 (a) and (b) show the zonal and meridional wind components as 5-day-averages from daily soundings at 9 am local time for the study period.

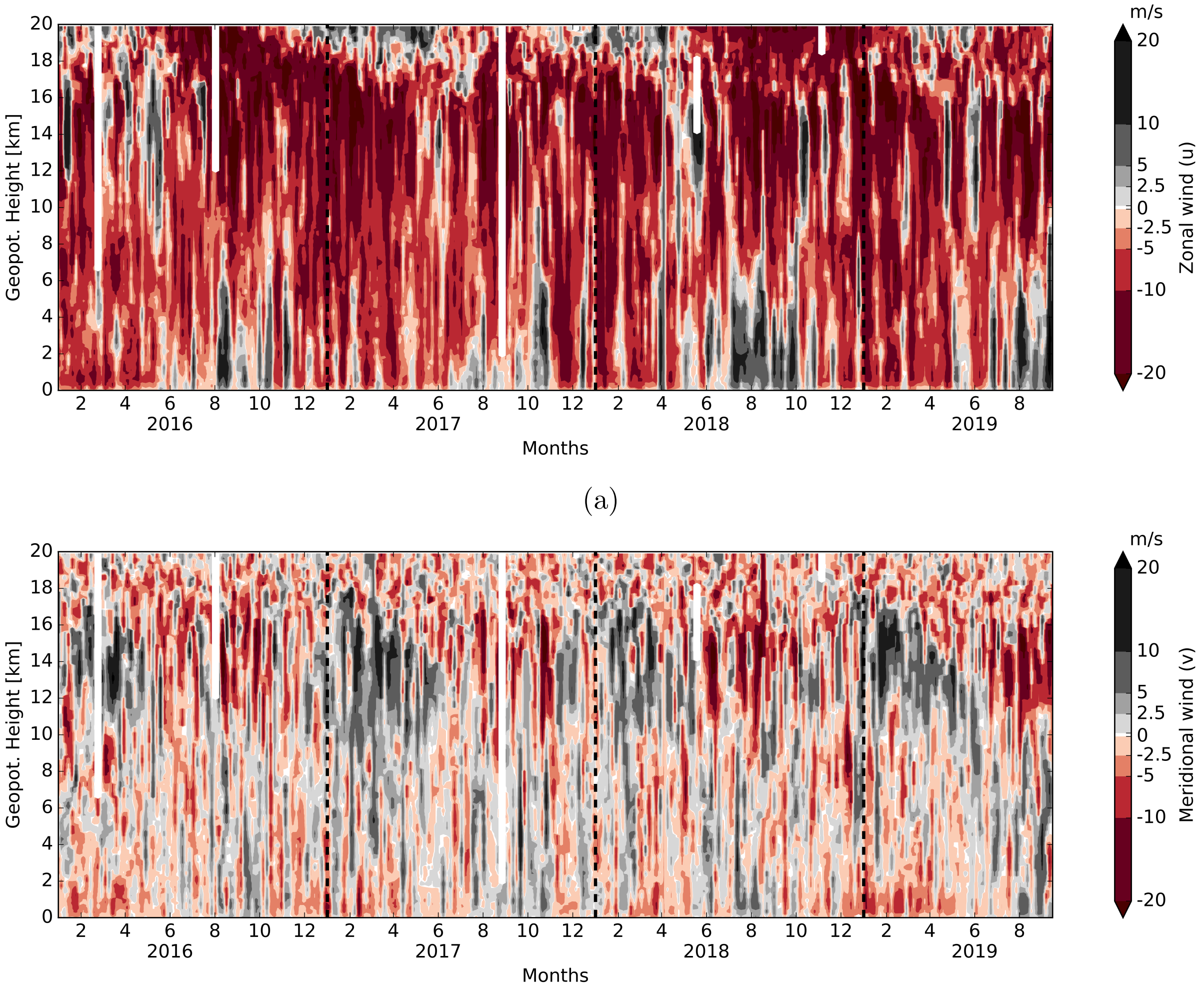

(a)

(b)

Figure 3.14.: Tropospheric time-height cross-section for zonal (a) and meridional (b) wind derived from daily radiosoundings (9 am local time) at the Palau weather station as 5-day-averages from the 01/2016 until 10/2019 (data from `weather.uwyo.edu/upperair/sounding.html`).

The changes in QBO phases during the study period are evident in the time series, which shows a downward propagation of the zonal wind signal. Comparison with temperature and O_3 measurements support the expectations regarding the differences in strength of the BD circulation for the Easterly and Westerly phase, which is however not further assessed in the scope of this study (compare Sect.4.1.3).

3.4. Modelling and Methods

3.4.1. Trajectory Analysis

Trajectory analyses for observed air masses are a common method in atmospheric sciences. The history of an air mass, revealed by tracing its conservative properties, can help to explain its current chemical and thermodynamic state. The underlying assumptions of parcel theory are legitimate until the air parcel looses its identity due to mixing. Hence, we limit our analysis to backward trajectories shorter than ten days to capture the dynamical footprint. An important chemical constraint on the parcel's identity is the typical lifetime of marine boundary layer O_3 of five days (compare Sect.2.2.1).

To investigate the origin of Palauan air masses measured by balloon soundings we used the trajectory scheme of the Lagrangian transport model ATLAS (Wohltmann and Rex, 2009; Wohltmann et al., 2010). The model was driven by 3D wind fields, temperatures and diabatic heating rates from the ECMWF ERA5 reanalysis (1.125° x 1.125°, 3 h temporal resolution) (compare Hoffmann et al., 2019). The model uses a hybrid vertical coordinate, which gradually transforms from "pressure" at the surface to "potential temperature" in the stratosphere (see Wohltmann and Rex, 2009). The corresponding vertical velocities change from vertical winds in pressure coordinates to diabatic heating rates. 30-days backward trajectories were initialized every tenth sonde reading of a profile measurement and with a time step of 10 minutes for the 138 soundings which had full metadata available.

Kernel Density Estimation

To assess the geo-spatial distribution of air mass origins we use visualization in geographic maps and a simple Gaussian Kernel Density Estimation (KDE) for the probability distribution function (PDF) of back-trajectory ending points. Coordinates are first transposed to a grid of horizontal and vertical lines of constant latitude and longitude. This equidistant cylindrical projection preserves distances along meridians by implementing an additional latitude scaling. We chose a cylindrical projection for its representativity in equatorial regions. For trajectories crossing the 30° latitude, distortions have to be considered. The KDE bandwith selection is done by Scott's Rule (Scott, 1992) and a squared Euclidean metric is used. With these parameters, the KDE works best for unimodal distributions and oversmoothes multiple modes.

Potential Vorticity Criterion

For a better interpretation of the vertical transport, especially in the TTL region and over a greater meridional range into the subtropics, we make use of a dynamical tracer: potential vorticity (PV)(compare e.g. Holton, 2004; Kunz et al., 2011). PV is conserved for adiabatic, frictionless motion, i.e. for constant potential temperature θ. The definition of Ertel's PV P in isentropic coordinates is

$$P \equiv (\zeta + f)(-g\frac{\partial\theta}{\partial p}) \tag{3.14}$$

with ζ is the vertical component of the relative vorticity, f the Coriolis parameter, g the gravitational acceleration, p as pressure. The units are summarized as standard potential vorticity unit ($1\mathrm{PVU} = 10^{-6}\mathrm{m}^2\mathrm{s}^{-1}\mathrm{K}\ \mathrm{kg}^{-1}$).

Whether an air parcel crosses the extra-tropical tropopause during its path or not is commonly determined using a threshold for the absolute value of PV $|P|$ at 2 PVU (e.g. Holton et al., 1995; Waugh and Polvani, 2000). By examination of operational ECMWF data, Kunz et al. (2011) found a variation of $|P|$ at the dynamical tropopause from 1.5 to 5 PVU, depending on the isentropic level and season. In our trajectory analysis, we therefore consider trajectories with values greater than 1.5 as well as 2 PVU as possible stratospheric intrusions. The tropical tropopause is dynamically denoted as an isentropic surface roughly at a potential temperature of 380 K (e.g. Holton et al., 1995, see Fig.A.1).

3.4.2. Chemical Box Model

The oxidizing capacity of the troposphere in the TWP is assessed using a chemical box model in this thesis. Box models neglecting transport and constrained to a set of observations are a very useful tool to estimate the local abundance of the short-lived radical OH and to analyze the controlling processes (e.g. Bloss et al., 2005).

Model Description

The model AWIP has been implemented successfully for stratospheric simulations and case studies (Krämer et al., 2003; Lehmann, 2004; Wohltmann et al., 2010). 46 active species and 171 reactions are incorporated in the model, including photolysis (42), gas phase (122) and heterogeneous (7) reactions. Reaction rate constants are based on the JPL catalogue (Jet Propulsion Laboratory, Sander et al., 2011). The photolysis rates as a function of pressure, temperature, solar zenith angle (SZA) and overhead O_3 column are taken from lookup-tables calculated by the radiative transfer model TUV (Tropospheric Ultraviolet-Visible Model, Madronich and Flocke, 1999). A more thorough description of the box model including a list of all included species and reactions can be found in Wohltmann et al. (2010).

In our setup, the model is initialized at 0:00 local time and then run for one day. The input parameters are pressure, temperature, SZA (dependent on latitude, longitude, date and time) and the VMR for various chemical species from either observations or estimates from model results and previous studies. OH VMR model output is aggregated hourly and then averaged over 24 hours.

A usage of AWIP in our specific tropospheric contexts depends on a few assumptions, i.e.:

- The set of reactions originally representing stratospheric chemistry is sufficient in the clean tropospheric air pool above Palau, i.e. we neglect organic chemistry and clouds.
- We focus on the mid-troposphere (400 hPa), where OH is proportional to the photolysis rate of $O(^1D)$ alone (Rohrer and Berresheim, 2006), further simplifying our input parameter space. In this context, small variations of this altitude level are assumed to be of minor relevance due to the homogeneity of the layer (compare Sect.2.1.3).

Reduced Parameter Space

Following these assumptions, the relevant involved active chemical species are HO_2, H_2O_2, H_2, CH_4, CO, CO_2, $O(^1D)$, O_3, H_2O, CH_2O, NO, NO_2 and fixed O_2 and N_2, as well as a minor contribution of HOBr and Br, respectively.

VMR inputs for O_3 and H_2O are derived from observations at the PAO. Quantities of other chemical species are initialized from available GEOS-Chem chemistry and transport model runs (compare Rex et al., 2014 and Ridder et al., 2012). As these runs represent conditions from a different year, snapshots from the first day of each month, 00:00 GMT, from February 2009 until January 2010 were aggregated for this purpose.

As explained in Section 2.2.2, NO_x is the rate-limiting factor in the tropospheric production of O_3 in the remote TWP and a crucial parameter in the recycling of OH. Furthermore, CH_4 and CO are the main reaction partners of OH. CH_4 can be assumed as constant and its derivative CH_2O only becomes relevant for OH loss mechanisms in the upper troposphere (compare Gao et al., 2014; Hanisco et al., 2001). Reaction with CO, however, can lead to substantial loss of OH in the free troposphere (reactions 2.1, 2.2, 2.12). To analyze the dependency of the O_3/OH relation we perform sensitivity studies with our box model using a range of typical NO_x and CO values.

Correlation Coefficients

In the analysis of our box model results we use a few measures to quantify dependencies between different input parameters. The correlation between three given variables x, y

and z can be estimated using the multiple correlation coefficient

$$R_{z,xy} = \sqrt{\frac{r_{xz}^2 + r_{yz}^2 - 2r_{xx}r_{yz}r_{xy}}{1 - r_{xy}^2}}, \tag{3.15}$$

where r_{ij} are the pairwise Pearson coefficients, x and y are considered as independent variables and z is the dependent variable. In our case we want to estimate the dependency of OH on combined O_3 and H_2O. The square of either correlation coefficient is called the coefficient of determination. It can be interpreted as percentage of variance in a dependent variable explainable by the independent variable(s).

Because statistically, we are dealing with a small set of observations, we can improve our correlation estimate to be more unbiased using an adjusted R (R_{adj}^2) defined as

$$R_{adj}^2 = 1 - \frac{(1 - R^2)(n - 1)}{(n - k - 1)}, \tag{3.16}$$

with k as the number of independent variables and n as the number of data elements in the sample.

4. Results and Discussion

A central achievement of this doctoral thesis is the generation of the 4-year data set of tropospheric O_3 profiles in Palau. Filling the observational gap with this unprecedented time series from the TWP will shed light on the region's unique air chemistry. This thesis presents the first description of the tropospheric O_3 variability above Palau and its seasonal characteristics (Sect.4.1). The locally controlled humid, ozone-poor atmospheric column is interrupted by air masses of non-local origin deviating in Relative Humidity and O_3 VMR. These quantities are excellent tracers for dynamical processes. Studies of air mass transport to the TWP have to account for variations of chemical sources (or sinks), atmospheric waves or physical processes altering the chemical composition along the path of transport (compare e.g. Schoeberl et al., 2015). An in-depth analysis of free-tropospheric O_3 and RH and comparison with other regional studies leads to a classification of observed air masses relative to the tracer backgrounds using a statistical approach (Sect.4.2). With a focus on source and path variability, a hypothesis for the origin of air masses tied to this classification is tackled in a back-trajectory analysis (Sect.4.3). Finally, the impact of tropospheric O_3 variations on the oxidizing capacity above the TWP is estimated using chemical box model simulations (Sect.4.4).

4.1. Tropospheric O_3 Variability

The atmospheric composition of the TWP is governed by non-local and local processes, which are both driven by the complex interplay of global circulation patterns and their seasonal variability. The boundary layer, free (mid-)troposphere and the TTL show different degrees of variability. The following descriptive statistical analysis therefore differentiates between altitude levels and timescales. The most interesting features and therefore focus of this thesis are the apparent annual cycles in the TTL (Sect.4.1.3) and the mid-troposphere (Sect.4.1.2), including the annual tropospheric O_3 minimum with its potential major impact for stratospheric entry of chemical compounds (compare Sect.2.2.3).

4.1.1. Overview

The shortness of the time series imposes a few challenges on this thesis. Interannual variations can only be assessed to a certain extent, but at the same time are affecting the annual statistical results. In anticipation of the impact of the strong El Niño in

2016, we begin with a multi-year comparison of tropospheric O_3. Annual variations of the trace gas are then described for a reduced time series, excluding the extreme event. Further temporal differentiation is done in seasons shifted by one month with respect to the common seasons of the mid-latitudes. Respective calculations of statistical measures are described in Section 3.2.3.

ENSO

Interannual variations between the 4 years of the study period are most obvious in connection with the ENSO cycle. The onset of measurements in the beginning of 2016 coincides with a very strong El Niño event (e.g. Diallo et al., 2018; Huang et al., 2016, compare 2.1.2). In analogy to the impact of the strong 1997/8 El Niño, Palau experienced a drought during spring 2016 with critical water reserves on the island (Di Liberto, 2016). We observed a clear, corresponding mid-tropospheric signature: an unusual very dry and ozone-rich mid-troposphere, compared to the other years (compare Fig.3.8). The time-height cross-sections in Figure 4.1 show a close-up on the TTL for O_3 VMR and temperature. O_3 levels are significantly enhanced in the upper troposphere (UT), from March until July 2016 (see Fig.4.1a), as a feedback of suppressed convection with less uplift of ozone-poor air from the ground and less wash-out of O_3 precursors. Singular observations of higher than average O_3 VMR in the UT are made in every year (May until July), visible as tongue-like features in Figure 4.1a, but only occur for a longer time period in 2016.

For a better comparison of the O_3 and temperature feedback, the absolute temperature minimum is shown in black dots against O_3 VMR (Fig. 4.1a) and the ozonopause, defined as the level of 90 ppb (compare Sect.2.1.4) is superimposed as a black solid line on temperature observations (Fig.4.1b). The altitude of the ozonopause differs significantly from the unusually cold thermal tropopause in spring 2016. This temperature anomaly is associated with warm ENSO events (e.g. Kiladis et al., 2001; Paulik and Birner, 2012; Randel and Thompson, 2011). In contrast, less O_3 was observed in the lower stratosphere (LS) (above 19 km) and a weaker corresponding vertical gradient over the whole TTL. Decreased LS O_3 has been documented as a zonal El Niño response by different studies and is attributed to enhanced tropical upwelling (Diallo et al., 2018; Konopka et al., 2016; Randel et al., 2009). A detailed description of the mechanisms governing TTL composition is done in Section 4.1.3.

The El Niño event in 2019 has a weaker feedback on O_3 VMR according to our observations. In between the two El Niños, neutral and moderate La Niña conditions were reported. These had less impact on a regional to global scale and our short time series does not allow further conclusions. The dependency on the whole ENSO cycle remains impossible to assess, but might reveal interesting features with a growing time series. As a consequence and in compliance with acknowledged ENSO indices (compare 2.1.2), data before August 2016 was disregarded in some of the following statistical seasonal analysis and will be referred to as “excluding El Niño”. The 2019 El Niño episode, weaker in nature, is still included.

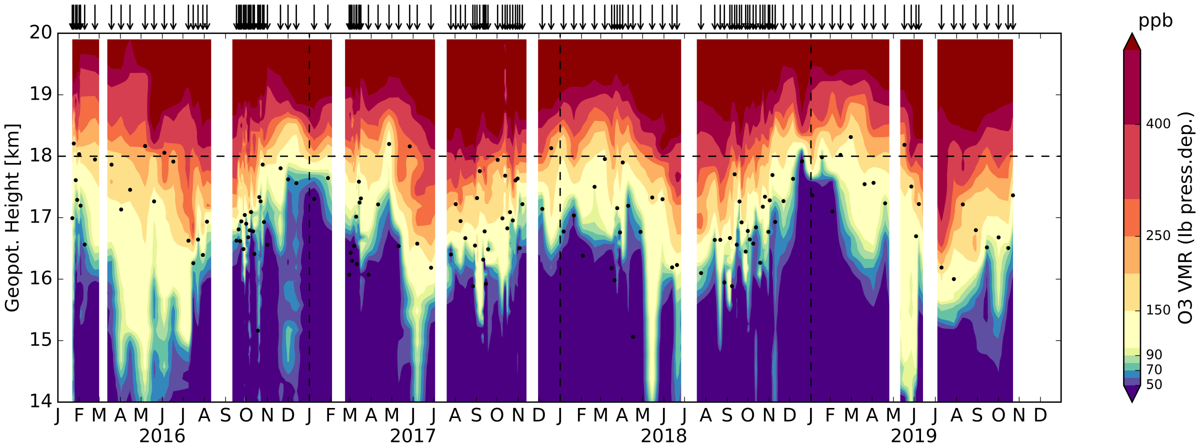

(a) O_3 VMR

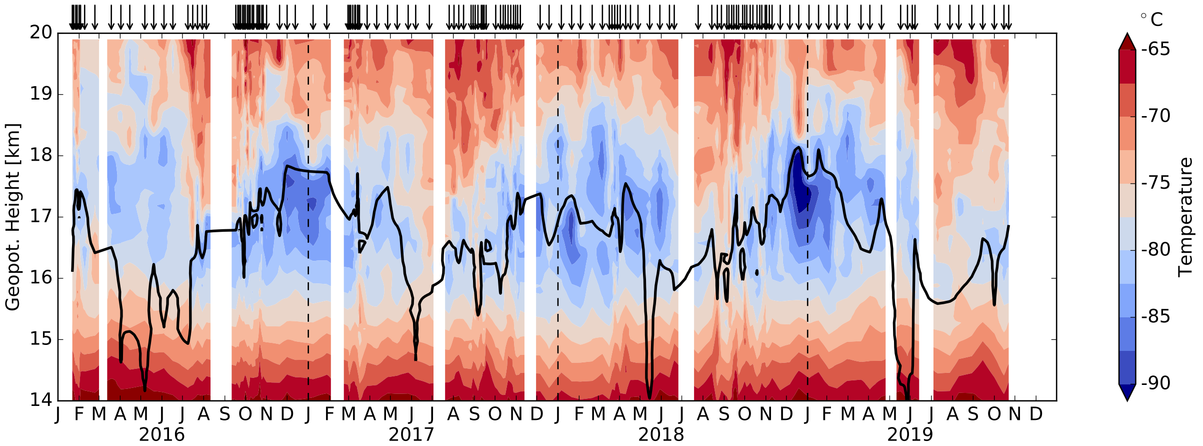

(b) Temperature

Figure 4.1.: TTL (14-20 km) time-height cross-section of the Palau sounding data for O_3 VMR (a) and temperature (b); black dots in (a) show locations of the absolute minimum temperature per profile, black horizontal dashed line in (a) at 18 km refers to the most prominent annual cycle as visualized in Fig.4.6, black solid line in (b) represents the ozonopause defined as O_3 VMR observations of 90 ppb (linearly interpolated); for more details, compare Fig.3.8 for the full troposphere, note adapted scales.

Annual Variability

Figure 4.2 shows the annual variability of tropospheric O_3 VMR using monthly means (a) and anomalies (b) from a “long term” annual mean profile (c), derived from climatological monthly means (Eq.3.11), excluding El Niño (compare Sect.3.2.3). In addition to this climatological mean, the right panel shows annual means for the three full years of measurements for comparison (colored thin lines, Fig.4.2c). The large difference of the 2016 El Niño year throughout the entire free and upper troposphere of approx. 5-10 ppb or 15-30 % supports our decision to exclude this year's data partially, even though it has to be mentioned, that the 2016 annual mean VMR mostly stay within the standard deviation (SD) from the long term annual mean (grey dashed lines).

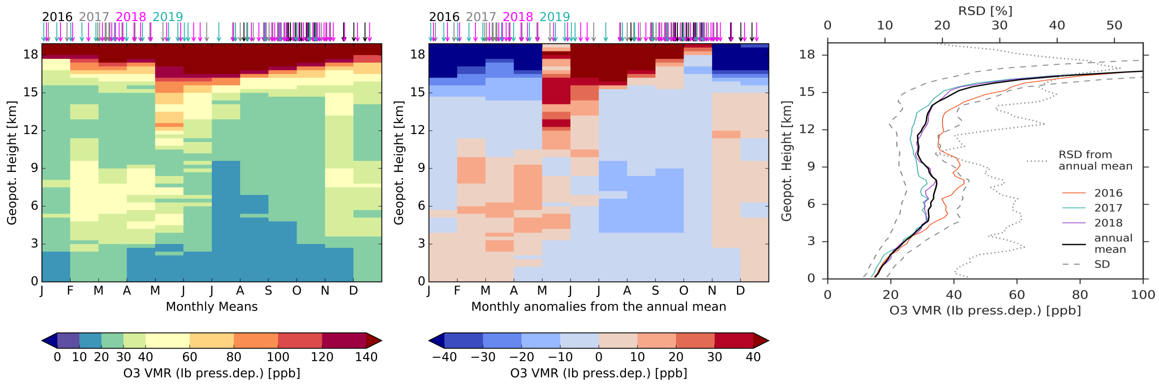

(a) (b) (c)

Figure 4.2.: Monthly arithmetic means (a), anomalies from the annual mean (b) and the annual mean profiles for certain years (thin colored lines) and "long term"(thick black line) with corresponding standard deviations (SD) (grey dashed lines) and relative standard deviation (RSD) (grey dotted line) (c), excluding El Niño, i.e. only data used between August 2016 an October 2019; individual soundings are marked as arrows above, with different colors for different years (compare full time series in e.g. Fig.3.8); climatological monthly means (see Eq.3.11) are aggregated for the annual means and explained in section 3.2.3.

The so-called "S-shape" of the long term annual mean profile is typical for the tropics, as for example observed at various SHADOZ stations (e.g. Folkins, 2002; Pan et al., 2015; Thompson et al., 2003a,b). O_3 levels are lowest in the boundary layer and also low between 10-12 km. They increase to around 35 ppb in the mid-troposphere and again from 12 km onwards to their atmospheric peak in the stratosphere. The annual monthly statistics (Fig.4.2a and Fig.4.2b) reveal two dominating signals:

- an annual cycle in the mid-troposphere ($\sim$ 5-10 km) of a factor 2-3 with a minimum from July until October ($\sim$ 10-30 ppb, maximum at 30-60 ppb), and

- a reverse, strong cycle in the TTL with maximum anomalies ($>$ 40 ppb) from June until September,

which will be described in more detail in dedicated subsections (4.1.2, 4.1.3). The differences in annual variability with altitude are emphasized by the relative standard deviation (RSD), shown alongside the annual mean profile in Fig.4.2c (dotted gray line). The RSD is the fraction of the SD relative to the annual mean and can here be considered as a measure of variability with altitude (compare Ogino et al., 2013). The peak in RSD at 50 % around 17 km reflects the strong TTL cycle. The enhanced variability in mid-tropospheric O_3 (RSD $\sim$ 30 %) over a greater altitude range corresponds with the annual cycle revealed by the monthly means. Annual variations in O_3 observations are smallest (RSD $\sim$ 20 %) in the boundary layer ($<$ 2 km) and around 10-12 km, thus coincidental with the O_3 minima of the annual profile. The UT O_3 low or chemopause (see Sect.2.1.4) can be explained by air masses of the local boundary layer being lifted to the UT by deep convection (see Sect.4.2.1). The dry environment at this altitude increases O_3 lifetimes and makes in situ O_3 destruction as an alternative explanation unlikely, although it is discussed as a consequence of convectively injected water vapor (see Schoeberl et al., 2015 and Anderson et al., 2016). The low UT variability can thus be explained by the persistence of deep convective activity and the level of convective outflow in association with the Hadley circulation (e.g. Folkins, 2002; Solomon et al., 2005; Takashima et al., 2008, see Sect.2.1.3 and 2.1.4). The inhibition of deep convection during El Ninõ 2016 is reflected in an anomalous peak in the RSD around 10 km ($>$ 50 %, not shown here). As a characteristic feature of tropical soundings, (low) UT O_3 is often used as an indicator for deep convective detrainment (Folkins, 2002; Gettelman et al., 2009; Kley et al., 1996; Paulik and Birner, 2012; Solomon et al., 2005). Exact identification of the level of convective outflow using O_3 observations is, however, not easy in an individual profile due to vertical stratification.

The boundary layer exhibits continuously low O_3 VMR ($<$ 20 ppb) with notable exceptions from December until March in alignment with the mid-tropospheric cycle above. The low levels are maintained by the efficient chemical O_3 destruction in the presence of sufficient UV radiation, high water vapor and low NO_x concentrations, typical for the remote marine boundary layer (compare Sect.2.2.1). Even though the diurnal cycle of O_3 has been neglected for the tropospheric profile (compare Sect.3.2), it plays an important role for ground O_3 (e.g. Dickerson et al., 1999; Hu et al., 2011; Read et al., 2008). Future studies with a continuously measuring ground UV photometer are aspired to better capture and explain ground and boundary layer O_3 variations.

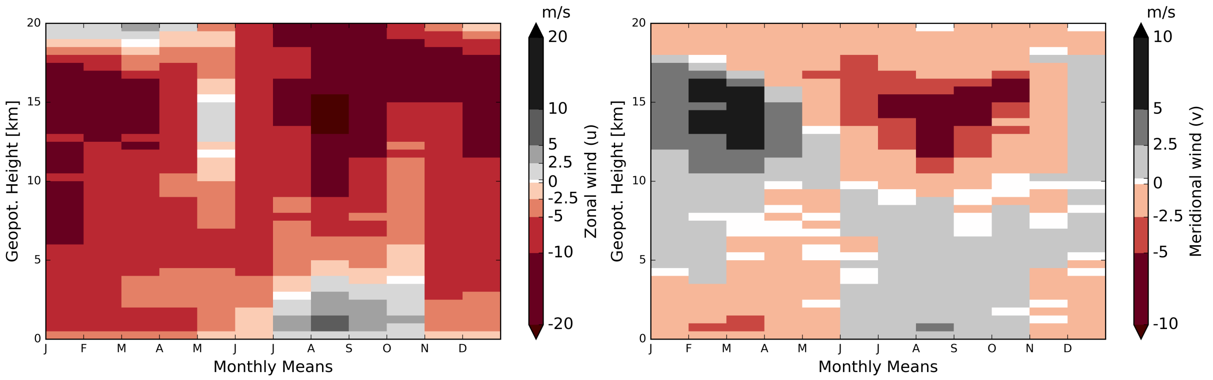

(a) (b)

Figure 4.3.: Zonal (a) and meridional (b) wind monthly means derived from daily radio soundings at the Palau weather station, Jan 2016 - Oct 2019 (see Sect.3.3.2).

The annual variability of the large scale circulation can explain the periodicity of the cycles. Figure 4.3 shows monthly means for the zonal and meridional wind components in a time-height cross-section derived from daily radiosoundings launched at the Palau weather station during the study period (see Sect.3.3.2 for details on the data). The monthly averages highlight the annual movement of the ITCZ (compare Sect.2.1.1). From July until November, the ITCZ is located north of Palau and the islands are under the influence of the Southern Hadley cell (compare Fig.2.1). Low-level and UT meridional wind directions are anti-correlated accordingly, with a turning point around 10 km (5-10 km from November until June). Strongest winds are occurring around 15 km when the ITCZ is furthest south or north of Palau and are associated with the outflow of the Hadley circulation. The easterly winds are dominating the whole tropospheric column, increasing in strength with altitude (maximum in summer, Fig.4.3a). The main current related to the deep trades is only interrupted from July to November when South-West monsoon winds are approaching Palau. These westerlies are confined to a shallow layer below 5 km in the wider region (compare e.g. Riehl, 1954). The slight increase in precipitation during this time coincides with the low O_3 VMR season. The full time series of the horizontal wind components for the study period (see Fig.3.14) further reveals the propagation of the QBO phases, anomalies during El Niño and a semiannual periodicity in the zonal wind, which relates to the ITCZ crossing Palau twice a year (compare Fig.2.2).

Shifted Seasons

In order to identify reoccurring seasonal characteristics of tropospheric O_3 and differences in controlling processes, we empirically chose a distinction into four seasons, shifted by one month compared to the temperate climate seasons: November-December-January (NDJ), February-March-April (FMA), May-June-July (MJJ) and August-September-October (ASO). These hereafter called "shifted seasons" (in the following also referred to simply as "seasons" in contrast to the "mid-latitude seasons") reflect four more or less different types of profile shapes as shown in Figure 4.4.

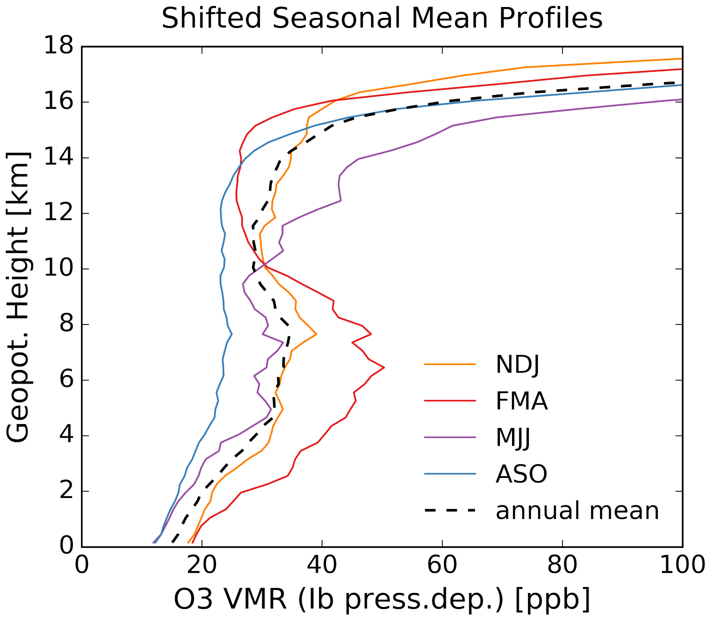

Figure 4.4.: Seasonal Mean O_3 VMR profiles for Palau (colored solid lines), dashed black line represents the long-term annual mean, all excluding El Niño, averaging according to the climatological seasonal mean in Equation 3.12, see Sect.3.2.3 (see also Fig.A.4 and Fig.A.5 in Appendix for comparison of averaging methods and with the median).

The best distinction between four types was achieved by manually sorting monthly profiles by similar shape first, considering the full altitude range (for individual monthly measurements, see Fig.A.6 in the Appendix). The centering around the equinoxes of the resulting seasons seems logical for a tropical station, although the general construction of 3-month-seasons remains arbitrary. In any case, the seasonal means convey additional information on the tropospheric O_3 variability, which relate to different meteorological/synoptic conditions.

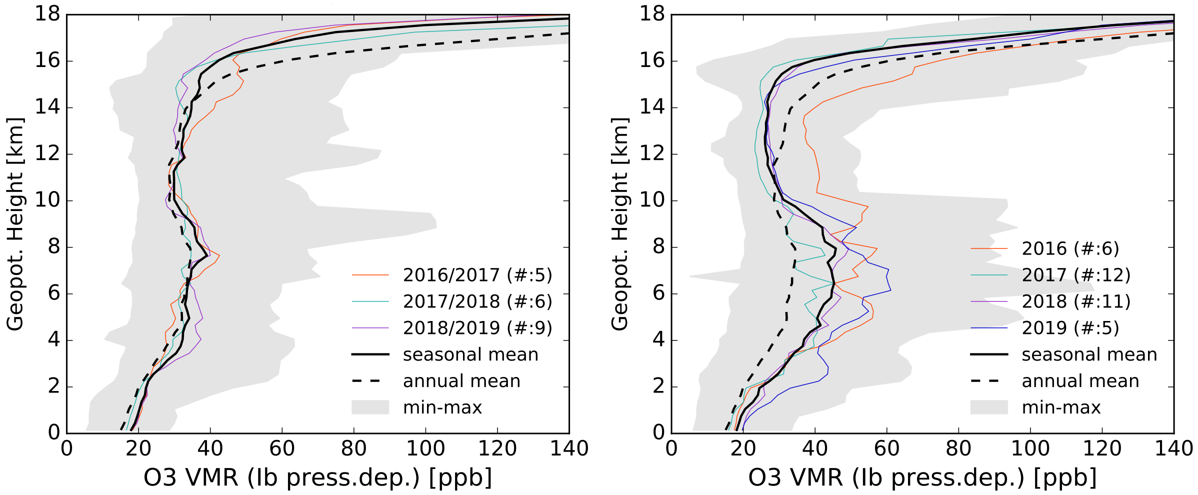
(a) NDJ
(b) FMA

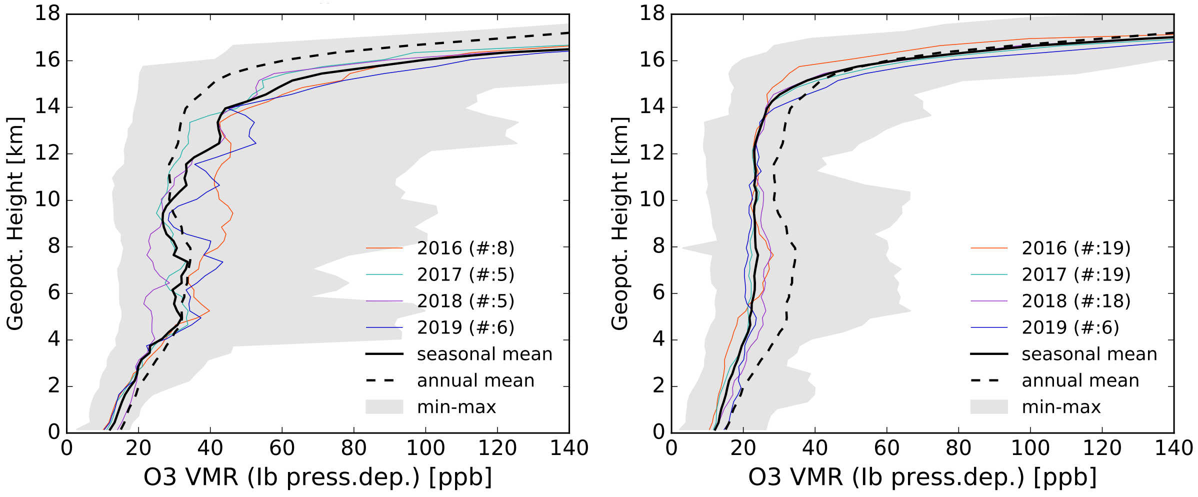
(c) MJJ
(d) ASO

Figure 4.5.: Variability of seasonal mean O_3 VMR profiles for Palau (black solid lines) against the long-term annual mean (dashed black line), all excluding El Niño, in individual panels per season (a-d); the gray shaded area encloses all observations, minimum to maximum, thin colored lines indicate seasonal means per year, number (#) of profiles included in the calculation given in brackets (compare Fig.4.4).

The panels in Figure 4.5 present the variability of the seasonal mean profiles (black solid lines) against the annual mean (black dashed lines). Variations are indicated as a gray shaded area from minimum to maximum measurement and by seasonal means from different years (colored thin lines). The "S"-shape of the annual mean profile prevails in the winter/spring seasons, NDJ and FMA (Fig.4.5a and 4.5b), most pronounced in the latter. The interannual variability is particularly high during FMA from 4 to 10 km with generally enhanced O_3 VMR (40-50 ppb). Here, FMA and ASO are most oppositional and represent the extrema of the mid-tropospheric cycle. ASO months (Fig.4.5d) show a uniform profile of O_3 VMR around 20-25 ppb with little interannual variability. The ASO profile can be explained by a well-mixed troposphere with boundary layer air of low O_3 being lifted up through the entire column (e.g. Pan et al., 2015, see Sect.2.1.3). We will refer to this as the locally controlled background profile (see Sect.4.2.1), which can be observed any time of the year. The steep onset of higher levels of (stratospheric) O_3 VMR in ASO occurs at lower altitudes than in winter and spring months. Due to the high sampling rate in ASO (numbers per year in brackets), day-to-day variations are captured best in this season, resulting in a robust average. Both extreme seasons share the pronounced O_3 minimum in the TTL, with the prominent exception of the 2016 El Niño FMA season (orange line, Fig.4.5b). A semi-annual cycle for convective intensity is not evident in other data, which rather suggests year-round deep convective activity in Palau (compare e.g. Fig.2.4), but could be expected due to the crossing of the ITCZ twice a year (Konopka et al., 2010).

During MJJ the profile resembles a "tilted" line with a weak O_3 gradient in the TTL and lacking a pronounced O_3 minimum in the UT. High, stratospheric O_3 concentrations are reached at the lowest altitude of the year. This corresponds well with the minimum annual tropopause height and coincides with a shift in wind regimes due to the crossing of the ITCZ around June (see Fig.2.2). The interannual and intraseasonal variability is high above 4 km, especially May is standing out in this context (for monthly profiles, see Fig.A.6). During May the horizontal wind is weakest throughout the entire tropospheric column as the subtropical ridge shifts South with increasing altitude (e.g. Riehl, 1954). Thus, quasi-horizontal STE may play a dominant role in May. The West Pacific monsoon (WPM) reaches Palau already in July. While the tropopause is comparable within the season, mid-tropospheric O_3 VMR in July are as low as observed in August and September, declaring July a transition month. For a longer time series, the shift in seasons and the 3-month averages should be re-evaluated in this regard. In any case, MJJ and NDJ can be considered as intermediate seasons with respect to the mid-tropospheric O_3 cycle and the similar location of the ITCZ during its annual movement (see Fig.2.2). They show the greatest discrepancy in upper tropospheric O_3, but mid-tropospheric values are close to the annual mean for both.

Stauffer et al. (2018) used a sophisticated clustering technique to characterize ozonesonde profile variability for various stations around the globe in terms of geophysical processes instead of seasonality. The ressemblance of the four clusters calculated for SHADOZ stations in Java and American Samoa with our Palau seasonal means is evident in parts, but needs further investigation. Especially the low O_3 cluster associated with convective lifting of low O_3 by Stauffer et al. (2018) compares well with the Palau ASO profile. The cluster with highest average O_3 VMR exhibits a similar "tilted line" profile like

MJJ with a lower tropopause and weak gradient, explained in the study by STE. A possible implication of this comparison is that the seasonal distinction in Palau already separates profiles with different underlying physical processes. In this thesis, we evaluate the disparity of the shifted seasons with respect to O_3 and RH variability in a trajectory analysis in Section 4.3.

4.1.2. Mid-tropospheric Cycle

The increased sampling frequency during the extremes of the mid-tropospheric cycle allow a robust capture of this atmospheric signal for Palau. Individual profile observations disclose differences in variability. Figure 4.6 shows layer mean O_3 VMR of individual soundings in all years for selected altitude layers of 300 m thickness; the left column refers to the mid-troposphere, the right column to the TTL discussed below. As already clear from the annual monthly means (Fig.4.2), the cycle is persistent within our time series with a minimum around August and a maximum in March/April. It is confined roughly between 5 and 10 km, i.e. the layer of suppressed convective outflow (compare Sect.2.1.3). Within this range, the maximal amplitude of the cycle is quite steady around 70 ppb (Fig.4.6.a and c). The extremes in O_3 VMR correspond with extremes in variability. Both day-to-day and interannual variations are lowest in the low O_3 season ASO (Fig.4.6.a and c, compare Fig.4.5d) and highest in the enhanced O_3 season FMA (compare Fig.4.5b). The increased mean variability at this altitude range, as illustrated by the RSD from the annual mean in Fig.4.2c, is thus seasonally limited. While low O_3 observations are encountered throughout the year, enhanced O_3 VMR greater 40 ppb hardly occur from July until October. This can be explained by the climatology of the ITCZ movement. In this context the Palau observations confirm results from previous campaign-oriented studies like e.g. PEM-Tropics B. Browell et al. (2001) found, that layers of high O_3 VMR in the TWP, advected from remote polluted areas, are mostly confined north of the ITCZ. Very low O_3 was only present in the "equatorial wedge" between ITCZ and SPCZ and associated with enhanced vertical mixing in convection (compare Sect.2.1.1). Dominance of a local regime over atmospheric transport to the TWP is thus regulated by these two major barriers: the ITCZ and SPCZ. An alternative mechanism creating high O_3 VMR locally in the troposphere could be accumulation in stagnant air with high temperatures, which increases the rates of O_3 formation (NRC, 1991). This happens in connection with slow moving high pressure systems and is rather unlikely for the TWP. Transport to the TWP from areas of increased O_3 production, such as the stratosphere or landmasses with sources of pollution in contrast to the local convectively controlled low O_3 profile is more likely (e.g. Pan et al., 2015, see Sect.4.2).

Different statistical measures for the 5-10 km altitude range capture the seasonal variability of the mid-tropospheric O_3 minimum as shown in Figure 4.7. The climatological monthly mean of the minimum, for example, confirms that an omnipresent low O_3 background is at its lowest during the ASO season (compare Fig.3.9). As the ASO profile is attributed to convective mixing, this quantity can be regarded as a measure for the degree of mixing and its seasonality. All example measures in Fig.4.7 generally support the choice of seasons by profile shapes, with July as the already noted exception.

mid-troposphere TTL

(a) 7.95 km (b) 19.95 km

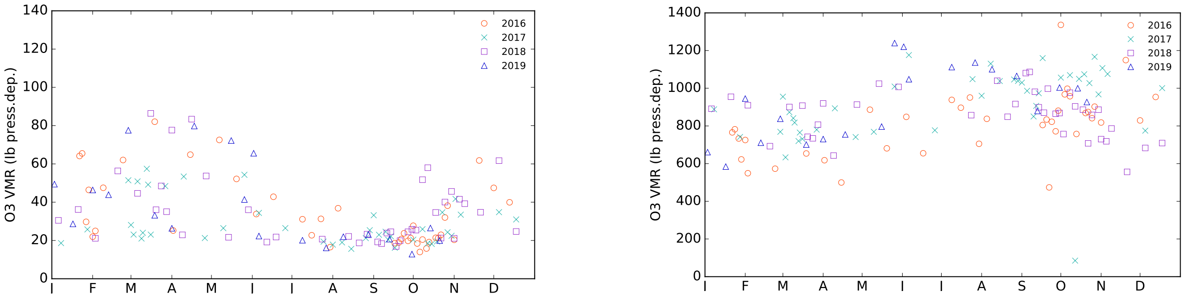

(c) 5.5 km (d) 18.15 km

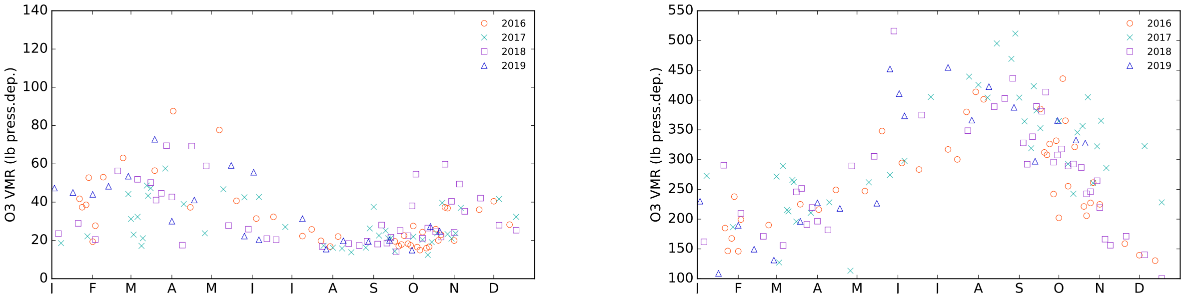

(e) 3.75 km (f) 16.95 km

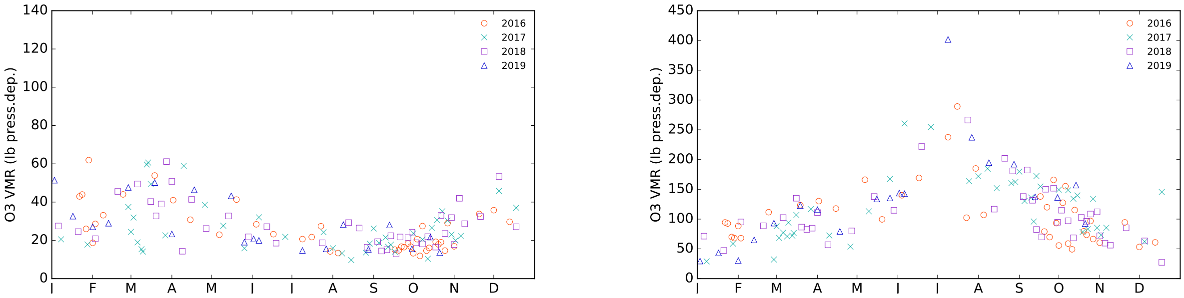

(g) 0.15 km (h) 9.75 km

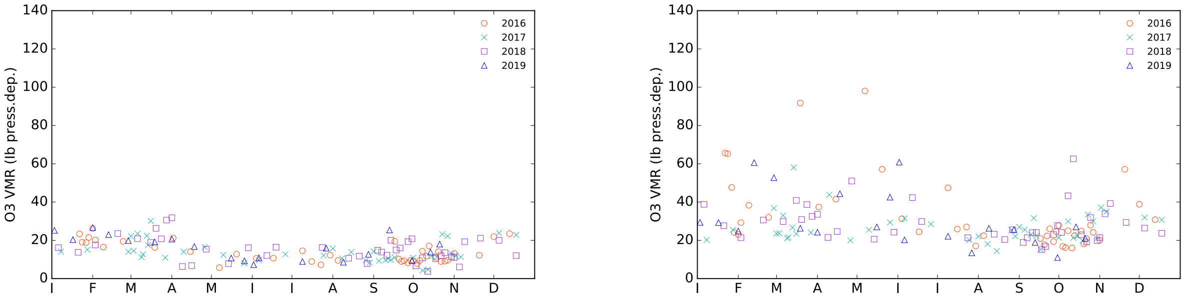

Figure 4.6.: Mean O_3 VMR of individual soundings of all years (different markers and colors) in 300 m layers (center altitudes in subcaptions), showing the persistence of the mid-tropospheric cycle from 5 to 10 km (left column, (a) and (c)) and in the TTL around 18 km (right column, (d)); note the differences in scaling in the right column.

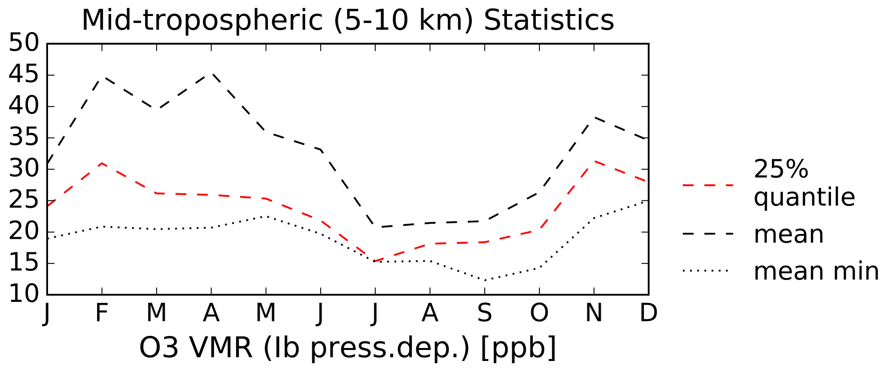

Figure 4.7.: Statistical measures for the 5-10 km altitude range: climatological monthly means from individual sounding's 25% quantile (red dashed line), mean (black dashed line) and minimum (black dotted line) (see Equ.3.11 and Sect.3.2.3; for comparison with individual measurements per month, see Fig.A.6).

An important observation from the Palau data set is the often occurring anti-correlation between O_3 and RH. Figure 4.8 shows the known time-height cross-section for tropospheric O_3 VMR with measurements of RH below 30 % highlighted by hatches and enclosed in black contours. A majority of O_3 VMR observations greater 40 ppb coincide with the dry signatures. Air masses of lowest O_3 VMR composing the local background are mainly wet (compare also Fig.3.8.b). We will further explore the relation between O_3 and RH in the next sections of this thesis (see Sect.4.2.4 in particular).

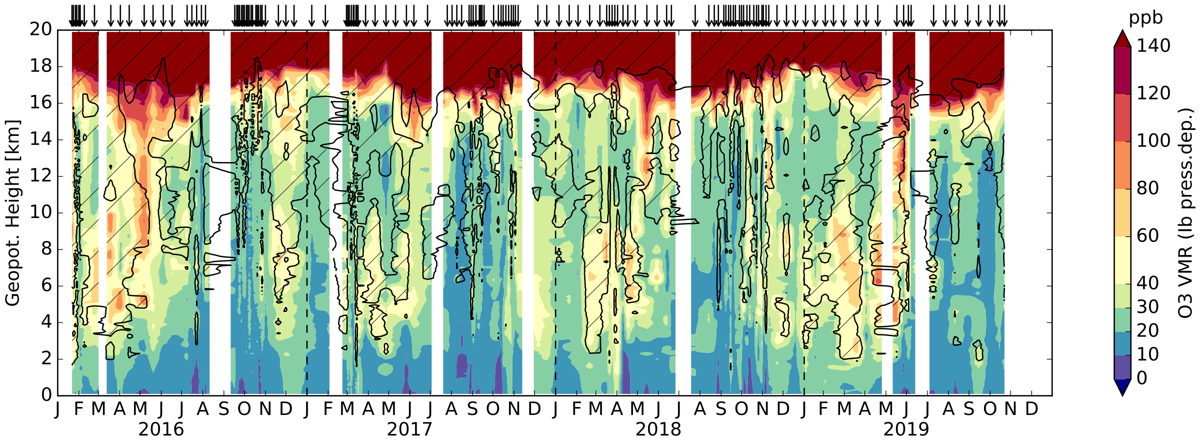

Figure 4.8.: Tropospheric (0-20 km) time-height cross-section of the Palau sounding data for O_3 VMR with coinciding RH observations below 30 % as hatched areas enclosed in black contours; for more details, see Fig.3.8.

4.1.3. TTL Cycle

The large annual cycle in O_3 VMR in the TTL above the cold point tropopause (CPT) is observed as a zonal, tropical phenomenon by satellites and balloon-soundings of near-equatorial SHADOZ sites (e.g. Randel et al., 2007; Thompson et al., 2003a,b). It is linked to the seasonality of both vertical convective transport and tropical upwelling (Folkins et al., 2006; Randel et al., 2007), as well as meridional in-mixing from the extra-tropics (Konopka et al., 2010). The exact hierarchy of the above mentioned processes causing the persistent signal is an active field of research, but the dominant dynamical influence of the seasonality of the Brewer-Dobson (BD) circulation and thus tropical upwelling seems undisputed (Randel and Jensen, 2013). Therefore TTL O_3 observations can be used to constrain models for estimates of seasonal variations of the general BD circulation driven STE (see Sect.2.1.4).

For Palau, this annual cycle is persistent throughout the whole time series and has a maximal amplitude of approx. 250 ppb (or factor 2) around 18 km, with a maximum around 450 ppb in August and a minimum of about 200 ppb in December/January (see Fig. 4.6, right column). Enhanced in-mixing in summer is possibly also influenced by the Asian Monsoon Anticyclone (Randel and Jensen, 2013). As for other SHADOZ stations, the cycle is vertically confined to a shallow layer (e.g. Randel et al., 2007), which is also displayed by the narrow maximum in RSD of the annual mean profile (see Fig.4.2c).

The O_3 cycle is approximately in phase with the temperature cycle in the TTL, thus supporting an ozone-based definition of the tropopause (see Fig.4.1 and Sect.2.1.4). The CPT is lowest and warmest in boreal summer (ca. 16.5 km, > -80 °C) and the opposite in winter (ca. 17.5 km, <-85°C, see Fig.4.1b). The extreme low winter temperatures correspond to the strongest wave drag driving the tropical upwelling of the BD circulation. The annual cycle in intensity of the upwelling is a consequence of hemispheric asymmetries (e.g. Konopka et al., 2010). TTL temperatures impose a seasonal cycle on stratospheric water vapor concentrations near the CPT, resulting in the so-called stratospheric tape recorder (e.g. Fueglistaler et al., 2004; Holton and Gettelman, 2001; Randel and Jensen, 2013). As the main source of stratospheric hydrogen oxide radicals, stratospheric water vapor, in turn, controls important gas-phase O_3 loss cycles and polar O_3 loss via heterogeneous chemistry on aerosols, promoting the formation of polar stratospheric clouds and chlorine activation (see references in Sect.2.1.4).

Here, the significant radiative impact of O_3 as a greenhouse gas comes into play: the O_3 seasonality actually has a positive feedback on the TTL temperature cycle (e.g. Folkins et al., 2006; Fueglistaler et al., 2011; Randel and Jensen, 2013). During boreal winter, an O_3 mediated reduction of the radiative heating rates would facilitate reduced upward mass fluxes into the stratosphere, “if not offset by an additional cooling of the tropopause region” (Folkins et al., 2006). A further decrease in TTL O_3 VMR could lead to colder tropical tropopause temperatures (Polvani and Solomon, 2012) and in turn alter stratospheric H_2O. This scenario could be a possible feedback of climate change. Increased SST possibly promote convection in the TWP and thus vertical transport of ozone-poor boundary layer air. A possible future intensification of the BD circulation would add to the reduction of TTL O_3 (Nowack et al., 2015).

During the following analysis, we focus on the mid-tropospheric cycle and the contrast of local control of air composition and transport to the TWP. The O_3 variability in the TTL will be center of another dedicated study with a longer time series. It is subject to wave variability and modulated intraseasonally by the MJO and equatorial Kelvin waves (see

Sect.2.1.4). In this context, the influence of the QBO and its interplay with the ENSO and MJO phenomena should be taken into account (see e.g. Diallo et al., 2018; Yoo and Son, 2016).

4.2. Background Atmosphere and Deviating Layers

The stand-alone characterization of tropospheric O_3 variability above Palau is valuable for studies targeting regional and global distributions. However, the measured O_3 and H_2O content of an air parcel bears information beyond the local air composition: the unique location of Palau allows us to use O_3 and RH as chemical tracers for air transport processes to the region. Free tropospheric O_3 life times in the order of weeks are comparable to the dynamical timescales of long-range transport within the Tropics and from the subtropics (e.g. Folkins, 2002; Ploeger et al., 2011). Thus, we can separate local or non-local influences via differences in the observed O_3 abundance. RH gives additional information about the vertical displacement during transport (e.g. Hayashi et al., 2008).

In this context, the seasonal, mid-tropospheric O_3 cycle in the Palau data set (shown in the previous Section 4.1.2) suggests a seasonality in air mass origin. In the following, we are using the observed O_3 to RH ratio to define a local background atmosphere and tackle the identification of intermittent layers deviating from this background, thus indicating a non-local origin. The results set ground for the subsequent back-trajectory analysis, which identifies actual source regions (Sect.3.4.1).

4.2.1. General Definition

Locally, the marine, low NO_x environment is a strong sink for O_3 (see Sect. 2.2.1). Lifting the clean boundary layer air up to the TTL, deep convective outflow in conjunction with convective overturning and a lack of in situ net O_3 production creates a well-mixed, humid tropospheric profile with a uniform vertical O_3 distribution (e.g. Pan et al., 2015). Under these conditions we expect O_3 and RH profiles for Palau as shown in Figure 4.9a. We will refer to this as the (tropospheric) O_3 background (atmosphere) or "clean state" of the atmosphere (compare Sect.4.1.1). Since the dominating wind direction throughout most of the year and the entire tropospheric column is easterly (compare Fig.4.3), most of the air reaching Palau has been cleaned of anthropogenic or other continental pollution (i.e. O_3 precursors) crossing the Pacific, therefore carrying low O_3 concentrations. Thus, typical dynamical conditions are conducive to the low local O_3 background (compare Sect.2.1).

Uniform tropospheric O_3 profiles are observed throughout the year. There is evident seasonal variability in the mean of these background profiles with lowest mid-tropospheric mean O_3 VMR ($\lesssim$ 25 ppb) from July until October compared to the rest of the year ($\gtrsim$ 35 ppb, compare Fig.4.7 and 3.9 and Sect.4.1.2). In the showcase profiles in Figure 4.9,

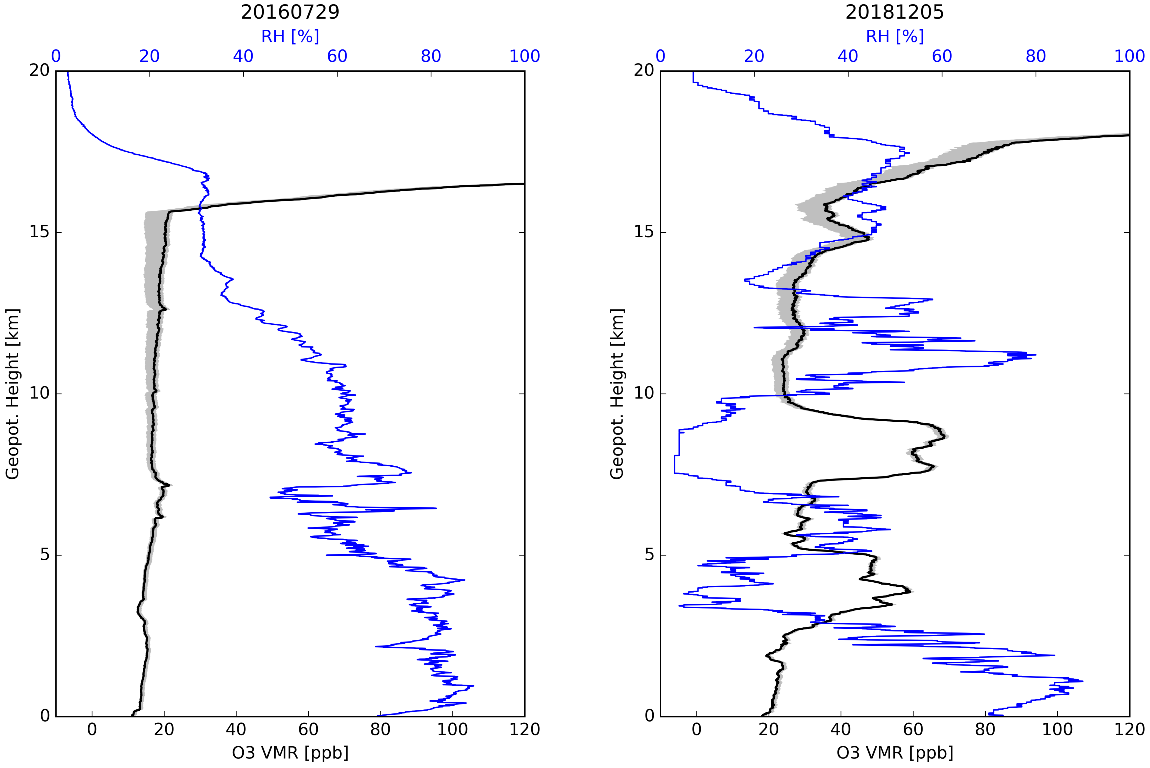

(a) Background

(b) Deviating Layers (O_3+RH-)

Figure 4.9.: Example tropospheric O_3 (black lines) and RH (blue lines) profiles for the background atmosphere (a) and deviating layers, here anti-correlated dry, enhanced O_3 layers (b); grey shading shows the uncertainty due to the background current calculation ((a) $I_b = 0.027\mu A$, (b) $I_b = 0.033\mu A$,see Fig.3.2 and Sect.3.1.3, compare Fig. 3.9 Sect. 3.2).

the O_3 background for late July 2016 is around 17 ppb and for December 2018 around 25 ppb. An atmospheric profile as an individual snapshot can more or less follow the seasonal background. It also often includes positive or negative deviations from this background (for both tracers) in layered structures with variable vertical extent (see Fig.4.9b). Observations from the whole tropical Pacific region attest to the typical nature of a humid, low O_3 background with intermittent, here called “deviating” layers, occurring predominantly in the mid-tropospheric altitudes (e.g. Browell et al., 2001; Hayashi et al., 2008; Newell et al., 1996; Oltmans et al., 2001; Pan et al., 2015; Thouret et al., 2000). Following previous studies, we also propose that these deviations from the clean state in turn indicate a departure from the above described dominating (local) conditions (e.g. Hayashi et al., 2008; Oltmans et al., 2001; Pan et al., 2015; Stoller et al., 1999). Though positive or negative anomalies are possible for both atmospheric tracers, referred to in the following by O_3±RH±, the focus of most studies is on dry layers of enhanced O_3 (O_3+RH-) (see details in Sect.4.2.4). We suggest, since in situ production of O_3 (of the observed magnitudes) is unlikely under local conditions (compare Sect. 2.2.1), layers of enhanced O_3 are controlled by transport, possibly different pathways and non-local mechanisms. We thereby acknowledge, that TWP tropospheric O_3 cannot only function as a passive tracer for local deep convective activity (“low” O_3, e.g. Folkins, 2002; Folkins et al., 1999; Kley et al., 1996; Paulik and Birner, 2012; Solomon et al., 2005), but also for air pollution or stratospheric air intrusions (“high” O_3, e.g. Anderson et al., 2016; Browell et al., 2001; Randel et al., 2016; Thouret et al., 2000) .

However, O_3 alone is rather an insufficient indicator of air mass origin. Often a combination of different chemical and dynamical tracers is needed to identify responsible processes or eliminate other pathways to the TWP (compare Sect.4.2.4). Additional information about water vapor is readily available from the simultaneous radiosonde measurements. The characteristics of the observed RH profile further support the hypothesis about local and non-local origin of air masses in relation to the O_3 profile (see Fig.4.9). If the RH of an air mass is higher than the surrounding air masses, it has recently been raised by convection (local control). In active convection, an atmospheric profile is expected to look like the one in Figure 4.9a, with RH values decreasing with altitude, but greater than 45 % throughout the mid-troposphere (see Mapes, 2001). Dehydration of air masses, on the contrary, occurs during downward transport, both from within and outside of the tropics (radiative cooling, see Sect.4.3.1), or horizontal advection from the mid-latitudes (stratospheric origin, compare Sect. 2.1.4) and may be indicative of different large-scale dynamical drivers during long-range transport (non-local control) (compare Anderson et al., 2016 and detailed discussion in Sect.4.2.4). Vertically thick intrusions of dry air in an otherwise wet background profile especially support the theory of non-local origin (see Fig.4.9b). Other processes, like remoistening (“high” RH despite non-local origin) or in-mixing of mid-latitude air during transit of air masses to the TWP could play a role and contradict the above described correlations (Cau et al., 2007; Schoeberl et al., 2015; Sherwood et al., 2010; Tao et al., 2018).

Due to the high variability among individual profiles, it is difficult to differentiate the local and non-local modes within one profile. However, the previous statistical analysis (Sect.4.1) already shows a seasonal pattern with the highest occurrence of mostly mid-tropospheric dry enhanced O_3 layers in FMA and the least in ASO (see Sect.4.1.2). In the mean FMA profile individual layers at varying altitudes in daily profiles, which interrupt a clean background, are disguised in the “belly” of the “S”-shape (compare Pan et al., 2015, see e.g. Fig.4.5b). For an improved understanding of the layer seasonality, we first need to isolate the O_3 background while considering its own seasonal variability. In the following subsections, we start by closely assessing the relation between O_3 and H_2O in comparison with observations from other locations (SHADOZ and CONTRAST, Sect.4.2.2), and then describe our method to establish an air mass classification relative to background conditions and our resulting statistical analysis of the Palau data set (see Sect.4.2.3).

4.2.2. Relation between O_3 and Relative Humidity

Comparison with SHADOZ

Looking at the tracer-tracer relation of individual, free-tropospheric air parcels for Palau in comparison to other selected SHADOZ stations gives an idea of the variability of the O_3

to RH ratio within the tropics. The station selection was based on geographical vicinity or, in the case of Costa Rica, a similar latitude at the eastern end of the Pacific (compare Fig.3.13 and Tab.3.2 in Sect.3.3.1). In Figure 4.10, 2D histograms for O_3 VMR (≤ 100 ppb) versus RH of the selected stations are shown for the free troposphere (3-14 km) and all seasons. Data is essentially unsmoothed, i.e. no spatial or temporal binning beyond original data processing has been applied, in order to preserve the simultaneously measured combination of the two tracers. This is an important advantage over averaging of data into mean seasonal or annual profiles, where the effects of deviating layers might be canceled out by an equally dominant background (compare Pan et al., 2015). The sampling frequencies are not regular and for different stations, data has been accumulated over different time periods and lengths (compare Tab.3.2). The resulting distributions therefore cannot be compared in a quantitative climatological manner, but we can assume a good representation of interannual variability for SHADOZ data (time series of 13 to 21 years, Tab.3.2). Histogram values in Figure 4.10 are normalized to the total number of observations in the free troposphere for each station. Thus, they can be interpreted as a statistical probability distribution for a certain O_3/H_2O combination to occur. In this sense, the given stations can be classified into three groups:

1. a fairly narrow, almost Gaussian distribution of O_3 VMR with evenly distributed RH (Costa Rica, Kuala Lumpur),

2. predominantly dry air spread over a wider range of O_3 VMR (Hanoi, Hilo), and

3. a mixture of the two previous categories: an “L”-shaped distribution with a dominant mode of low O_3 over the whole RH range and a tail towards higher O_3 VMR corresponding to low RH values (Palau, Fiji, Java, American Samoa).

Referring to these group categories and additionally focusing on O_3 distributions, the eight stations are arranged as a longitudinal cross-section over the Pacific Ocean in Figure 4.11 (compare Thompson et al., 2012, 2017), from West to East: Kuala Lumpur - Hanoi - Java - Palau - Fiji - American Samoa - Hilo - Costa Rica. The most frequently observed O_3 VMR (maxima in the marginal 1D histograms of Figure 4.10) are superimposed as orange circles on the boxplots, which themselves illustrate the commonly defined statistics: the interquartile range ($IQR = Q3 - Q1$), median (central line) and whiskers representing the original relation $\pm 1.5 \cdot IQR$ above or below the 25th (Q1) or 75th (Q3) quartile (Tukey, 1977).

The similarity between the Western Pacific stations in group 3 is not surprising. Though as much as 8000 km apart from each other, with all but Palau located in the Southern hemisphere, they are equally influenced by a tropical marine climate. Most importantly, these stations are located far from industrial centers, resulting in predominantly low tropospheric O_3 air concentrations. In this sense, we can interpret O_3 as an indicator for its precursor NO_x (compare Sect.2.2.1) and would expect a decrease from East to West, while crossing the Pacific and following the trade winds within the ITCZ, until reaching the Asian continent again. This has been already pointed out by Thompson et al. (2012). Air becomes cleaner as more and more NO_x is lost by conversion to HNO_3 and subsequent washout in convection, outweighing NO_x production in the remote Pacific. With a lack of

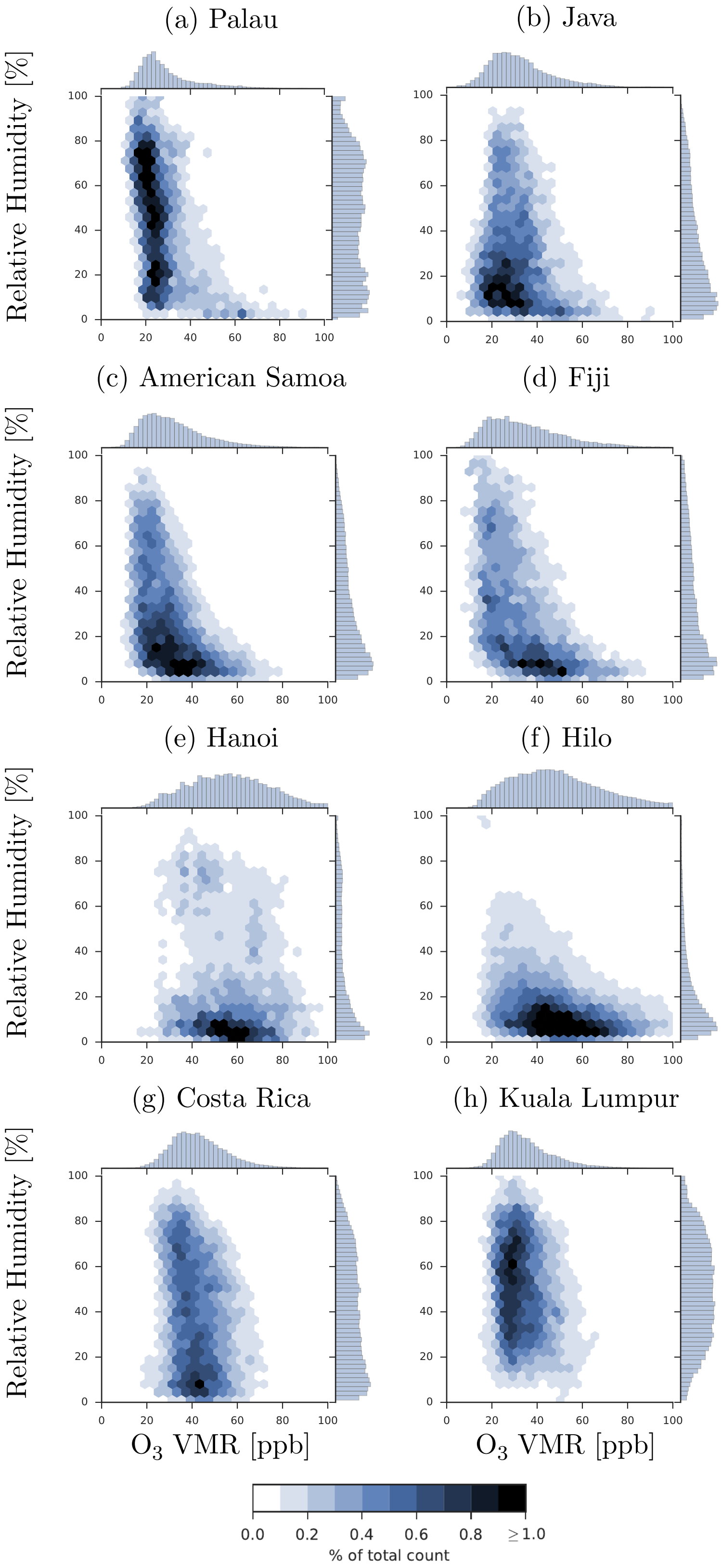

Figure 4.10.: Free-tropospheric (3-14 km) relation between O_3 and RH in a 2D (hexagonal binned) histogram, normalized to the total count of data points per station, using all measured data pairs with $\leq$ 100 ppb O_3 VMR for Palau (upper left) and selected SHADOZ stations; color shading indicates percentage of total count per gridpoint and marginal plots give individual 1D histograms, normalized to unity.

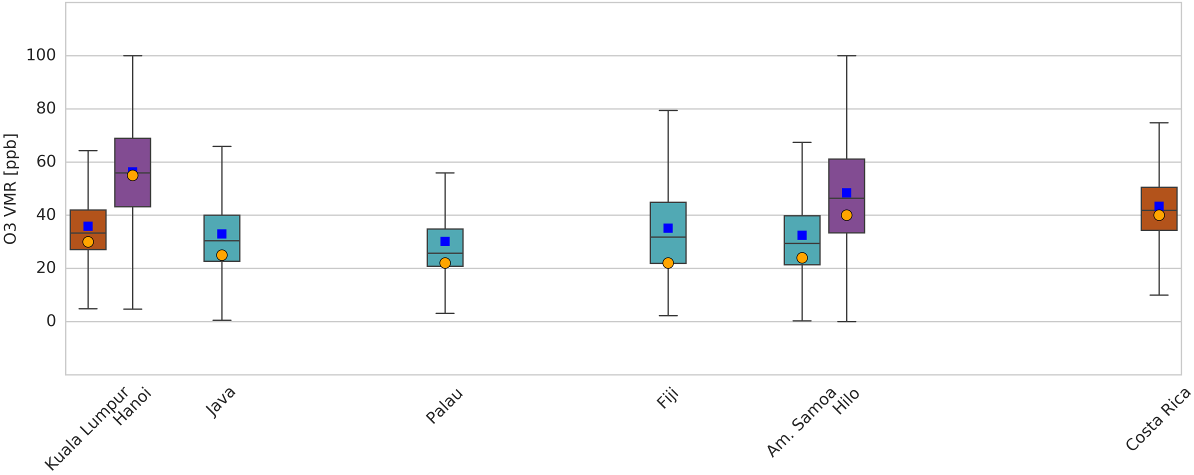

Figure 4.11.: Boxplots for free-tropospheric (3-14 km) O_3 VMR ≤100 ppb, colored by the group categories derived from O_3/RH distributions (Fig.4.10): brown for group 1, purple for group 2, turquoise for group 3; outliers are not shown and whiskers are a function of the interquartile range ($IQR = Q3 - Q1$), i.e. $Q3$ or $Q1$ + or - $1.5 \cdot IQR$ respectively); blue squares are mean values; orange circles refer to the most frequent O_3 VMR as illustrated in the marginal 1-D histograms in Fig.4.10; arrangement of boxplots on the horizontal axis is an approximation to longitudinal positions.

NO_x, O_3 loss in a marine, humid environment will dominate over O_3 production (compare Sect. 2.2.1). In Figure 4.11, we see the separation of the Pacific island stations (turquoise boxes) from the other groups in terms of O_3 VMR (lowest median, mean values and maximum frequency), but an East-West gradient within group 3 is not apparent in any of our statistical measures. Instead, according to the statistics for the free troposphere, Palau sets the lowest boundaries for all selected stations, except for the minimum range value (excluding outliers). The Palau data further stands out due to the exceptionally narrow O_3 distribution around $\sim$ 22 ppb (compare marginal 1-D histogram in Fig.4.10). The fairly even distribution of RH rather resembles histograms classified into group 1. This consistency within the near-equatorial Northern hemispheric stations, all located within ± 5° latitude of Palau, is caused by their close vicinity to the average position of the ITCZ around 6° North (e.g. Schneider et al., 2014, compare Sect.2.1). The RH distributions of the other group 3 stations are skewed towards lower values, which will be explained below within a seasonal comparison. Weak overall anti-correlation of O_3 and RH occurs for Fiji and American Samoa data (Fiji: r=-0.46, American Samoa: r=-0.42).

Kuala Lumpur and Costa Rica (group 1) constitute the boundaries of the longitudinal Pacific cross-section (brown boxes in Fig.4.11) and are continuously influenced by continental pollution and deep convection, with most frequent O_3 VMR observations at around 30 and 40 ppb, respectively, and evenly distributed RH. That means O_3 VMR are indeed enhanced compared to the most frequent O_3 measurements in group 3, but there are hardly any observations greater than 60 ppb, possibly due to local mixing processes and O_3 loss in the humid free troposphere. Kuala Lumpur is almost completely lacking observations below 10 % RH (see Fig.4.10h).

Both subtropical stations, Hanoi and Hilo, in group 2 (purple boxes in Fig.4.11) are similarly affected by pollution with a significantly wider spread in their O_3 distributions compared to all others, especially towards higher values (Fig.4.10e, f). Their free-tropospheric O_3 to RH ratio is therefore especially different from the one for Palau. The tendency towards lower RH values is tied to their location close to the subsiding branch of the Hadley circulation. The less humid troposphere chemically acts in favor of higher O_3 VMR (compare Sect.2.2.1). The semi-permanent North Pacific High above Hawaii, together with the cold SST in the East Pacific, is responsible for a stable trade wind inversion which suppresses deep convective activity above Hilo and enables long-range transport of potentially polluted air masses from both Asia and North America (e.g. Oltmans et al., 2004). Hanoi, in turn, is affected by Asian outflow within shorter distances to the sources (e.g. Ogino et al., 2013).

Figures 4.10 and 4.11 together already point out the uniqueness of the Palau data set regarding O_3 and RH. We now take a closer look into the seasonal distribution in shifted seasons, keeping in mind that the temporal shift by one month compared to the meteorological seasons, as suggested by the Palau soundings (see Sect.4.1.1), does not necessarily accommodate seasonal features of the other stations. The temporal aggregation of three consecutive months, however, reduces possible biases due to variations in sampling frequencies (compare Sect.3.2.3) and reveals differences within the three groups while underlining the unique nature of the troposphere above Palau (see Figures 4.12 and 4.13). As expected, the occurrence of dry enhanced O_3 air masses over Palau is essentially limited to the seasons NDJ and FMA, with the greatest disparity between FMA and ASO (Fig.4.12, top row). The joint distribution in the O_3/RH space furthermore helps us to identify distinct groups of high or low O_3 by their corresponding RH. In the FMA season, the dominant mode of low O_3 air masses centered at around 25 ppb is present for RH values between around 10 and 80 % (compare marginal 1D histogram in Fig.4.12, top row). However, there is a slightly overlapping group of air masses below 20 % RH present in the 2D histogram, with O_3 VMR greater than 40 ppb. This O_3+RH- group constitutes the lower, horizontal part of the prominent “L”-shape in the 2D histogram. This separation into two groups, a low O_3 mode, as the vertical part of the “L”-shape, and a low RH mode, is not as distinct but still present in NDJ. The NDJ O_3 distribution is roughly unimodal and centered at around 30 ppb with a tail towards higher VMR. RH values are stretched out quite evenly over the whole range, except for a peak at around 10 %.

Within group 3, a similar separation between dominant low O_3 air and enhanced O_3 levels is most apparent for Java and American Samoa, with two main differences: first, the seasonality is reversed, with O_3+RH- air masses in MJJ and ASO only, and second, moist air masses above 40 % RH are barely existent during the elevated O_3 seasons. The latter is also partially true for the Costa Rica (FMA) and Hanoi data (NDJ, FMA, see Fig.4.13, first and third row) and obviously tied to the occurrence of a dry season, which is essentially absent in Palau. The year-round high rainfall rates in Palau can be explained by the continuous proximity to the ITCZ and its location in the global warm pool area. A slight increase in rainfall during late summer, early fall is due to the influence of the Western Pacific Monsoon (compare Sect.2.1.1). With all other stations of group 3 located on the Southern hemisphere ($> 7°$ S), the reversal of the seasons is caused by hemispherical differences and the movement of the ITCZ and SPCZ (compare Sect.2.1.1

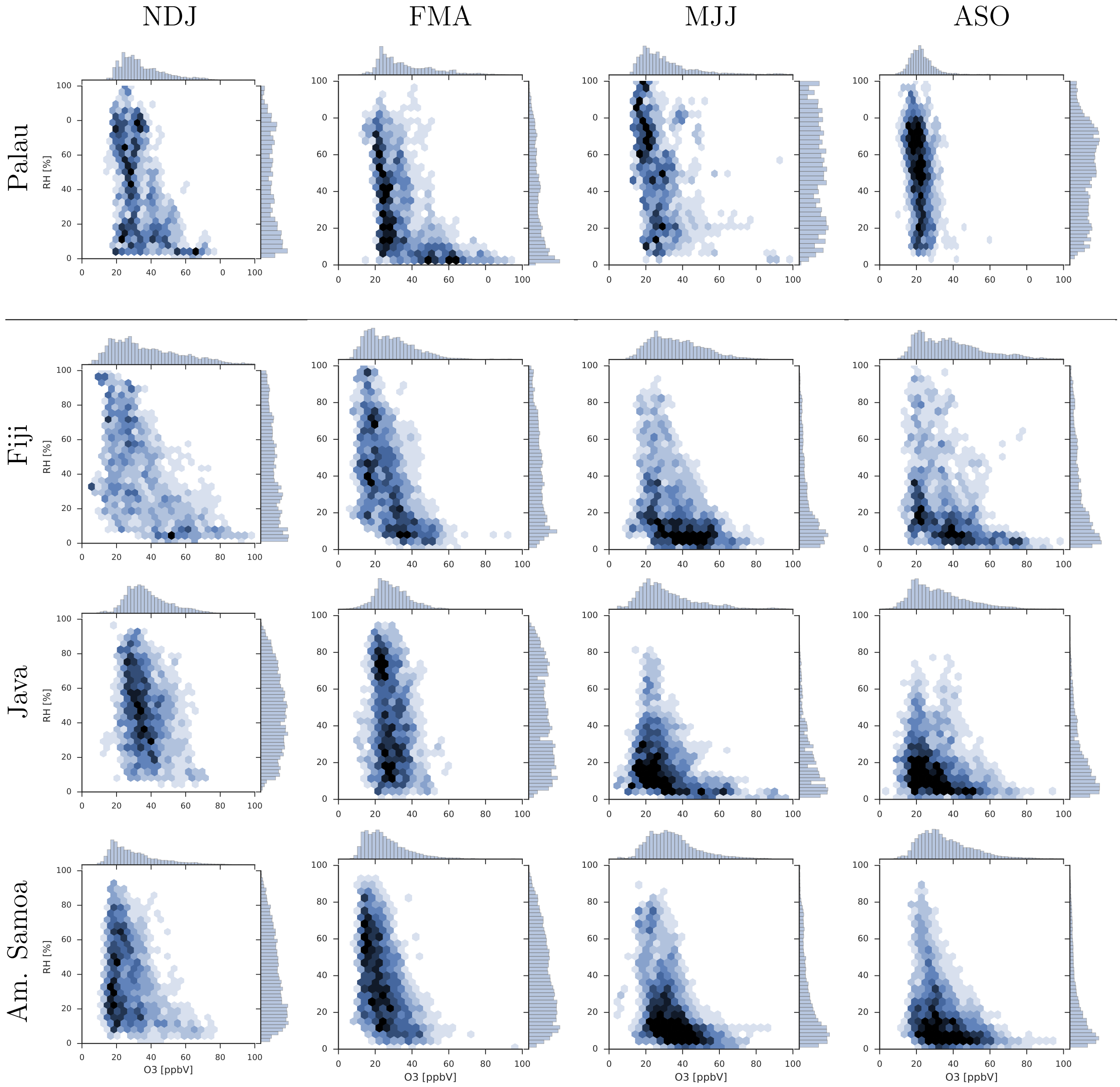

Figure 4.12.: Seasonal free-tropospheric (3-14 km) relation between O_3 and RH for group 3 stations, including Palau (top line); for more details see Fig.4.10.

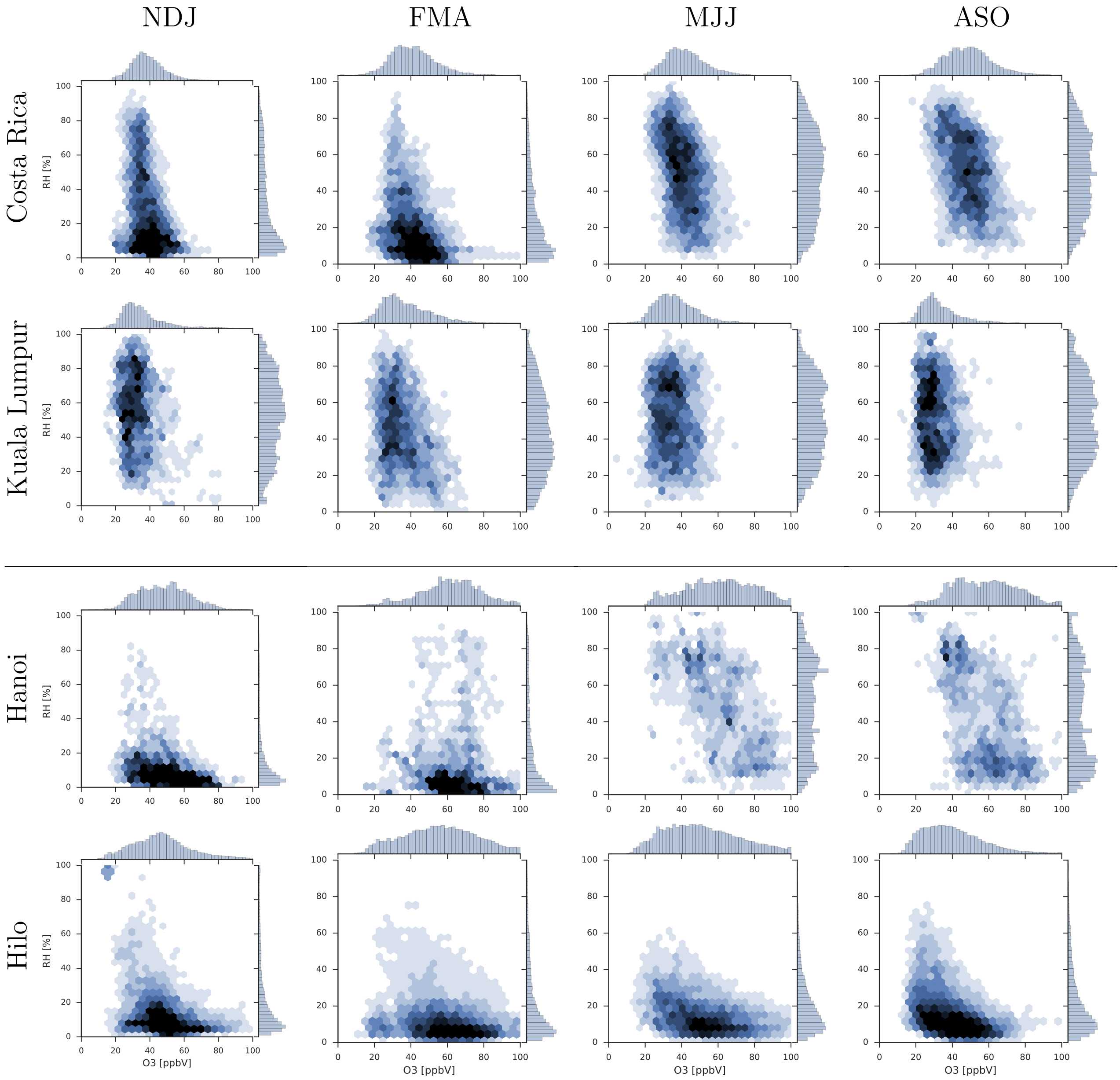

Figure 4.13.: Seasonal free-tropospheric (3-14 km) relation between O_3 and RH for group 1 (two upper lines) and group 2 stations (two lower lines); for more details see Fig.4.10.

and 4.1.2). In contrast to Palau's wet climate, Fiji, Java and American Samoa experience a clear dry season, when the ITCZ and SPCZ are furthest north, and the sinking branch of the Hadley circulation has shifted closer to the equator. The Fiji data set shows the least seasonality and a wide range of O_3 VMR is observed year-round, but the dry bias of season MJJ and ASO is present.

Kuala Lumpur's tropical climate resembles the one of Palau, with abundant rainfall in all seasons and thus an even distribution of free-tropospheric RH (see Fig.4.13, second row, compare Yonemura et al., 2002). O_3 observations are steady at around 30 ppb all year, pointing towards a continuous source of air pollution and convective turnover, as discussed above. In conclusion, there are no different modes present in the free-tropospheric tracer-tracer distribution of Kuala Lumpur as in Palau, which could help separating deviating layers from a background following our definition (Sect.4.2.1). The other group 1 station, Costa Rica, differs from Kuala Lumpur only during the winter seasons (NDJ, FMA) with the above mentioned dry bias (see Fig.4.13, first row). Here, despite the dominance of low RH air masses, the all-together free-tropospheric O_3 distribution barely changes (see marginal 1D histograms), though the range of O_3 values is wider for RH below 30 %, compared to above this threshold, i.e. no "L"-shape is present.

The seasonal separation of the O_3 to RH ratio for the subtropical stations (group 2) points out differences in their RH distributions (see Fig.4.13, third and fourth row). Hilo shows least seasonality in both tracers, which can probably be related to the stable high and continuous influence of STE (see Oltmans et al., 2004, and above). Hanoi, as mentioned above, has dry and wet seasons in association with the Asian summer monsoon (Ogino et al., 2013). The more humid free troposphere during MJJ and ASO in Hanoi, however, does not shift the O_3 distributions towards lower values, but is accompanied by an even spread of O_3 VMR in the O_3/RH space, a unique feature within our selected SHADOZ stations. Like Hilo, Hanoi is located in an area of active STE at the edge of the TTL. Ogino et al. (2013) propose transport of stratospheric air from the mid-latitudes in summer in connection with the Asian Monsoon circulation as responsible for high O_3 VMR in the UT above Hanoi. Low O_3 air in the UTLS is observed in winter and attributed to equatorial tropospheric origin. They further mention tropopause folds and biomass burning as plausible causes for a lower tropospheric spring maximum in O_3 VMR around 3 km, but observed a weak seasonal variability in the middle troposphere (5-10 km). It is therefore possible, that our data aggregation over the selected altitude range of 3-14 km is not suitable for a separation of local background conditions and deviating layers of non-local origin in the Hanoi case.

In general, although intermittent layers have been reported for the whole tropical region (see Sect.4.2.1), the underlying processes might not be entirely comparable between stations. Thus, the free-tropospheric tracer-tracer relation as examined here might not be universally applicable. The unique "L"-shape signal for the special case of Palau, which is most prominent during the season of highest occurrence of O_3+RH- air masses, FMA, suggests a possible separation of background and layers here. Turning again to the counterpart season ASO, already identified as the minimum O_3 season for Palau (see Sect.4.1.2), we see not only that the O_3+RH- air masses are missing (no tail in the 1D histogram in Fig.4.12, top row), also, the distribution of low O_3, centered around 20 ppb, is especially narrow and almost Gaussian. This particular form of distribution is unique among all selected stations in this seasonal analysis. While distributions for Fiji and American Samoa (Fig.4.12, second and fourth row) peak at even lower O_3 values (< 20 ppb) during their equivalent background season (FMA), they never fully lose their tail and maintain a larger full width at half maximum. Palau's ASO season seems to experience the greatest homogenization of air masses in the free troposphere during the course of the year. If we assume, that this O_3/RH pattern can be explained by convection only, its reappearance during the other seasons can be related to the same process. Thus, we can identify a background in all seasons shifted towards higher mean O_3 VMR for the background compared to ASO, and with more air masses deviating from the background.

In summary, the comparison between Palau and selected SHADOZ stations for the free troposphere in the O_3/RH space emphasizes the uniqueness of Palau. Low O_3 values attributed to a background atmosphere occur year-round in dry or humid conditions within the free troposphere, but show a seasonality. Dry elevated O_3 air masses are limited to the winter seasons, which are characterized by the horizontal part of an "L"-shape in the O_3/RH distribution.

So far, we have neglected variations in altitude. Setting the limits of 3-14 km in altitude purposely excluded the boundary layer and TTL (according to the definition of Fueglistaler et al., 2009, compare Sect.2.1.4), but O_3 is not homogeneously distributed with altitude in the free troposphere. In particular, we included the level of deep convective outflow at which low O_3 levels are typical in the Western Pacific region (see Sect.4.1.1 and 2.1.4). Figure 4.14 shows O_3 VMR below 20 ppb as a fraction of all observations within the same altitude range for Palau and selected stations (see Solomon et al., 2005 for details on binning). Data has been aggregated for the period 1998-2004 for the SHADOZ stations. For Palau, annual averages (in resemblance to Eq.3.13 in Sect 3.2.3) from the available study period are shown. The group 3 stations (black lines) all exhibit a maximal fraction at 200 hPa (20-40 %) and at 900 hPa (50-80 %) (except for Java, dashed line, triangles). For Palau (different colors for lines, no markers), the frequency of low O_3 measurements is high in the boundary layer in all years and generally lower than the other group 3 stations at the chemopause, best resembling the Java profile. In 2016, no upper tropospheric maximum is present, which can be attributed to suppressed convection during El Niño (compare Sect.2.1.2). At 150 hPa, Palau compares better with Hilo and Kuala Lumpur (cyan lines). Despite Hilo's location at 22° N, the station generally shows tropical characteristics such as a seasonal pattern in mid-tropospheric O_3 with deviating layers in otherwise even O_3 profiles, which the joint free-tropospheric visualization in Fig.4.13 does not reveal (Oltmans et al., 2004). In the mid-troposphere, low O_3 observations make up 24-32 % of all measurements in Palau, while all other stations stay well below 20 %. This relates to the persistence of the background throughout the whole tropospheric column and again illustrates the uniqueness of the tropospheric O_3 variability above Palau. The fraction of all O_3 VMR below 25 ppb (not shown here), for example, is above 40% from ground up to 150 hPa ($>$ 50 % at 200 hPa for all years except 2016).

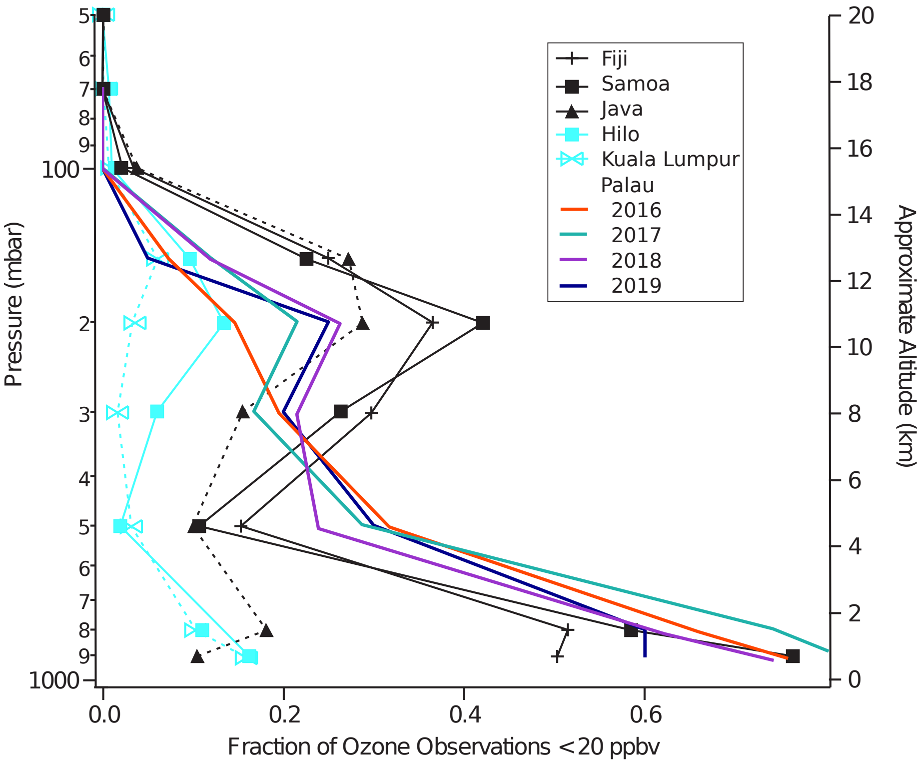

Figure 4.14.: Fraction of occurrences of O_3 VMR below 20 ppb at different altitude levels; average profiles are calculated from 1998 to 2004 for SHADOZ stations (black and cyan lines and markers) and as annual means for Palau (lines per year in various colors, no markers), adapted from Solomon et al., 2005 (see study for further information on the binning).

Comparison with CONTRAST

For a better understanding of the background atmosphere, we examine variations in O_3 and RH with altitude. Analyzing data from the CONTRAST campaign (see Tab.1.1 and Sect.4.4), Pan et al. (2015) found a bi-modal distribution of free-tropospheric O_3 VMR in the altitude profile. The O_3 background or "primary mode" (Pan et al., 2015) was isolated by simply removing all "dry" data with RH less than 45 %, which indicated an entirely convective control of the primary mode. The study thus still refrains from resolving the individual vertical structure of layers, but proposes the RH threshold as an overall free-tropospheric criterion. For Palau a similar analysis reveals no bi-modal distribution for the full data set (Fig.4.15c), and a threshold of 45 % does not separate all higher O_3 observations from the primary low O_3 mode (Fig.4.15d). Figure 4.15a depicts the layer-normalized density distribution for all Palau O_3 observations from the ground to 15 km derived from all 145 measured profiles, with data binning according to Pan et al. (2015). Using the same method of analysis, the panel on the right, Fig.4.15b, shows only "wet" data, with RH greater than 45%. The primary mode, i.e. the layer maximum, is highlighted in dark colors and clear for both data sets. The "wet" data features less frequent occurrences of O_3 measurements with more than 45 ppb. However, the highest frequency of O_3 observations in the mid-tropospheric layer of expected highest occurrence of enhanced O_3 air masses (from 320 to 340 K potential temperature) is approximately the same for both the full and the "wet" data set at around 20 ppb (see Fig.4.15c and 4.15d). The tail in the "wet" distribution is reduced, but not completely absent, as it was shown for the CONTRAST data set (see Pan et al., 2015, Fig.3f). The Palau data shows no clear separation into two modes in the first place (compare 4.15c and Fig.3c in Pan et al., 2015).

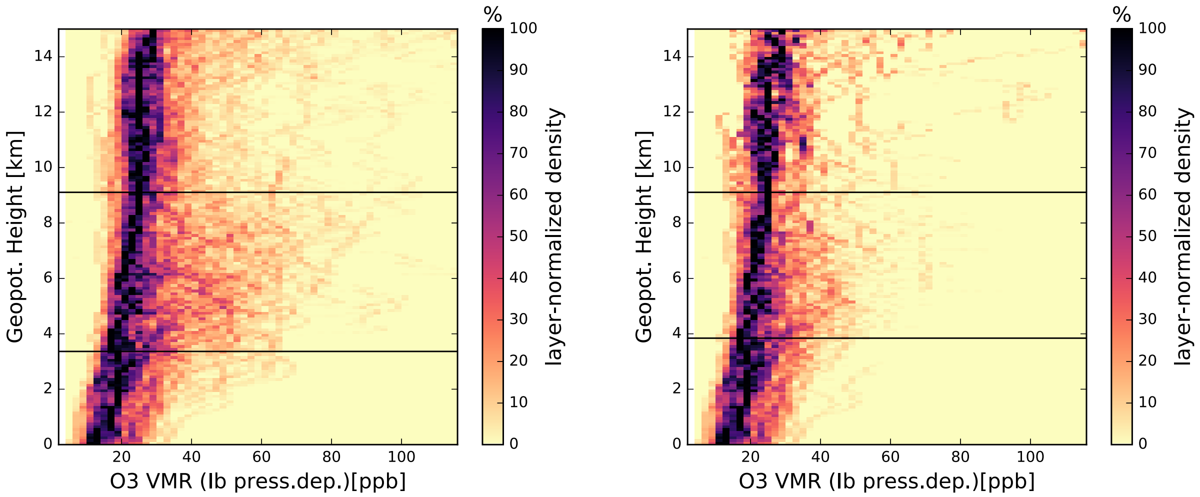

(a) All data (b) Data with RH > 45 %

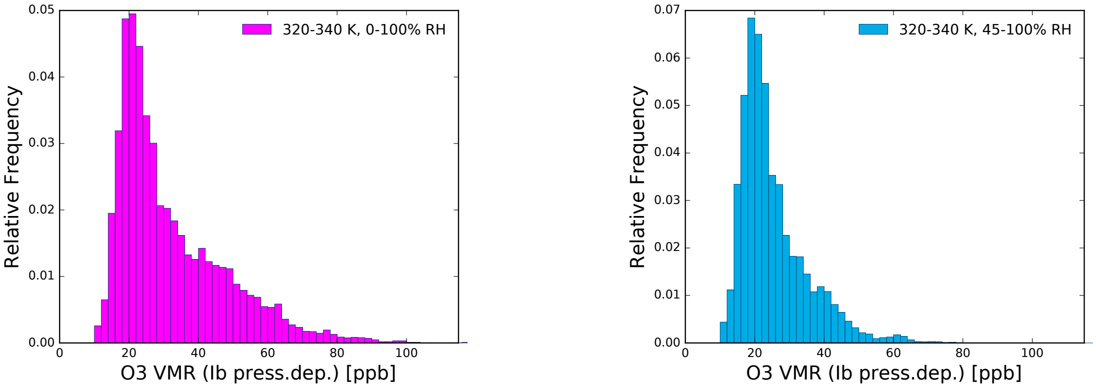

(c) All data (d) Data with RH > 45 %

Figure 4.15.: Relative frequency distribution (normalized to the layer maximum) of tropospheric (0-15 km) O_3 VMR with altitude (100 m bins) for all observations (a) and "wet" observations with RH greater 45 % (b) for Palau during the whole study period, (c) and (d) histograms show relative frequency distributions of O_3 for a layer between 320 and 340 K potential temperature for all (c) and "wet" observations (d) respectively; black horizontal lines in (a,b) indicate the approximate location of the boundaries for the potential temperature based selection of data in (c,d) (compare Fig.3 in Pan et al., 2015).

The differences with the aircraft measurements performed in the TWP from the Guam airbase can be understood by looking at the uniqueness and seasonality of the free-tropospheric O_3 to RH relation at Palau as shown in Figures 4.10a and 4.12 (top row). In the multi-year Palau time series, air masses with higher O_3 content ($>$ 40 ppb) also occur under wet conditions ($>$ 45 %). Likewise, dry and ozone-poor air is frequently observed, presumably measured in higher altitudes and explained by the temperature-dependent vertical RH-gradient (see e.g. Mapes, 2001). The central role of local convection in homogenizing air masses, lifting ozone-poor air from the ground and further depleting O_3 in the tropospheric column, is inevitable. But RH is not sufficient as a stand-alone indicator for a convective and thus local profile in the TWP. In particular, it does not account for possible, though rare, wet and ozone-rich air observations. Potential mechanisms for transport of such air masses to the TWP are discussed in Section 4.3.1. Further data differentiation between seasons and years reveals that a clear bimodal O_3 distribution occurs for most FMA seasons (2/3 of FMA profiles, except in 2018) and other singular seasons of particular years. These cases are summarized in Figure A.7, but make up only 26 % of all measured profiles. The mid-tropospheric distributions in general show least variability in the mostly unimodal ASO season (not shown here). The CONTRAST measurements present a snapshot from the time of the year with greatest occurence of enhanced O_3 (Pan et al., 2017). From the analysis of the Palau time series we therefore conclude that the proposed "fundamental bimodal distribution of tropical tropospheric ozone" (Pan et al., 2015) does not apply for the whole TWP in all years and seasons.

4.2.3. Identification of the Background Atmosphere

Method

There have been various attempts to detect deviating layers and assess the O_3 background quantitatively from balloon and aircraft measurements in the TWP (Hayashi et al., 2008; Pan et al., 2015; Stoller et al., 1999). Using data from the PEM-Tropics and the PEM-West A and B campaigns, Stoller et al. (1999) calculate a free tropospheric background mode for different atmospheric constituents (O_3, H_2O, CO, CH_4) and for individual profiles. Their method includes a specific data binning approach and a least square fit on data in the most dominant mode bin (see Stoller et al., 1999 for further details). The study focuses on the deviating layers yielding extensive statistics for their frequent occurrences during the three NASA campaigns, which together sampled the whole tropical Pacific region in two different seasons. The same methodology was used on MOZAIC aircraft data by Thouret et al. (2000) (see Tab.1.1). The main disadvantage of this mode-based method lies within the arbitrary threshold used to determine the required number of data points to signify the dominant mode bin. Leaving the "technical" caveats of any detection method aside, the sole definition of a "layer" of certain vertical extent within a highly variable profile measurement requires many assumptions. Slight changes in the parameters defining layer boundaries, could significantly alter any statistical outcome. However, an important conclusion of Stoller et al. (1999) is the recognition of importance of these layered structures in the tropical Pacific region owing to their frequency, and the demand for their inclusion in dynamical models mapping chemical processes. A similar analysis of longer time series from three SHADOZ sites (Java, American Samoa and San Cristobal) confirms the frequent occurrence of dry enhanced O_3 layers below 12 km (Hayashi et al., 2008). Using a different method of layer detection, the study found O_3+RH- air masses in approx. 50 % of profiles per year at each station with differing seasonal variations.

Without formulating any definition of a concise vertical layer in individual profiles, we loosely follow the approach of Hayashi et al. (2008) to define a reasonable background profile first. As a starting point, Hayashi et al. (2008) identified two disparate seasons from their data sets. For every individual profile they only considered layers as enhanced in O_3 concentration which exceed the 83.3th percentile of all observed VMR of the corresponding time period. They excluded layers with a vertical thickness below 1 km, finding these insignificant in their number of occurrences and difficult to assess using follow-up trajectory analysis. The dryness or wetness of the identified O_3+ layers was determined by the comparison of the RH within the layer to the RH profile above and below. For the Palau data set, we chose monthly statistics, and defined the background as the 20th percentile for O_3 VMR and the 83.3th percentile for RH values respectively. This less conservative approach in respect of O_3 accounts for the uniqueness of Palau's free tropospheric air as described above (see Sect.4.2.2) and our understanding of the background atmosphere as the uniform low O_3 profile in active convection (see Sect.4.2.1), without focusing on the layered structure within the deviating air masses. Hence, neither the layer thickness nor the altitude of the individual observed O_3/RH pairs within the profile are considered.

Results

Figure 4.16 shows monthly medians, central 66 % ranges and a highlighted 20 % quantile for O_3 VMR for all months, including the number of samples used (in brackets). The 20th percentile was chosen after examination of various different percentiles and their convergence towards an even profile in all months. It corresponds well to the expected seasonality of the background, with e.g. values below 20 ppb from July until October (compare Fig.3.9). However, months with more frequent deviating layers and large mid-tropospheric variability (compare 66 % ranges in Fig.4.16) still show a lot of structure in their background profiles, i.e. departures from the straight line (February, April, November). May, as a transitional month, again stands out (compare Sect.4.1.1). The smoothed profile (green line) can be perceived as a "tilted line" with a "bump" in the mid-troposphere, i.e. it shows characteristics from June/July ("tilted line") and FMA ("bump"). Monthly RH background profiles are shown in Figure 4.17. Here, February and April stand out as particularly dry.

In this study, we look at the deviations from the respective tracer's monthly background profile for each measurement point in an individual profile. We arrive at an O_3/RH distribution relative to the individual tracer backgrounds for all seasons and altitudes as shown in Figure 4.18b. The distribution of absolute values, as discussed in detail in Section 4.2.2 (see Fig.4.10a), is shown again in Figure 4.18a for comparison. Data points

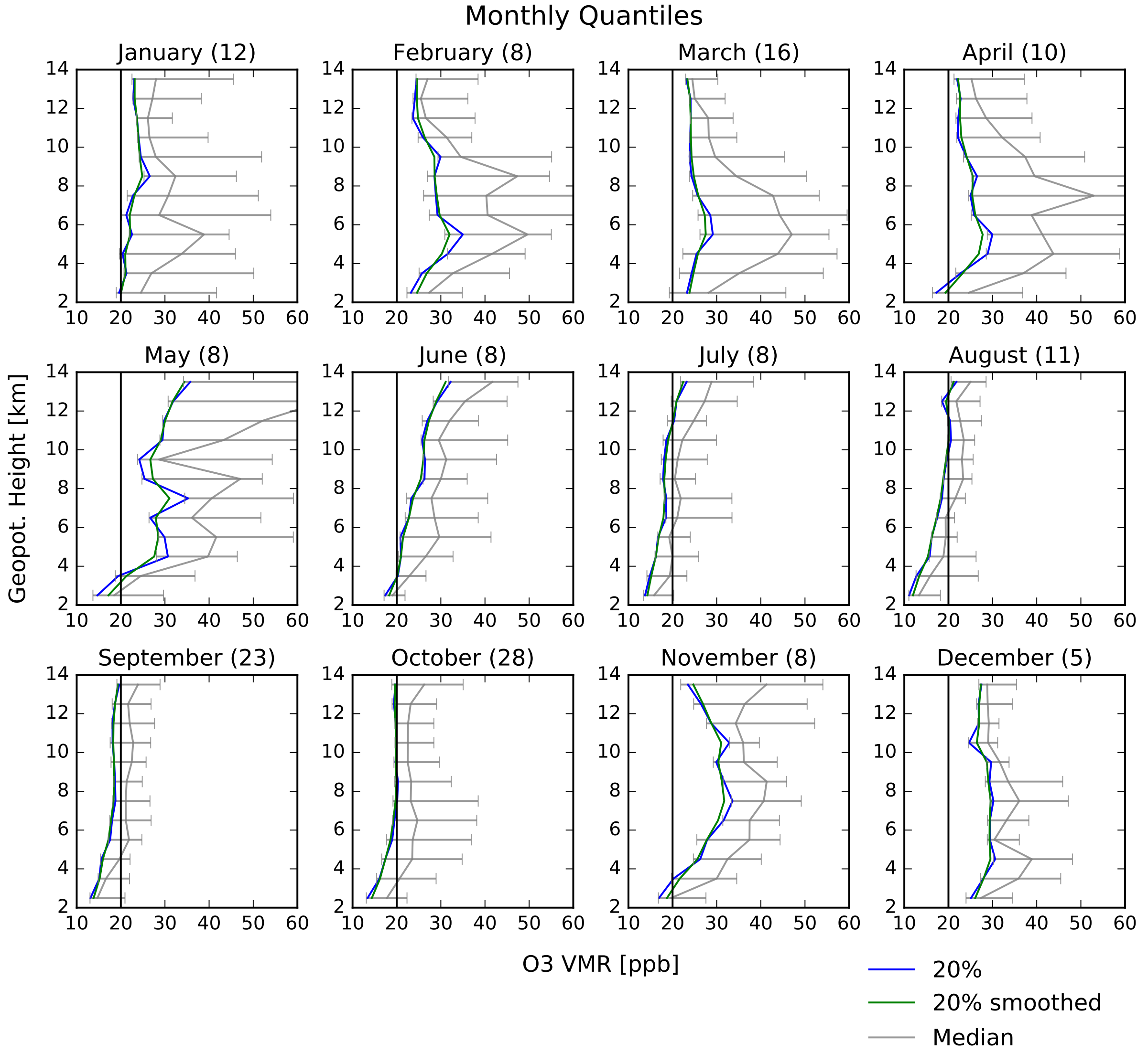

Figure 4.16.: Monthly O_3 VMR statistics (20 % quantile in blue, median in gray and central 66 % range in gray horizontal bars) for Palau tropospheric profiles per km; a vertically smoothed profile of the 20 % quantile (green line) is calculated using exponentially weighted averages; number of included individual profiles per month in brackets; 20 ppb O_3 VMR is highlighted by a vertical black line.

in Figure 4.18b represent anomalies from the background and are generally clustered along the O_3 VMR axis, which itself indicates zero O_3 anomalies. Given the choice of quantiles, the majority of data points occupies the lower right quadrant of the graph, the overall O_3+RH- section (light brown in Fig.4.18c). The axes represent respective background values; marked boundaries (dashed black lines) are chosen manually with respect to the shape of the distributions in order to separate finer regimes of high (+), neutral (∘) and low (-) O_3 and RH respectively, creating a 3 times 3 grid. The central grid cell in Figure 4.18b (O_3∘RH∘) represents background conditions in both parameters within a range of -5/+15 ppb for O_3 and -20/+5 % for RH.

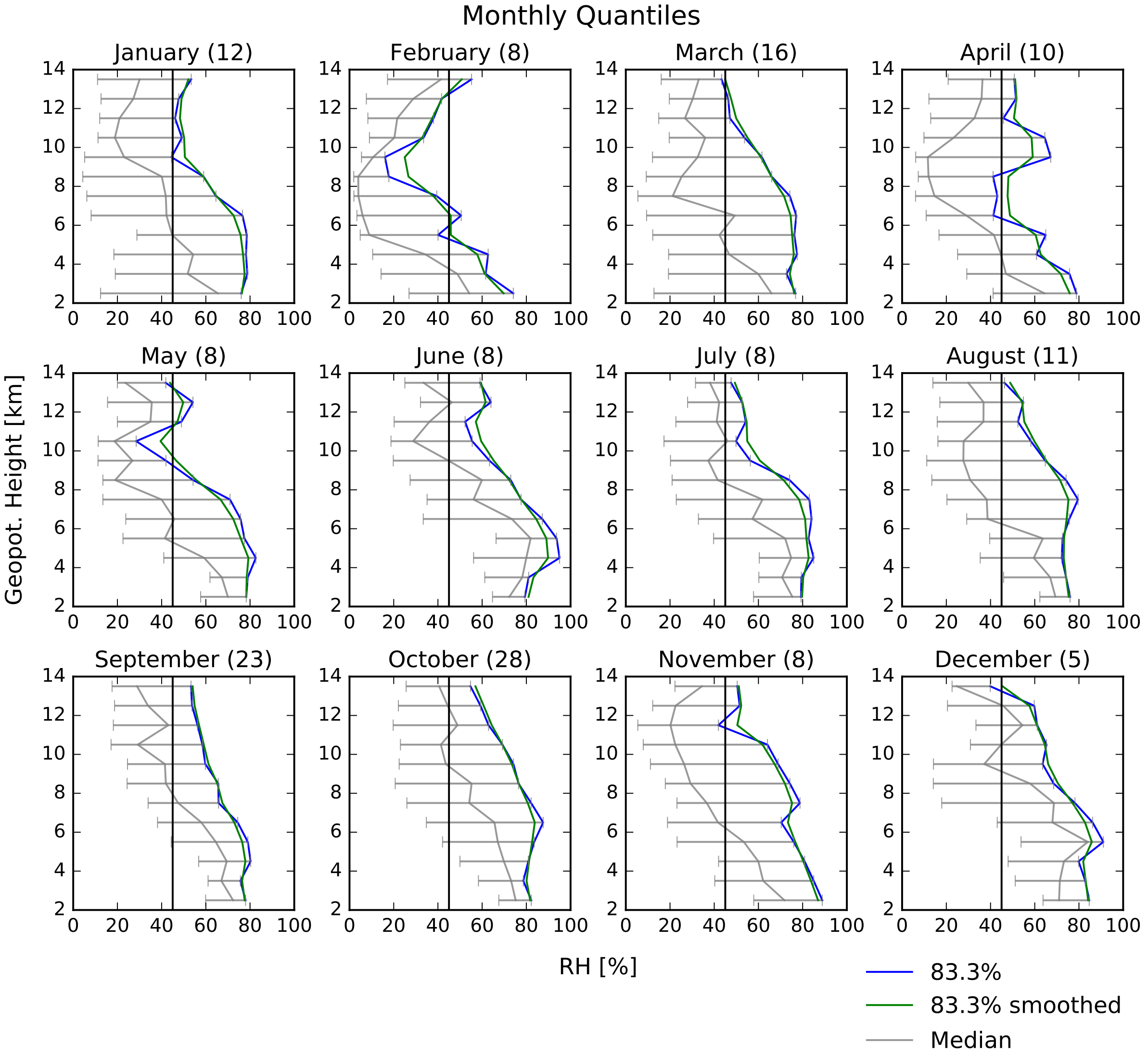

Figure 4.17.: Monthly RH statistics (83.3 % quantile in blue) per km; 45 % RH is highlighted by a vertical black line; for more details, see Fig.4.16.

An interesting feature is the clear bimodality of the RH anomalies, which is persistent in all seasons except MJJ (purple histogram, Fig.4.19c). The primary mode is essentially co-located with the background (NDJ, Fig.4.19a), representing the 83th percentile of the respective time-altitude bin. In all seasons except for NDJ it is slightly shifted towards negative anomalies (Fig.4.19b, 4.19c and 4.19d). Apart from MJJ, a secondary mode occurs at -40 %, i.e. measured RH values are 40 % lower than their background estimates. Our assumption of the background being a consequence of local convection, leads to the definition of the primary, wet mode as our local mode. This includes shallow or deep convective activity as the dominant processes in control of tracer composition. The secondary dry mode possibly contains all air masses affected by non-local processes. There are, however, various possible mechanisms involved in determining the moisture of an air mass such as remoistening during transit or mixing. These add to the uncertainty of a clear separation of a dominance of local and non-local influence on air composition (see next Sect.4.2.4).

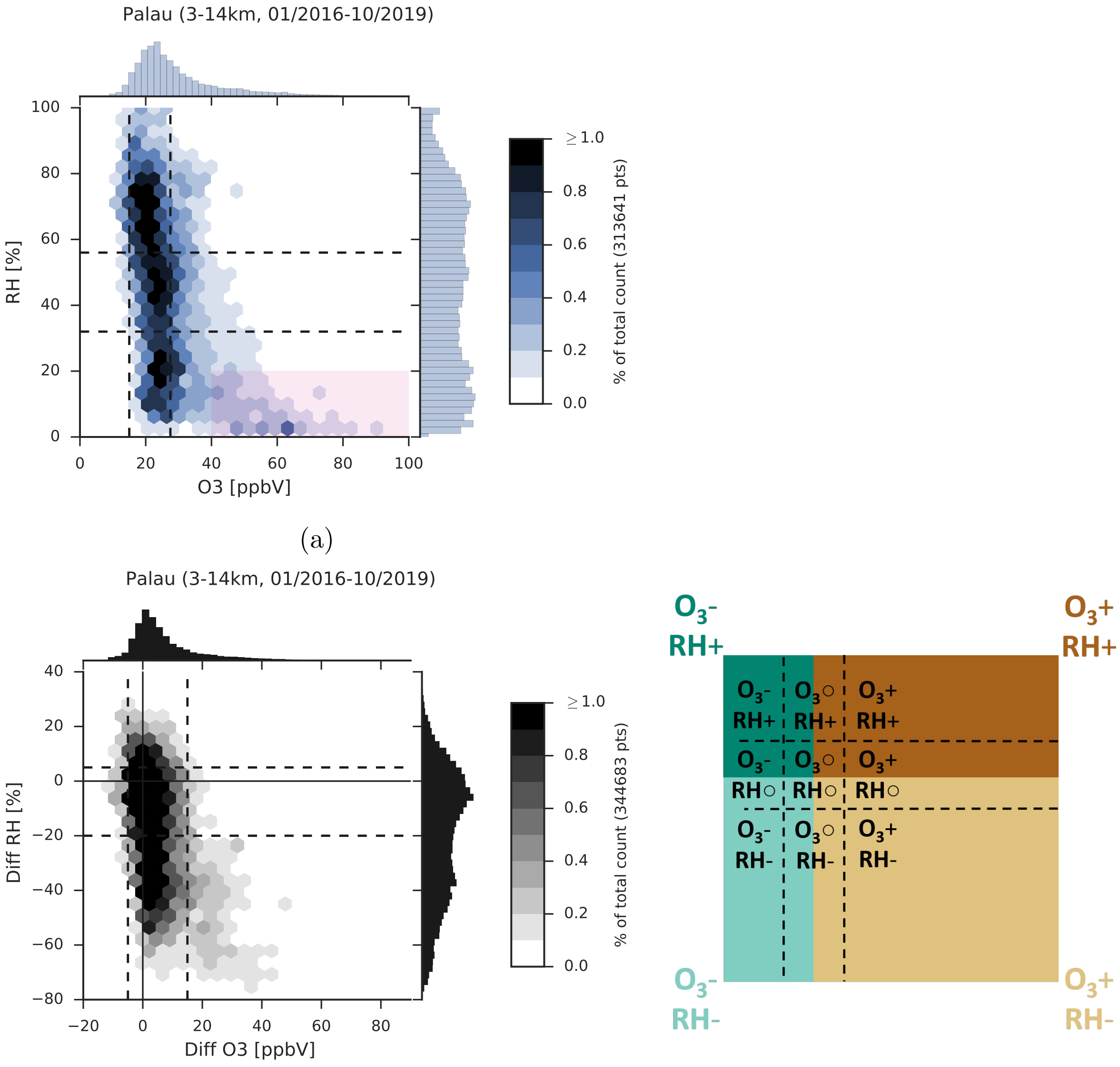

(a)

(b)

(c)

Figure 4.18.: Free-tropospheric (3-14 km) relation between O_3 and RH for Palau in absolute values (a) and as an anomaly from the monthly background profiles (b); dashed lines in (a,b) refer to the definition of different O_3RH groups in a 3 times 3 grid (boundary values for the central grid cell are -5/+15 ppb for O_3 and -20/+5 % for RH, compare Sect.3.4.1), while (c) illustrates the nomenclature of the different groups (2 times 2 grid in colors, 3 times 3 grid in black); the light pink shading in (a) indicates the O_3+RH- layer definition by Anderson et al. (2016), Nicely et al. (2016) and Tao et al. (2018) (compare Sect.4.4); see also Fig.4.10.

The bimodality in RH anomalies further justifies our separation between RH○ and RH- air masses in the 3 times 3 grid classification (see dashed lines in Fig.4.18b and 4.19). The differentiation of free-tropospheric air mass anomalies by season in Figure 4.19 again reproduces the known absence of O_3+RH- air in ASO and MJJ compared to their dominant appearance in NDJ and FMA (see marginal 1D histograms for RH in Fig.4.19a and

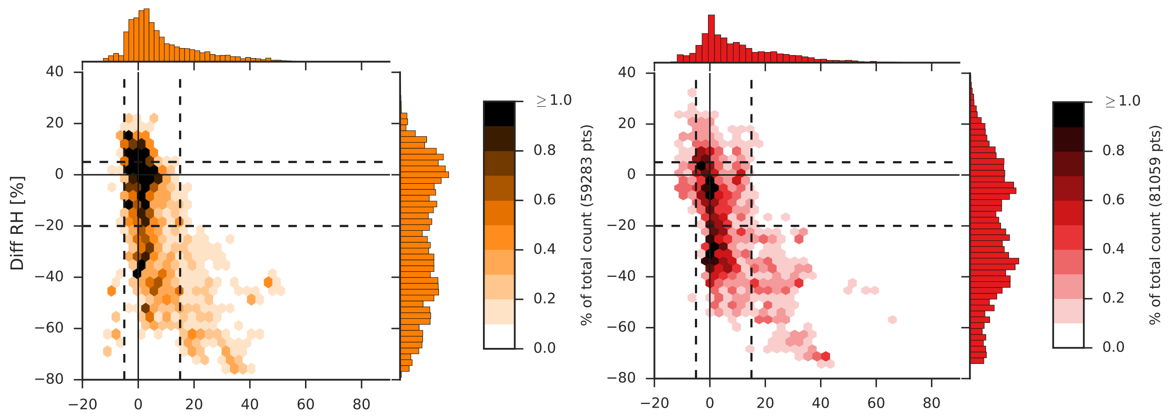

(a) NDJ (b) FMA

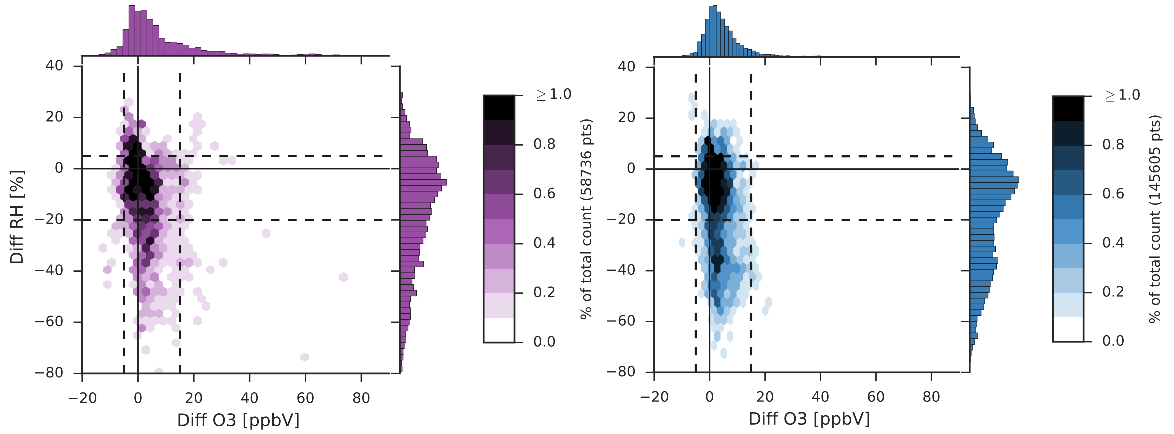

(c) MJJ (d) ASO

Figure 4.19.: Seasonal free-tropospheric (3-14 km) relation between O_3 and RH for Palau; for more details, see Fig.4.18 and 4.10.

4.19b). During the latter seasons, both maxima in RH are of similar amplitude, which emphasizes the importance of dry air masses intruding into the otherwise wet troposphere.

Figure 4.20 presents the relative occurrences of each O_3RH group in the 5-10 km altitude range per season in a heatmap format. The data base for these statistics is still a representative reduction of the full Palau data set in preparation for the following trajectory analysis (138 profiles, every 10th measurement of a profile, see Section 3.4.1 for details). The 5-10 km altitude range excludes the levels of main convective outflow and focuses on the relevant level of most frequent deviating layers (see Sect.4.2.4). There is a lot of information conveyed by these graphics, regarding the quality and applicability of the classification itself and the individual groups in particular. Here, we want to focus on the background (O_3∘RH∘) and the most prominent category of deviating layers, dry enhanced O_3 air (O_3+RH-). Not surprisingly, within an individual sounding, background air masses (O_3∘RH∘) occur in the majority of profiles in all seasons (74-88 %, see Fig.4.20a). Furthermore, O_3+RH- air masses occur in 71 % of all FMA profiles, a similar fraction as background air in FMA (74 %), but only in 25 % of all ASO profiles (Fig.4.20a).

Figure 4.20b lists the occurrence of O_3RH groups as a fraction of the total number of data points within a season, i.e. adding up to 100 % of measurements per season. This can be interpreted as an indicator for the group's fraction within individual profiles and thus, the vertical thickness of either background or deviating layers within the profiles of the respective season. The heatmap in Figure 4.20b shows the discrepancy between FMA and ASO more clearly, with the dominating group of 40 % of seasonal data points either being part of the $O_3\circ$RH$\circ$(ASO) or the O_3+RH- group (FMA). This contrast becomes even more apparent, when adding up all groups with background O_3 ($O_3\circ$) (88 % for ASO compared to 47 % for FMA) or enhanced O_3 (O_3+) (10 % for ASO compared to 47 % for FMA). The MJJ and NDJ seasons appear as transitional seasons in the given statistics as expected, and are comparable with each other in some aspects (compare Sect.4.1.1). Regarding the transitional character, Figure 4.20a expresses that the frequency of O_3+RH- air mass observations in MJJ is double compared to the ASO season (54 % in MJJ compared to 25 % in ASO, see Fig.4.20a), but in absolute numbers of data points, MJJ better resembles the following ASO instead of the previous FMA season (16 % in MJJ, compared to 9 % in ASO and 40 % in FMA, see Fig.4.20b). A similar comparison can be made for NDJ, with its greater resemblance to the FMA season. Common characteristics of MJJ and NDJ are revealed by again adding up all seasonal occurrences regarding data points for background and enhanced O_3 (MJJ compared to NDJ: 73 % to 68 % for $O_3\circ$ and 24 % to 26 % for O_3+, see Fig.4.20b).

4.2.4. Relevance of O_3+RH- Layers

Dry layers of enhanced O_3 (O_3+RH-) intruding a wet ozone-poor background atmosphere are a characteristic feature in the TWP and have been observed by numerous campaigns (e.g. Browell et al., 2001; Hayashi et al., 2008; Newell et al., 1999; Oltmans et al., 2001; Pan et al., 2017; Thouret et al., 2000). The vertical confinement of the layers and predominant occurrence in the mid-troposphere suggest that these air masses were advected from remote regions. The relevance of the O_3+RH- filaments for local air composition and climate forcing is commonly acknowledged (e.g. Anderson et al., 2016; Kley et al., 1997; Mapes and Zuidema, 1996; Yoneyama and Parsons, 1999). O_3 is a powerful greenhouse gas and intrusions of dry air inhibit convection, increase OLR and thus promote radiative cooling with linear dependency on their vertical extent (Cau et al., 2005; Myhre et al., 2013). The effect of transported pollutants into the clean air of the TWP as a key region of STE is under investigation (Nicely et al., 2016; Rex et al., 2014, see Sect.2.2.3).

The debate about the origin of these layers is ongoing and controversial (see Anderson et al., 2016 for a short review on controversial studies). Most recently, based on the same data sets from the CONTRAST campaign (Pan et al., 2017), a direct conflict revolves around two concurring theses (Anderson et al., 2016; Nicely et al., 2016; Randel et al., 2016; Tao et al., 2018). Elevated O_3 concentrations originate either from pollution in high NO_x regimes or photo-dissociation of O_2 in the extra-tropical stratosphere (compare Fig.4.21). Different dynamical processes are under debate to explain depressed water vapor compared to the humid tropical column (e.g. Cau et al., 2007; Dessler and Minschwaner, 2007). With low RH signatures possible for both cases, a separation of the two

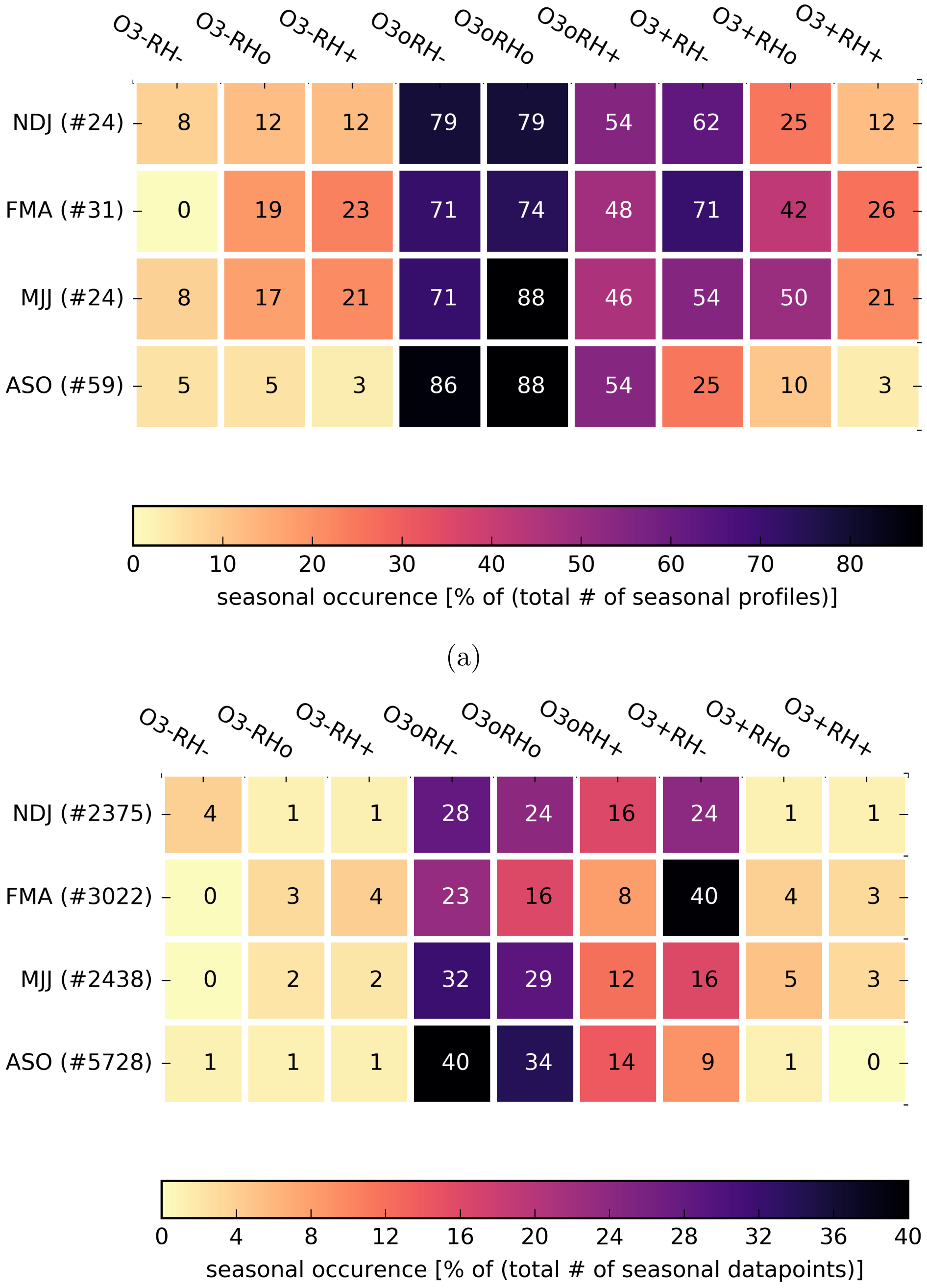

(a)

(b)

Figure 4.20.: Occurrence of air masses classified in nine O_3RH groups (+, - or neutral/background ∘, for O_3 or RH in relation the background definition in Sect.4.2.3) within each season for Palau observations in the 5-10 km altitude range, relative to the total numbers (#) of seasonal profiles (a) and seasonal data points (b); total numbers are given in brackets per seasons; for this statistical analysis a subset of the Palau data was used, with the number of data points referring to the data points used in the trajectory analysis, i.e. every 10th measurement of a sonde profile and a total number of 138 profiles (compare Sect.3.4.1).

pathways requires information from additional chemical or dynamical tracers. Coinciding elevated CO levels would suggest a tropospheric origin (e.g. Anderson et al., 2016; Newell et al., 1999; Stoller et al., 1999), additional species could further differentiate between tropospheric sources, such as fuel combustion or biomass burning. Emission of HCN, for example, occurs almost exclusively during biomass burning events (Anderson et al., 2016; Randel et al., 2010). In addition to trajectory analysis, Singh et al. (1996) used the ratio of reactive nitrogen (NO_y) and sulfur species to identify Asian continental outflow as a source for Western Pacific air (compare Folkins et al., 1997; Kondo et al., 2004).

The high potential temperature of the tropical tropopause compared to the dynamical 2 PVU tropopause of the extra-tropics, which crosses isentropes, allows quasi-horizontal advection of ozone-rich stratospheric air from the mid-latitudes to the tropical UTLS (e.g. Hayashi et al., 2008; Kley et al., 1997; Randel et al., 2016; Stoller et al., 1999; Tao et al., 2018; Waugh, 2005; Waugh and Polvani, 2000; Yoneyama and Parsons, 1999, compare Sect.2.1.4 and Fig.A.1). Besides in-mixing along the subtropical jet, occasional intrusions of tropopause folds could be of relevance, although they usually do not reach the deep tropics (Cau et al., 2007; Sprenger et al., 2003; Waugh and Polvani, 2000). Typical aerosol distributions or increased PV are considered as stratospheric tracers (e.g. Foltescu and Zahn, 1995; Holton et al., 1995; Kremser et al., 2016). The growing time series of O_3 soundings in Palau is predestined to contribute to the solution of this ongoing controversy (see results of the trajectory analysis in Sect.4.3.2). If the attribution to tropical biomass burning holds, this might become a strong argument for policy makers as “present legislation to limit emission of O_3 precursors in the extra-tropics may have little, if any, positive impact for the radiative forcing of climate due to tropospheric O_3” (Anderson et al., 2016).

4.2.5. Discussion

In light of the unique tropospheric variability above Palau a separation of air masses under predominantly local or non-local control seems possible using only two tracers. The analysis of the tracer-tracer relation for O_3 VMR and RH can be used to identify a background atmosphere. This background is characterized by low O_3 VMR and an evenly spread RH distribution in the free troposphere, suggesting a recent convective imprint on air masses and thus a local origin. O_3 enhanced air masses with low RH can be explained by transport processes to the TWP and identified in the 2D histogram for the frequency of O_3/RH pair observations as the horizontal part of an “L”-shaped distribution.

The comparison with a selected number of SHADOZ stations puts Palau in the context of other tropical and Western Pacific stations, while underlining the unique characteristics of the free troposphere of the TWP. This includes the lowest O_3 VMR statistics (see Fig.4.11) and the seasonal development of the “L”-shaped O_3/RH distribution. Despite seasonal variations, the local mode (vertical part of the “L”-shape in Fig.4.12, top row) is present throughout the year, i.e. local processes dominate the tropospheric composition. A basic analysis of mean seasonal or monthly profiles of O_3 VMR (with altitude) does not reveal this relevant feature of individual observations. Here, a frequent occurrence of

O_3+RH- layers in the mid-troposphere is masked in the "belly" of the "S"-shaped profile (compare Sect.4.2.1 and Pan et al., 2015).

A bimodal distribution of free-tropospheric O_3 VMR as suggested by Pan et al. (2015) is only found in certain years and seasons (Fig.4.15 and A.7). A separation between local or non-local control of air masses therefore needs to include information from both tracers. Additionally, a vertical resolution finer than the simple reduction to the free-troposphere needs to be taken into account.

To consider variations with altitude and both tracers, we use profiles of monthly quantiles to determine background profiles per month for O_3 VMR (20th percentile) and RH (83.3th percentile). For each individual sounding, anomalies from this background are calculated. Aggregation of all free-tropospheric anomalies yields O_3/RH distributions as shown in Figures 4.18b and 4.19, thus suggesting a separation of different groups in relation to the background. The resulting bimodality of the RH distribution not only justifies our separation into distinct "dry" and "wet" categories. It also emphasizes the relevance of deviating layers of non-local origin associated with the dry mode and enhanced O_3 air masses in contrast to the local mode, indicating the dominance of recent convective and thus local processes.

Our method of air mass categorization is a fairly simple statistical approach using time series data in bulk. In principal, it is also applicable for sounding data time series from other tropical stations, though it may not yield the best results as atmospheric processes and mechanisms determining air composition might be specific to this geographic location (compare with Sect.4.2.4). The advantage of our method compared to algorithms of layer detection in individual profiles (e.g. Stoller et al., 1999) lies within its simplicity and the use of the identified bimodality in the RH anomalies.

However, a few caveats could be investigated to improve the classification of air masses and layer detection:

- The selection of the 83th quantile for RH, also in context of the RH bimodality, should be revisited, as the maximum of the anomalies is mostly just below the background values, e.g. visualized by the RH axis in Fig.4.19. This is also reflected in the dominant occurrence of both $O_3\circ$RH$\circ$ and $O_3\circ$RH- found for the 5-10 km subset of the Palau data (see Fig.4.20). An adjustment of the RH quantile and corresponding center on the $O_3\circ$RH$\circ$ group could still improve the air mass selection.

- The hence established monthly profiles are not uniform throughout the column, which is proposed as the ideal, purely convective profile (see Fig.4.9a). During the months of increased occurrence of deviating layers, i.e. FMA and NDJ, the 20th percentile profile still incorporates the "S"-shape, presumable caused by these layers. This could possibly be reduced by changing the temporal resolution from monthly to seasonal statistics, which has not been assessed yet. A growing time series will certainly help to validate our approach as it reduces possible biases caused by different sampling frequencies per season.

- While the relevance of O_3+RH- filaments is undisputed (see Sect.4.2.4), other categories of deviating air masses are encountered less and thus more difficult to relate to underlying atmospheric processes.

Our resulting categorization into O_3RH groups relative to the background atmosphere is used in the following trajectory analysis and thus a prerequisite to linking air mass origin and tracer variability. The corresponding results (see Sect.4.3.2) support our assumptions on combined O_3 and RH as tracers for local and non-local air masses. A satisfying automated computational detection of the deviating layers per profile in analogy to Stoller et al. (1999) is in preparation. A comparison with our method will reveal, how well individual layers are captured in both approaches. A combination of methods could be an improvement for an extended trajectory analysis, which combines climatology and tracking of individual layers (compare Sect.4.3.3). In the future, the methodology could be tested for the TTL altitude region to analyse the seasonality of deep convective outflow and STE processes.

4.3. Transport and Origin

Our previous analysis of the Palau time series suggests, that the low O_3 background atmosphere is caused by low boundary layer O_3 lifted by convection. Deviations from this background profile in the free troposphere are indications of non-local influence via synoptic to larger-scale transport processes. Considerations in atmospheric dynamics and chemistry of the TWP already point at possible source regions related to air masses of certain O_3/RH content, which are summarized in an overview of transport pathways (Sect.4.3.1). We test our hypothesis and identify transport pathways and origin of air masses by back-trajectory calculations with the ATLAS trajectory module driven by meteorological data from ECMWF ERA5 (see Sect.3.4.1) and compare the results with the O_3 and RH observations from our Palau soundings (Sect.4.3.2).

4.3.1. Transport Pathways

The origin of air masses transported to Palau is linked dynamically to the position of the ITCZ. Air masses under non-local influence are identified as anomalies from the local, convectively controlled, humid, low O_3 background. The impact of transport versus local convection is reflected in the tropospheric O_3 and RH seasonality (see Sect.4.1 and 4.2). We propose five different transport pathways to the TWP related to the four major categories of non-local air masses in respect of their O_3/RH relation (compare Fig.4.18c) based on our understanding of the dynamics and chemistry of the TWP. Figure 4.21 presents a simplified scheme for these pathways to Palau on the zonal plane including major dynamical drivers.

In our hypothesis, deviating layers of ozone-depleted air (O_3-, turquoise colors) are of Pacific and ozone-rich air masses (O_3+, brown colors) either of (South East) Asian or stratospheric origin (see Fig.4.21). We consider RH as an indicator for the vertical displacement of air masses during transport, i.e. rather a measure of path and not necessarily source variability (compare Hayashi et al., 2008; Schoeberl et al., 2015). Right after detrainment, air masses have a RH of 100 %. We then assume that the absolute humidity remains constant during transport in clear sky conditions, so that a descent and warming of an air mass results in a decrease in RH. A convective event, lifting air masses, would reset RH to 100 % again. Dehydration of air masses (RH-, lighter colors in Fig.4.21) can hence either be explained by net clear sky radiative cooling and subsequent subsidence (compare Sect.2.1.3) or quasi-horizontal transport from the extra-tropical stratosphere (compare Sect.2.1.4). The first process includes boundary layer air raised by convection in the area of origin, i.e. a direct relation to a source of O_3 production (or depletion) on the ground (light brown transport pathway from the ground and light turquoise pathway in Fig.4.21).

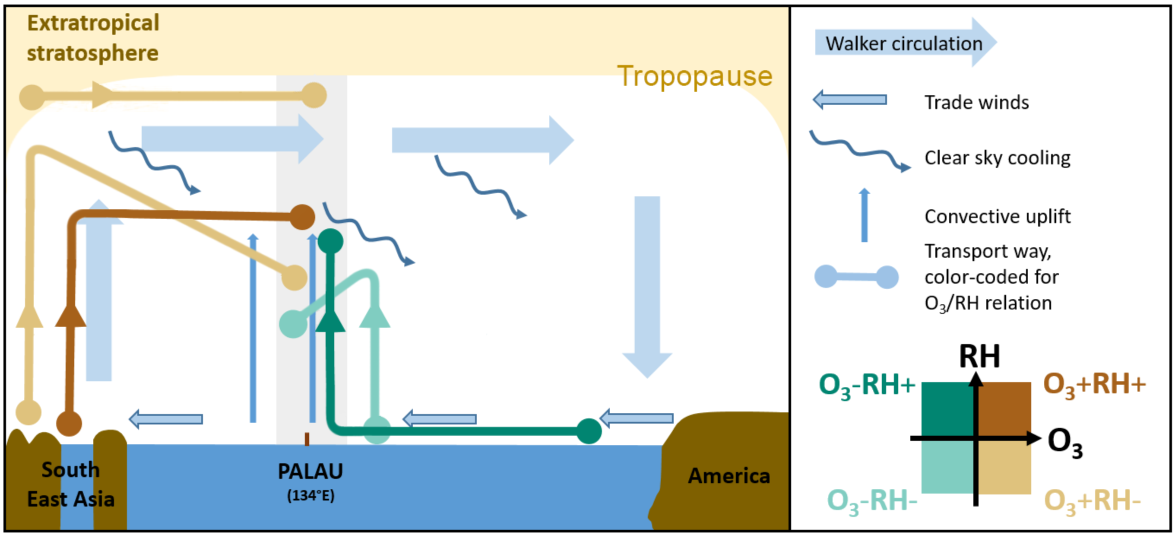

Figure 4.21.: Schematic for transport pathways to Palau and the TWP on the zonal plane, major dynamical drivers are marked with different arrows (blue colors), transport pathways are color-coded by air mass group (O_3±RH±) in relation to the background atmosphere; compare air mass classification and observed O_3/RH relation in Figure 4.18c and Section 4.2.3.

Air masses more humid than the background atmosphere (RH+, darker colors in Fig.4.21), which is defined as the 83th percentile of monthly profile measurements, are less frequent and thus difficult to address in a trajectory analysis (compare e.g. Fig.4.18b and 4.20). For O_3-RH+ air masses (dark turquoise in Fig.4.21) a strong and very recent convective local uplift of air originating in the humid tropical Pacific, reaching Palau with the trade winds, can be assumed. Air within O_3+RH+ layers (dark brown in Fig.4.21) originates in the (South East) Asian boundary layer and is subject to convective uplift in the area of origin with following short-term direct horizontal transport to the TWP. This thesis will focus on the most abundant group of deviating air masses: O_3+RH- (light brown in Fig.4.21, compare also Fig.4.20). The two possible pathways and thus origins for these air masses have been discussed in detail in Section 4.2.4.

4.3.2. Trajectory Analysis Results

The hypothesis above is tested in an analysis of the backward trajectory ending points calculated by the ATLAS trajectory scheme as described in Section 3.4.1. We study a climatology of trajectories from all available soundings within the 4-year time series and examine air masses “in bulk”. Due to missing meta data, we use a slightly reduced number of 138 profiles. The vertical profile resolution is reduced by selecting every 10th sonde reading for the trajectory analysis. In order to identify similar air masses and pathways, we examine the following parameters:

- length of the trajectory in days,
- (shifted) season (see Sect.4.1.1) of the sounding,
- measured sonde geopotential altitude (i.e. arrival in altitude ranges, see below),
- difference between pressure altitude of start (measured by sonde) and ending point of the trajectory (i.e. ascended or descended air parcels, neglecting changes along the path),
- and the O_3 VMR and RH measured by sonde in absolute values or relative to the background described in Section 4.2.3.

We look at trajectories in three different altitude ranges in accordance with the three distinct layers of the free troposphere motivated in Section 2.1.3: “2-5 km” as the layer of shallow convective outflow, the “5-10 km” layer with suppressed detrainment and a stratification of the pseudoadiabtic temperature and the “10-14 km” layer including the level of deep convective outflow, but excluding most of the TTL with greater stratospheric influence. We focus our analysis mostly on the pseudoadiabatic layer (5-10 km) because of the high variability in O_3 VMR (see Fig.4.2c and Sect.4.1.1) and greatest abundance of O_3+RH- layers (compare Sect.4.2.4). An overview of the fractional distribution of the data within the 5-10 km altitude range, sorted by O_3RH groups, is already presented in Fig.4.20. Table 4.1 summarizes the absolute number of data points and profiles per season and altitude range. In the following, we will first present our trajectory calculations and then compare identified seasonal and regional patterns with our tracer observations.

Season	NDJ	FMA	MJJ	ASO
# profiles	24	31	24	59
# data points				
2-5 km	1433	1900	1520	3581
5-10 km	2375	3075	2444	5733
10-14 km	1856	2261	1861	4367

Table 4.1.: Overview of the number (#) of profiles and data points per season and altitude range used in the trajectory analysis, compare Fig.4.20.

Source Regions and O_3

Figure 4.22 gives an overview over all trajectory calculations for the study period, showing a representative subset (every 20th trajectory of a day/profile, for better visualization) of 10-days backward trajectories sorted by season (in rows) and altitude level (in columns). A seasonal classification of all Palau trajectories already separates the two main path ways and source regions: air masses originating north west of Palau on the Asian continent are observed mostly from November until April (NDJ, FMA, upper rows in Fig.4.22), while (Eastern) Pacific air predominantly reaches Palau from May until October (MJJ, ASO, lower rows in Fig.4.22).

As expected from the statistical profile analysis (see e.g. Sect.4.1.2), the strongest seasonal differences are between FMA and ASO seasons; NDJ and MJJ resemble FMA and ASO respectively. Differences between altitude levels within a given season are present, though not as prominent (e.g. the main direction for incoming air masses to Palau in NDJ shifts from east north east to south east with increasing altitude). An exception are the trajectories reaching Palau from the West, which are mostly limited to the 2-5 km layer during MJJ and ASO. These pathways are caused by equatorial westerlies within a narrow band during the active Western Pacific Monsoon (WPM) from July to October (compare Sect.2.1.1) and as such are mostly confined to lower altitude levels (maximum up to 10 km). In accordance with the local wind direction climatology, air masses are approaching Palau mainly from the East throughout all seasons and levels (see Fig.4.3).

The temporal length of the trajectory in Figure 4.22 can be related to the influence of local mixing versus long-range advection on air mass composition ("shorter" versus "longer" distances traveled in time). Fast transport from remote regions, however, cannot rule out a possible dominance of local processes. Single convective events cannot be captured by the model. Thus, we cannot detect sonde measurements taken inside an active convection cell, which would render any trajectory based on the average grid-cell wind field useless. Also, due to mixing and deterministic chaos, the trajectory becomes less reliable with increasing length. Colored line-segments in Figure 4.22 are indicating three different time periods backwards: 3, 5 and 10 days. Air masses have traveled faster and longer distances in FMA, particularly those arriving in the 5-10 km altitude range. At the same time, the convective activity in the TWP is lowest (see e.g. Fig.2.4), allowing the conclusion of a greater impact of long-range transport. Originating at higher northern latitudes further west, air in FMA is moving anticyclonic over the North West Pacific towards Palau. Thus, air masses within the low latitude upper-air polar westerlies can reach Palau during this season, because the subtropical ridge shifts towards lower latitudes in winter (lowest in February/March) and in general closer to the equator with increasing altitude (e.g. Riehl, 1954). Once air parcels reach the West to central Pacific they are either diverted eastwards by the (subtropical high) anticyclone, possibly associated with the upper air mass divergence from air rising above the warm pool, or are picked up by the general trade wind circulation. All air masses eventually reach Palau from the East. In contrast, with a subtropical ridge or base of the polar westerlies in higher latitudes (highest in August/September) and a subtropical high residing further north east, transport is governed by the trade winds and monsoon circulation. Thus, most ASO air masses never leave the Pacific ocean area within 10 days.

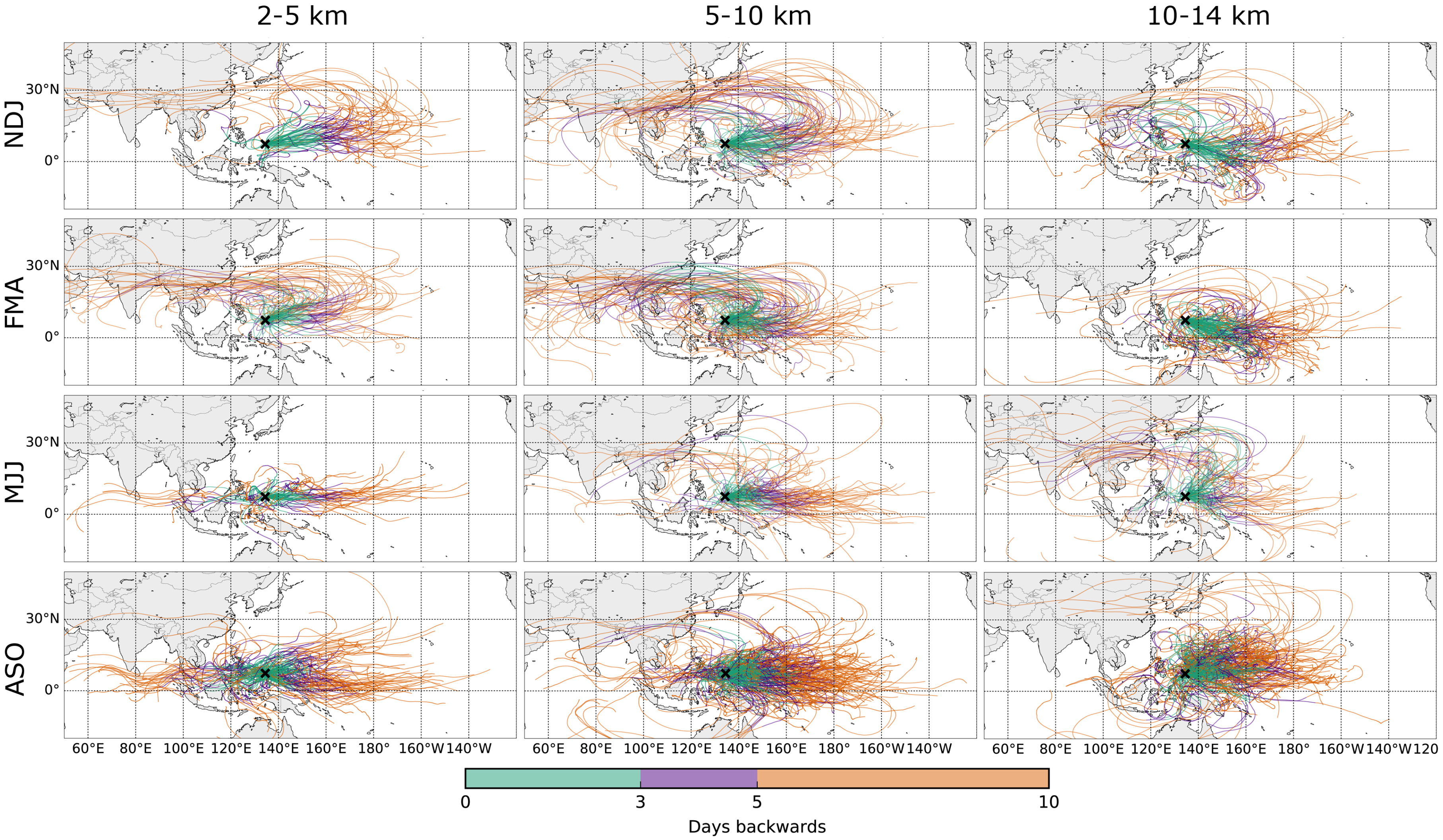

Figure 4.22.: 10-days backward trajectories by season (rows) and altitude level upon arrival in Palau (columns), colored segments represent time periods of maximal 3 (green), 5 (purple) and 10 (orange) days backwards respectively, the x marks the location of Palau; only a selection from all calculated trajectories is shown: every 20th data point of a profile.

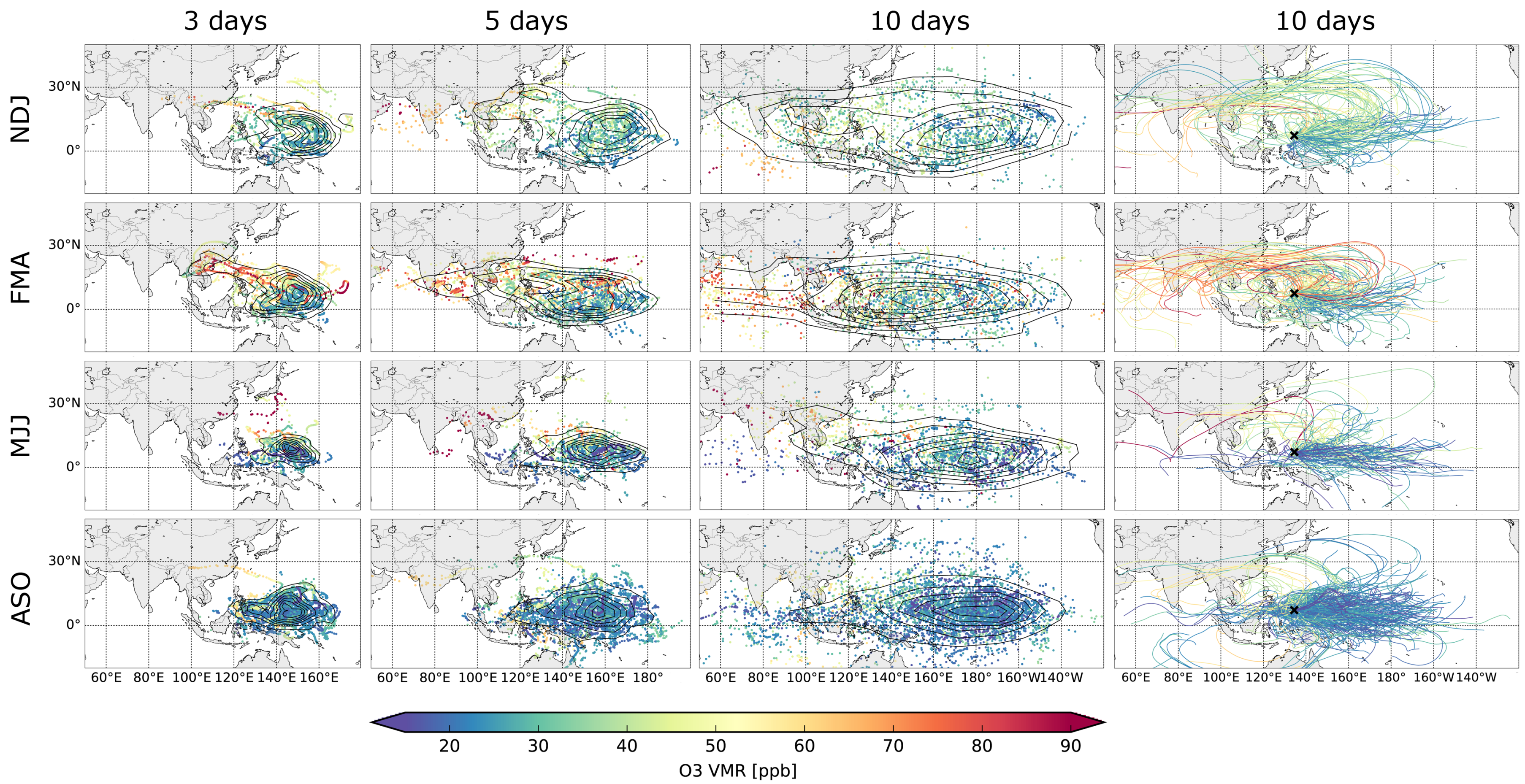

Figure 4.23.: Backward trajectory ending points arriving at 5-10 km geopotential altitudes in Palau by season (in rows) and 3, 5 or 10 days backwards (in first three columns), color-coded by O_3 VMR at arrival (measured by sonde); black contours show the geo-spatial probability density function (PDF) approximated by a KDE (compare Sec.3.4.1), for number of trajectories/profiles, see Table 4.1; right column: matching 10-days backward trajectories, same color-coding, compare Fig. 4.22 and A.10.

One goal of this study is to examine the connection between source region and O_3 VMR measured at arrival in Palau. Figure 4.23 shows the 3, 5 and 10 days trajectory ending points color-coded by O_3 VMR for the 5-10 km altitude range (for other altitudes, see Fig.A.10). The geo-spatial probability density function (PDF) of data points is approximated by a Kernel Density Estimation (KDE, see 3.4.1) and highlighted as black contour lines in Figure 4.23. The KDE contours provide a visual aid to capture the spread of trajectory ending points and the spatial extent of source regions. The columns in Figure 4.23 once more refer to the intermediate time periods already presented as line-segments in Figure 4.22 (3, 5, 10 days). Over the course of 10 days backwards, the spatial coverage of the trajectories naturally broadens. All distributions are centered east of Palau at all times and low O_3 values are dominant here. Comparison between the seasons reveals expected differences in conjunction with observed O_3 VMR variability:

- For ASO and MJJ the center of the distribution moves further east backwards in time (approx. 30° in longitude). In FMA, the primary maximum stays close to Palau (15° East). 5 days before arrival, a stretching or even splitting of this center in latitudinal direction emerges with the dominant maximum and corresponding lower O_3 VMR ($\lesssim$ 30 ppb, blue to green colors) further south. The northern FMA maximum is characterized by high O_3 VMR ($\gtrsim$ 70 ppb, orange to red colors). These two almost separate centers of most frequent occurrence of ending points correspond with the two dominating pathways during FMA: the East wind, Pacific route and the anticyclonic, continental/Asian route approaching Palau from north east. Enhanced O_3 VMR are mostly limited to latitudes north of Palau and the anticyclonic, northern route.

- The summer seasons (MJJ, ASO) retain unimodal distributions in time, i.e. the majority of trajectories always ends east of Palau in the Pacific, mainly in a narrow zonal band centered on Palau's latitude and show low O_3 VMR ($<$ 30 ppb in ASO). Observations of enhanced O_3 are predominantly found outside the main cluster. For FMA and NDJ, secondary centers reaching into Asia appear 5 days before measurement (east of China and reaching into South East Asia in NDJ, stretching over South East Asia into the Indian Ocean in FMA). Especially during FMA, these are characterized by air masses with exclusively high O_3 content.

- The latitudinal extent of the distributions 5 days backwards is greater in FMA and NDJ. Another 5 days earlier, the spatial coverage is greater in both latitude and longitude. This larger "catchment area" in winter has already been evident in Figure 4.22. The occurrence of 10 days trajectory ending points in the more northern parts of the West Pacific is most frequent within the NDJ season (in terms of the extent of the KDE distribution), but also possible during ASO with comparable absolute counts. This seasonal feature conforms with the seasonal movement of the position of the subtropical ridge as discussed above.

The comparison of O_3 VMR between the seasonal 10 days trajectories (right column in Fig.4.23) underlines the connection between longer-range transport and enhanced O_3 on the one hand (non-local control, NDJ and FMA) and low O_3 air masses with Pacific origin on the other (MJJ and ASO). The most frequent occurrence of ending points, i.e. the center of the KDE distribution (5 days backwards, second column in Fig.4.23), coincides with low O_3 VMR in most seasons (not clear in NDJ) and therefore can be associated with the clean background state (O_3∘RH∘, compare Fig.4.20). The close proximity of this maximum to Palau supports the general dominance of local control.

With this overview of trajectories at different points in time before measurement in mind, the time parameter is kept at 5 days backwards in the following analysis. Since we treat O_3 as a passive tracer and did not implement chemical reactions during transport calculations (compare Sect.3.4.1), we cannot make conclusion about production or loss of O_3 along the path from origin to Palau, but assume minor variations in O_3 content during a maximum of 10 days of transport. From a chemical point of view, this assumption will be more robust on a shorter timescale and for dry and mid- to upper tropospheric air masses because of the increasing photo-chemical lifetime of O_3 from the boundary layer to the TTL (compare Sect.2.2.1 and Thompson et al., 1997). Convective mixing alters chemical lifetimes significantly and the chances of an air mass to encounter a convective cell increase further back in time. Very shortly before arrival the information of the spatial range of air mass transport needed to separate between non-local and local control of air composition in Palau, is not yet showing at all. Thus, the choice of 5 days backwards seems reasonable (compare e.g. Browell, 2003; Tao et al., 2018).

Vertical Displacement, RH and PV

After establishing a picture of the seasonality of air mass origin, we examine the vertical displacement of air masses and underlying processes. We neglect variations along the path for simplicity and distinguish between uplifted and subsided air masses upon arrival in Palau using the differences between pressure altitude of start and ending point. Our initial assumption of RH as a tracer for vertical displacement (see Sect.4.3.1) seems justified by our results and visual comparison of the trajectory ending points either color-coded by RH or altitude difference, which are shown side by side in Figure 4.24. Rows show different seasons and we limit the analysis to the 5-10 km range (see Appendix for other altitude levels in Fig.A.8, A.9). With exceptions, air masses that subsided on their way to Palau (red colors, Fig.4.24, first column) are also low in RH (pink colors, same Fig., central column) and most ascended air masses are moist (blue and cyan colors, respectively).

The most striking seasonal difference in Figure 4.24 is the spatial separation of uplifted and subsided air masses upon arrival in Palau in the winter seasons. Especially in FMA, descending trajectories originate mainly in latitudes north of Palau, while the origin of ascending air masses from lower altitudes is almost exclusively south and east of Palau (first column, Fig.4.24). MJJ and ASO exhibit a more mixed distribution in terms of ascending and descending air masses. Generally, during the summer months data points with large negative differences in pressure altitudes (darker red colors) are less frequent, i.e. subsiding air masses originate mostly at altitude levels close to the arrival level. Convective uplift, and correspondingly, humid well-mixed air masses (blue to cyan colors, central column, Fig.4.24) are dominant. During winter, the range of the vertical displacement is largest with both strong uplift (deep blue color) and strong subsidence (deep red color) present. We will not further elaborate on the TTL in this study, but want to point out in this context, that strongest uplift (i.e. largest difference in altitude from start to ending point of the trajectory) throughout the free troposphere occurs in the 10-14 km altitude range including the level of main deep convective outflow (see Fig.A.9, compare Sect.2.1.4). This is consistent for all seasons and in accordance with a year-round deep convective activity (see Sect.2.1.3).

While the connection between uplift and humid air can be explained by convection (see Sect.2.1.3), the observed correlation between the dryness of air masses and their descent in altitude from origin to arrival in Palau can have two different causes: either resulting from dehydration along the path of originally more humid air masses or related to a dry stratospheric origin (compare Sect.4.3.1). To separate between different pathways, we again examine the source regions. North of Palau and during winter seasons source regions correspond to sonde observations of predominantly dry air masses (RH $\lesssim$ 30%, purple to pink colors, central column, Fig.4.24). The according area extends from the western edge of the Indian Ocean until the Philippines, in a narrow band over India, but reaching further north along the east coast of China. The according trajectories are associated with higher O_3 VMR observations and are thus the main source region of O_3+RH- air masses (see Sect.4.2.4). The two possible causes for low RH are connected to those for enhanced O_3: dehydration in the stratosphere or during transport of polluted air masses originally lifted from the ground. As most trajectories remain within the tropics or travel along the edge, the subtropical ridge, a reasonable explanation for dehydration is large-scale descent associated with the Hadley circulation (Dessler and Minschwaner, 2007, compare Anderson et al., 2016). Within the scope of this study, we additionally assess the stratospheric pathway by looking at the potential vorticity (PV) of air masses along the path (compare Sect.3.4.1).

Following previous studies (e.g. Waugh and Polvani, 2000), we assume that the absolute value of PV of air masses, which have crossed the extra-tropical tropopause on their way to Palau and experienced significant in-mixing of stratospheric air, will be greater than 2 PVU for an extended time period of at least one day (compare Sect.3.4.1). The right column in Figure 4.24 shows 5-days backwards time series of PV for all trajectories of the corresponding season (in rows). Only one single trajectory in MJJ crosses the 2 PVU threshold towards the end of the 5 days (green line) and four trajectories in NDJ only briefly show values close to the threshold. 10 days prior to the sonde measurement (not shown here), there is still just a limited number of trajectories with PV greater 2 PVU, including seven staying above the threshold for more than one day during transit (2 in ASO, 5 in NDJ). An even stricter threshold of 1.5 PV as demanded by some studies (Hayashi et al., 2008; Kunz et al., 2011; Postel and Hitchman, 1999) is still only crossed by singular trajectories 4 days backwards (in NDJ, FMA, MJJ, see black horizontal line in Fig.4.24). During 10 days backwards, this stricter criterion is reached more often, especially during FMA and NDJ, but the number of trajectories is still roughly under 1% of all calculated data. In conclusion, this climatological overview of the 4-year Palau time series does not suggest the extra-tropical stratosphere as a major source region of TWP air. According to our analysis, O_3+RH- air masses measured in Palau are of tropical tropospheric origin.

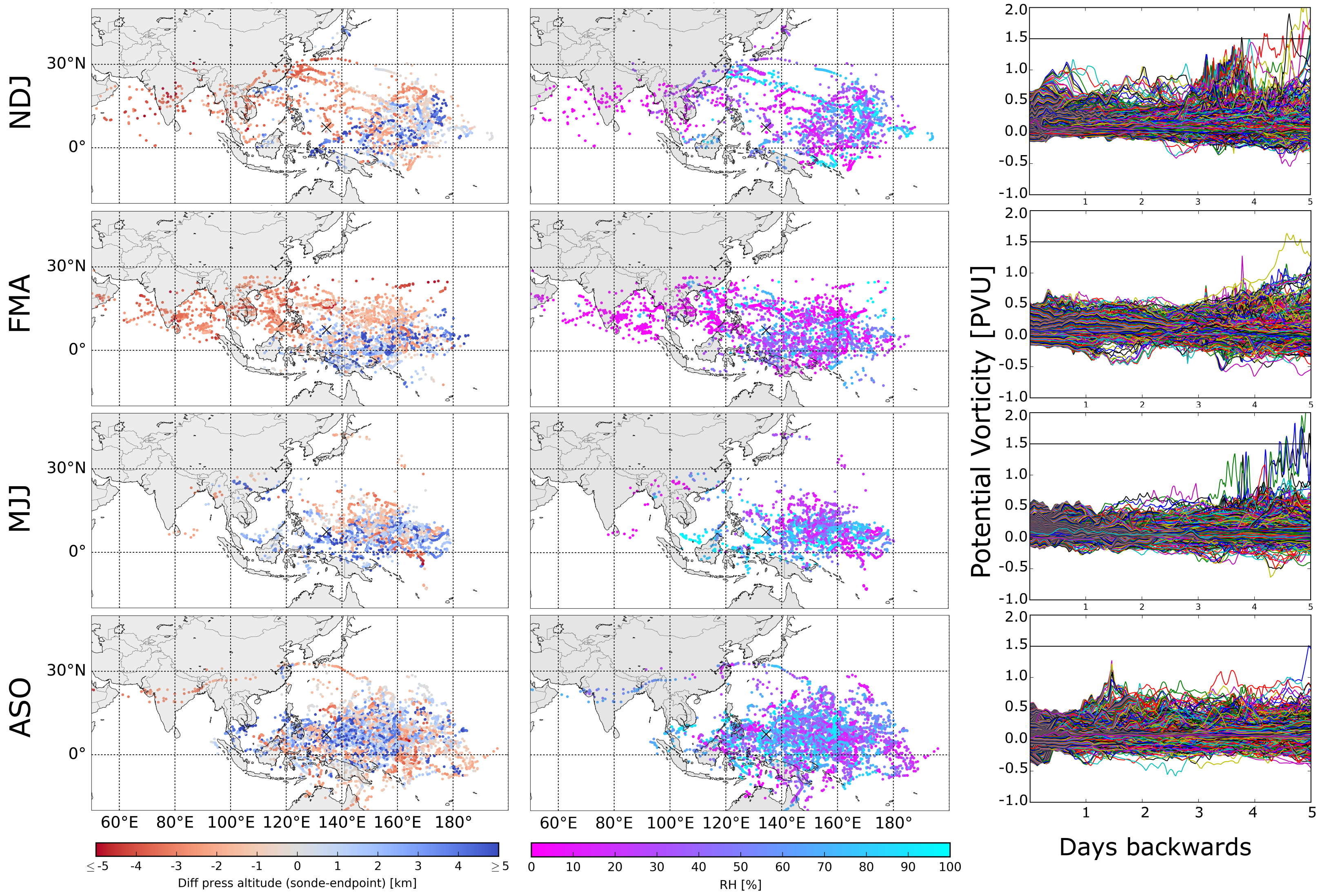

Figure 4.24.: 5-days backward trajectory ending points arriving at 5-10 km in Palau by season (rows), color-coded either by difference in pressure altitude (left column) or RH (middle column); right column shows the corresponding time series for PV of all seasonal trajectories, 1.5 PVU highlighted as a black line; see Tab.4.1 for number of trajectories.

Background Atmosphere and Deviating Layers

For a confined deviating layer of anomalous O_3/RH content within an individual profile (vertical extent greater 1 km), we would expect a definite attribution to a specific source by back trajectory analysis (compare e.g. Hayashi et al., 2008). Looking into the O_3RH air mass categories "in bulk" leads to more overlap of source regions. However, the consideration of anomalies instead of absolute values, to a certain extent compensates for the neglect of the characteristic individual structure of filaments (see also Sect.4.3.3). Anomalies imply the departure from local conditions and can therefore be seen as a measure of local influence on air composition.

The seasonality of the different O_3/RH air masses was already summarized in a heatmap in Figure 4.20 (Sect.4.2.3). We now sort trajectory ending points of our Palau data set (5 days backwards, 5-10 km altitude range) by O_3RH group. Rows in Figure 4.25 show results for the background, O_3○RH○ , and the two relevant opposite groups, O_3-RH+ and O_3+RH-, with respect to seasonality (central column) and vertical displacement of air masses (right column, for orientation, see pictograms in left column with air mass color-coding according to Fig.4.21).

Throughout the seasons, the distinction into different O_3/RH air masses in the 5-10 km altitude range supports our hypothesis that the background atmosphere (O_3○RH○) is comprised of mostly uplifted, local low O_3 air masses. The center of the distribution of ending points is located east of Palau in the Pacific (approx. 20°, see Fig.4.25, central row) with a unimodal spatial PDF for all seasons (found by the KDE based PDF analysis, shown in Fig. A.12). This is still conform with the background definition and the Pacific origin of air masses amplifying the local low O_3 background (compare Sect.4.2.1). Dry ozone-rich air (O_3+RH-) is predominantly of non-local origin and most frequent during FMA and NDJ (see Fig.4.25, bottom row). During the ASO season, the smaller number of ending points for O_3+RH- air masses (total number of 490 data points in 15 profiles) is clustered in three main areas, which geographically suggest different sources of tropospheric O_3 production (compare Fig. A.12): 1. north east of Palau in the West Pacific, 2. between Borneo/Kalimantan and the Southern Philippines and 3. in the New Guinea region, extending towards Northern Australia. The first center can be related to the anticyclonic pathway from Asia dominating in FMA and thus possibly anthropogenic O_3 production. The other two source regions point towards a biomass burning origin (compare e.g. Anderson et al., 2016; Oltmans et al., 2001).

4.3.3. Discussion

In summary, the back-trajectory analysis supports our transport hypothesis: in 5-10 km altitude range O_3+RH- air originates north west of Palau and the ozone-poor O_3○RH○ background consists of local or Pacific air. Ascended air masses upon arrival in Palau are humid and thus consistent with convective uplift. Modeled descent towards Palau correlates with low RH observations. Our PV analysis gives no evidence for a stratospheric

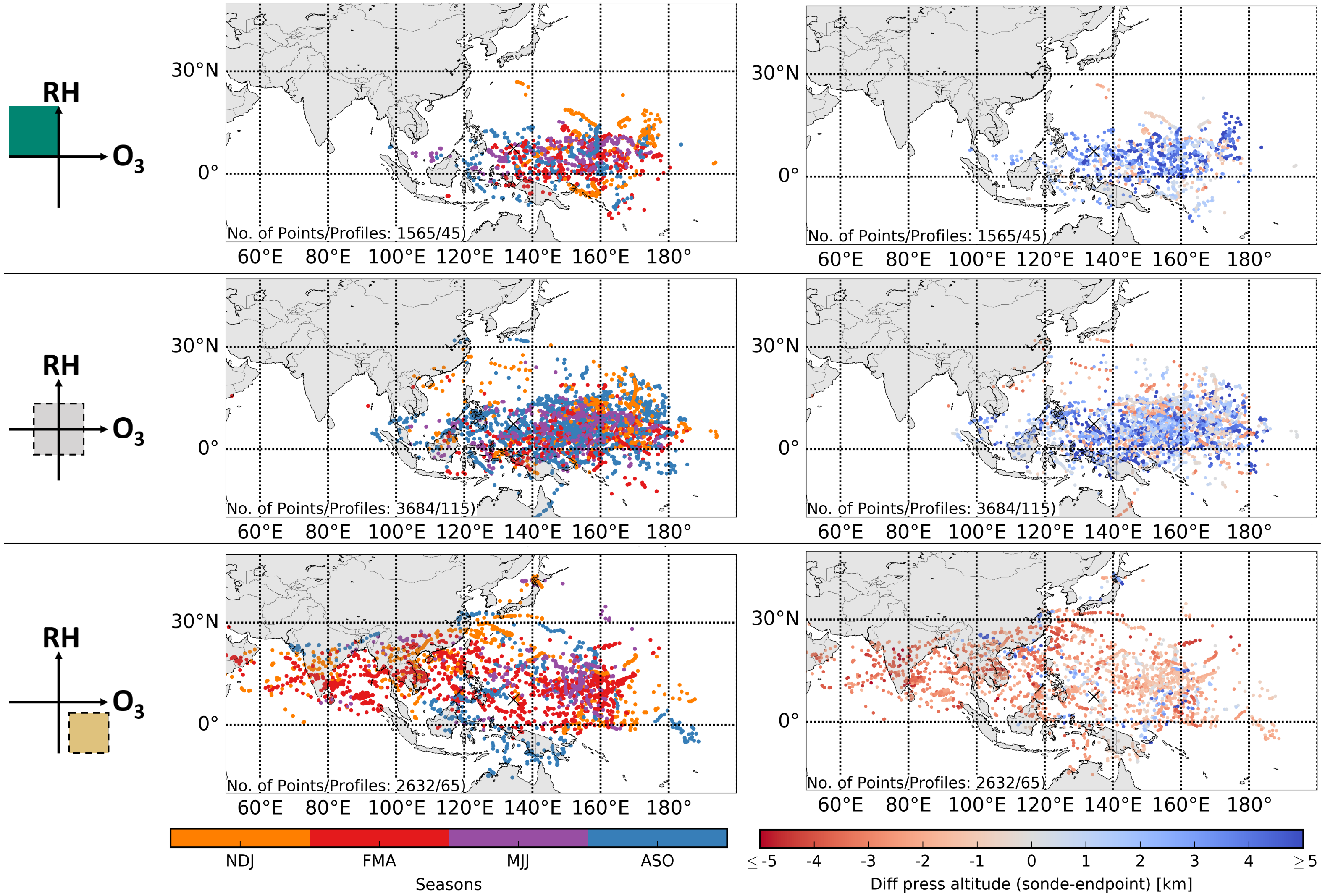

Figure 4.25.: 5-days backward trajectory ending points at 5-10 km, color-coded by season (central column) and difference in pressure altitude (right column) for air masses of different O$_3$RH groups: O$_3$-RH+ (2 times 2 scheme, top row), O$_3$∘RH∘ (3 times 3 scheme, central row) and O$_3$+RH- (3 times 3 scheme, bottom row); left column shows pictograms of groups (compare Fig.4.18c and Fig.4.21), compare Fig.A.11.

origin of air masses. We suggest clear-sky radiative cooling and large-scale subsidence as mechanism for dehydration of air parcels during transport to the TWP, which is consistent with the results in Anderson et al. (2016) for the CONTRAST campaign.

Tao et al. (2018) conducted a quantitative study of the origin of O_3+RH- layers for the same campaign using an artificial stratospheric tracer in the Lagrangian transport model CLaMS. They found a stratospheric influence in 60% of O_3+RH- air masses due to in-mixing during isentropic transport and point out the limitations of calculating pure Lagrangian trajectories without chemical transport. According to our analysis, the anticyclonic route identified for O_3+RH- air masses reaching Palau is indeed a pathway along the subtropical ridge, i.e. in close proximity of mid-latitude UTLS air masses. But a lack of high PV air masses and the clustering of the trajectory ending points near centers of pollution sources on the ground are strong evidence for the tropical tropospheric origin. Other supporting arguments are the seasonality of O_3+RH- layers coinciding with the annual low in convective activity and the confinement of higher O_3 VMR observations to origins north of the ITCZ as also shown by Browell et al. (2001). More clarification in this controversial debate (Sect.4.2.4) could be achieved by an improved method of layer detection, e.g. a combination of individual tracking of confined filament structures and the overall "in bulk" climatology (see Sect.4.2.5). An analysis of additional tracers, e.g. aerosols (see Kremser et al., 2016) from coinciding measurements of the ComCAL system at the Palau Observatory, is planned in future studies.

Why did we choose anomalies from a background over actual measured values for the air mass classification? We tested a similar 3 times 3 scheme using the original O_3 and RH measurements (compare Sect.4.2.3). The boundaries are indicated in Figure 4.18a and based on the 2D histogram, with the central grid cell including air masses with 15-27.5 ppb for O_3 VMR and RH of 32-56 %. Figure A.11 shows the resulting selection of data points according to different groups in analogy to Figure 4.25. Results for the O_3+RH- group are similar to the classification relative to the tracer backgrounds. For the background case, $O_3\circ$RH$\circ$, the extent of the source region is even more concise and limited to the Pacific area, but it apparently does not separate different underlying processes as well, as the amount of descending or ascending air masses is approximately even. Also, the choice of boundary values is rather arbitrary. The bimodality in the RH anomalies in turn, seems a more reasonable criterion for a separation of air masses (compare 4.2.2).

Further validation of the air mass classification will be done by refining the trajectory calculations for an improved representation of convection by coupling of the ATLAS trajectory scheme with a statistical convective scheme (Wohltmann et al., 2019). This will allow a physically more sound definition for the origin of an air masses, namely the point of last detrainment of an air parcel as the final determination of its chemical imprint instead of the 5 days backward criterion.

4.4. Oxidizing Capacity

The lack of tropospheric O_3 observations in the TWP increases uncertainties in atmospheric model simulations. Even fewer in situ observations of the short-lived OH radical due its lifetime, low mixing ratio (< 1 ppt) and the limitations of modern measurement technology make estimations of this important atmospheric constituent mostly dependent on chemical model simulations (e.g. Nicely et al., 2016). Several studies highlight the close coupling of O_3 and OH in the clean ozone-poor air of the TWP (e.g. Gao et al., 2014; Kley et al., 1996; Rex et al., 2014). Rex et al. (2014) in particular remark that the unrealistic absence of a subsequent OH minimum in model results is due to an overestimation of O_3. The Palau measurements are therefore a very valuable observational constraint for future model studies assessing the oxidizing capacity of the TWP. Resulting consequences for chemical lifetimes and possible enhanced transport to the stratosphere are of great relevance on a global scale (see Sect.2.1.4 and 2.2.3).

With O_3 and H_2O as the major sources of OH (see Sect.2.2.2), an assessment of the tropospheric oxidizing capacity above Palau using our sounding observations is possible by constraining a simple chemical box model (compare Bloss et al., 2005; Bozem et al., 2017; Rohrer and Berresheim, 2006). In this thesis, we present results from a first analysis focusing on atmospheric background conditions and dry enhanced O_3 air (O_3+RH-) using the AWIP chemical box model (see Sect.3.4.2).

4.4.1. Chemical Box Model Constraints

The current debate on the possibly lowest oxidizing capacity of the TWP as a whole region or in a global context (e.g. Nicely et al., 2016; Rex et al., 2014) is difficult to solve within the scope of this study. Motivated by the relevance of the deviating layers disturbing the clean O_3 background (see Sect.4.3.2 and 4.2.4), the Palau time series enables first calculations of the local OH background and its seasonality in box model case studies. Due to the dominant occurrence of O_3+RH- layers during FMA, their influence on the oxidizing capacity is revealed in the seasonal mean. The resulting impact on chemical lifetimes and thus stratospheric input needs to be tackled in a follow-up study.

The relation between OH, O_3 and H_2O and their sensitivity to different NO_x and CO concentrations is examined in the mid-troposphere at 400 hPa, the center of the characteristic 5-10 km altitude range (see Sect.2.1.3, 4.3.2). The model is most robust within the clean tropospheric air above Palau, i.e. a clear-sky scenario and no significant amount of organic compounds present. We further constrain our simulations with fixed CH_4 (1.8 ppm) and seasonally variable SZA and CH_2O (from GEOS-Chem, see Sect.3.4.2 for further details). The mean temperature at 400 hPa is almost constant throughout the year at 259 ± 0.5 K, based on soundings.

4.4.2. Chemical Box Model Results

First, we compare the impact of different seasonal mean O_3/H_2O VMR combinations at 400 hPa derived from Palau observations on OH. The comparison is done as a sensitivity test for typical ranges of NO_x (1-50 ppt) and CO VMR (50-70 ppb) for the TWP region (e.g. Crawford et al., 1997; Nicely et al., 2016; Singh et al., 1996) (see Fig.4.26 and Tab.4.2). As previously shown, the Palau seasonal O_3 means are representative for the background atmosphere (ASO and MJJ) and a dominance of dry enhanced O_3 layers (FMA and NDJ) respectively (see e.g. Sect.4.1.1). Additionally, using the Palau measurement database, we generated two less common but realistic very low O_3 cases to assess extreme background conditions: the absolute minimum (ASO min) and the fifth percentile (ASO 5 %) of all O_3 measurements at 400±10 hPa paired with the median H_2O of the respective ten nearest measurements (see Fig.4.26 and Tab.4.2). Figure 4.26 gives an overview of the cases and box model results for daily mean OH and their sensitivity on NO_x and CO variations in relation to O_3.

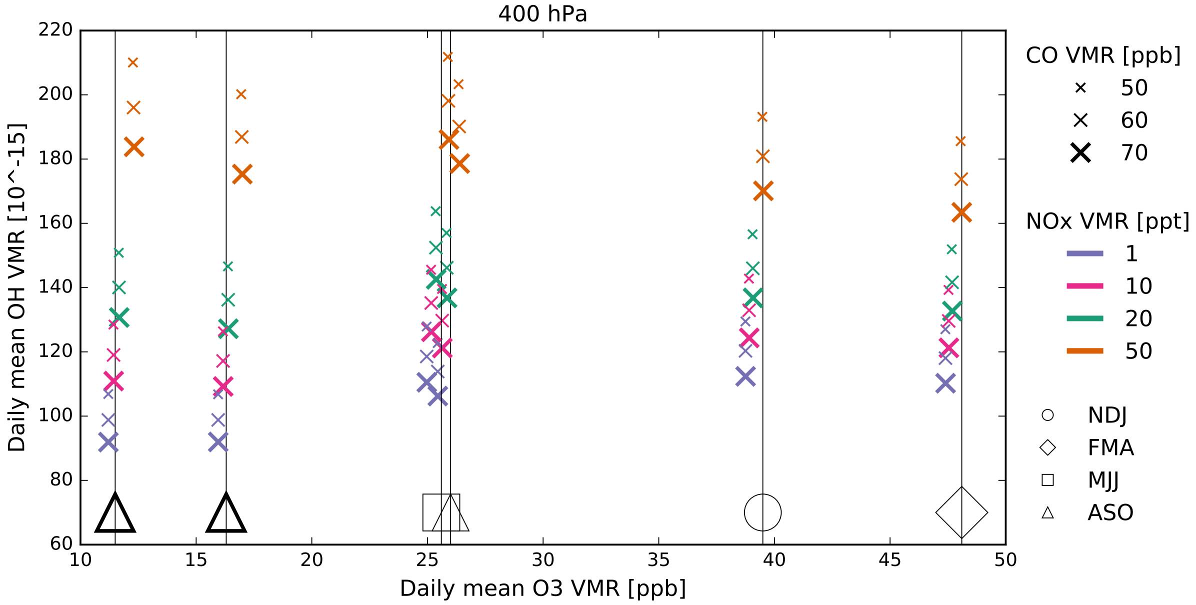

Figure 4.26.: Box modeled daily mean OH VMR in relation to daily mean O_3 VMR for varying NO_x (in colors) and CO VMR (by size and thickness of data points as crosses): overview of selected seasonal (thin circle, diamond, square, triangle) and low O_3 ASO (thick edged triangles) cases; vertical lines mark the model input O_3 VMR with markers at the bottom indicating the season; total number of simulations: 84; compare Table 4.2.

Dependency on CO

The reaction chain initiated by the oxidation of CO (reaction 2.1) can only preserve OH in the presence of O_3 and NO (reactions 2.6, 2.12 and 2.17). With low VMR for both these chemical species, the recycling rate from HO_2 back to OH is too slow and OH is essentially lost, i.e. CO acts as a significant sink for OH in our simulations. The negative linear correlation of OH and CO leads to variations of 20 ppb in CO corresponding to our input range causing linear variations of $15\text{-}25\cdot10^{-15}$ for OH VMR. Keeping this dependency in mind, we only show calculations for 60 ppb of CO in the following. The threshold value for CO for which the above OH/CO relation is not valid anymore has not been assessed.

O_3 Dependency on NO_x

NO_x is correlated with both O_3 and OH and we start by examining its relation with O_3. NO is the crucial factor for daily net O_3 production in the free troposphere (compare equation 2.11, reaction 2.6 and section 2.2.2). This is captured well in our box model simulations, where for a given initial O_3 input the variation of NO_x inputs causes fluctuations in daily mean O_3. In Figure 4.26 these are visible as the displacement of data points representing the daily mean O_3 VMR of different model runs from the vertical black line indicating initial input O_3 VMR. We can estimate the NO_x threshold value between daily O_3 net production or loss to around 20 ppt for the background cases, which is in accordance with typical NO threshold values (compare e.g. Bozem et al., 2017; Graedel et al., 1994). In these cases, the highest NO_x input in our model (50 ppt) yields a net production. For elevated O_3 cases (NDJ and FMA) daily net production has not set in yet at 50 ppt NO_x. The expected daily net destruction of O_3 in the marine NO_x-poor mid-troposphere is evident for the background cases and independent of CO in our given range.

The direct effect of different NO_x on daily mean OH is also clearly shown in Figure 4.26. Besides the HO_x self-reactions (2.22, 2.23), NO_2 is the primary sink of OH via reaction 2.21. Thus, the evident direct correlation between NO, NO_2 and OH throughout the seasons is not surprising.

Dependency on O_3/H_2O

As we know, the primary source of OH is the photolysis of O_3 in the presence of H_2O (reactions 2.15, 2.18). To better understand the effect of different combinations of O_3 and H_2O concentrations on OH, we choose another form of visualization for our box model results. Now performing box model runs for a greater range of theoretical O_3/H_2O combinations, we vary NO_x while keeping CO fixed at 60 ppb. A total number of 176 simulations allows us further statistical assessment. Figure 4.27 shows the above described cases (seasonal means and ASO minima) in large markers in the O_3/H_2O space superimposed on a filled contour plot, colored by daily mean OH for ASO conditions at 400 hPa; each subfigure represents a different NO_x scenario. The seasonal mean cases aside, we limit our simulations of the broad O_3/H_2O space (small triangles in Fig. 4.27) to the background season ASO for this study, with according SZA and CH_2O.

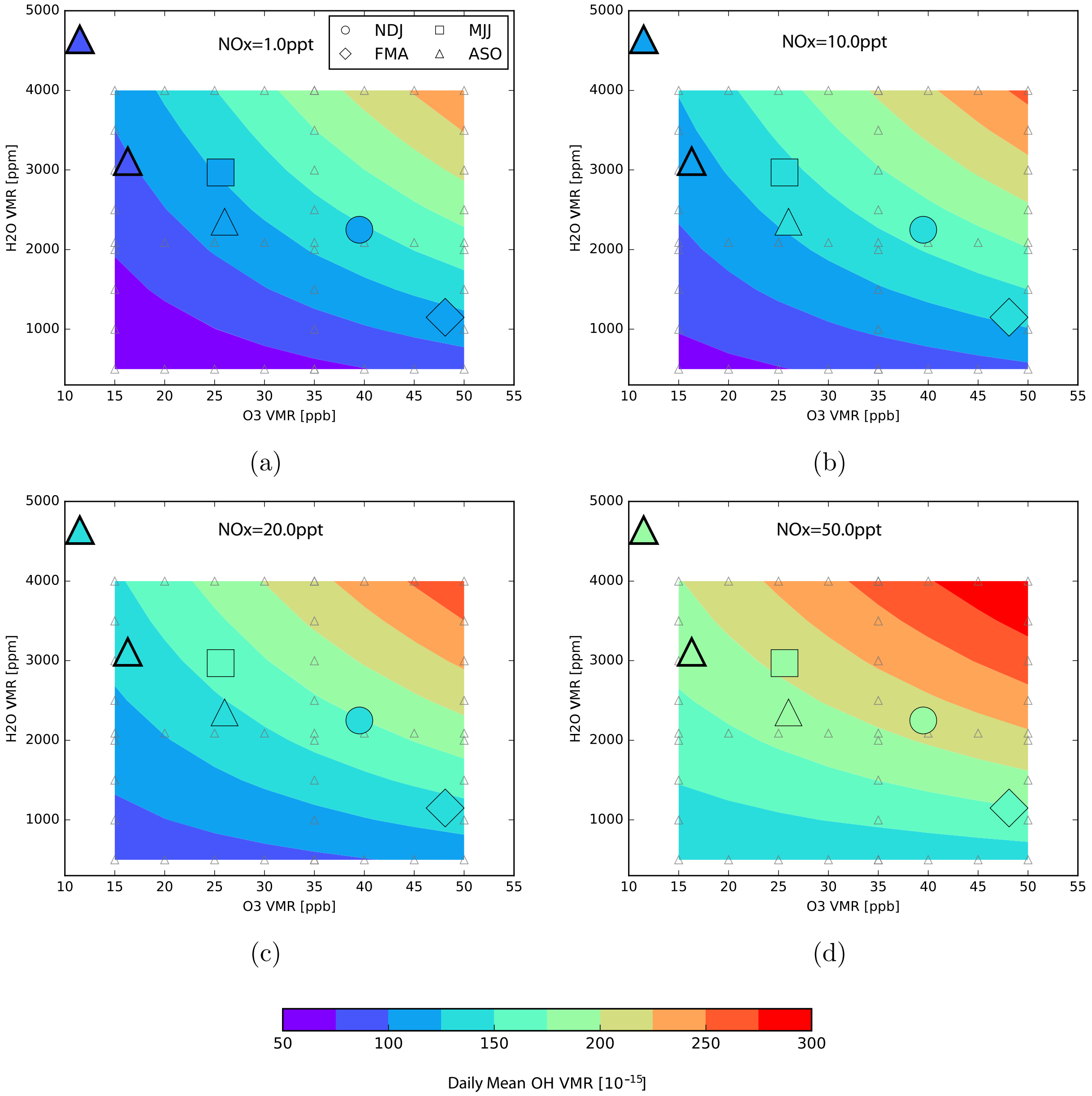

(a)

(b)

(c)

(d)

Figure 4.27.: Box modeled daily mean OH VMR at 400 hPa for varying O_3 and H_2O VMR, with fixed NO_x (1 ppt (a), 10 ppt (b), 20 ppt (c), 50 ppt (d)) and CO VMR (60 ppb) in clear-sky conditions; filled contours are interpolated from box modeled OH VMR for ASO conditions at locations of the small triangles (44 simulations per subfigure, central ranges of triangles are related to annual mean values: 2090 ppm for H_2O and 35 ppb for O_3 VMR); marker style refers to the different seasons; large markers indicate OH calculated for seasonal mean O_3/H_2O combinations and two low O_3 cases (compare Fig. 4.26 and Tab. 4.2).

As expected, daily NO VMR are negatively correlated well with O_3 VMR initial values (r^2_{adj}=0.79, comparable with results of Gao et al., 2014). Daily mean VMR for OH and NO also show a negative correlation, but not very strong (r_{OH-NO}=-0.84, r^2_{adj}=0.49). Thus, the subfigures of Figure 4.27 show different ranges of OH. The previous Figure (4.26) revealed a greater range of OH values for our lower O_3 cases, suggesting a higher sensitivity in regard to NO_x (e.g. 90-210$\cdot10^{-15}$ OH for 11.5 ppb O_3 compared to 110-185$\cdot10^{-15}$ OH for 48.1 ppb O_3, see also Tab.4.2). In the O_3/H_2O plane we now see a greater variation of OH for higher O_3 with variable H_2O. Pairwise correlations are stronger between OH and H_2O in the ASO O_3/H_2O space compared to OH and O_3, attesting to the greater role of H_2O in controlling the oxidizing capacity ($r^2_{OH-H_2O}$=0.65 compared to $r^2_{OH-O_3}$=0.29). Indeed, for low water vapor conditions, a correlation with O_3 almost vanishes, especially in a high NO_x environment (see Fig.4.27d).

The most important conclusion from our results is, that an anti-correlation of O_3 and H_2O VMR, which is an intrinsic trait of the seasonal mean O_3/H_2O combinations, essentially buffers the effects of variations in both atmospheric constituents on the OH budget. Thus, for a given NO_x VMR, all seasonal mean cases have approximately the same OH VMR at 400 hPa (e.g. 145 $\cdot10^{-15}$ for 20 ppt NO_x, see Tab.4.2). While direct correlations of OH with all other chemical input parameters are not significant, possibly due to cancellation effects of correlations between OH sources and sinks (compare e.g. Rohrer and Berresheim, 2006), the correlation of OH with O_3 and H_2O together is very strong (R^2_{adj}=0.94, for ASO conditions, all 176 simulations, see Tab.4.2). When considering only simulations for the seasonal mean and minimal O_3 cases, this correlation remains solid (R^2_{adj}=0.81, 84 simulations, all NO_x and CO scenarios included). That means, theoretically, our combined O_3 and H_2O measurements alone can explain more than 80 % of the daily mean OH variance (compare Sect. 3.4.2).

	O_3 [ppb]	H_2O [ppm]		daily mean OH [10^{-15}]			
case			NO_x [ppt]	1	10	20	50
NDJ	39.5	2250		120	133	146	181
FMA	48.1	1150		118	130	142	174
MJJ	25.6	2970		119	135	152	198
ASO	26	2350		113	130	146	190
ASO 5%	16.3	3110		99	117	136	187
ASO min	11.5	4640		99	119	140	196
176 cases (ASO)			daily mean NO				
ASO r_{OH-X}	0.54	0.81	-0.84				
ASO r^2_{adj}	0.29	0.65	0.49				
ASO R^2_{adj}	0.94						

Table 4.2.: Box modeled daily mean OH VMR for different NO_x VMR, CO VMR at 60 ppb and for seasonal mean O_3/H_2O VMR cases and two extra ASO cases for absolute minimum (ASO min) and 5th percentile of O_3 VMR (ASO 5 %) at 400 hPa derived from the Palau data set ; r_{OH-X} is the pairwise Pearson correlation coefficient between OH and O_3, H_2O and daily mean NO respectively; R^2_{adj} is the adjusted multiple correlation coefficient of determination (see Sect. 3.4.2) for the correlation between OH and combined O_3/H_2O in ASO simulations.

OH in Background Air

Our results express the high sensitivity of background air to NO_x variations. The lowest OH VMR (just below $100 \cdot 10^{-15}$), in agreement with GEOS-Chem model results from Rex et al. (2014), are captured by the two wet, ozone-poor cases in an essentially NO_x-free environment (1 ppt NO_x, see thick edged triangles in subfigure 4.27a). Ozone-poor air masses also depleted in water vapor correspond to lowest possible OH, which has been proposed for upper tropospheric air masses by dedicated studies (Gao et al., 2014; Rex et al., 2014).

The seasonal mean OH VMR from seasons other than ASO follow the O_3/H_2O relation described above and are comparable with the ASO O_3/H_2O space. Deviations towards lower OH values, especially in the NDJ season (see e.g. Fig. 4.27d), can be explained by the difference in SZA and its effect on the O_3 photolysis rate in reaction 2.15. In fact, the dependency of OH on SZA is the most robust correlation in the free troposphere (Rohrer and Berresheim, 2006; Wennberg, 2006).

OH in Dry Enhanced Ozone Air

From our back-trajectory analysis we learned that O_3+RH- air masses are related to non-local source regions and most likely pollution events. Thus, we can expect NO_x to be elevated as well in contrast to a presumably NO_x-poor environment in Palau. Recent measurements in the TWP during the CONTRAST campaign in January/February 2014 confirm NO_x levels between 60 and 90 ppt at 7 km altitude for air with O_3 VMR > 40 ppb and RH < 20 % compared to 20-40 ppt NO_x VMR for background conditions (O_3 VMR < 25 ppb, RH > 70 %) (Nicely et al., 2016; Pan et al., 2017). Other previous campaigns in the area reported similar or even lower background NO_x concentrations < 10 ppt (e.g. Crawford et al., 1997; Jaegle et al., 2001).

Within the limitations of our box model, we revisit the dependency of the oxidizing capacity on NO_x in an illustration on the O_3/OH plane in Figure 4.28. For fixed low, mean, and high H_2O regimes during the background season ASO, we find an almost perfect linear relation between O_3 and OH for given NO_x (solid, dashed, dotted lines, standard deviation errors for line parameters < 1 %).

As already shown in Figure 4.27, for low H_2O (500 ppm) and high NO_x (50 ppt) (yellow solid line in 4.28) the OH VMR ($\sim 130 \cdot 10^{-15}$) is almost constant with respect to O_3. For higher H_2O (purple and orange shaded areas) the dependency of OH on O_3 increases. The colored ranges for varying H_2O and NO_x are intercepting for O_3 values < 30 ppb. This implies that variations in water vapor have a smaller impact on OH in background O_3 conditions compared to enhanced O_3 levels. Differentiation in NO_x thus becomes more relevant.

Daily mean OH calculated for the FMA seasonal mean case with elevated NO_x in comparison to ASO background cases with low NO_x are highlighted in Figure 4.28 as well. According to our box model results, the oxidizing capacity is slightly lower for the background atmosphere than for dry enhanced O_3 layers, differing by around 50 ppt of OH VMR. However, this difference can easily decrease to zero with increased dehydration of the air mass. It should be noted that we kept CO levels constant as well. Elevated CO due to pollution would possibly have an additional diminishing effect on the oxidizing capacity.

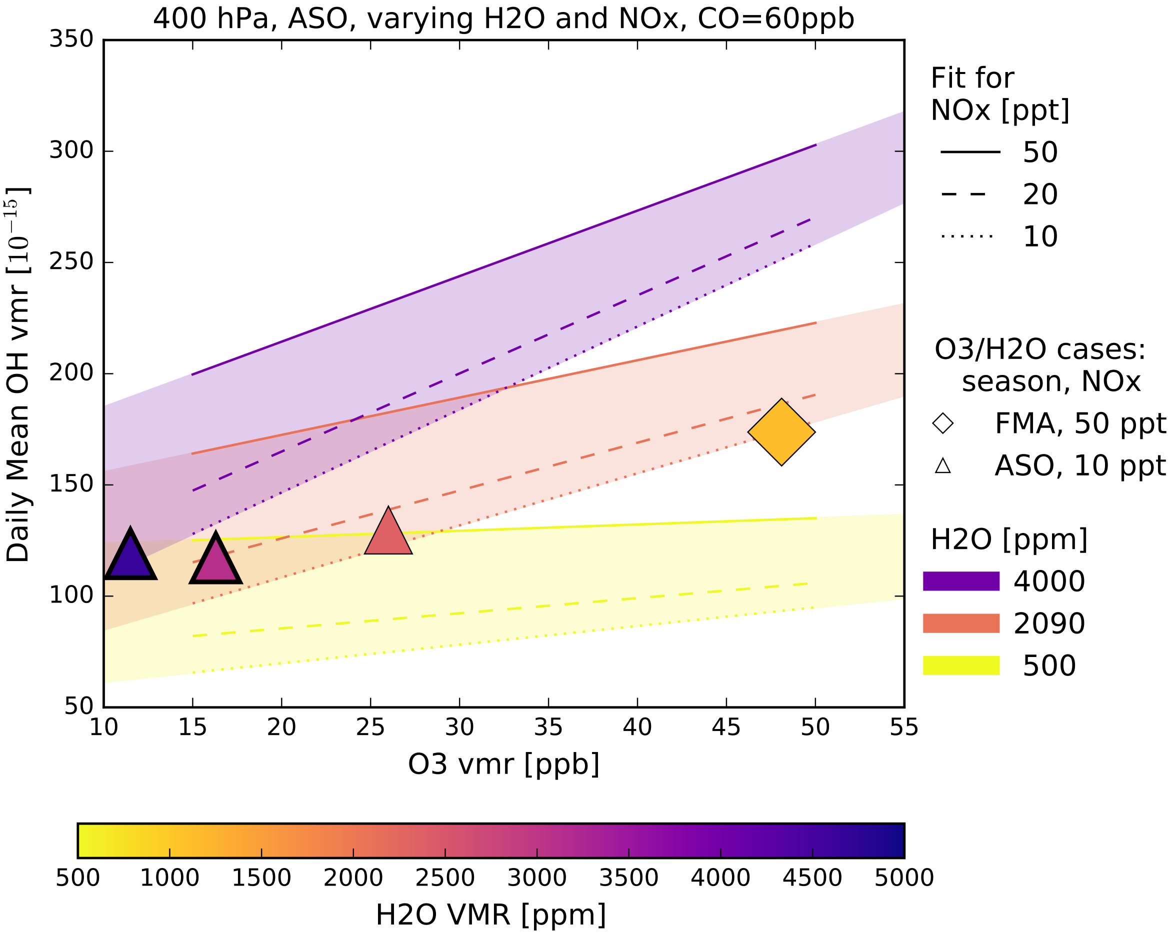

Figure 4.28.: Box modeled daily mean OH VMR in relation to O_3 VMR input for varying H_2O and NO_x, with fixed CO (60 ppb) at 400 hPa in clear-sky conditions in ASO; total number of simulations: 64, 8 per NO_x/H_2O case; lines of constant NO_x (solid, dashed, dotted for 50, 20, 10 ppt) are linear fits (standard deviation errors < 1 %)to data points corresponding to a given H_2O scenario indicated by color (purple, orange, yellow for 4000, 2090, 500 ppm); superimposed large markers are O_3/H_2O cases with different NO_x inputs, also colored by H_2O content, see also Fig.4.27.

4.4.3. Discussion

In this study, we narrowed down our analysis to the mid-tropospheric layer centered around 400 hPa to focus on the background atmosphere and the effect of the strong annual O_3 cycle on OH. The AWIP model captures the expected general tropospheric chemical relations between O_3, OH and NO_x well. Our model setup is most robust for the clean pollution-free atmosphere, representing the dominating background state. Our analysis reveals that in such conditions the anti-correlation of O_3 and H_2O has a buffering effect on OH. This result supports the small interannual variability of global OH levels reported by Montzka et al. (2011) and their conclusion of well buffered OH against perturbations on a global scale (compare also Gao et al., 2014).

The assumed pollution-related origin of O_3+RH- air masses causes elevated NO_x and CO concentrations in contrast to the low NO_x background in the TWP. Enhanced levels of organic compounds, which would normally accompany and survive transport in polluted air masses, are, however, not considered in our box model. Our estimation of the oxidizing capacity of O_3+RH- air masses may therefore be unrealistic for high NO_x scenarios. Putting the caveats of our box model aside, our results suggest a slightly enhanced oxidizing capacity in layers deviating from the wet low O_3 background (ASO compared to FMA seasonal mean).

Using tropospheric box model simulations constrained by observations from the TWP in January-February 2014 (CONTRAST, O_3, H_2O, NO, photolysis rates and several organic chemicals a.o.) Nicely et al. (2016) concluded the opposite, while questioning the existence of a tropospheric OH minimum in the TWP in general. They estimated a daily mean OH VMR of 0.18 ppt for background air (NO_x VMR of 30 ppt) and 0.1 ppt for O_3+RH- air (NO_x VMR of 70 ppt; see above for air mass definitions). However, the study is limited to the season with dominant transport of air masses from possible source regions of pollution (compare Sect.3.4.1). Thus, the CONTRAST measurements are possibly not representative for the local background conditions, and do not undermine our assumptions for the Palau ASO season. A more thorough analysis for the different seasons and layers according to our classification scheme (compare Sect.4.2) and additional sensitivity studies of our box model are needed to clarify the discrepancy with Nicely et al. (2016).

Future analysis similar to ours for the TTL, i.e. the level of minimal O_3 and strong convective outflow, in comparison to previous dedicated studies would be a valuable extension of this analysis with regard to the transport of chemicals into the stratosphere (compare Gao et al., 2014; Hanisco et al., 2001; Jaegle et al., 2001; Nicely et al., 2016). While low O_3 air masses are lifted up to this level (e.g. Folkins, 2002; Kley et al., 1996; Solomon et al., 2005), the H_2O VMR are lower due to the cold temperatures. Neglecting all parameters related with altitude for a moment, our model results would suggest lower OH VMR for dry ozone-poor air, as has been found by e.g. Gao et al. (2014). But our box model represents TTL conditions only insufficiently. OH concentrations in the TTL are no longer proportional to the photolysis rate $J(O(^1D))[O_3]$ alone, but a linear combination of the rates yielding O^1D and CH_2O (e.g. Gao et al., 2014; Hanisco et al., 2001). The greater relevance of formaldehyde and possibly other species due to a more complex chemistry in the TTL would require a more careful choice or database for these species. Also, more reactions would have to be included in the box model to include organic chemistry.

Our chemical box model results provide a relative perspective on OH VMR in the clean versus disturbed state of the mid-troposphere above Palau in clear-sky conditions. The effect of clouds on photolysis rates could yield results differing in magnitudes, but is in general difficult to include in chemical box model simulations. The impact of dry enhanced O_3 layers in a convective atmosphere on the HO_x budget and resulting lifetimes for chemicals, also in comparison to the rest of the tropics and extra-tropics could not be assessed within the scope of this study and remains an open question (see e.g. Nicely et al., 2016).

5. Summary and Outlook

Motivated by previous measurements of very low tropospheric O_3 concentrations in the Tropical West Pacific (TWP) (Kley et al., 1996; Rex et al., 2014) and the resulting low oxidizing capacity of this key region of transport into the stratosphere (Fueglistaler et al., 2004; Krüger et al., 2008; Newell and Gould-Stewart, 1981), we set up an atmospheric research station in the center of the warm pool in Palau (7°N 134°E) and established a continuous balloon-borne O_3 measurement program with Electrochemical Concentration Cell (ECC) ozonesondes.

Due to controversies around near-zero O_3 measurements in the upper troposphere (UT) of the TWP (Newton et al., 2016; Nicely et al., 2016), we carefully followed the Standard Operating Procedures (SOP) as recommended by Smit, 2014. The sensitivity to the so-called background current was tackled with the development of an attachable device to measure this parameter in-flight. Measurements with hence modified ECC sondes in Palau suggest the usage of a pressure-dependent background current correction, while some technical issues with the device remain unsolved. In general, the background currents measured in Palau are sufficiently low (median $< 0.03\ \mu A$) to yield robust results within the full tropospheric column.

A total of 145 successful ECC sondes were carried out and examined in this thesis, launched at the Palau Observatory from 01/2016 until 10/2019, providing for a thorough seasonal characterization of tropospheric O_3. Our analysis of the time series confirms the year-round dominance of a low O_3 background in the mid-troposphere (compare e.g. Pan et al., 2015; Rex et al., 2014; Thompson et al., 2003a) and a strong annual O_3 cycle in the Tropical Tropopause Layer (TTL) in this part of the TWP (compare Folkins et al., 2006; Randel et al., 2007). Layers of enhanced O_3 in the free troposphere (3-14 km) deviating from the background are often anti-correlated with water vapor and occur frequently, as it has been found for the wider region (e.g. Hayashi et al., 2008; Kley et al., 1997; Newell et al., 1999; Oltmans et al., 2001; Pan et al., 2015; Stoller et al., 1999; Thouret et al., 2000). A previously proposed universal bimodal structure of free tropospheric O_3 in the TWP in this context (Pan et al., 2015) could not be verified. Moreover, the occurrence of mid-tropospheric dry ozone-rich air masses (O_3+RH-) shows a strong seasonality in Palau. The seasons FMA (February-March-April) and ASO (August-September-October), shifted by one month compared to the mid-latitude seasons, differ the most, both regarding the frequency of enhanced O_3 intrusions and the seasonal O_3 background values. We quantified their differences by defining a monthly atmospheric background profile for O_3 and relative humidity (RH) based on monthly quantiles and by further analyzing air masses relative to this background. Deviations from the background reveal a bimodal distribution of RH anomalies for all seasons except the MJJ (May-June-July) season. Observations of

O_3+RH- air in the 5-10 km altitude range were made in 71 % of profiles in FMA compared to 25 % in ASO.

Back trajectory calculations confirm that throughout the year the mid-tropospheric background is controlled by local convective processes and the origin of air masses is the Pacific Ocean, mainly east of Palau. Dry and ozone-rich air reaches Palau via an anticyclonic route originating in tropical Asia, in an area stretching from India to the Philippines, supporting the hypothesis of several studies which attribute O_3 enhancement against the low O_3 background to pollution events on the ground such as biomass burning (e.g. Anderson et al., 2016; Folkins et al., 1997; Kondo et al., 2004; Oltmans et al., 2001). Additionally, we could not find a significant stratospheric influence based on a 2 PVU threshold for trajectories up to 10 days backwards in a potential vorticity (PV) analysis. We thus propose large-scale descent within the tropical troposphere and subsequent radiative cooling in connection with the Hadley circulation as responsible for the vertical displacement and dehydration of air masses on their way to Palau (compare Anderson et al., 2016; Cau et al., 2007; Dessler and Minschwaner, 2007).

The relevance of layers deviating from the local background led us to question their influence on the otherwise low oxidizing capacity of the TWP (compare e.g. Gao et al., 2014; Nicely et al., 2016; Rex et al., 2014). Chemical box model calculations constrained by our O_3 and H_2O measurements for clear sky conditions at 400 hPa in Palau in ASO revealed that the predominant anti-correlation of O_3 with H_2O buffers the effect of both constituents on OH (compare Gao et al., 2014; Montzka et al., 2011). Statistically, our combined measurements of O_3 and RH averaged to seasonal mean cases can explain 80 % of the variance in daily mean OH. If we assume a pollution-related origin and thus elevated NO_x concentrations for O_3+RH- air masses in contrast to the low NO_x background in the TWP, we find a slightly lower oxidizing capacity for mean O_3/RH background conditions in ASO than within mean O_3+RH- air masses in FMA. This result is contrary to Nicely et al. (2016), who concluded a significant reduction of the oxidizing capacity in O_3+RH- air from box model simulations constrained with observations from the TWP in January-February 2014 (CONTRAST campaign) and questioned the existence of a tropospheric OH minimum in the TWP in general. Their measurements are however not representative for the background season with lowest O_3 concentrations. Our box model results provide a relative perspective on the clean versus disturbed state of the mid-troposphere above Palau in clear-sky conditions. The impact of dry enhanced O_3 layers in a convective atmosphere on the HO_x budget and resulting lifetimes for chemicals, also in comparison to the rest of the tropics and extra-tropics, remains an open question.

A growing record of ECC ozone soundings as well as measurements by other instrumentation at the Palau Observatory, such as water vapor by CFH sondes, clouds and aerosols with the co-located lidar system ComCAL (Immler et al., 2006) or tropospheric columns of a number of chemical species by FTIR and the MaxDOAS Pandora-2S will complement the results of this thesis and provide sufficient material to answer various new research questions. In particular, interannual and intra-seasonal variations of tropospheric O_3, e.g. related to the ENSO and MJO, will extend the seasonal characterization presented here and further improve our understanding of the processes governing local atmospheric composition. A closer analysis of dynamical and chemical processes in the TTL and the boundary layer will shed more light on this relevant region of STE. The back trajectory analysis performed in this thesis will be extended for the UTLS, including the UT O_3 minimum. We will include a convective scheme in the calculations (Wohltmann et al., 2019) to improve the simulation of convective effects by examining last detrainment events instead of backward time periods. Coinciding measurements of aerosols will help to further distinguish the stratospheric from the tropical boundary layer origin of O_3+RH- air masses, and validate our air mass classification scheme. The identification of layers deviating from the background based on monthly quantiles will be expanded by an algorithm to detect layers in individual profiles. Case studies deploying coincident comprehensive aircraft measurements from the POSIDON campaign (three close-by flights and soundings) and the upcoming ACCLIP initiative by NASA and NCAR in the wider Pacific (2021, see Tab.1.1) will further help to attribute air masses observed in Palau to source regions. A comparison of total O_3 columns and convective signatures in the O_3 profile with ground-based FTIR (as part of the TroStra project, see Tab.1.1) and satellite observations (e.g. OMI/MLS, TROPOMI and Himawari-8) is planned in the near future. Complementary data from these observations could also be deployed to quantify the stratospheric entry of various chemical species in the clean air pool versus its disturbed state, i.e. in the presence of O_3+RH- layers. Furthermore, it is envisioned to put our box model analysis into a wider geographical context by analyzing calculations from the global chemistry transport model TM5 (Huijnen et al., 2010) in cooperation with the Institute of Environmental Physics (IUP) Bremen.

Last but not least, the presence and visibility of the research station in Palau has raised the scientific capacity of the small island nation. An extension of the ongoing outreach program for schools, the local college and policy makers will further strengthen the country's position in international negotiations on climate change mitigation.

Acknowledgements

Many people have supported this PhD project and helped and encouraged me along the way. The establishment of the research station in Palau in the first place, my engineering project and the progress of my scientific analysis of the Palau time series would not have been possible without them. First of all, I am grateful to my supervisor Markus Rex who recruited me in a bar in New Zealand on the side of a SPARC meeting. He gave me the opportunity to pursue this academic endeavor and trusted in my abilities despite my own initial skepticism. The IUP at the University of Bremen, was a perfect partner institution for my PhD project. I want to thank Justus Notholt for our collaboration and his supervision and support and look forward to continue our joint efforts in Palau. My gratitude goes to the whole StratoClim consortium for fruitful meetings and logistical support.

The ”Ozoni”-group at AWI was a fruitful environment for developing my scientific skills. I was very lucky to meet Daniel Kreyling there, who became a best friend and flat mate and who – in between and now for the final thesis – was always available to help, give invaluable comments on code and writing and to deal with the struggles and downsides of a PhD challenge together. Peter von der Gathen jumped in as a very supportive and engaged supervisor in Markus' absence and shared his great experience in ozone research and contacts in the community. Ralph Lehmann's unparalleled knowledge of chemical processes in the atmosphere and his curiosity were very helpful and I am thankful for his support in the chemical modeling part of this thesis. Ingo Wohltmann's expertise in transport modeling and all-round atmospheric physics helped dealing with integral parts of my work and extending my skills.

Discussions with many other colleagues at AWI ensured progress of my thesis and, most essentially, the needed joy at the workplace: in order of proximity to my office: Christoph Ritter, Alexander Schulz, Ralph Jaiser, Markus Kayser, Erik Romanowsky, Raphael Köhler, Berit Crasemann, Heidrun Matthes (special thanks for helping with graphics and maths), Marion Maturilli, Roland Neuber, Sabine Helbig and others.

Without technical and logistical support, the experimental base of this thesis would not exist. I want to thank Hamish Chisholm for introducing me to the ”art” of ozonesonde preparations at Lauder, New Zealand, and all colleagues at NIWA, who entrusted me their instrumentation, setting the grounds for my future in this scientific field. At AWI, I am most indebted to Juergen “Egon” Graeser for his relentless support and endurance, sharing his skills in balloon soundings and other measurements, but also Siggi (”good soul” of our group) Debatin, Holger Deckelmann, Jan Kahl and Leena Viitanen. Without the ”guys” from impres GmbH, neither the Palau station, some of the sounding campaigns,

nor my instrumental development would have happened - and it for sure wouldn't have been so much fun, thanks to: Ingo Beninga, Wilfried Ruhe and Joann Schmid. From IUP, Tine Weinzierl and Winfried Markert were not only the best kayaking partners in Palau, but also creative and dedicated engineers, that I was happy to work and be with.

Jordis Tradowsky from Bodeker Scientific was a great help in the field, performing campaigns in my absence, but also proofreading our proposal and parts of this thesis – and she remains an ally in the jungle of academia outside the Palau business. Jürgen Fischer from FU Berlin, who initiated the joint Pandora activities in Palau, remained curious and supportive of my future research plans.

Within the “ozone research community”, I met many friendly and helpful people. Foremost, I need to thank Herman Smit at FZJ for an open ear and helpful discussions on instrumental issues at any time, as well as the unbureaucratic provision of a UV photometer and invitation to work at his facility. Laura Pan at NCAR was supportive from first contact onward and I'm thankful for her invitation to the ACCLIP consortium and support of my first research proposal. Other notable people I am thankful to are Ru-Shan Gao, Roeland van Malderen, Anne Thompson and Henri Selkirk as well as people at the DWD in Lindenberg: Dirk Ruudsen and Peter Oelsner.

The Palau O_3 time series would not have been an ongoing success without the support of the local community. The honorary consul of Germany in Palau, Thomas Schubert, opened doors for us in many ways: press and public relations, logistics, politics... Personally, I am grateful for his open mind and heart, and his dedicated way. He helped me to extend my research stay into a cultural experience and to continuously learn more about the country and its citizens. Logistical support from CTSI, with Ronnie Giman as a representative, was always friendly and as creative and quick as possible. For scientific support, we could not have found a better partner than CRRF, run by Pat and Lori Colin. They and their team provide high quality technical support for all kinds of instrumentation in our lab container. Most of all, I am thanking Sharon Patris, our main local operator, who launched most of the sondes presented in this thesis and remains an excellent and careful first-contact on site.

In Palau, I also want to thank: our host, the Palau Community College (PCC), with president Patrick Tellei, for welcoming us, providing space for our lab containers and regularly opening their lecture rooms; many friendly and engaged people in the government, e.g. Minister of Education, Sinton Soalabai; our second local operator Gerda Ucharm; Noel Reyes, teacher at Palau High School; Peter Polloi from Palau National Aviation Administration; our handyman Oscar Page; Maura and Greg Gordon from the local Rotary Club; Maria Ngemaes from the Palau Weather Service – and what would I have done without Kramer's (thank you, Rene and crew!)?

In the end, my friends and family probably had to cope with the biggest challenges of my PhD project: my moods in stressful times before deadlines, travels, motivational lows – and they always had my back. Thanks go to my WG (especially Robert Becker and Verena Mohaupt), Matthias Buschmann for enduring (last minute) support from the first day of our studies until the very last day of my PhD (and hopefully beyond), Paul Hezel

for excellent feedback on my writing and general motivational talks, Stefan Bast, Elena Scholl, Verena Nees and the girls, the SKA'm'peace, my Marburg buddies, Stefan and Michi Kruse, Ireen Werner, Cati Kahl, my hoop buddies, and my parents, for helping me develop a free and curious mind.

Finally, but most importantly, I am indebted deeply to the closest persons in my life, Sebastian and Peer Ferenczy, who supported me with great endurance from start to finish of these turbulent PhD times, with Peer born right in the middle of this endeavor. I could not have done it without you. ♡

Funding

This thesis was mostly funded by the European Union under the 7th Framework Program as part of the StratoClim project (`www.stratoclim.org`). The AWI provided for additional funding of 8 months after the end of my EU-funded contract.

Data

Apart from the Palau time series generated as part of this thesis, other sources of data need to be acknowledged:

- SHADOZ archive, accessible via `https://tropo.gsfc.nasa.gov/shadoz/Archive.html`; special thanks go to Anne Thompson and Jacquie Witte.
- NOAA for operating the general weather station in Palau (station code: PTRO 91408); used database: the upper-air sounding database provided by the University of Wyoming (`weather.uwyo.edu/upperair/sounding.html`).
- MLS database, accessible via `https://mls.jpl.nasa.gov/data`, courtesy of the NASA MLS team (Froidevaux et al. (2008)).
- TES database, accessible via `http://tes.jpl.nasa.gov/data/`, courtesy of the NASA TES team (Worden et al. (2007)).
- for ECMWF ERA5 data used in the trajectory analysis, the Copernicus Climate Change Service Climate Data Store (CDS) is used: `https://cds.climate.copernicus.eu/cdsapp#!/home`.

Most calculations in this thesis were performed in Python – thanks go to all developers in the open source community.

Acronyms

ACCLIP	Asian Summer Monsoon Chemical Impact Project.
ASO	August-September-October.
ATLAS	Alfred Wegener InsTitute LAgrangian Chemistry/Transport System.
AWIP	Alfred-Wegener-Institute Potsdam Chemical Box Model.
BD	Brewer-Dobson.
CFH	Cryogen Frostpoint Hygrometer.
CLaMS	Chemical Lagrangian Model of the Stratosphere.
COBALD	Compact Optical Backscatter Aerosol Detector.
ComCAL	Compact Cloud and Aerosol Lidar.
CONTRAST	Convective Transport of Active Species in the Tropics.
CPT	Cold Point Tropopause.
CRRF	Coral Reef Research Foundation.
DJF	December-January-February.
ECC	Electrochemical Concentration Cell.
ECMWF	European Centre for Medium-Range Weather Forecasts.
ENSO	El Niño Southern Oscillation.
EOF	Empirical Orthogonal Function.
ERA	ECMWF re-analysis.
EU	European Union.
FMA	February-March-April.
FTIR	Fourier Transform InfraRed.
FZJ	ForschungsZentrum Jülich.
GAW	Global Atmosphere Watch.
GEOS-Chem	Goddard Earth Observing System global 3-D model of atmospheric chemistry.

GRUAN	Global Climate Observing System Reference Upper-Air Network.
Ib press.dep.	pressure dependent background current correction applied.
ITCZ	InterTropical Convergence Zone.
IUP	Institute of Environmental Physics.
JJA	June-July-August.
JOSIE	Juelich OzoneSonde Intercomparison Experiment.
JPL	Jet Propulsion Laboratory.
KDE	Kernel Density Estimation.
LCP	Lagrangian Cold Point.
LMS	Level of Minimum Stability.
LNB	Level of Neutral Buoyancy.
LRM	Lapse Rate Minimum.
LS	Lower Stratosphere.
LZH	Level of Zero Heating.
MaxDOAS	Multi Axis Differential Optical Absorption Spectroscopy.
MEI	Multivariate ENSO Index.
MJJ	May-June-July.
MJO	Madden-Julian Oscillation.
MLS	Microwave Limb Sounder.
MOZAIC	Measurement of Ozone and Water Vapor by Airbus In-Service Aircraft.
MuLid	Compact elastic polarization two-channel Micro Lidar.
NASA	National Aeronautics and Space Administration.
NCAR	National Center for Atmospheric Research.
NCEP	National Centers for Environmental Prediction.
NDJ	November-December-January.
NH	Northern Hemisphere.
NMHC	Non-Methane HydroCarbons.
NOAA	National Oceanic and Atmospheric Administration.
OLR	Outgoing Longwave Radiation.
OMI	Ozone Monitoring Instrument.

ONI	Oceanic Nino Index.
PAO	Palau Atmospheric Observatory.
PDF	Probability Density Function.
PEM	Pacific Exploratory Missions.
POSIDON	Pacific Oxidants, Sulfur, Ice, Dehydration, and cON-vection.
PV	Potential Vorticity.
QBO	Quasi-Biennial Oscillation.
RF	Radiative Forcing.
RH	Relative Humidity.
RSD	Relative Standard Deviation.
SD	Standard Deviation.
SH	Southern Hemisphere.
SHADOZ	Southern Hemispheric ADditional OZonesondes.
SN	Serial Number.
SOI	Southern Oscillation Index.
SOP	Standard Operating Procedures.
SPC	Science Pump Corporation.
SPCZ	South Pacific Convergence Zone.
SST	Sea Surface Temperatures.
STE	Stratosphere-Troposphere Exchange.
StratoClim	Stratospheric and upper tropospheric processes for better Climate predictions.
SZA	Solar Zenith Angle.
TES	Tropospheric Emissions Spectrometer.
TM5	Tracer Model 5.
TROPOMI	TROPOspheric Monitoring Instrument.
TroStra	Transport of tracegases via the tropopause region in the West Pacific observed by FTIR spectrometry.
TTL	Tropical Tropopause/Transition Layer.
TUV	Tropospheric Ultraviolet-Visible Model.
TWP	Tropical West Pacific.
UT	Upper Troposphere.
UTLS	Upper Troposphere Lower Stratosphere.
UV	Ultra Violet.

VMR	Volume Mixing Ratio.
VOC	Volatile Organic Compounds.
WCCOS	World Calibration Center for Ozone Sondes.
WMO	World Meteorological Organisation.
WPM	West Pacific Monsoon.

Bibliography

R. J. Allan, N. Nicholls, P. D. Jones, and I. J. Butterworth. A further extension of the Tahiti-Darwin SOI, early ENSO events and Darwin pressure. *Journal of Climate*, 4 (7):743–749, 1991. doi: 10.1175/1520-0442(1991)004⟨0743:AFEOTT⟩2.0.CO;2. URL `https://doi.org/10.1175/1520-0442(1991)004<0743:AFEOTT>2.0.CO;2`.

D. C. Anderson et al. A pervasive role for biomass burning in tropical high ozone/low water structures. *Nature Communications*, 7(1):10267, April 2016. ISSN 2041-1723. doi: 10.1038/ncomms10267. URL `http://www.nature.com/articles/ncomms10267`.

M. G. Atticks and G. D. Robinson. Some features of the structure of the tropical tropopause. *Quarterly Journal of the Royal Meteorological Society*, 109(460): 295–308, April 1983. ISSN 00359009. doi: 10.1002/qj.49710946004. URL `http://doi.wiley.com/10.1002/qj.49710946004`.

A. G. Bamston, M. Chelliah, and S. B. Goldenberg. Documentation of a highly ENSO-related sst region in the equatorial pacific: Research note. *Atmosphere-Ocean*, 35(3): 367–383, September 1997. ISSN 0705-5900, 1480-9214. doi: 10.1080/07055900.1997.9649597. URL `http://www.tandfonline.com/doi/abs/10.1080/07055900.1997.9649597`.

C. A. Barton and J. P. McCormack. Origin of the 2016 QBO disruption and its relationship to extreme el niño events. *Geophysical Research Letters*, 44(21):11,150–11,157, November 2017. ISSN 0094-8276, 1944-8007. doi: 10.1002/2017GL075576. URL `https://onlinelibrary.wiley.com/doi/abs/10.1002/2017GL075576`.

D. G. Bell and S. M. Halpert. Climate assessment for 1997. *Bulletin of the American Meteorological Society*, 79(5):1–50, 1998.

J. Bjerknes. Atmospheric teleconnections from the equatorial pacific. *Monthly Weather Review*, 97(3):163–172, 1969. doi: 10.1175/1520-0493(1969)097⟨0163:ATFTEP⟩2.3.CO;2. URL `https://doi.org/10.1175/1520-0493(1969)097<0163:ATFTEP>2.3.CO;2`.

W. J. Bloss, M. J. Evans, J. D. Lee, R. Sommariva, D. E. Heard, and M. J. Pilling. The oxidative capacity of the troposphere: Coupling of field measurements of OH and a global chemistry transport model. *Faraday Discussions*, 130(0):425–436, 2005. doi: 10.1039/B419090D. URL `http://dx.doi.org/10.1039/B419090D`.

H. Bozem, T. M. Butler, M. G. Lawrence, H. Harder, M. Martinez, D. Kubistin, J. Lelieveld, and H. Fischer. Chemical processes related to net ozone tendencies in the free troposphere. *Atmospheric Chemistry and Physics*, 17(17):10565–10582, September 2017. ISSN 1680-7324. doi: 10.5194/acp-17-10565-2017. URL `https://www.atmos-chem-phys.net/17/10565/2017/`.

G. P. Brasseur, R. G. Prinn, and A. A. P. Pszenny. *Atmospheric Chemistry in a Changing World: an Integration and Synthesis of a Decade of Tropospheric Chemistry Research.* Springer Berlin Heidelberg, Berlin, Heidelberg, 2003. ISBN 978-3-642-18984-5 978-3-642-62396-7. URL `http://public.ebookcentral.proquest.com/choice/publicfullrecord.aspx?p=3087668`.

A. W. Brewer. Evidence for a world circulation provided by the measurements of helium and water vapour distribution in the stratosphere. *Quarterly Journal of the Royal Meteorological Society*, 75(326):351–363, October 1949. ISSN 00359009, 1477870X. doi: 10.1002/qj.49707532603. URL `http://doi.wiley.com/10.1002/qj.49707532603`.

E. V. Browell. Large-scale ozone and aerosol distributions, air mass characteristics, and ozone fluxes over the western Pacific Ocean in late winter/early spring. *Journal of Geophysical Research*, 108(D20):8805, 2003. ISSN 0148-0227. doi: 10.1029/2002JD003290. URL `http://doi.wiley.com/10.1029/2002JD003290`.

E. V. Browell et al. Large-scale air mass characteristics observed over the remote tropical Pacific Ocean during March-April 1999: Results from PEM-Tropics B field experiment. *Journal of Geophysical Research: Atmospheres*, 106(D23):32481–32501, December 2001. ISSN 2156-2202. doi: 10.1029/2001JD900001@10.1002/(ISSN)2169-8996.PEMTROP2. URL `https://agupubs.onlinelibrary.wiley.com/doi/10.1029/2001JD900001@10.1002/(ISSN)2169-8996.PEMTROP2`.

J. R. Brown, R. A. Colman, A. F. Moise, and I. N. Smith. The western Pacific monsoon in CMIP5 models: Model evaluation and projections. *Journal of Geophysical Research: Atmospheres*, 118(22):12,458–12,475, November 2013. ISSN 2169897X. doi: 10.1002/2013JD020290. URL `http://doi.wiley.com/10.1002/2013JD020290`.

N. Butchart. The Brewer-Dobson circulation. *Reviews of Geophysics*, 52(2):157–184, June 2014. ISSN 87551209. doi: 10.1002/2013RG000448. URL `http://doi.wiley.com/10.1002/2013RG000448`.

P. Cau, J. Methven, and B. Hoskins. Representation of dry tropical layers and their origins in ERA-40 data. *Journal of Geophysical Research: Atmospheres*, 110(D6), March 2005. ISSN 01480227. doi: 10.1029/2004JD004928. URL `http://doi.wiley.com/10.1029/2004JD004928`.

P. Cau, J. Methven, and B. Hoskins. Origins of Dry Air in the Tropics and Subtropics. *Journal of Climate*, 20(12):2745–2759, June 2007. ISSN 0894-8755, 1520-0442. doi: 10.1175/JCLI4176.1. URL `http://journals.ametsoc.org/doi/10.1175/JCLI4176.1`.

D. J. Cecil, D. E. Buechler, and R. J. Blakeslee. Gridded lightning climatology from TRMM-LIS and OTD: Dataset description. *Atmospheric Research*, 135-136:404–414, January 2014. ISSN 01698095. doi: 10.1016/j.atmosres.2012.06.028. URL `https://linkinghub.elsevier.com/retrieve/pii/S0169809512002323`.

W. Chameides and J. C. G. Walker. A photochemical theory of tropospheric ozone. *Journal of Geophysical Research*, 78(36):8751–8760, December 1973. ISSN 01480227. doi: 10.1029/JC078i036p08751. URL `http://doi.wiley.com/10.1029/JC078i036p08751`.

S. Chapman. A theory of upperatmospheric ozone. *Memoirs of the Royal Meteorological Society*, 3:103–125, 1930.

H. J. Christian. Global frequency and distribution of lightning as observed from space by the Optical Transient Detector. *Journal of Geophysical Research*, 108(D1):4005, 2003. ISSN 0148-0227. doi: 10.1029/2002JD002347. URL `http://doi.wiley.com/10.1029/2002JD002347`.

J. H. Crawford et al. Implications of large scale shifts in tropospheric NO $_x$ levels in the remote tropical Pacific. *Journal of Geophysical Research: Atmospheres*, 102(D23): 28447–28468, December 1997. ISSN 01480227. doi: 10.1029/97JD00011. URL `http://doi.wiley.com/10.1029/97JD00011`.

P. J. Crutzen, J. U. Grooss, C. Bruhl, R. Muller, and J. M. Russell. A Reevaluation of the Ozone Budget with HALOE UARS Data: No Evidence for the Ozone Deficit. *Science*, 268(5211):705–708, May 1995. ISSN 0036-8075, 1095-9203. doi: 10.1126/science.268.5211.705. URL `https://www.sciencemag.org/lookup/doi/10.1126/science.268.5211.705`.

P. Crutzen. A discussion of the chemistry of some minor constituents in the stratosphere and troposphere. *Pure and Applied Geophysics*, 106-108(1):1385–1399, December 1973. ISSN 0033-4553, 1420-9136. doi: 10.1007/BF00881092. URL `http://link.springer.com/10.1007/BF00881092`.

J. Davies, D. W. Tarasick, C. T. McElroy, J. B. Kerr, P. F. Fogal, and V. Savastiouk. Evaluation of ECC Ozonesonde Preparation Methods from Laboratory Tests and Field Comparisons during MANTRA. In *Proceedings of the Quadrennial Ozone Symposium—Sapporo, Japan, 2000*, pages 137–138, Tokyo, 2000. National Space Development Agency of Japan.

D. De Muer and H. Malcorps. The frequency response of an electrochemical ozone sonde and its application to the deconvolution of ozone profiles. *Journal of Geophysical Research*, 89(D1):1361, 1984. ISSN 0148-0227. doi: 10.1029/JD089iD01p01361. URL `http://doi.wiley.com/10.1029/JD089iD01p01361`.

T. Deshler et al. Atmospheric comparison of electrochemical cell ozonesondes from different manufacturers, and with different cathode solution strengths: The Balloon Experiment on Standards for Ozonesondes. *Journal of Geophysical Research*, 113 (D4):D04307, February 2008. ISSN 0148-0227. doi: 10.1029/2007JD008975. URL `http://doi.wiley.com/10.1029/2007JD008975`.

T. Deshler, R. Stübi, F. J. Schmidlin, J. L. Mercer, H. G. J. Smit, B. J. Johnson, R. Kivi, and B. Nardi. Methods to homogenize electrochemical concentration cell (ECC) ozonesonde measurements across changes in sensing solution concentration or ozonesonde manufacturer. *Atmospheric Measurement Techniques*, 10

(6):2021–2043, June 2017. ISSN 1867-8548. doi: 10.5194/amt-10-2021-2017. URL `https://www.atmos-meas-tech.net/10/2021/2017/`.

A. E. Dessler and K. Minschwaner. An analysis of the regulation of tropical tropospheric water vapor. *Journal of Geophysical Research: Atmospheres*, 112(D10), May 2007. ISSN 01480227. doi: 10.1029/2006JD007683. URL `http://doi.wiley.com/10.1029/2006JD007683`.

T. Di Liberto. Drought in the Pacific (NOAA), 2016. URL `https://www.climate.gov/news-features/event-tracker/drought-pacific`. (last visited: 2020-05-01).

M. Diallo, M. Riese, T. Birner, P. Konopka, R. Müller, M. I. Hegglin, M. L. Santee, M. Baldwin, B. Legras, and F. Ploeger. Response of stratospheric water vapor and ozone to the unusual timing of El Niño and the QBO disruption in 2015–2016. *Atmospheric Chemistry and Physics*, 18(17):13055–13073, September 2018. ISSN 1680-7324. doi: 10.5194/acp-18-13055-2018. URL `https://www.atmos-chem-phys.net/18/13055/2018/`.

R. R. Dickerson, K. P. Rhoads, T. P. Carsey, S. J. Oltmans, J. P. Burrows, and P. J. Crutzen. Ozone in the remote marine boundary layer: A possible role for halogens. *Journal of Geophysical Research: Atmospheres*, 104(D17):21385–21395, September 1999. ISSN 01480227. doi: 10.1029/1999JD900023. URL `http://doi.wiley.com/10.1029/1999JD900023`.

R. J. Dirksen, M. Sommer, F. J. Immler, D. F. Hurst, R. Kivi, and H. Vömel. Reference quality upper-air measurements: GRUAN data processing for the Vaisala RS92 radiosonde. *Atmospheric Measurement Techniques*, 7(12):4463–4490, December 2014. ISSN 1867-8548. doi: 10.5194/amt-7-4463-2014. URL `https://www.atmos-meas-tech.net/7/4463/2014/`.

R. J. Dirksen et al. Progress in managing the transition from the RS92 to the Vaisala RS41 as the operational radiosonde within the GCOS Reference Upper-Air Network. December 2019. URL `https://www.geosci-instrum-method-data-syst-discuss.net/gi-2019-36/`.

I. Folkins. Tropical ozone as an indicator of deep convection. *Journal of Geophysical Research*, 107(D13):4184, 2002. ISSN 0148-0227. doi: 10.1029/2001JD001178. URL `http://doi.wiley.com/10.1029/2001JD001178`.

I. Folkins and R. V. Martin. The Vertical Structure of Tropical Convection and Its Impact on the Budgets of Water Vapor and Ozone. *Journal of the Atmospheric Sciences*, 62(5):1560–1573, May 2005. ISSN 0022-4928, 1520-0469. doi: 10.1175/JAS3407.1. URL `http://journals.ametsoc.org/doi/10.1175/JAS3407.1`.

I. Folkins, R. Chatfield, D. Baumgardner, and M. Proffitt. Biomass burning and deep convection in southeastern Asia: Results from ASHOE/MAESA. *Journal of Geophysical Research: Atmospheres*, 102(D11):13291–13299, June 1997. ISSN 01480227. doi: 10.1029/96JD03711. URL `http://doi.wiley.com/10.1029/96JD03711`.

I. Folkins, M. Loewenstein, J. Podolske, S. J. Oltmans, and M. Proffitt. A barrier to vertical mixing at 14 km in the tropics: Evidence from ozonesondes and aircraft measurements. *Journal of Geophysical Research: Atmospheres*, 104(D18): 22095–22102, 1999. ISSN 2156-2202. doi: 10.1029/1999JD900404. URL `https://agupubs.onlinelibrary.wiley.com/doi/abs/10.1029/1999JD900404`.

I. Folkins, P. Bernath, C. Boone, G. Lesins, N. Livesey, A. M. Thompson, K. Walker, and J. C. Witte. Seasonal cycles of O_3 , CO, and convective outflow at the tropical tropopause. *Geophysical Research Letters*, 33(16):L16802, 2006. ISSN 0094-8276. doi: 10.1029/2006GL026602. URL `http://doi.wiley.com/10.1029/2006GL026602`.

V. Foltescu and A. Zahn. Aerosols used as tracers for stratosphere-troposphere exchange in the arctic. *Atmospheric Environment*, 29(15):1777–1784, August 1995. ISSN 13522310. doi: 10.1016/1352-2310(95)00095-G. URL `https://linkinghub.elsevier.com/retrieve/pii/135223109500095G`.

L. Froidevaux et al. Validation of Aura Microwave Limb Sounder stratospheric ozone measurements. *Journal of Geophysical Research*, 113(D15):D15S20, May 2008. ISSN 0148-0227. doi: 10.1029/2007JD008771. URL `http://doi.wiley.com/10.1029/2007JD008771`.

Q. Fu, Y. Hu, and Q. Yang. Identifying the top of the tropical tropopause layer from vertical mass flux analysis and CALIPSO lidar cloud observations. *Geophysical Research Letters*, 34(14):L14813, July 2007. ISSN 0094-8276. doi: 10.1029/2007GL030099. URL `http://doi.wiley.com/10.1029/2007GL030099`.

S. Fueglistaler. Stepwise changes in stratospheric water vapor? *Journal of Geophysical Research: Atmospheres*, 117(D13), July 2012. ISSN 01480227. doi: 10.1029/2012JD017582. URL `http://doi.wiley.com/10.1029/2012JD017582`.

S. Fueglistaler, H. Wernli, and T. Peter. Tropical troposphere-to-stratosphere transport inferred from trajectory calculations. *Journal of Geophysical Research: Atmospheres*, 109(D3), February 2004. ISSN 01480227. doi: 10.1029/2003JD004069. URL `http://doi.wiley.com/10.1029/2003JD004069`.

S. Fueglistaler, A. E. Dessler, T. J. Dunkerton, I. Folkins, Q. Fu, and P. W. Mote. Tropical tropopause layer. *Reviews of Geophysics*, 47(1):RG1004, February 2009. ISSN 8755-1209. doi: 10.1029/2008RG000267. URL `http://doi.wiley.com/10.1029/2008RG000267`.

S. Fueglistaler, P. H. Haynes, and P. M. Forster. The annual cycle in lower stratospheric temperatures revisited. *Atmospheric Chemistry and Physics*, 11(8):3701–3711, April 2011. ISSN 1680-7324. doi: 10.5194/acp-11-3701-2011. URL `https://www.atmos-chem-phys.net/11/3701/2011/`.

M. Fujiwara, K. Kita, and T. Ogawa. Stratosphere-troposphere exchange of ozone associated with the equatorial Kelvin wave as observed with ozonesondes and rawinsondes. *Journal of Geophysical Research: Atmospheres*, 103(D15):19173–19182, August 1998. ISSN 01480227. doi: 10.1029/98JD01419. URL `http://doi.wiley.com/10.1029/98JD01419`.

R. S. Gao, J. Ballard, L. A. Watts, T. D. Thornberry, S. J. Ciciora, R. J. McLaughlin, and D. W. Fahey. A compact, fast UV photometer for measurement of ozone from research aircraft. *Atmospheric Measurement Techniques*, 5(9):2201–2210, September 2012. ISSN 1867-8548. doi: 10.5194/amt-5-2201-2012. URL `https://www.atmos-meas-tech.net/5/2201/2012/`.

R. S. Gao, K. H. Rosenlof, D. W. Fahey, P. O. Wennberg, E. J. Hintsa, and T. F. Hanisco. OH in the tropical upper troposphere and its relationships to solar radiation and reactive nitrogen. *Journal of Atmospheric Chemistry*, 71(1):55–64, March 2014. ISSN 0167-7764, 1573-0662. doi: 10.1007/s10874-014-9280-2. URL `http://link.springer.com/10.1007/s10874-014-9280-2`.

C. I. Garfinkel and D. L. Hartmann. Effects of the El Niño–Southern Oscillation and the Quasi-Biennial Oscillation on polar temperatures in the stratosphere. *Journal of Geophysical Research*, 112(D19):D19112, October 2007. ISSN 0148-0227. doi: 10.1029/2007JD008481. URL `http://doi.wiley.com/10.1029/2007JD008481`.

A. Gettelman and P. d. F. Forster. A Climatology of the Tropical Tropopause Layer. *Journal of the Meteorological Society of Japan*, 80(4B):911–924, 2002. ISSN 0026-1165. doi: 10.2151/jmsj.80.911. URL `http://joi.jlc.jst.go.jp/JST.JSTAGE/jmsj/80.911?from=CrossRef`.

A. Gettelman, P. H. Lauritzen, M. Park, and J. E. Kay. Processes regulating short-lived species in the tropical tropopause layer. *Journal of Geophysical Research*, 114 (D13):D13303, July 2009. ISSN 0148-0227. doi: 10.1029/2009JD011785. URL `http://doi.wiley.com/10.1029/2009JD011785`.

T. Graedel, P. J. Crutzen, F. Kläger, and C. Brühl. *Chemie der Atmosphäre: Bedeutung für Klima und Umwelt*. Spektrum-Lehrbuch. Spektrum Akademischer Verlag, Heidelberg, 1994. ISBN 978-3-86025-204-8.

A. J. Haagen-Smit. Chemistry and Physiology of Los Angeles Smog. *Industrial & Engineering Chemistry*, 44(6):1342–1346, June 1952. ISSN 0019-7866, 1541-5724. doi: 10.1021/ie50510a045. URL `https://pubs.acs.org/doi/abs/10.1021/ie50510a045`.

T. F. Hanisco et al. Sources, Sinks, and the Distribution of OH in the Lower Stratosphere. *The Journal of Physical Chemistry A*, 105(9):1543–1553, March 2001. ISSN 1089-5639, 1520-5215. doi: 10.1021/jp002334g. URL `https://pubs.acs.org/doi/10.1021/jp002334g`.

D. Hartmann et al. Observations: Atmosphere and Surface. In *Climate Change 2013: The Physical Science Basis. Contribution of Working Group I to the Fifth Assessment Report of the Intergovernmental Panel on Climate Change [Stocker, T.F., D. Qin, G.-K. Plattner, M. Tignor, S.K. Allen, J. Boschung, A. Nauels, Y. Xia, V. Bex and P.M. Midgley (eds.)]*. Cambridge University Press, 2013.

H. Hayashi, K. Kita, and S. Taguchi. Ozone-enhanced layers in the troposphere over the equatorial Pacific Ocean and the influence of transport of midlatitude UT/LS air. *Atmospheric Chemistry and Physics*, page 14, 2008.

H. H. Hendon and S. Abhik. Differences in Vertical Structure of the Madden-Julian Oscillation Associated With the Quasi-Biennial Oscillation. *Geophysical Research Letters*, 45(9):4419–4428, May 2018. ISSN 00948276. doi: 10.1029/2018GL077207. URL `http://doi.wiley.com/10.1029/2018GL077207`.

E. J. Highwood and B. J. Hoskins. The tropical tropopause. *Quarterly Journal of the Royal Meteorological Society*, 124(549):1579–1604, July 1998. ISSN 00359009, 1477870X. doi: 10.1002/qj.49712454911. URL `http://doi.wiley.com/10.1002/qj.49712454911`.

J. M. Hoell, D. D. Davis, D. J. Jacob, M. O. Rodgers, R. E. Newell, H. E. Fuelberg, R. J. McNeal, J. L. Raper, and R. J. Bendura. Pacific Exploratory Mission in the tropical Pacific: PEM-Tropics A, August-September 1996. *Journal of Geophysical Research: Atmospheres*, 104(D5):5567–5583, March 1999. ISSN 01480227. doi: 10.1029/1998JD100074. URL `http://doi.wiley.com/10.1029/1998JD100074`.

L. Hoffmann, G. Günther, D. Li, O. Stein, X. Wu, S. Griessbach, Y. Heng, P. Konopka, R. Müller, B. Vogel, and J. S. Wright. From ERA-Interim to ERA5: the considerable impact of ECMWF's next-generation reanalysis on Lagrangian transport simulations. *Atmospheric Chemistry and Physics*, 19(5):3097–3124, March 2019. ISSN 1680-7324. doi: 10.5194/acp-19-3097-2019. URL `https://www.atmos-chem-phys.net/19/3097/2019/`.

J. R. Holton. On the global exchange of mass between the stratosphere and troposphere. *Journal of the Atmospheric Sciences*, 47(3):392–395, 1990. doi: 10.1175/1520-0469(1990)047⟨0392:OTGEOM⟩2.0.CO;2. URL `https://doi.org/10.1175/1520-0469(1990)047<0392:OTGEOM>2.0.CO;2`.

J. R. Holton. *An introduction to dynamic meteorology*. Number v. 88 in International geophysics series. Elsevier Academic Press, Burlington, MA, 4th ed edition, 2004. ISBN 978-0-12-354015-7 978-0-12-354016-4.

J. R. Holton and A. Gettelman. Horizontal transport and the dehydration of the stratosphere. *Geophysical Research Letters*, 28(14):2799–2802, July 2001. ISSN 00948276. doi: 10.1029/2001GL013148. URL `http://doi.wiley.com/10.1029/2001GL013148`.

J. R. Holton, P. H. Haynes, M. E. McIntyre, A. R. Douglass, R. B. Rood, and L. Pfister. Stratosphere-troposphere exchange. *Reviews of Geophysics*, 33(4):403–439, 1995.

X.-M. Hu, J. M. Sigler, and J. D. Fuentes. Variability of ozone in the marine boundary layer of the equatorial Pacific Ocean. *Journal of Atmospheric Chemistry*, 66(3):117, 2011.

B. Huang, M. L'Heureux, Z.-Z. Hu, and H.-M. Zhang. Ranking the strongest ENSO events while incorporating SST uncertainty. *Geophysical Research Letters*, 43(17):9165–9172, 2016.

D. Hubert et al. Ground-based assessment of the bias and long-term stability of 14 limb and occultation ozone profile data records. *Atmospheric Measurement Techniques*, 9 (6):2497–2534, June 2016. ISSN 1867-8548. doi: 10.5194/amt-9-2497-2016. URL `https://www.atmos-meas-tech.net/9/2497/2016/`.

V. Huijnen et al. The global chemistry transport model TM5: description and evaluation of the tropospheric chemistry version 3.0. *Geoscientific Model Development*, 3(2):445–473, October 2010. ISSN 1991-9603. doi: 10.5194/gmd-3-445-2010. URL `https://www.geosci-model-dev.net/3/445/2010/`.

F. Immler, I. Beninga, W. Ruhe, B. Stein, B. Mielke, S. Rutz, O. Terli, and O. Schrems. A new LIDAR system for the detection of Cloud and aerosol backscatter, depolarization, extinction, and fluorescence. *Reviewed and revised papers presented at the 23rd International Laser Radar Converence, 24-28 July 2006 Nara Japan, Editors: Chikao Nagasawa, Nobuo Sugimoto,I*, pages 35–38, 2006.

L. Jaegle, D. J. Jacob, W. H. Brune, and P. O. Wennberg. Chemistry of HOV radicals in the upper troposphere. *Atmospheric Environment*, page 21, 2001.

L. Jaeglé et al. Observed OH and HO_2 in the upper troposphere suggest a major source from convective injection of peroxides. *Geophysical Research Letters*, 24(24):3181–3184, December 1997. ISSN 00948276. doi: 10.1029/97GL03004. URL `http://doi.wiley.com/10.1029/97GL03004`.

E. J. Jensen et al. The NASA Airborne Tropical Tropopause Experiment: High-Altitude Aircraft Measurements in the Tropical Western Pacific. *Bulletin of the American Meteorological Society*, 98(1):129–143, January 2017a. ISSN 0003-0007, 1520-0477. doi: 10.1175/BAMS-D-14-00263.1. URL `http://journals.ametsoc.org/doi/10.1175/BAMS-D-14-00263.1`.

E. J. Jensen et al. Physical processes controlling the spatial distributions of relative humidity in the tropical tropopause layer over the Pacific. *Journal of Geophysical Research: Atmospheres*, 122(11):6094–6107, June 2017b. ISSN 2169-897X, 2169-8996. doi: 10.1002/2017JD026632. URL `https://onlinelibrary.wiley.com/doi/abs/10.1002/2017JD026632`.

D. N. Joanes and C. A. Gill. Comparing measures of sample skewness and kurtosis. *Journal of the Royal Statistical Society: Series D (The Statistician)*, 47(1):183–189, March 1998. ISSN 0039-0526, 1467-9884. doi: 10.1111/1467-9884.00122. URL `http://doi.wiley.com/10.1111/1467-9884.00122`.

B. J. Johnson. Electrochemical concentration cell (ECC) ozonesonde pump efficiency measurements and tests on the sensitivity to ozone of buffered and unbuffered ECC sensor cathode solutions. *Journal of Geophysical Research*, 107(D19):4393, 2002. ISSN 0148-0227. doi: 10.1029/2001JD000557. URL `http://doi.wiley.com/10.1029/2001JD000557`.

R. H. Johnson, T. M. Rickenbach, S. A. Rutledge, P. E. Ciesielski, and W. H. Schubert. Trimodal characteristics of tropical convection. *Journal of Climate*, 12(8):2397–2418, 1999. doi: 10.1175/1520-0442(1999)012⟨2397:TCOTC⟩2.0.CO;2. URL `https://doi.org/10.1175/1520-0442(1999)012<2397:TCOTC>2.0.CO;2`.

C. E. Junge. Global ozone budget and exchange between stratosphere and troposphere. *Tellus*, 14(4):363–377, November 1962. ISSN 00402826, 21533490. doi: 10.1111/j.

2153-3490.1962.tb01349.x. URL `http://tellusa.net/index.php/tellusa/article/view/9563`.

L. E. Kalnajs and L. M. Avallone. A Novel Lightweight Low-Power Dual-Beam Ozone Photometer Utilizing Solid-State Optoelectronics. *Journal of Atmospheric and Oceanic Technology*, 27(5):869–880, May 2010. ISSN 0739-0572, 1520-0426. doi: 10.1175/2009JTECHA1362.1. URL `http://journals.ametsoc.org/doi/10.1175/2009JTECHA1362.1`.

G. N. Kiladis, K. H. Straub, G. C. Reid, and K. S. Gage. Aspects of interannual and intraseasonal variability of the tropopause and lower stratosphere. *Quarterly Journal of the Royal Meteorological Society*, 127(576):1961–1983, July 2001. ISSN 00359009, 1477870X. doi: 10.1002/qj.49712757606. URL `http://doi.wiley.com/10.1002/qj.49712757606`.

G. N. Kiladis, M. C. Wheeler, P. T. Haertel, K. H. Straub, and P. E. Roundy. Convectively coupled equatorial waves. *Reviews of Geophysics*, 47(2):RG2003, April 2009. ISSN 8755-1209. doi: 10.1029/2008RG000266. URL `http://doi.wiley.com/10.1029/2008RG000266`.

J. Kim and S.-W. Son. Tropical Cold-Point Tropopause: Climatology, Seasonal Cycle, and Intraseasonal Variability Derived from COSMIC GPS Radio Occultation Measurements. *Journal of Climate*, 25(15):5343–5360, August 2012. ISSN 0894-8755, 1520-0442. doi: 10.1175/JCLI-D-11-00554.1. URL `http://journals.ametsoc.org/doi/10.1175/JCLI-D-11-00554.1`.

K. Kita et al. Photochemical production of ozone in the upper troposphere in association with cumulus convection over Indonesia. *Journal of Geophysical Research*, 108(D3): 8400, November 2002. ISSN 0148-0227. doi: 10.1029/2001JD000844. URL `http://doi.wiley.com/10.1029/2001JD000844`.

D. Kley, P. J. Crutzen, H. G. J. Smit, H. Vomel, S. J. Oltmans, H. Grassl, and V. Ramanathan. Observations of Near-Zero Ozone Concentrations Over the Convective Pacific: Effects on Air Chemistry. *Science*, 274(5285):230–233, October 1996. ISSN 0036-8075, 1095-9203. doi: 10.1126/science.274.5285.230. URL `https://www.sciencemag.org/lookup/doi/10.1126/science.274.5285.230`.

D. Kley, H. G. J. Smit, H. Vömel, H. Grassl, V. Ramanathan, P. J. Crutzen, S. Williams, J. Meywerk, and S. J. Oltmans. Tropospheric water-vapour and ozone cross-sections in a zonal plane over the central equatorial Pacific Ocean. *Quarterly Journal of the Royal Meteorological Society*, 123(543):2009–2040, October 1997. ISSN 00359009, 1477870X. doi: 10.1002/qj.49712354312. URL `http://doi.wiley.com/10.1002/qj.49712354312`.

W. D. Komhyr. Electrical concentration cells for gas analysis. *Annales Geophysicae*, 25: 203–210, 1969.

W. D. Komhyr. Operations handbook - ozone measurements to 40-km altitude with model 4A electrochemical concentration cell (ECC) ozonesondes (used with 1680-MHz radiosondes). Technical Memorandum ERL ARL-149, National Oceanic and Atmospheric Administration (NOAA), Silver Spring, MD, United States, September 1986.

W. D. Komhyr, R. A. Barnes, G. B. Brothers, J. A. Lathrop, and D. P. Opperman. Electrochemical concentration cell ozonesonde performance evaluation during STOIC 1989. *Journal of Geophysical Research*, 100(D5):9231, 1995. ISSN 0148-0227. doi: 10.1029/94JD02175. URL `http://doi.wiley.com/10.1029/94JD02175`.

Y. Kondo, M. Ko, M. Koike, S. Kawakami, and T. Ogawa. Preface to Special Section on Biomass Burning and Lightning Experiment (BIBLE). *Journal of Geophysical Research*, 108(D3):8397, November 2002. ISSN 0148-0227. doi: 10.1029/2002JD002401. URL `http://doi.wiley.com/10.1029/2002JD002401`.

Y. Kondo et al. Photochemistry of ozone over the western Pacific from winter to spring. *Journal of Geophysical Research: Atmospheres*, 109(D23), December 2004. ISSN 01480227. doi: 10.1029/2004JD004871. URL `http://doi.wiley.com/10.1029/2004JD004871`.

P. Konopka, J.-U. Grooß, G. Günther, F. Ploeger, R. Pommrich, R. Müller, and N. Livesey. Annual cycle of ozone at and above the tropical tropopause: observations versus simulations with the Chemical Lagrangian Model of the Stratosphere (CLaMS). *Atmospheric Chemistry and Physics*, 10(1):121–132, January 2010. ISSN 1680-7324. doi: 10.5194/acp-10-121-2010. URL `https://www.atmos-chem-phys.net/10/121/2010/`.

P. Konopka, F. Ploeger, M. Tao, and M. Riese. Zonally resolved impact of ENSO on the stratospheric circulation and water vapor entry values. *Journal of Geophysical Research: Atmospheres*, 121(19):11,486–11,501, October 2016. ISSN 2169897X. doi: 10.1002/2015JD024698. URL `http://doi.wiley.com/10.1002/2015JD024698`.

S. Kremser et al. Stratospheric aerosol-Observations, processes, and impact on climate: Stratospheric Aerosol. *Reviews of Geophysics*, 54(2):278–335, June 2016. ISSN 87551209. doi: 10.1002/2015RG000511. URL `http://doi.wiley.com/10.1002/2015RG000511`.

M. Krämer et al. Intercomparison of Stratospheric Chemistry Modelsunder Polar Vortex Conditions. *Journal of Atmospheric Chemistry*, 45(1):51–77, 2003. ISSN 01677764. doi: 10.1023/A:1024056026432. URL `http://link.springer.com/10.1023/A:1024056026432`.

K. Krüger and B. Quack. Introduction to special issue: the TransBrom Sonne expedition in the tropical West Pacific. *Atmospheric Chemistry and Physics*, 13(18):9439–9446, September 2013. ISSN 1680-7324. doi: 10.5194/acp-13-9439-2013. URL `https://www.atmos-chem-phys.net/13/9439/2013/`.

K. Krüger, S. Tegtmeier, and M. Rex. Long-term climatology of air mass transport through the Tropical Tropopause Layer (TTL) during NH winter. *Atmospheric Chemistry and Physics*, 8(4):813–823, February 2008. ISSN 1680-7324. doi: 10.5194/acp-8-813-2008. URL `https://www.atmos-chem-phys.net/8/813/2008/`.

A. Kunz, P. Konopka, R. Müller, and L. L. Pan. Dynamical tropopause based on isentropic potential vorticity gradients. *Journal of Geophysical Research*, 116(D1): D01110, January 2011. ISSN 0148-0227. doi: 10.1029/2010JD014343. URL `http://doi.wiley.com/10.1029/2010JD014343`.

R. Lehmann. An Algorithm for the Determination of All Significant Pathways in Chemical Reaction Systems. *Journal of Atmospheric Chemistry*, 47(1):45–78, January 2004. ISSN 0167-7764. doi: 10.1023/B:JOCH.0000012284.28801.b1. URL `http://link.springer.com/10.1023/B:JOCH.0000012284.28801.b1`.

J. Lelieveld and F. J. Dentener. What controls tropospheric ozone? *Journal of Geophysical Research: Atmospheres*, 105(D3):3531–3551, 2000. ISSN 2156-2202. doi: 10.1029/1999JD901011. URL `https://agupubs.onlinelibrary.wiley.com/doi/abs/10.1029/1999JD901011`.

H. Levy. Normal Atmosphere: Large Radical and Formaldehyde Concentrations Predicted. *Science*, 173(3992):141–143, July 1971. ISSN 0036-8075, 1095-9203. doi: 10.1126/science.173.3992.141. URL `https://www.sciencemag.org/lookup/doi/10.1126/science.173.3992.141`.

S. C. Liu, M. McFarland, D. Kley, O. Zafiriou, and B. Huebert. Tropospheric NO $_x$ and O_3 budgets in the equatorial Pacific. *Journal of Geophysical Research*, 88(C2):1360, 1983. ISSN 0148-0227. doi: 10.1029/JC088iC02p01360. URL `http://doi.wiley.com/10.1029/JC088iC02p01360`.

J. A. Logan, D. B. A. Jones, I. A. Megretskaia, S. J. Oltmans, B. J. Johnson, H. Vömel, W. J. Randel, W. Kimani, and F. J. Schmidlin. Quasibiennial oscillation in tropical ozone as revealed by ozonesonde and satellite data. *Journal of Geophysical Research*, 108(D8):4244, 2003. ISSN 0148-0227. doi: 10.1029/2002JD002170. URL `http://doi.wiley.com/10.1029/2002JD002170`.

R. A. Madden and P. R. Julian. Detection of a 40–50 day oscillation in the zonal wind in the tropical pacific. *Journal of the Atmospheric Sciences*, 28(5):702–708, 1971. doi: 10.1175/1520-0469(1971)028⟨0702:DOADOI⟩2.0.CO;2. URL `https://doi.org/10.1175/1520-0469(1971)028<0702:DOADOI>2.0.CO;2`.

R. A. Madden and P. R. Julian. Observations of the 40–50-Day tropical Oscillation—A review. *Monthly Weather Review*, 122(5):814–837, 1994. doi: 10.1175/1520-0493(1994)122⟨0814:OOTDTO⟩2.0.CO;2. URL `https://doi.org/10.1175/1520-0493(1994)122<0814:OOTDTO>2.0.CO;2`.

S. Madronich and S. Flocke. The role of solar radiation in atmospheric chemistry. In *Environmental photochemistry*, pages 1–26. Springer, 1999.

G. L. Manney et al. Chemical depletion of ozone in the Arctic lower stratosphere during winter 1992–93. *Nature*, 370(6489):429–434, August 1994. ISSN 0028-0836, 1476-4687. doi: 10.1038/370429a0. URL `http://www.nature.com/articles/370429a0`.

B. E. Mapes and P. Zuidema. Radiative-dynamical consequences of dry tongues in the tropical troposphere. *Journal of the Atmospheric Sciences*, 53(4):620–638, 1996.

doi: 10.1175/1520-0469(1996)053⟨0620:RDCODT⟩2.0.CO;2. URL `https://doi.org/10.1175/1520-0469(1996)053<0620:RDCODT>2.0.CO;2`.

B. E. Mapes. Water's two height scales: The moist adiabat and the radiative troposphere. *Quarterly Journal of the Royal Meteorological Society*, 127(577):2353–2366, October 2001. ISSN 00359009, 1477870X. doi: 10.1002/qj.49712757708. URL `http://doi.wiley.com/10.1002/qj.49712757708`.

S. A. Montzka, M. Krol, E. Dlugokencky, B. Hall, P. Jockel, and J. Lelieveld. Small Interannual Variability of Global Atmospheric Hydroxyl. *Science*, 331(6013):67–69, January 2011. ISSN 0036-8075, 1095-9203. doi: 10.1126/science.1197640. URL `https://www.sciencemag.org/lookup/doi/10.1126/science.1197640`.

G. Myhre et al. Anthropogenic and Natural Radiative Forcing. In *Climate Change 2013: The Physical Science Basis. Contribution of Working Group I to the Fifth Assessment Report of the Intergovernmental Panel on Climate Change*, page 82. Cambridge University Press, Cambridge, United Kingdom and New York, NY, USA, 2013.

R. E. Newell and S. Gould-Stewart. A stratospheric fountain? *Journal of the Atmospheric Sciences*, 38(12):2789–2796, 1981.

R. E. Newell, Y. Zhu, E. V. Browell, S. Ismail, W. G. Read, J. W. Waters, K. K. Kelly, and S. C. Liu. Upper tropospheric water vapor and cirrus: Comparison of DC-8 observations, preliminary UARS microwave limb sounder measurements and meteorological analyses. *Journal of Geophysical Research: Atmospheres*, 101(D1):1931–1941, 1996.

R. E. Newell, V. Thouret, J. Y. N. Cho, P. Stoller, A. Marenco, and H. G. Smit. Ubiquity of quasi-horizontal layers in the troposphere. *Nature*, 398(6725):316–319, March 1999. ISSN 0028-0836, 1476-4687. doi: 10.1038/18642. URL `http://www.nature.com/articles/18642`.

R. Newton, G. Vaughan, H. M. A. Ricketts, L. L. Pan, A. J. Weinheimer, and C. Chemel. Ozonesonde profiles from the West Pacific Warm Pool: measurements and validation. *Atmospheric Chemistry and Physics*, 16(2):619–634, January 2016. ISSN 1680-7324. doi: 10.5194/acp-16-619-2016. URL `https://www.atmos-chem-phys.net/16/619/2016/`.

J. M. Nicely et al. An observationally constrained evaluation of the oxidative capacity in the tropical western Pacific troposphere: Observationally Constrained OH in TWP. *Journal of Geophysical Research: Atmospheres*, 121(12):7461–7488, June 2016. ISSN 2169897X. doi: 10.1002/2016JD025067. URL `http://doi.wiley.com/10.1002/2016JD025067`.

P. J. Nowack, N. Luke Abraham, A. C. Maycock, P. Braesicke, J. M. Gregory, M. M. Joshi, A. Osprey, and J. A. Pyle. A large ozone-circulation feedback and its implications for global warming assessments. *Nature Climate Change*, 5(1):41–45, January 2015. ISSN 1758-678X, 1758-6798. doi: 10.1038/nclimate2451. URL `http://www.nature.com/articles/nclimate2451`.

NRC. The Effects of Meteorology on Tropospheric Ozone. In *Rethinking the Ozone Problem in Urban and Regional Air Pollution*. National Academies Press, Washington, D.C., January 1991. ISBN 978-0-309-04631-2. doi: 10.17226/1889. URL `http://www.nap.edu/catalog/1889`. Pages: 1889.

S.-Y. Ogino, M. Fujiwara, M. Shiotani, F. Hasebe, J. Matsumoto, T. H. T. Hoang, and T. T. T. Nguyen. Ozone variations over the northern subtropical region revealed by ozonesonde observations in Hanoi. *Journal of Geophysical Research: Atmospheres*, 118 (8):3245–3257, April 2013. ISSN 2169897X. doi: 10.1002/jgrd.50348. URL `http://doi.wiley.com/10.1002/jgrd.50348`.

S. J. Oltmans et al. Ozone in the Pacific tropical troposphere from ozonesonde observations. *Journal of Geophysical Research: Atmospheres*, 106(D23):32503–32525, December 2001. ISSN 2156-2202. doi: 10.1029/2000JD900834@10.1002/(ISSN) 2169-8996.PEMTROP2. URL `https://agupubs.onlinelibrary.wiley.com/doi/10.1029/2000JD900834@10.1002/(ISSN)2169-8996.PEMTROP2`.

S. Oltmans, B. Johnson, J. Harris, A. M. Thompson, H. Liu, C. Chan, H. Vömel, T. Fujimoto, V. Brackett, W. Chang, and others. Tropospheric ozone over the North Pacific from ozonesonde observations. *Journal of Geophysical Research*, 109(D15), 2004. doi: 10.1029/2003JD003466. URL `http://doi.wiley.com/10.1029/2003JD003466`. Publisher: Wiley Online Library.

L. L. Pan et al. Bimodal distribution of free tropospheric ozone over the tropical western Pacific revealed by airborne observations. *Geophysical Research Letters*, 42(18):7844–7851, September 2015. ISSN 0094-8276, 1944-8007. doi: 10.1002/2015GL065562. URL `https://onlinelibrary.wiley.com/doi/abs/10.1002/2015GL065562`.

L. L. Pan et al. The Convective Transport of Active Species in the Tropics (CONTRAST) Experiment. *Bulletin of the American Meteorological Society*, 98(1):106–128, January 2017. ISSN 0003-0007, 1520-0477. doi: 10.1175/BAMS-D-14-00272.1. URL `http://journals.ametsoc.org/doi/10.1175/BAMS-D-14-00272.1`.

L. L. Pan, L. C. Paulik, S. B. Honomichl, L. A. Munchak, J. Bian, H. B. Selkirk, and H. Vömel. Identification of the tropical tropopause transition layer using the ozone-water vapor relationship. *Journal of Geophysical Research: Atmospheres*, 119(6):3586–3599, March 2014. ISSN 2169897X. doi: 10.1002/2013JD020558. URL `http://doi.wiley.com/10.1002/2013JD020558`.

L. L. Pan, S. B. Honomichl, T. V. Bui, T. Thornberry, A. Rollins, E. Hintsa, and E. J. Jensen. Lapse Rate or Cold Point: The Tropical Tropopause Identified by In Situ Trace Gas Measurements. *Geophysical Research Letters*, 45(19):10,756–10,763, October 2018. ISSN 0094-8276, 1944-8007. doi: 10.1029/2018GL079573. URL `https://onlinelibrary.wiley.com/doi/abs/10.1029/2018GL079573`.

L. L. Pan, S. B. Honomichl, T. Thornberry, A. Rollins, T. P. Bui, L. Pfister, and E. E. Jensen. Observational Evidence of Horizontal Transport-Driven Dehydration in the TTL. *Geophysical Research Letters*, 46(13):7848–7856, July 2019. ISSN 0094-8276, 1944-8007. doi: 10.1029/2019GL083647. URL `https://onlinelibrary.wiley.com/doi/abs/10.1029/2019GL083647`.

L. C. Paulik and T. Birner. Quantifying the deep convective temperature signal within the tropical tropopause layer (TTL). *Atmospheric Chemistry and Physics*, 12(24): 12183–12195, December 2012. ISSN 1680-7324. doi: 10.5194/acp-12-12183-2012. URL `https://www.atmos-chem-phys.net/12/12183/2012/`.

PCCSR. Pacific Climate Change Science Program. Current and Future Climate of Palau, 2011. URL `https://www.pacificclimatechangescience.org/wp-content/uploads/2013/06/2_PCCSP_Palau_8pp.pdf`. (last visited: 2020-05-01).

S. G. H. Philander, D. Gu, G. Lambert, T. Li, D. Halpern, N.-C. Lau, and R. C. Pacanowski. Why the ITCZ is mostly north of the equator. *Journal of Climate*, 9(12): 2958–2972, 1996. doi: 10.1175/1520-0442(1996)009⟨2958:WTIIMN⟩2.0.CO;2. URL `https://doi.org/10.1175/1520-0442(1996)009<2958:WTIIMN>2.0.CO;2`.

F. Ploeger, S. Fueglistaler, J.-U. Grooß, G. Günther, P. Konopka, Y. Liu, R. Müller, F. Ravegnani, C. Schiller, A. Ulanovski, and M. Riese. Insight from ozone and water vapour on transport in the tropical tropopause layer (TTL). *Atmospheric Chemistry and Physics*, 11(1):407–419, January 2011. ISSN 1680-7324. doi: 10.5194/acp-11-407-2011. URL `https://www.atmos-chem-phys.net/11/407/2011/`.

L. M. Polvani and S. Solomon. The signature of ozone depletion on tropical temperature trends, as revealed by their seasonal cycle in model integrations with single forcings. *Journal of Geophysical Research: Atmospheres*, 117(D17), September 2012. ISSN 01480227. doi: 10.1029/2012JD017719. URL `http://doi.wiley.com/10.1029/2012JD017719`.

G. A. Postel and M. H. Hitchman. A climatology of rossby wave breaking along the subtropical tropopause. *Journal of the Atmospheric Sciences*, 56(3):359–373, 1999. doi: 10.1175/1520-0469(1999)056⟨0359:ACORWB⟩2.0.CO;2. URL `https://doi.org/10.1175/1520-0469(1999)056<0359:ACORWB>2.0.CO;2`.

M. J. Prather, X. Zhu, Q. Tang, J. Hsu, and J. L. Neu. An atmospheric chemist in search of the tropopause. *Journal of Geophysical Research*, 116(D4):D04306, February 2011. ISSN 0148-0227. doi: 10.1029/2010JD014939. URL `http://doi.wiley.com/10.1029/2010JD014939`.

W. J. Randel, M. Park, L. Emmons, D. Kinnison, P. Bernath, K. A. Walker, C. Boone, and H. Pumphrey. Asian Monsoon Transport of Pollution to the Stratosphere. *Science*, 328 (5978):611–613, April 2010. ISSN 0036-8075, 1095-9203. doi: 10.1126/science.1182274. URL `https://www.sciencemag.org/lookup/doi/10.1126/science.1182274`.

W. J. Randel and E. J. Jensen. Physical processes in the tropical tropopause layer and their roles in a changing climate. *Nature Geoscience*, 6(3):169–176, March 2013. ISSN 1752-0894, 1752-0908. doi: 10.1038/ngeo1733. URL `http://www.nature.com/articles/ngeo1733`.

W. J. Randel and A. M. Thompson. Interannual variability and trends in tropical ozone derived from SAGE II satellite data and SHADOZ ozonesondes. *Journal of Geophysical Research*, 116(D7):D07303, April 2011. ISSN 0148-0227. doi: 10.1029/2010JD015195. URL `http://doi.wiley.com/10.1029/2010JD015195`.

W. J. Randel, M. Park, F. Wu, and N. Livesey. A Large Annual Cycle in Ozone above the Tropical Tropopause Linked to the Brewer–Dobson Circulation. *Journal of the Atmospheric Sciences*, 64(12):4479–4488, December 2007. ISSN 0022-4928, 1520-0469. doi: 10.1175/2007JAS2409.1. URL `http://journals.ametsoc.org/doi/10.1175/2007JAS2409.1`.

W. J. Randel, R. R. Garcia, N. Calvo, and D. Marsh. ENSO influence on zonal mean temperature and ozone in the tropical lower stratosphere. *Geophysical Research Letters*, 36(15), August 2009. ISSN 00948276. doi: 10.1029/2009GL039343. URL `http://doi.wiley.com/10.1029/2009GL039343`.

W. J. Randel, L. Rivoire, L. L. Pan, and S. B. Honomichl. Dry layers in the tropical troposphere observed during CONTRAST and global behavior from GFS analyses: DRY LAYERS IN THE TROPICAL TROPOSPHERE. *Journal of Geophysical Research: Atmospheres*, 121(23):14,142–14,158, December 2016. ISSN 2169897X. doi: 10.1002/2016JD025841. URL `http://doi.wiley.com/10.1002/2016JD025841`.

K. A. Read et al. Extensive halogen-mediated ozone destruction over the tropical Atlantic Ocean. *Nature*, 453(7199):1232–1235, June 2008. ISSN 0028-0836, 1476-4687. doi: 10.1038/nature07035. URL `http://www.nature.com/articles/nature07035`.

M. Rex, I. Wohltmann, T. Ridder, R. Lehmann, K. Rosenlof, P. Wennberg, D. Weisenstein, J. Notholt, K. Krüger, V. Mohr, and S. Tegtmeier. A tropical West Pacific OH minimum and implications for stratospheric composition. *Atmospheric Chemistry and Physics*, 14(9):4827–4841, May 2014. ISSN 1680-7324. doi: 10.5194/acp-14-4827-2014. URL `https://www.atmos-chem-phys.net/14/4827/2014/`.

T. Ridder, C. Gerbig, J. Notholt, M. Rex, O. Schrems, T. Warneke, and L. Zhang. Ship-borne FTIR measurements of CO and O_3 in the Western Pacific from 43° N to 35° S: an evaluation of the sources. *Atmospheric Chemistry and Physics*, 12(2):815–828, January 2012. ISSN 1680-7324. doi: 10.5194/acp-12-815-2012. URL `https://www.atmos-chem-phys.net/12/815/2012/`.

H. Riehl. *Tropical Meteorology*. McGraw-Hill, London, 1954.

F. Rohrer and H. Berresheim. Strong correlation between levels of tropospheric hydroxyl radicals and solar ultraviolet radiation. *Nature*, 442(7099):184–187, July 2006. ISSN 0028-0836, 1476-4687. doi: 10.1038/nature04924. URL `http://www.nature.com/articles/nature04924`.

K. H. Rosenlof and J. R. Holton. Estimates of the stratospheric residual circulation using the downward control principle. *Journal of Geophysical Research*, 98(D6):10465, 1993. ISSN 0148-0227. doi: 10.1029/93JD00392. URL `http://doi.wiley.com/10.1029/93JD00392`.

M. L. Salby and M. L. Salby. *Physics of the atmosphere and climate*. Cambridge University Press, Cambridge , New York, 2nd edition, 2012. ISBN 978-0-521-76718-7.

S. P. Sander, R. R. Friedl, J. P. D. Abbatt, J. R. Barker, J. Burkholder, D. M. Golden, C. E. Kolb, M. J. Kurylo, G. K. Moortgat, P. H. Wine, and others. Chemical kinetics and photochemical data for use in atmospheric studies, evaluation number 14. *JPL publication*, 10, 2011.

T. Schneider, T. Bischoff, and G. H. Haug. Migrations and dynamics of the intertropical convergence zone. *Nature*, 513(7516):45–53, September 2014. ISSN 0028-0836, 1476-4687. doi: 10.1038/nature13636. URL `http://www.nature.com/articles/nature13636`.

M. R. Schoeberl and A. E. Dessler. Dehydration of the stratosphere. *Atmospheric Chemistry and Physics*, 11(16):8433–8446, August 2011. ISSN 1680-7324. doi: 10.5194/acp-11-8433-2011. URL `https://www.atmos-chem-phys.net/11/8433/2011/`.

M. R. Schoeberl, H. B. Selkirk, H. Vömel, and A. R. Douglass. Sources of seasonal variability in tropical upper troposphere and lower stratosphere water vapor and ozone: Inferences from the Ticosonde data set at Costa Rica. *Journal of Geophysical Research: Atmospheres*, 120(18):9684–9701, September 2015. ISSN 2169-897X, 2169-8996. doi: 10.1002/2015JD023299. URL `https://onlinelibrary.wiley.com/doi/abs/10.1002/2015JD023299`.

D. W. Scott. *Multivariate Density Estimation: Theory, Practice, and Visualization.* Wiley Series in Probability and Statistics. Wiley, 1 edition, August 1992. ISBN 978-0-471-54770-9 978-0-470-31684-9. URL `https://onlinelibrary.wiley.com/doi/book/10.1002/9780470316849`.

S. C. Sherwood, R. Roca, T. M. Weckwerth, and N. G. Andronova. Tropospheric water vapor, convection, and climate. *Reviews of Geophysics*, 48(2):1, 2010. ISSN 1944-9208. doi: 10.1029/2009RG000301. URL `https://agupubs.onlinelibrary.wiley.com/doi/abs/10.1029/2009RG000301`.

S. C. Sherwood and A. E. Dessler. Convective mixing near the tropical tropopause: Insights from seasonal variations. *Journal of the Atmospheric Sciences*, 60(21):2674–2685, 2003. doi: 10.1175/1520-0469(2003)060⟨2674:CMNTTT⟩2.0.CO;2. URL `https://doi.org/10.1175/1520-0469(2003)060<2674:CMNTTT>2.0.CO;2`.

M. Shiotani. Annual, quasi-biennial, and El Niño-Southern Oscillation (ENSO) timescale variations in equatorial total ozone. *Journal of Geophysical Research*, 97(D7):7625, 1992. ISSN 0148-0227. doi: 10.1029/92JD00530. URL `http://doi.wiley.com/10.1029/92JD00530`.

J. K. P. Shonk, E. Guilyardi, T. Toniazzo, S. J. Woolnough, and T. Stockdale. Identifying causes of Western Pacific ITCZ drift in ECMWF System 4 hindcasts. *Climate Dynamics*, 50(3-4):939–954, February 2018. ISSN 0930-7575, 1432-0894. doi: 10.1007/s00382-017-3650-9. URL `http://link.springer.com/10.1007/s00382-017-3650-9`.

H. B. Singh et al. Reactive nitrogen and ozone over the western Pacific: Distribution, partitioning, and sources. *Journal of Geophysical Research: Atmospheres*, 101(D1):1793–1808, January 1996. ISSN 01480227. doi: 10.1029/95JD01029. URL `http://doi.wiley.com/10.1029/95JD01029`.

V. Sivakumar, H. Bencherif, N. Bègue, and A. M. Thompson. Tropopause Characteristics and Variability from 11 yr of SHADOZ Observations in the Southern Tropics and Subtropics. *Journal of Applied Meteorology and Climatology*, 50(7):1403–1416, July 2011. ISSN 1558-8424, 1558-8432. doi: 10.1175/2011JAMC2453.1. URL `http://journals.ametsoc.org/doi/10.1175/2011JAMC2453.1`.

H. G. J. Smit, S. Oltmans, T. Deshler, D. W. Tarasick, B. J. Johnson, F. J. Schmidlin, R. Stuebi, and J. Davies. SI2N/O3S-DQA Activity: Guide Lines for Homogenization of Ozone Sonde Data. SPARC-IGACO-IOC Report, 2012. URL `27/05/2020`.

H. G. J. Smit. Quality Assurance and Quality Control for Ozonesonde Measurements in GAW. GAW Report No. 201, WMO, 2014. URL `https://library.wmo.int/doc_num.php?explnum_id=7167`.

H. G. J. Smit and W. Sträter. JOSIE-2000 Jülich Ozone Sonde Intercomparison Experiment 2000: the 2000 WMO international intercomparison of operating procedures for ECC-ozone sondes at the environmental simulation facility at Jülich. GAW Report No. 158, WMO, 2004a.

H. G. J. Smit et al. Assessment of the performance of ECC-ozonesondes under quasi-flight conditions in the environmental simulation chamber: Insights from the Juelich Ozone Sonde Intercomparison Experiment (JOSIE). *Journal of Geophysical Research*, 112(D19):D19306, October 2007. ISSN 0148-0227. doi: 10.1029/2006JD007308. URL `http://doi.wiley.com/10.1029/2006JD007308`.

H. G. Smit and D. Kley. JOSIE: The 1996 WMO International intercomparison of ozonesondes under quasi flight conditions in the environmental simulation chamber at Jülich. WMO Global Atmosphere Watch Report No. 130, WMO, Genf, 1998.

H. G. Smit and W. Sträter. JOSIE-1998 performance of ECC ozone sondes of SPC-6A and ENSCI-Z type. GAW Report No. 157, WMO, Genf, 2004b.

H. G. Smit, W. Sträter, D. Kley, and M. Helten. Environmental simulation facility to calibrate airborne ozone and humidity sensors. Juelich Research Center Report Juel-3796, July 2000.

I. N. Smith, A. F. Moise, and R. A. Colman. Large-scale circulation features in the tropical western Pacific and their representation in climate models. *Journal of Geophysical Research: Atmospheres*, 117(D4), February 2012. ISSN 01480227. doi: 10.1029/2011JD016667. URL `http://doi.wiley.com/10.1029/2011JD016667`.

S. Solomon, D. W. J. Thompson, R. W. Portmann, S. J. Oltmans, and A. M. Thompson. On the distribution and variability of ozone in the tropical upper troposphere: Implications for tropical deep convection and chemical-dynamical coupling. *Geophysical Research Letters*, 32(23):L23813, 2005. ISSN 0094-8276. doi: 10.1029/2005GL024323. URL `http://doi.wiley.com/10.1029/2005GL024323`.

S. Solomon, R. R. Garcia, F. S. Rowland, and D. J. Wuebbles. On the depletion of Antarctic ozone. *Nature*, 321(6072):755–758, June 1986. ISSN 0028-0836, 1476-4687. doi: 10.1038/321755a0. URL `http://www.nature.com/articles/321755a0`.

M. Sprenger, M. C. Maspoli, and H. Wernli. Tropopause folds and cross-tropopause exchange: A global investigation based upon ECMWF analyses for the time period March 2000 to February 2001. *Journal of Geophysical Research*, 108(D12):8518, 2003. ISSN 0148-0227. doi: 10.1029/2002JD002587. URL `http://doi.wiley.com/10.1029/2002JD002587`.

R. M. Stauffer, A. M. Thompson, and J. C. Witte. Characterizing Global Ozonesonde Profile Variability From Surface to the UT/LS With a Clustering Technique and MERRA-2 Reanalysis. *Journal of Geophysical Research: Atmospheres*, 123(11):6213–6229, June 2018. ISSN 2169897X. doi: 10.1029/2018JD028465. URL `http://doi.wiley.com/10.1029/2018JD028465`.

P. Stoller et al. Measurements of atmospheric layers from the NASA DC-8 and P-3B aircraft during PEM-Tropics A. *Journal of Geophysical Research: Atmospheres*, 104 (D5):5745–5764, March 1999. ISSN 01480227. doi: 10.1029/98JD02717. URL `http://doi.wiley.com/10.1029/98JD02717`.

B. Sun, T. Reale, S. Schroeder, M. Pettey, and R. Smith. On the Accuracy of Vaisala RS41 versus RS92 Upper-Air Temperature Observations. *Journal of Atmospheric and Oceanic Technology*, 36(4):635–653, April 2019. ISSN 0739-0572, 1520-0426. doi: 10.1175/JTECH-D-18-0081.1. URL `http://journals.ametsoc.org/doi/10.1175/JTECH-D-18-0081.1`.

M. Taguchi. Observed connection of the stratospheric quasi-biennial oscillation with El Niño–Southern Oscillation in radiosonde data. *Journal of Geophysical Research*, 115 (D18):D18120, September 2010. ISSN 0148-0227. doi: 10.1029/2010JD014325. URL `http://doi.wiley.com/10.1029/2010JD014325`.

H. Takashima, M. Shiotani, M. Fujiwara, N. Nishi, and F. Hasebe. Ozonesonde observations at Christmas Island (2°N, 157°W) in the equatorial central Pacific. *Journal of Geophysical Research*, 113(D10):D10112, May 2008. ISSN 0148-0227. doi: 10.1029/2007JD009374. URL `http://doi.wiley.com/10.1029/2007JD009374`.

D. Tan et al. OH and HO2 in the tropical Pacific: Results from PEM-Tropics B. *Journal of Geophysical Research: Atmospheres*, 106(D23):32667–32681, December 2001. ISSN 2156-2202. doi: 10.1029/2001JD900002@10.1002/(ISSN)2169-8996.PEMTROP2. URL `https://agupubs.onlinelibrary.wiley.com/doi/10.1029/2001JD900002@10.1002/(ISSN)2169-8996.PEMTROP2`.

M. Tao, L. L. Pan, P. Konopka, S. B. Honomichl, D. E. Kinnison, and E. C. Apel. A Lagrangian Model Diagnosis of Stratospheric Contributions to Tropical Midtropospheric Air. *Journal of Geophysical Research: Atmospheres*, 123(17):9764–9785, September 2018. ISSN 2169-897X, 2169-8996. doi: 10.1029/2018JD028696. URL `https://onlinelibrary.wiley.com/doi/abs/10.1029/2018JD028696`.

A. M. Thompson, W.-K. Tao, K. E. Pickering, J. R. Scala, and J. Simpson. Tropical deep convection and ozone formation. *Bulletin of the American Meteorological Society*, 78 (6):1043–1054, 1997. doi: 10.1175/1520-0477(1997)078⟨1043:TDCAOF⟩2.0.CO;2. URL `https://doi.org/10.1175/1520-0477(1997)078<1043:TDCAOF>2.0.CO;2`.

A. M. Thompson et al. Southern Hemisphere Additional Ozonesondes (SHADOZ) 1998–2000 tropical ozone climatology 1. Comparison with Total Ozone Mapping Spectrometer (TOMS) and ground-based measurements. *Journal of Geophysical Research*, 108(D2):8238, 2003a. ISSN 0148-0227. doi: 10.1029/2001JD000967. URL `http://doi.wiley.com/10.1029/2001JD000967`.

A. M. Thompson et al. Southern Hemisphere Additional Ozonesondes (SHADOZ) 1998–2000 tropical ozone climatology 2. Tropospheric variability and the zonal wave-one. *Journal of Geophysical Research*, 108(D2):8241, 2003b. ISSN 0148-0227. doi: 10.1029/2002JD002241. URL `http://doi.wiley.com/10.1029/2002JD002241`.

A. M. Thompson, J. C. Witte, H. G. J. Smit, S. J. Oltmans, B. J. Johnson, V. W. J. H. Kirchhoff, and F. J. Schmidlin. Southern Hemisphere Additional Ozonesondes (SHADOZ) 1998–2004 tropical ozone climatology: 3. Instrumentation, station-to-station variability, and evaluation with simulated flight profiles. *Journal of Geophysical Research*, 112(D3):D03304, February 2007. ISSN 0148-0227. doi: 10.1029/2005JD007042. URL `http://doi.wiley.com/10.1029/2005JD007042`.

A. M. Thompson, A. L. Allen, S. Lee, S. K. Miller, and J. C. Witte. Gravity and Rossby wave signatures in the tropical troposphere and lower stratosphere based on Southern Hemisphere Additional Ozonesondes (SHADOZ), 1998–2007. *Journal of Geophysical Research*, 116(D5):D05302, March 2011. ISSN 0148-0227. doi: 10.1029/2009JD013429. URL `http://doi.wiley.com/10.1029/2009JD013429`.

A. M. Thompson et al. Southern Hemisphere Additional Ozonesondes (SHADOZ) ozone climatology (2005-2009): Tropospheric and tropical tropopause layer (TTL) profiles with comparisons to OMI-based ozone products: SHADOZ OZONE DURING AURA. *Journal of Geophysical Research: Atmospheres*, 117(D23):n/a–n/a, December 2012. ISSN 01480227. doi: 10.1029/2011JD016911. URL `http://doi.wiley.com/10.1029/2011JD016911`.

A. M. Thompson et al. First Reprocessing of Southern Hemisphere Additional Ozonesondes (SHADOZ) Ozone Profiles (1998–2016): 2. Comparisons With Satellites and Ground-Based Instruments. *Journal of Geophysical Research: Atmospheres*, 122(23), December 2017. ISSN 2169-897X, 2169-8996. doi: 10.1002/2017JD027406. URL `https://onlinelibrary.wiley.com/doi/abs/10.1002/2017JD027406`.

A. M. Thompson et al. Ozonesonde Quality Assurance: The JOSIE–SHADOZ (2017) Experience. *Bulletin of the American Meteorological Society*, 100(1):155–171, January 2019. ISSN 0003-0007, 1520-0477. doi: 10.1175/BAMS-D-17-0311.1. URL `http://journals.ametsoc.org/doi/10.1175/BAMS-D-17-0311.1`.

D. C. Thornton and N. Niazy. Sources of background current in thr ECC ozonesonde: Implications for total ozone measurements. *Journal of Geophysical Research*, 87(C11): 8943, 1982. ISSN 0148-0227. doi: 10.1029/JC087iC11p08943. URL `http://doi.wiley.com/10.1029/JC087iC11p08943`.

D. C. Thornton and N. Niazy. Effects of solution mass transport on the ECC ozonesonde background current. *Geophysical Research Letters*, 10(2):148–151, February 1983. ISSN

00948276. doi: 10.1029/GL010i002p00148. URL `http://doi.wiley.com/10.1029/GL010i002p00148`.

V. Thouret, J. Y. N. Cho, R. E. Newell, A. Marenco, and H. G. J. Smit. General characteristics of tropospheric trace constituent layers observed in the MOZAIC program. *Journal of Geophysical Research: Atmospheres*, 105(D13):17379–17392, 2000. ISSN 2156-2202. doi: 10.1029/2000JD900238. URL `https://agupubs.onlinelibrary.wiley.com/doi/abs/10.1029/2000JD900238`.

A. J. Troup. The 'Southern Oscillation'. *Quarterly Journal of the Royal Meteorological Society*, 91(390):490–506, October 1965. ISSN 00359009, 1477870X. doi: 10.1002/qj.49709139009. URL `http://doi.wiley.com/10.1002/qj.49709139009`.

J. W. Tukey. *Exploratory data analysis*, volume 2. Reading, Mass., 1977. ISBN 978-0-201-07616-5.

Vaisala. Vaisala Radiosonde RS41 Measurement Performance. Technical report, 2017. URL `https://www.vaisala.com/sites/default/files/documents/WEA-MET-RS41-Performance-White-paper-B211356EN-B-LOW-v3.pdf`.

C. Vigouroux et al. Evaluation of tropospheric and stratospheric ozone trends over Western Europe from ground-based FTIR network observations. *Atmospheric Chemistry and Physics*, 8(23):6865–6886, December 2008. ISSN 1680-7324. doi: 10.5194/acp-8-6865-2008. URL `https://www.atmos-chem-phys.net/8/6865/2008/`.

H. Voemel and K. Diaz. Ozone sonde cell current measurements and implications for observations of near-zero ozone concentrations in the tropical upper troposphere. *Atmospheric Measurement Techniques*, 3(2):495–505, April 2010. ISSN 1867-8548. doi: 10.5194/amt-3-495-2010. URL `https://www.atmos-meas-tech.net/3/495/2010/`.

D. E. Waliser and C. Gautier. A satellite-derived climatology of the ITCZ. *Journal of Climate*, 6(11):2162–2174, 1993. doi: 10.1175/1520-0442(1993)006⟨2162:ASDCOT⟩2.0.CO;2. URL `https://doi.org/10.1175/1520-0442(1993)006<2162:ASDCOT>2.0.CO;2`.

C. Wang. Atmospheric Circulation Cells Associated with the El Niño–Southern Oscillation. *Journal of Climate*, 15:21, 2002.

D. W. Waugh. Impact of potential vorticity intrusions on subtropical upper tropospheric humidity. *Journal of Geophysical Research*, 110(D11):D11305, 2005. ISSN 0148-0227. doi: 10.1029/2004JD005664. URL `http://doi.wiley.com/10.1029/2004JD005664`.

D. W. Waugh and L. M. Polvani. Climatology of intrusions into the tropical upper troposphere. *Geophysical Research Letters*, 27(23):3857–3860, December 2000. ISSN 00948276. doi: 10.1029/2000GL012250. URL `http://doi.wiley.com/10.1029/2000GL012250`.

P. O. Wennberg et al. Hydrogen Radicals, Nitrogen Radicals, and the Production of O_3 in the Upper Troposphere. *Science*, 279(5347):49–53, January 1998. ISSN 00368075, 10959203. doi: 10.1126/science.279.5347.49. URL `https://www.sciencemag.org/lookup/doi/10.1126/science.279.5347.49`.

P. O. Wennberg. Radicals follow the Sun. *Nature*, 442(7099):145–146, July 2006. ISSN 0028-0836, 1476-4687. doi: 10.1038/442145a. URL `http://www.nature.com/articles/442145a`.

J. C. Witte et al. First reprocessing of Southern Hemisphere ADditional OZonesondes (SHADOZ) profile records (1998-2015): 1. Methodology and evaluation: SHADOZ Reprocessed Ozonesonde Profiles. *Journal of Geophysical Research: Atmospheres*, 122 (12):6611–6636, June 2017. ISSN 2169897X. doi: 10.1002/2016JD026403. URL `http://doi.wiley.com/10.1002/2016JD026403`.

J. C. Witte, A. M. Thompson, H. G. J. Smit, H. Vömel, F. Posny, and R. Stübi. First Reprocessing of Southern Hemisphere ADditional OZonesondes Profile Records: 3. Uncertainty in Ozone Profile and Total Column. *Journal of Geophysical Research: Atmospheres*, 123(6):3243–3268, March 2018. ISSN 2169897X. doi: 10.1002/2017JD027791. URL `http://doi.wiley.com/10.1002/2017JD027791`.

I. Wohltmann and M. Rex. The Lagrangian chemistry and transport model ATLAS: validation of advective transport and mixing. *Geoscientific Model Development*, 2(2): 153–173, November 2009. ISSN 1991-9603. doi: 10.5194/gmd-2-153-2009. URL `https://www.geosci-model-dev.net/2/153/2009/`.

I. Wohltmann, R. Lehmann, and M. Rex. The Lagrangian chemistry and transport model ATLAS: simulation and validation of stratospheric chemistry and ozone loss in the winter 1999/2000. *Geoscientific Model Development*, 3(2):585–601, November 2010. ISSN 1991-9603. doi: 10.5194/gmd-3-585-2010. URL `https://www.geosci-model-dev.net/3/585/2010/`.

I. Wohltmann, R. Lehmann, G. A. Gottwald, K. Peters, A. Protat, V. Louf, C. Williams, W. Feng, and M. Rex. A Lagrangian convective transport scheme including a simulation of the time air parcels spend in updrafts (LaConTra v1.0). *Geoscientific Model Development*, 12(10):4387–4407, 2019. doi: 10.5194/gmd-12-4387-2019. URL `https://www.geosci-model-dev.net/12/4387/2019/`.

K. Wolter and M. S. Timlin. El Niño Southern Oscillation behaviour since 1871 as diagnosed in an extended multivariate ENSO index (MEI.ext). *International Journal of Climatology*, 31(7):1074–1087, June 2011. ISSN 08998418. doi: 10.1002/joc.2336. URL `http://doi.wiley.com/10.1002/joc.2336`.

H. M. Worden et al. Comparisons of Tropospheric Emission Spectrometer (TES) ozone profiles to ozonesondes: Methods and initial results. *Journal of Geophysical Research*, 112(D3):D03309, February 2007. ISSN 0148-0227. doi: 10.1029/2006JD007258. URL `http://doi.wiley.com/10.1029/2006JD007258`.

S. Yonemura, H. Tsuruta, S. Kawashima, S. Sudo, L. C. Peng, L. S. Fook, Z. Zohar, and M. Hayashi. Tropospheric ozone climatology over Peninsular Malaysia from 1992 to 1999. *Journal of Geophysical Research*, 107(D15):4229, 2002. ISSN 0148-0227. doi: 10.1029/2001JD000993. URL `http://doi.wiley.com/10.1029/2001JD000993`.

K. Yoneyama. Moisture Variability over the Tropical Western Pacific Ocean. *Journal of the Meteorological Society of Japan*, 81(2):317–337, 2003. ISSN 0026-1165. doi:

10.2151/jmsj.81.317. URL `http://joi.jlc.jst.go.jp/JST.JSTAGE/jmsj/81.317?from=CrossRef`.

K. Yoneyama and D. B. Parsons. A proposed mechanism for the intrusion of dry air into the tropical western pacific region. *Journal of the Atmospheric Sciences*, 56(11):1524–1546, 1999. doi: 10.1175/1520-0469(1999)056⟨1524:APMFTI⟩2.0.CO;2. URL `https://doi.org/10.1175/1520-0469(1999)056<1524:APMFTI>2.0.CO;2`.

C. Yoo and S. Son. Modulation of the boreal wintertime Madden-Julian oscillation by the stratospheric quasi-biennial oscillation. *Geophysical Research Letters*, 43(3):1392–1398, February 2016. ISSN 0094-8276, 1944-8007. doi: 10.1002/2016GL067762. URL `https://onlinelibrary.wiley.com/doi/abs/10.1002/2016GL067762`.

C. Zhang and B. Zhang. QBO-MJO Connection. *Journal of Geophysical Research: Atmospheres*, 123(6):2957–2967, March 2018. ISSN 2169897X. doi: 10.1002/2017JD028171. URL `http://doi.wiley.com/10.1002/2017JD028171`.

J. R. Ziemke, S. Chandra, M. R. Schoeberl, L. Froidevaux, W. G. Read, P. F. Levelt, and P. K. Bhartia. Intra-seasonal variability in tropospheric ozone and water vapor in the tropics. *Geophysical Research Letters*, 34(17):L17804, September 2007. ISSN 0094-8276. doi: 10.1029/2007GL030965. URL `http://doi.wiley.com/10.1029/2007GL030965`.

A. Appendix

A.1. Stratosphere-Troposphere Exchange (Sect.2.1.4)

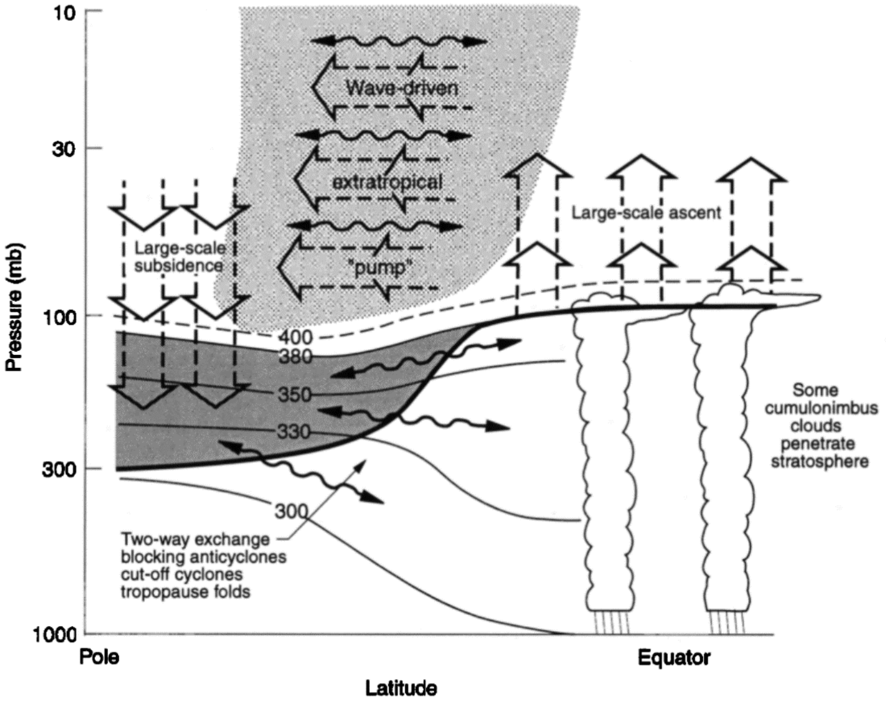

Figure A.1.: Meridional cross-section illustrating major dynamical aspects of Stratosphere-Troposphere Exchange incl. the Brewer Dobson circulation, cited from Holton et al. (1995), see original for more details, see Sect.2.1.4.

A.2. Instrumental Development (Sect.3.1.4)

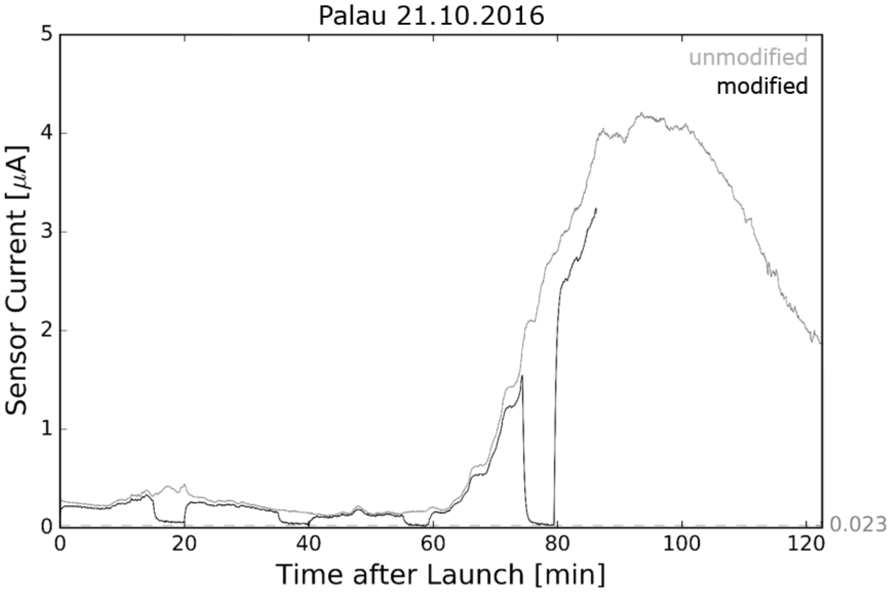

Figure A.2.: Sensor current measurements for a twin launches with one modified (black line) and one unmodified (gray line) ECC sonde on the same balloon, conducted in Palau in 2016, 5 minute no-ozone periods were measured at 15, 35, 55 and 75 minutes after launch, background current of the modified sonde indicated by a gray dashed line and noted in gray on the right; compare Fig.3.5.

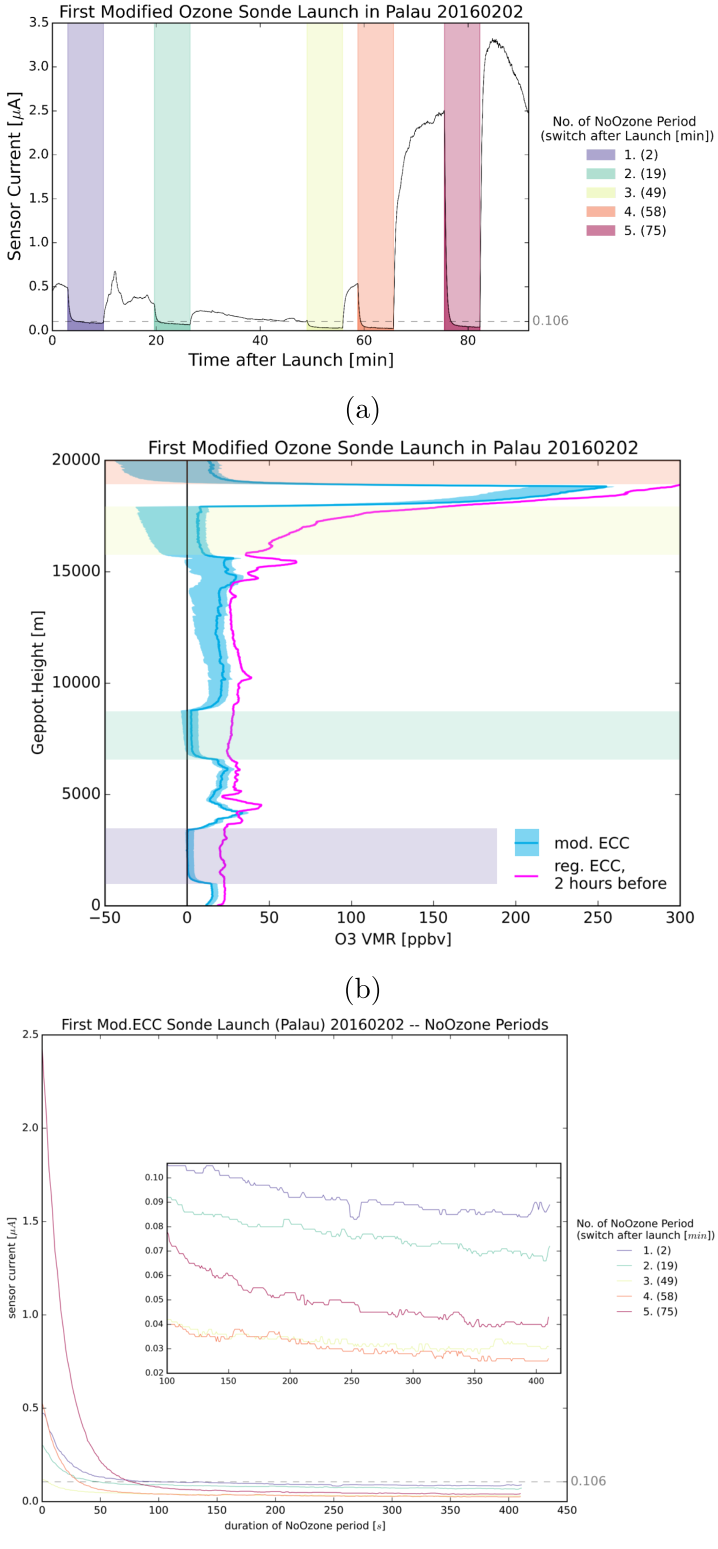

(a)

(b)

(c)

Figure A.3.: Modified ECC sonde launched in Palau, 02.02.2016, (a) shows the development of the sensor current with time, (b) the profile of calculated O_3 VMR for different background current corrections (in blue, compare Fig.3.2) and a profile of an unmodified ECC sonde launched 2 hours later with a pressure dependent background current correction (in pink), (c) gives a close-up of the no-ozone periods, which are color-coded in all three subfigures; compare Fig.3.5 and Fig.3.6.

A.3. Tropospheric O_3 Variability (Sect.4.1)

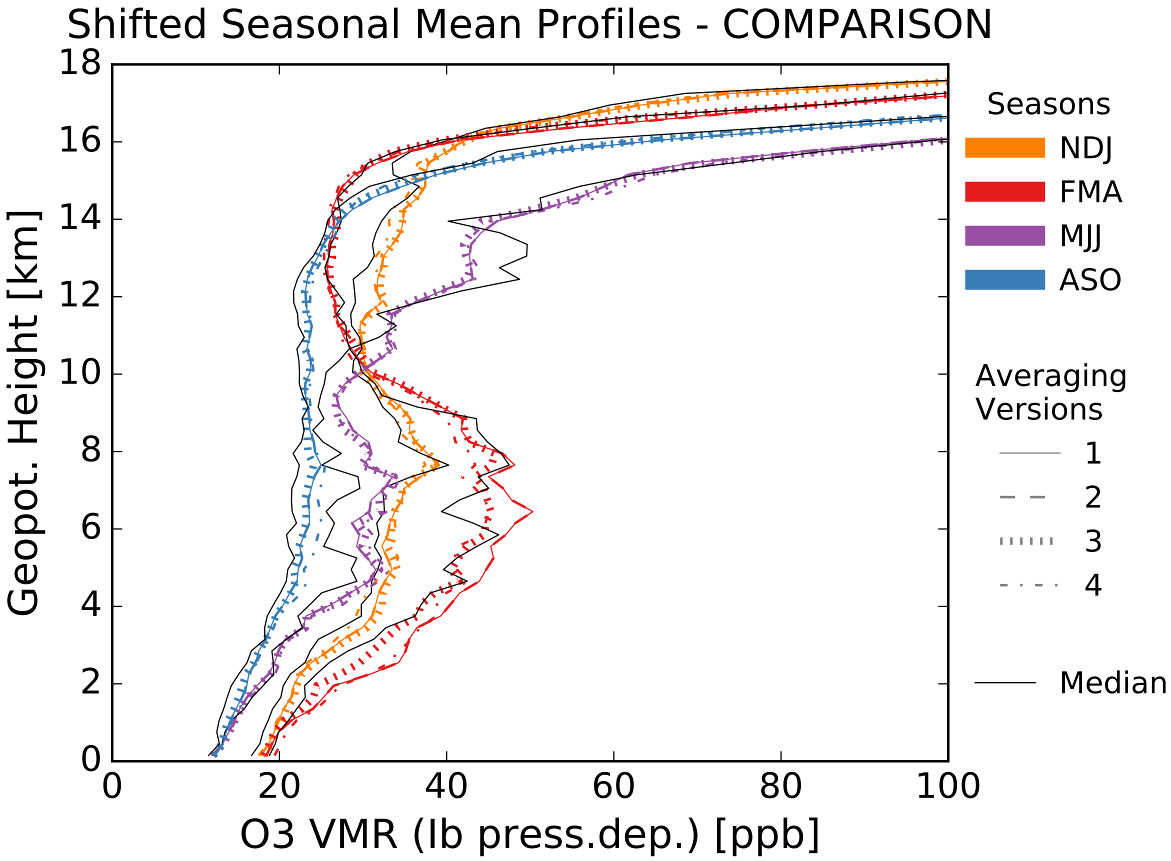

Figure A.4.: Comparison of all averaging versions (colored lines) for the seasonal mean, see Sect.3.2.3, median (black solid line) derived in analogy to climseasmean$_3(s)$.

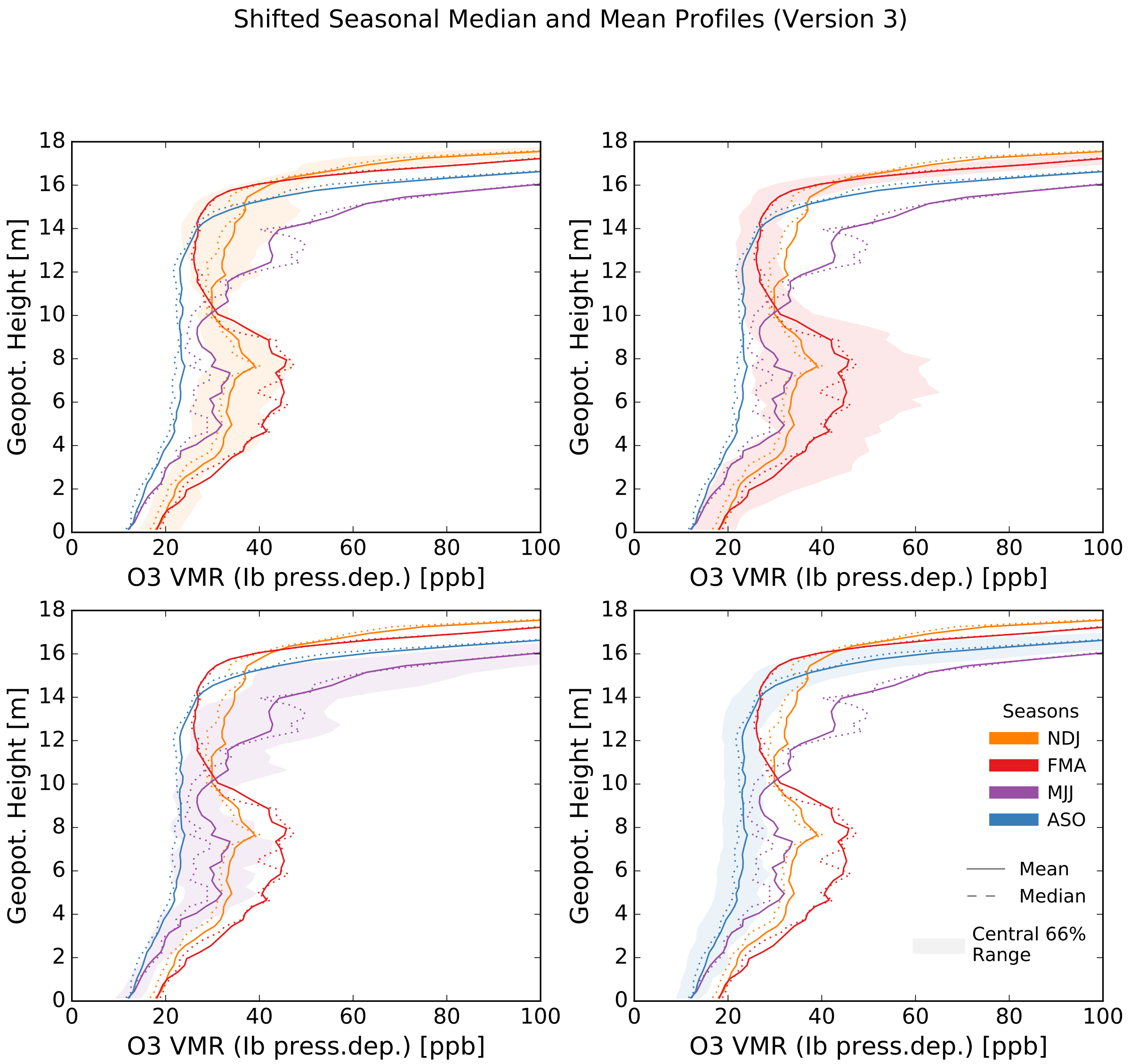

Figure A.5.: Comparison between mean (solid line) and median (dashed line) for seasonal averages climseasmean$_3(s)$ (different colors), shadings indicate central 66% ranges for different seasons per subfigure, see Sect.3.2.3.

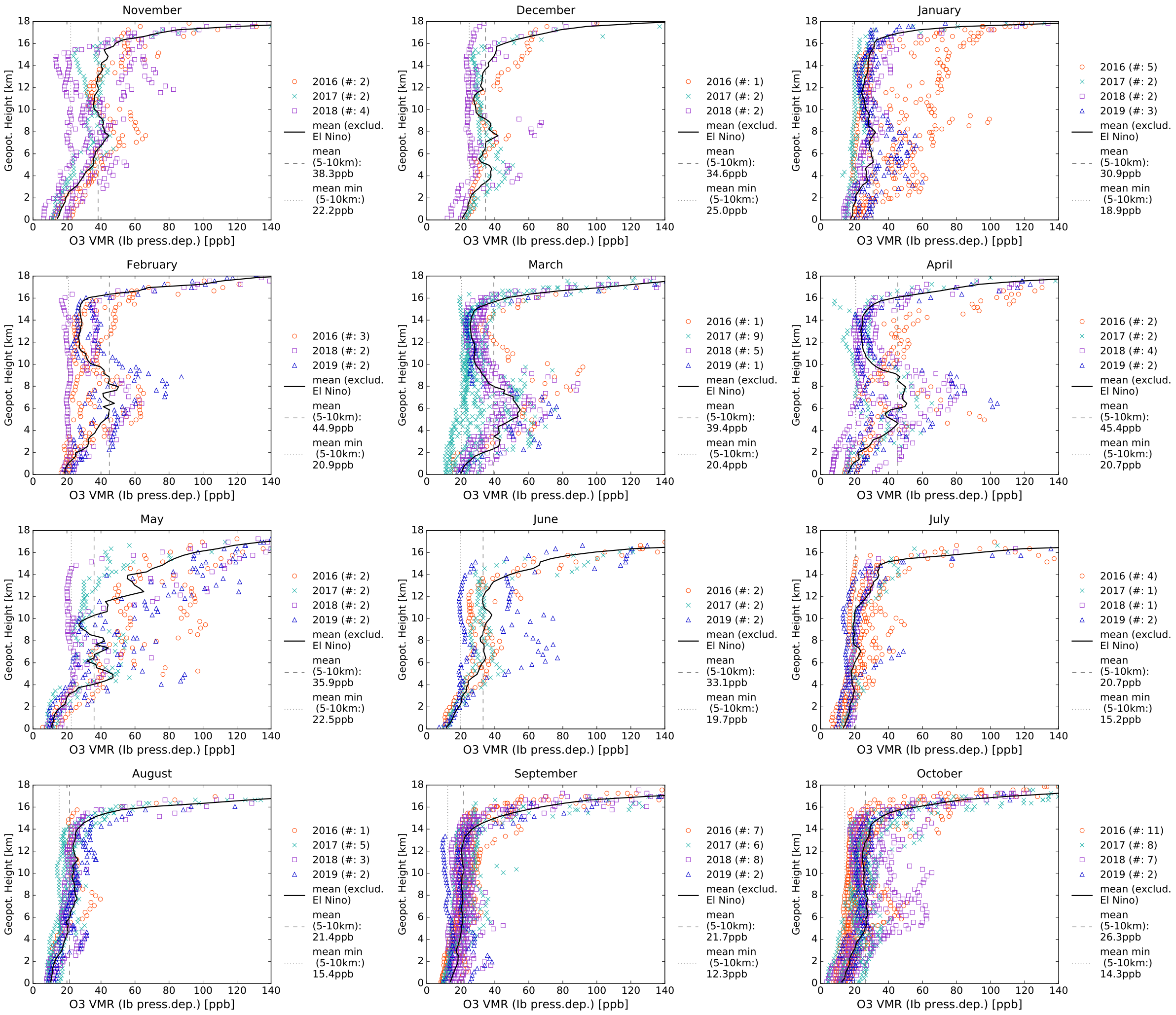

Figure A.6.: All measured individual O_3 VMR profiles sorted by month and year (colored markers), the monthly mean (solid black line) and monthly statistics as in Fig.4.7; number (#) of individual profiles per year given in brackets.

A.4. Relation between O_3 and Relative Humidity (Sect.4.2.2)

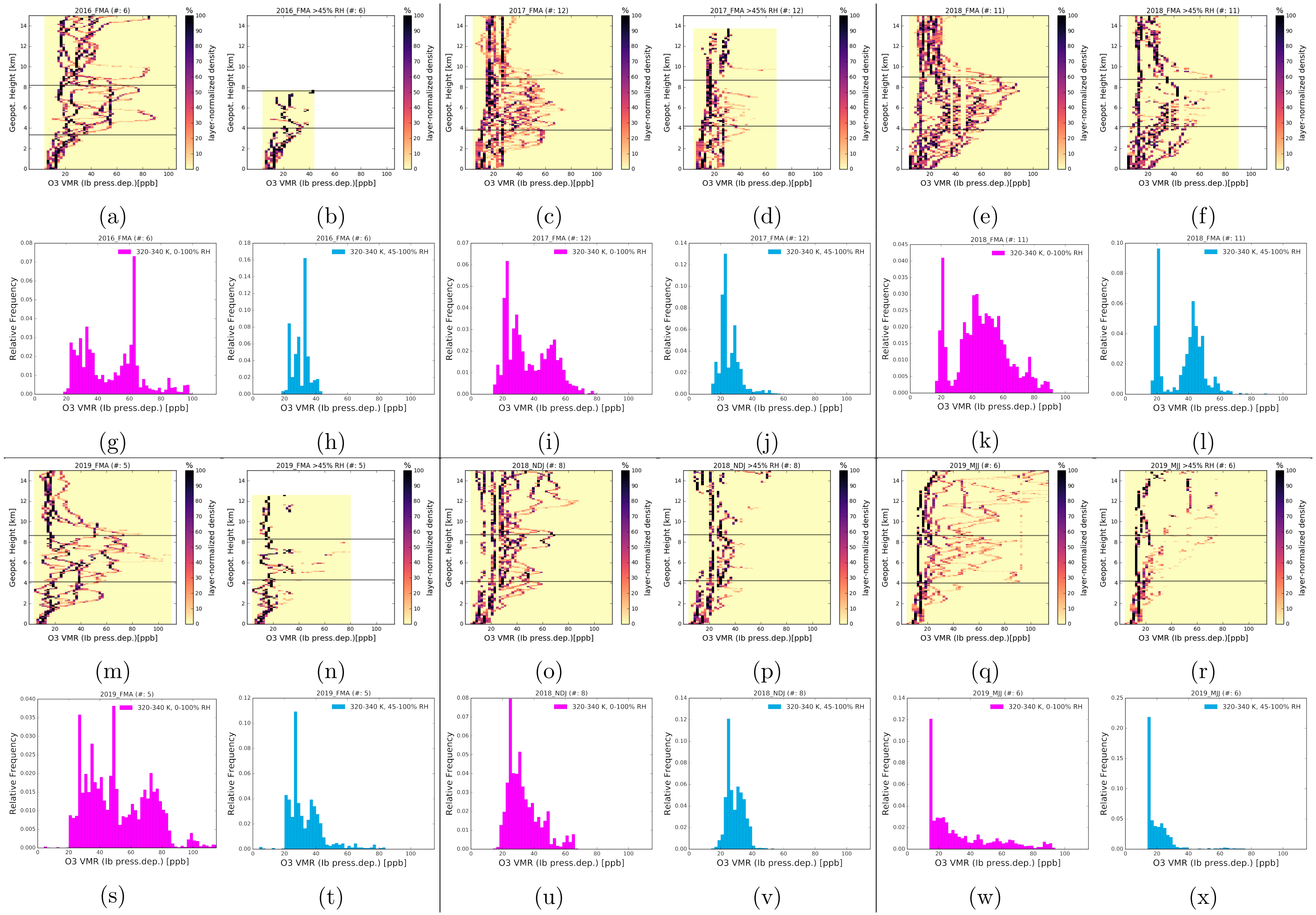

(a) (b) (c) (d) (e) (f)

(g) (h) (i) (j) (k) (l)

(m) (n) (o) (p) (q) (r)

(s) (t) (u) (v) (w) (x)

Figure A.7.: Seasonal relative frequency distribution (normalized to the layer maximum) of tropospheric (0-15 km) O_3 VMR with altitude for selected cases, for details see Fig.4.15.

A.5. Trajectory Analysis Results (Sect.4.3.2)

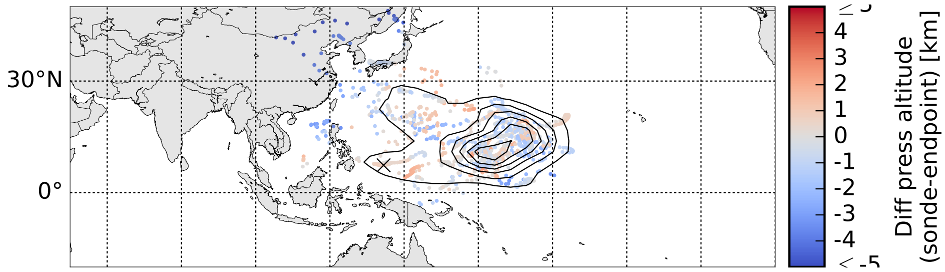

(a) NDJ (2377/24)

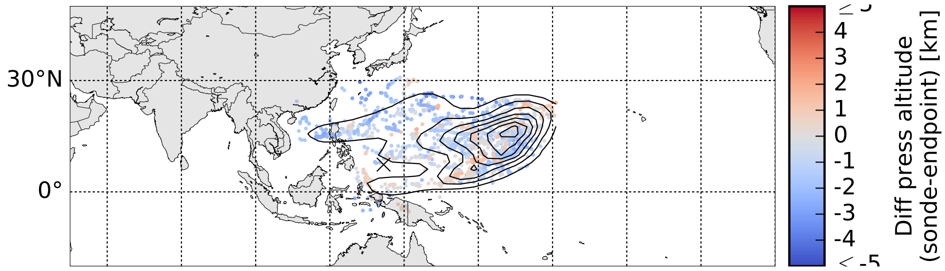

(b) FMA (3085/31)

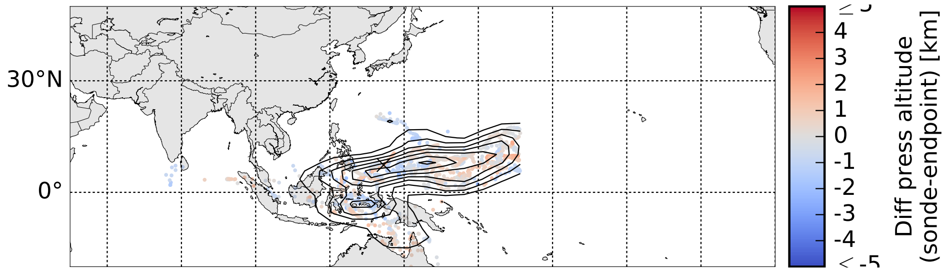

(c) MJJ (2465/24)

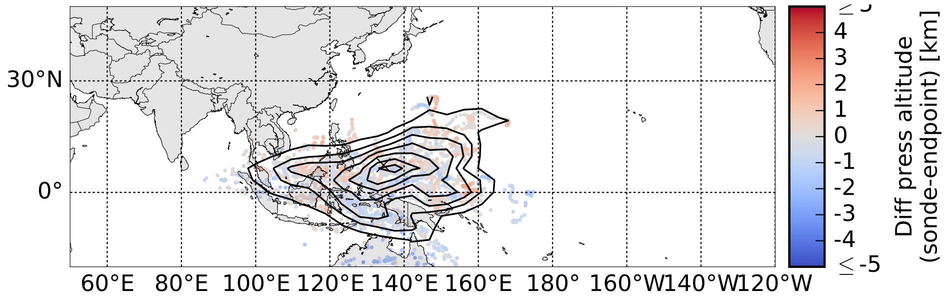

(d) ASO (5753/59)

Figure A.8.: 5 days backward trajectory ending points arriving at 2-5 km in Palau per season (compare Fig.4.24), color-coded by difference in pressure altitudes (measured sonde height - ending point height); contours show the KDE (compare Sect.3.4.1) distribution, in brackets: number of trajectories/profiles.

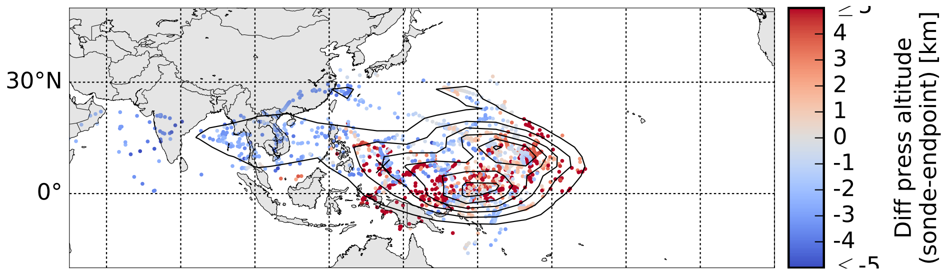

(a) NDJ (2377/24)

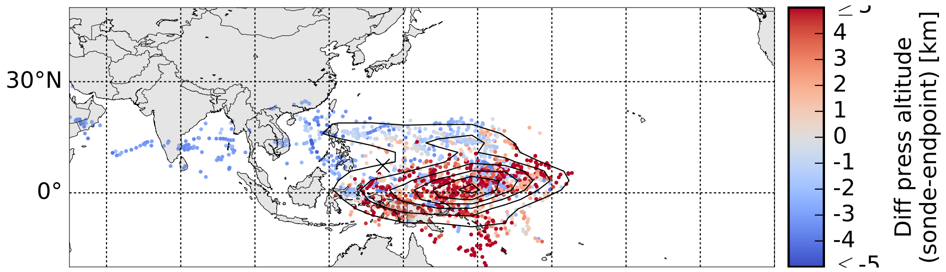

(b) FMA (3085/31)

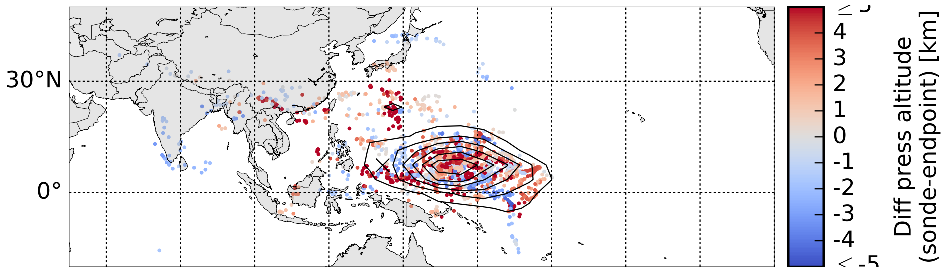

(c) MJJ (2465/24)

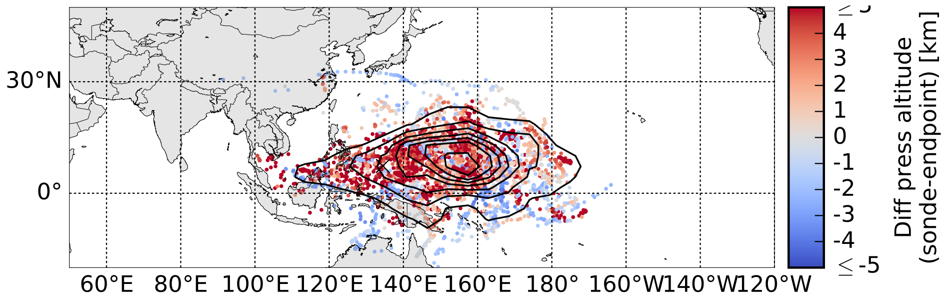

(d) ASO (5753/59)

Figure A.9.: 5-days backward trajectory ending points arriving at 10-14 km in Palau per season (compare Fig.4.24), color-coded by difference in pressure altitudes (measured sonde height - ending point height); contours show the KDE (compare Sect.3.4.1) distribution, in brackets: number of trajectories/profiles.

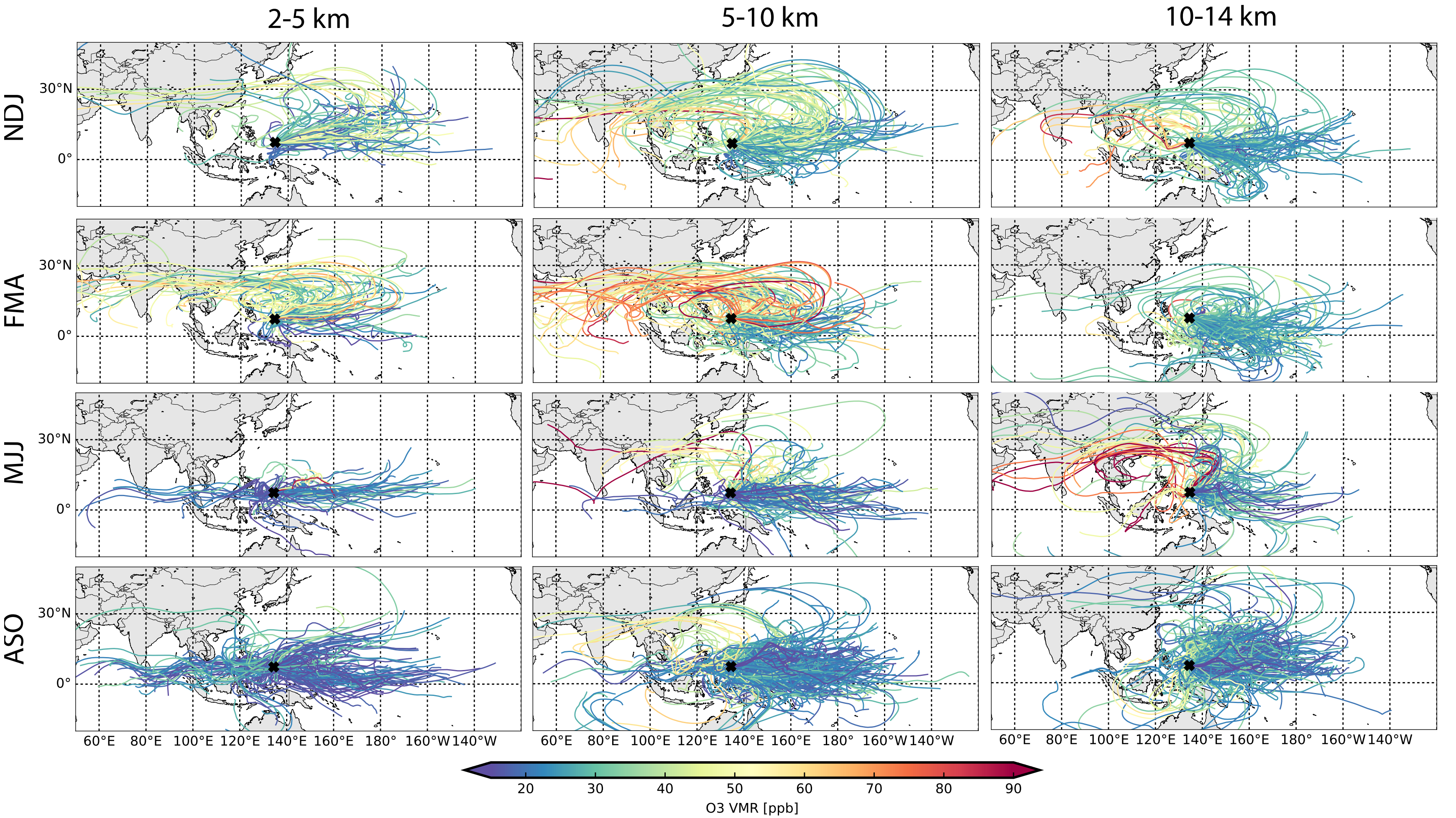

Figure A.10.: 10-days backward trajectories arriving at 2-5 km, 5-10 km and 10-14 km (in columns) in Palau by season (in rows), color-coded by O_3 VMR at arrival (measured by sonde); for number of trajectories/profiles, see Tab.4.1; compare Fig.4.23 in Sect.4.3.2.

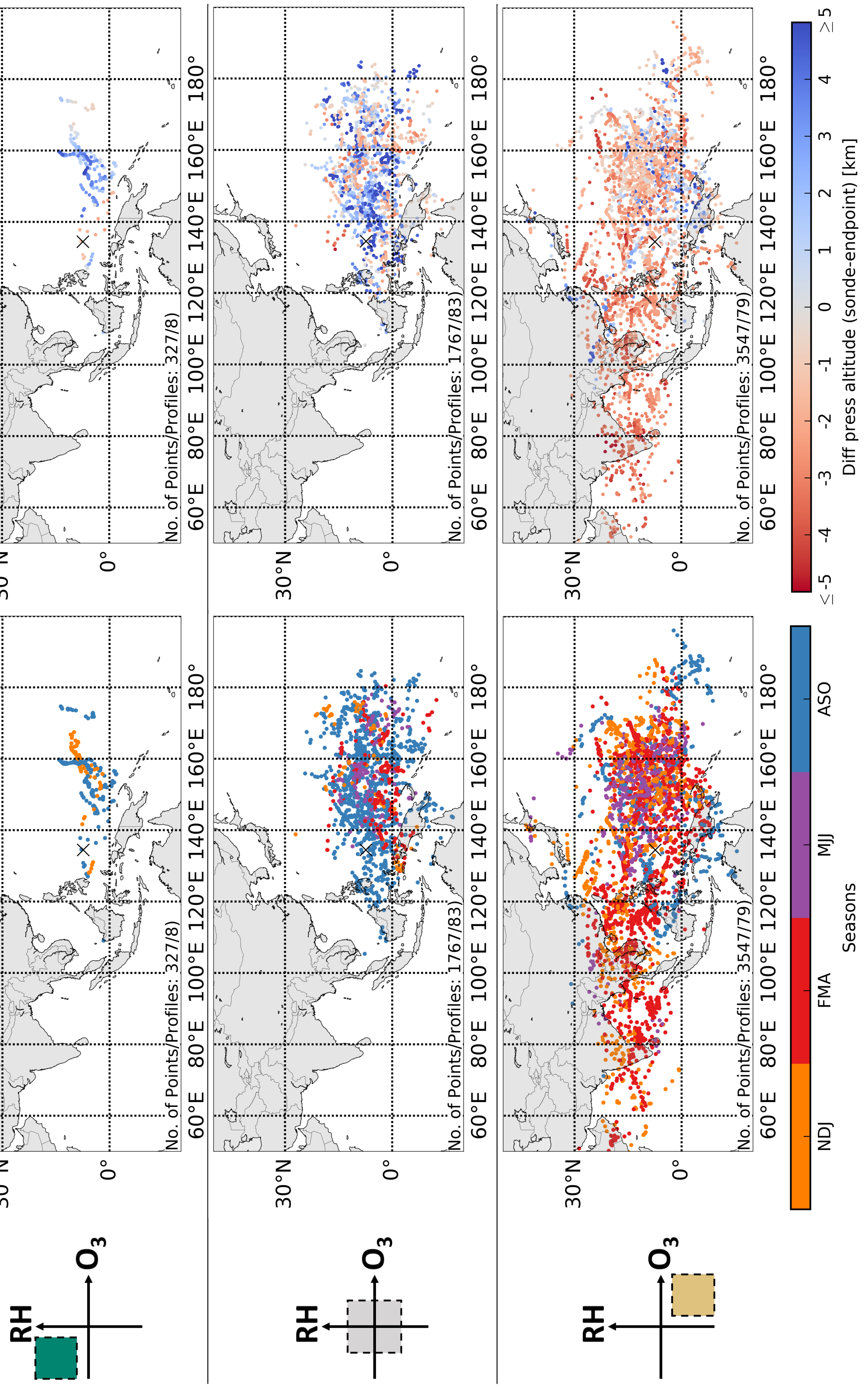

Figure A.11.: 5-days backward trajectory ending points arriving at 5-10 km in Palau, color-coded by season (central column) and difference in pressure altitude (right column) for air masses of different O_3RH groups using measured values: O_3-RH+ (3 times 3 scheme, top row), $O_3\circ$RH$\circ$ (3 times 3 scheme, central row) and O_3+RH- (3 times 3 scheme, bottom row); left column shows pictograms of groups (compare Fig.4.18a,4.18c and Fig.4.25).

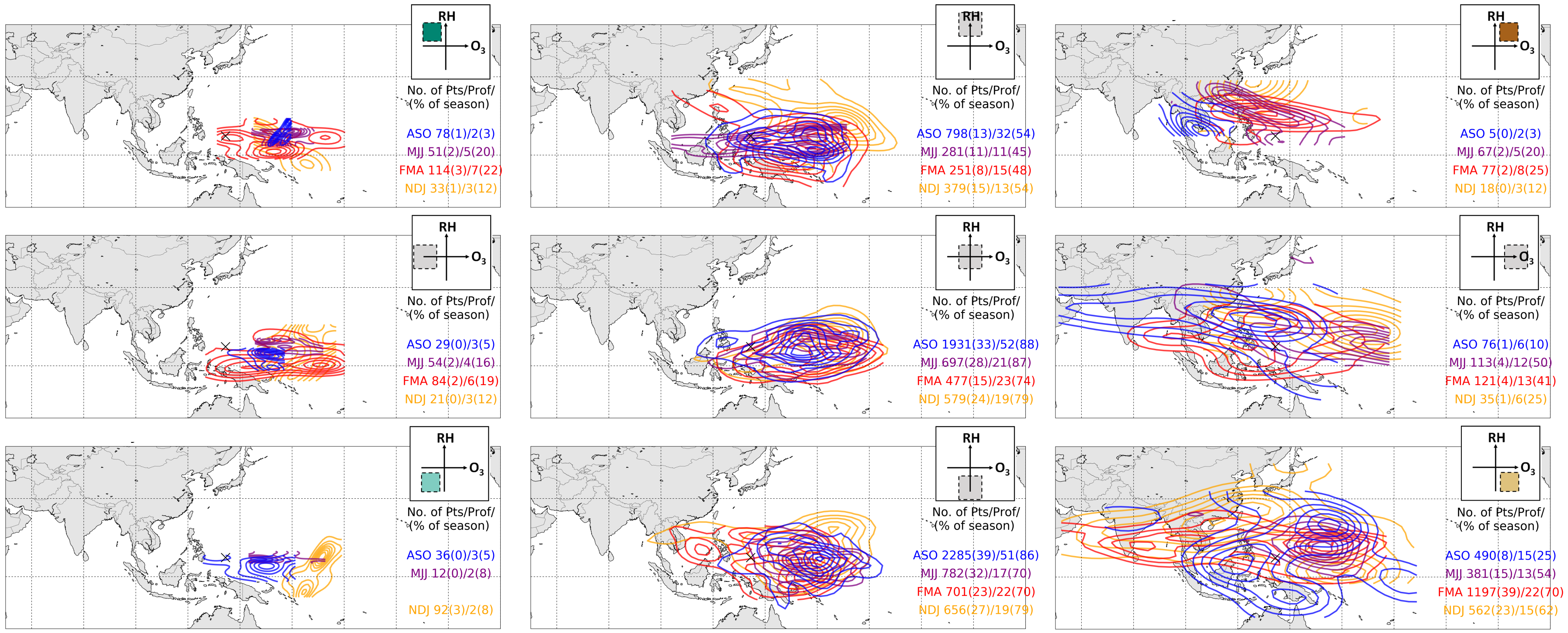

Figure A.12.: Seasonal KDE distributions of O$_3$RH groups according to the classification in Fig.4.18b and 4.18c from 5-days backward trajectory ending points within 5-10 km, number of ending points and profiles per season given in absolute values and as seasonal fraction in brackets; compare Fig.4.25 and 4.20.